Electrodynamics of the Auroral Ionosphere During Magnetospheric Substorms

Thesis submitted for the degree of
Doctor of Philosophy
at the University of Leicester

James Wild
Radio and Space Plasma Physics Group
Department of Physics and Astronomy
University of Leicester

October 2000

UMI Number: U129321

All rights reserved

INFORMATION TO ALL USERS
The quality of this reproduction is dependent upon the quality of the copy submitted.

In the unlikely event that the author did not send a complete manuscript
and there are missing pages, these will be noted. Also, if material had to be removed,
a note will indicate the deletion.

UMI®
Dissertation Publishing

UMI U129321
Published by ProQuest LLC 2013. Copyright in the Dissertation held by the Author.
Microform Edition © ProQuest LLC.
All rights reserved. This work is protected against
unauthorized copying under Title 17, United States Code.

ProQuest®

ProQuest LLC
789 East Eisenhower Parkway
P.O. Box 1346
Ann Arbor, MI 48106-1346

Electrodynamics of the Auroral Ionosphere During Magnetospheric Substorms

James Wild

Abstract: One of the principal consequences of magnetic reconnection at the dayside magnetopause is the transfer of solar wind energy in the Earth's magnetotail. The expansion phase of a magnetospheric substorm corresponds to the sudden release of this energy and is characterised in the ionosphere by the sudden brightening and poleward expansion of the auroral oval near midnight and the intensification of the ionospheric currents flowing in the auroral zone. Observations of various high-latitude ionospheric phenomena associated with magnetospheric substorm are presented. In particular, use is made of the Co-operative UK Twin Located Auroral Sounding System (CUTLASS), a high frequency bistatic coherent-scatter radar with sites in Finland and Iceland.

Azimuthally Propagating Vortical Currents (APVCs) are the ionospheric flow signatures of upward directed field-aligned currents in the nightside ionosphere. Two case studies of APVCs are presented and their structure examined in detail. In addition, the results of a statistical study of APVC occurrence encompassing over 1000 hours of high-time resolution data are discussed with particular focus on the relationship of APVCs to magnetospheric substorm phase. Omega bands are a distinct class of auroral form that have previously been observed in the morning sector during the recovery phase of magnetospheric substorms. High-time resolution measurements of the ionospheric flow within a series of omega bands from the CUTLASS Finland radar are presented. Complementary observations from the Scandinavian Twin Auroral Radar Experiment (STARE) and ground magnetometers of the IMAGE array are employed in order to characterise the electric and magnetic field structure of omega bands. Revised descriptions of omega band structure and formation mechanism are proposed. Finally, multi-instrument observations of the evolution of a high-latitude polar auroral arc during the recovery phase of an isolated substorm are presented and its relation to upstream interplanetary magnetic field conditions discussed.

This thesis is dedicated to
Mum and Dad,
and the memory of
Prof. Leonard Roberts (1929-1999)

ACKNOWLEDGEMENTS

I would like to thank the following people without whom this thesis would not have been written:

Prof. Stan Cowley, head of the Radio and Space Plasma Physics Group, for the opportunity to carry out this research and PPARC for funding my studentship. My supervisor, Dr. Tim Yeoman, for his guidance, seemingly infinite patience, and outstanding samosas. For his encouragement, insight into physics, and above all friendship I shall be eternally grateful. Dr. Mark Lester for always being ready to offer support and encouragement, despite there not being enough hours in the day, and Prof. Tudor Jones for sharing his wealth of experience in ionospheric physics.

Prof. Hermann Opgenoorth and Paul 'the dog' Eglitis of the Finnish Meteorological Institute for their help in unravelling the omega bands.

My many friends in the Radio and Space Plasma Physics Group, especially; Steve Milan for providing software, endless good ideas, and fine red wine; Hina Khan for ensuring I never ran out of chocolate; Darren Wright for demonstrating the wonders of C, squash and strange sandwiches, and Jackie Davies for her advice on all things incoherent. Emma Bunce for always saying exactly the right thing and Kathryn McWilliams for not being American. Gabby Provan, Ranvir Dhillon, Jon 'part-time' Storey, Jonny Rae, Nigel Wade, Adrian Grocott, Emma 'Evil Edna' Woodfield, Jon Gauld and Lisa Baddeley for all those happy times spent in hostelries world-wide. Chris Thomas and Julian Thornhill for providing computing support and Peter Chapman for instructing me in the art of antenna climbing. The workshop technicians Stuart Crooks, Mick Parsons, and David Payne for keeping everything running and Alison Wesley for looking after all the paperwork and the gossip.

All the great friends I have made in the solar-terrestrial physics community over that last three years; Clare Watt, Gareth Chisham, Raphael Andre, Rob Lewis, Vikki Howells, Ian McCrea, Anastasia (*a.k.a.* Molly) Stockton-Chalk and Ian Robinson to name but a few.

Ben, Dave, Drew, Rob, Tim and Wil (the Bistro posse) for buying so many rounds over the years. Bev Sherbon and the many other friends I made working behind the bars of the Student's Union. Thanks especially to Suzy for complaining about my loud music.

Finally, thanks to my whole family, Mum and Dad in particular, for their continuous support and understanding throughout the course of my studies. Thank you all.

CONTENTS

Chapter 1: Introduction & background

1.1 Introduction **1**

1.2 The Sun-Earth system **1**

1.2.1 The solar wind & the interplanetary magnetic field 1

1.2.2 The terrestrial magnetosphere 2

1.2.3 Reconnection and the "open" magnetosphere 3

1.3 The ionosphere **5**

1.3.1 The structure of the ionosphere 6

1.3.2 Ionospheric currents and conductivity 7

1.3.3 Magnetosphere-Ionosphere coupling and the aurora 7

1.4 Summary **8**

Chapter 2: Fundamental ionospheric and magnetospheric electrodynamics

2.1 Introduction **9**

2.2 Ionospheric conductivity **9**

2.2.1 Conductivity of an unmagnetised plasma 9

2.2.2 Conductivity of a magnetised plasma 10

2.3 Large-scale ionospheric electrodynamics **13**

2.3.1 High-latitude ionospheric convection 13

2.3.2 The auroral electrojets 14

2.3.3 Auroral arc associated electric fields 16

2.4 Magnetospheric substorms **17**

2.4.1 The development of the substorm concept 17

2.4.2 Phenomenological models of substorms 19

2.4.3 The near-Earth neutral-line model 20

2.4.4 The current sheet-disruption model 23

2.4.5 Recent developments in substorm models 24

2.5 Summary **25**

Chapter 3: Ionospheric diagnostic instruments

3.1 Introduction **27**

3.2 Radio wave diagnosis of the ionosphere **27**

3.2.1 The development of radar 27
3.2.2 Radio wave propagation in the ionosphere 28
3.2.3 Ionospheric irregularities 30
3.2.4 The principles of coherent scatter 32
3.3 Coherent-scatter radars 34
3.3.1 CUTLASS 34
3.3.2 SuperDARN 37
3.3.3 STARE 38
3.4 Incoherent-scatter radars 39
3.4.1 Incoherent-scatter theory 39
3.4.2 EISCAT 40
3.5 Magnetic field observations 41
3.5.1 The measurement of magnetic fields 41
3.5.2 Magnetometer arrays 42
3.6 Summary 43

Chapter 4: CUTLASS HF radar observations of high-latitude azimuthally propagating vortical currents in the nightside ionosphere during magnetic substorms
4.1 Introduction 44
4.2 Instrumentation 46
4.3 APVC case study: 27th August 1996 46
4.3.1 Ground-based magnetometer observations 46
4.3.2 Radar measurements of ionospheric convection 47
4.4 APVC case study: 1st July 1998 48
4.4.1 Ground-based magnetometer observations 48
4.4.2 Radar measurements of ionospheric convection 49
4.5 Discussion of case studies 49
4.5.1 27th August 1996 50
4.5.2 1st July 1998 53
4.6 Statistical analysis of APVC observations 55
4.7 Discussion 56
4.8 Summary 57

Chapter 5: Multi-instrument observations of the electric and magnetic field structure of omega bands

5.1 Introduction **59**

5.2 Instrumentation **60**

5.3 Observations of omega bands **61**

5.3.1 Ground magnetometer response 61

5.3.2 Radar measurements of ionospheric convection 62

5.3.3 Derived equivalent current features 63

5.3.4 Derived ionospheric Hall conductances 64

5.4 Discussion **67**

5.4.1 Omega band structure 67

5.4.2 Omega band formation 68

5.5 Summary **70**

Chapter 6: High-time resolution radar observations of high-latitude flows during the recovery phase of an isolated substorm

6.1 Introduction **72**

6.2 Instrumentation **73**

6.3 Observations **75**

6.3.1 Interplanetary conditions 75

6.3.2 Ground-based magnetometer observations 76

6.3.3 HF radar observations of ionospheric flow 77

6.3.4 Incoherent-scatter radar observations 78

6.3.5 Two-dimensional ionospheric flow measurements 80

6.4 Discussion **83**

6.5 Summary **86**

Chapter 7: Summary and suggestions for further work

7.1 Introduction **88**

7.1.1 Azimuthally propagating vortical currents 89

7.1.2 Auroral omega bands 89

7.1.3 High-latitude arc evolution 90

7.2 Suggestions for further work **91**

Appendices:

Appendix A	**SuperDARN radar locations**	**94**
Appendix B	**Ground magnetometer locations**	**95**
B.1	Greenland coastal magnetometers	95
B.2	IMAGE magnetometers	96
B.3	NIPR magnetometers	97
B.4	SAMNET magnetometers	97
B.5	Tromsø auroral observatory magnetometers	98
Appendix C	**List of acronyms**	**99**

References **101**

CHAPTER 1

Introduction & background

1.1 Introduction

This thesis explores several phenomena that occur in the high-latitude ionosphere during periods of magnetospheric substorm activity. Magnetospheric substorms are one of the principal mechanisms by which energy is transferred from the magnetosphere to the ionosphere yet the evolution and triggering processes involved remain poorly understood. Although these processes take place far from the surface of the Earth, magnetospheric substorms give rise to some of the most impressive high-latitude auroral displays. As a result, ground-based instruments routinely observe the ionospheric signatures of magnetospheric processes and these observations are exploited in order to derive information regarding the configuration and dynamics of the magnetosphere. Chapter 1 summarises the basic properties of the ionosphere, the magnetosphere and the solar-terrestrial environment. Chapter 2 contains a more detailed examination of the electrodynamic behaviour of the ionospheric medium and the complex system of currents that pervade the high-latitude ionosphere. In addition, a review of the competing theories of substorm evolution and triggering is included. A comprehensive description of the instrumentation employed to undertake observations of the geophysical phenomena under scrutiny is presented in Chapter 3 and results are offered in Chapters 4, 5 and 6.

1.2 The Sun-Earth system

1.2.1 The solar wind & the interplanetary magnetic field

The Sun's overall mass of ~2×10^{30} kg is predominantly composed of hydrogen (~90%) and helium (~10%) constrained by its own gravity (e.g. Priest, 1995). At its peak, the temperature of the Sun's outer atmosphere, or *Corona*, reaches ~2×10^{6} K, high enough to ionise both hydrogen and helium atoms resulting in the formation of a fully ionised plasma. At the base of the corona the gas pressure of this plasma is sufficiently high that it can no longer be contained by the Sun's gravity and the plasma expands outwards into the solar system forming the *solar wind.* Within ~10 solar radii of the Sun the solar wind is accelerated to ~400 km s^{-1} after which its speed remains approximately constant until it is confined by the

interstellar medium at distances of ~100-150 AU. Embedded in the solar wind are the remnants of the solar magnetic field and this is generally termed the *Interplanetary Magnetic Field* (IMF).

There are many excellent texts that discuss in detail the formation and dynamics of the solar wind and the IMF (e.g. Kivelson and Russell, 1995; Baumjohann and Treumann, 1997) and it is therefore appropriate that these processes are discussed only briefly here. Assuming the Sun's magnetic field to be approximately dipolar, if one considers a single field line as it is carried away from the Sun by the solar wind then after a suitably long time the field near the sun points either radially inwards or outwards. Plasma streams away from the Sun along the radial field lines and an azimuthal current sheet separates the oppositely-directed fields on either side of the equatorial plane. As it streams outward from the Sun, there are two important factors that perturb the configuration of the IMF from this "ideal" description. Firstly, as any given element of the solar wind moves out radially, its IMF footprint which is frozen into the Sun rotates with a period of approximately 25 days. As a consequence the field line is wound up into spirals often referred to as *Parker spirals* (Figure 1.1). Secondly, the dipole axis of the solar magnetic field is not aligned parallel to the rotation axis implying that the azimuthal current sheet does not lie in equatorial plane. In practice the current sheet is distorted and contains folds or flutes as shown in Figure 1.2. As a consequence, depending on the relative position of the Earth to the current sheet the IMF orientation and magnitude measured at the Earth will vary between sectors of "towards" and "away" magnetic field. This variability in the IMF observed at the Earth exerts an influence on the coupling between the Sun and the Earth's magnetic fields (Yeoman *et al.*, 1990a; Freeman and Farrugia, 1995)

1.2.2 The terrestrial magnetosphere

The Earth's magnetic field can be approximated in the first order to a dipole which is tilted with respect to the axis of rotation by ~11°, the source of which is the complex pattern of currents that flow within the molten, electrically conducting core of the Earth. The magnetic field is directed away from the Earth in the southern hemisphere and towards the Earth in the northern hemisphere with the northern geomagnetic pole shifted toward the North American continent from the geographic pole.

As first postulated by Chapman and Ferraro (1931, 1932) the Earth's magnetic field behaves as an effective obstacle to the highly supersonic solar wind. As the solar wind sweeps by, a cavity is formed in which the Earth's magnetic field rather than the IMF dominates. This

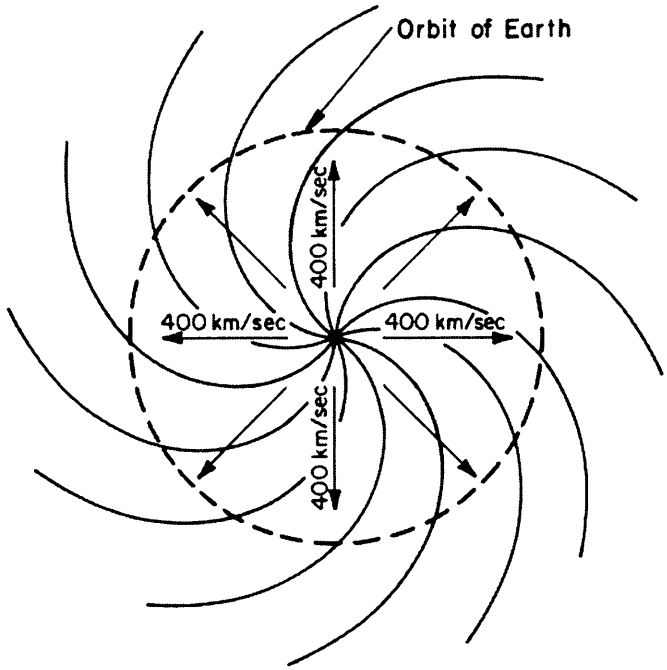

Figure 1.1. The configuration of the interplanetary magnetic field in the solar equatorial plane due to a radial solar wind outflow of 400 km s^{-1} and the rotation of the sun in an anticlockwise sense (adapted from Parker, 1963).

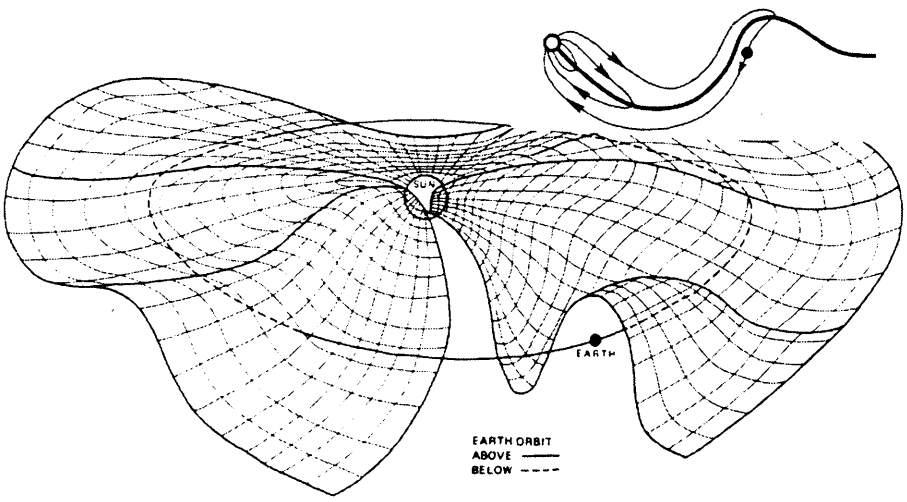

Figure 1.2. A schematic representation of the solar equatorial current sheet and associated magnetic field lines. The current sheet is shown as lying near to the solar equator with spiralled, outward-pointing magnetic fields lying above it and inward-pointing fields lying below it. Because the current sheet is distorted and contains folds an observer near the ecliptic will alternately lie above and below the current and see a changing local magnetic field. The inset shows a meridional cross section with the Earth below the current sheet (from Kelley, 1989).

cavity is known as the *magnetosphere*. On the dayside the Earth's magnetic field is compressed toward the Earth and on the nightside it is drawn out to form the *magnetotail*. In the early 1930's Chapman and Ferraro envisaged plasma and magnetic field to be "frozen" together perfectly. However, they were unaware of the existence of the interplanetary magnetic field. The frozen-in theory does not allow plasma to be exchanged between the solar wind and the magnetosphere; regions are populated by either one plasma variety or another, not a combination. The Chapman and Ferraro description can be readily extended to include two sources of magnetised plasma as depicted in Figure 1.3, where the fundamental concept of frozen-in flow still applies. Plasma is strictly divided between regions of solar wind and terrestrial origin and the location of the boundaries between these regions will be determined by pressure balances. Furthermore, these boundaries will represent current sheets since in general the magnetic field magnitude and direction will vary abruptly across them. This description of magnetospheric formation whereby plasma is partitioned according to its source is often referred to as the "closed" magnetosphere description.

1.2.3 Reconnection and the "open" magnetosphere

Fundamental plasma theory demonstrates that charged particles subject to a magnetic field orbit the magnetic field line at a distance known as the *gyroradius*. Inherent in the frozen-in approximation of a magnetised plasma is the assumption that the scale length of the magnetic field is large compared with a typical plasma particle gyroradius. Although this is a valid approximation over most of the magnetosphere it begins to break down at the magnetopause current sheet, the boundary which separates the two plasma populations. At the magnetopause there exists a large magnetic shear across the current sheet. In a process first suggested by Dungey (1961) the magnetic fields on either side of the boundary may diffuse relative to the plasma into the current sheet from either side (Figure 1.4). In the resulting X-type magnetic field geometry, field lines connect the two plasma regimes across the boundary. This process is known as *magnetic reconnection*. Magnetic tension will then cause the newly reconnected field lines to retreat along the current sheet, away from the reconnection site allowing further field lines from the two original populations to diffuse into the current sheet and undergo reconnection.

The implications of reconnection and the breakdown of the frozen-in description are significant. The plasma regimes associated with the solar wind and the magnetosphere are now able to mix. Reconnection has provided a mechanism by which "open" field lines arise, straddling the magnetopause such that one end remains connected to the solar wind and the

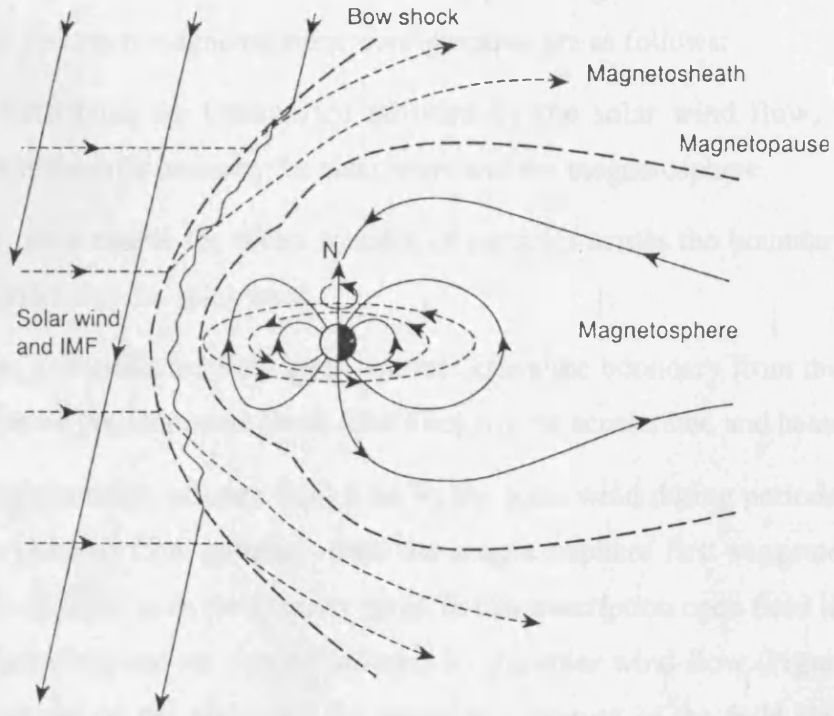

Figure 1.3. Schematic view of magnetospheric configuration in the noon-midnight meridian plane expected through application of the frozen-in flow approximation. *Solid lines* represent magnetic field lines, *arrowed dashed lines* the plasma streamlines and the *heavy dashed lines* the principal boundaries. Inside the magnetospheric cavity the plasma rotates with the planetary rotation period. Outside a bow shock lies upstream of the magnetopause, across which the plasma is slowed, compressed and heated. The turbulent plasma from the shock is termed the *magnetosheath* downstream (from Cowley, 1993).

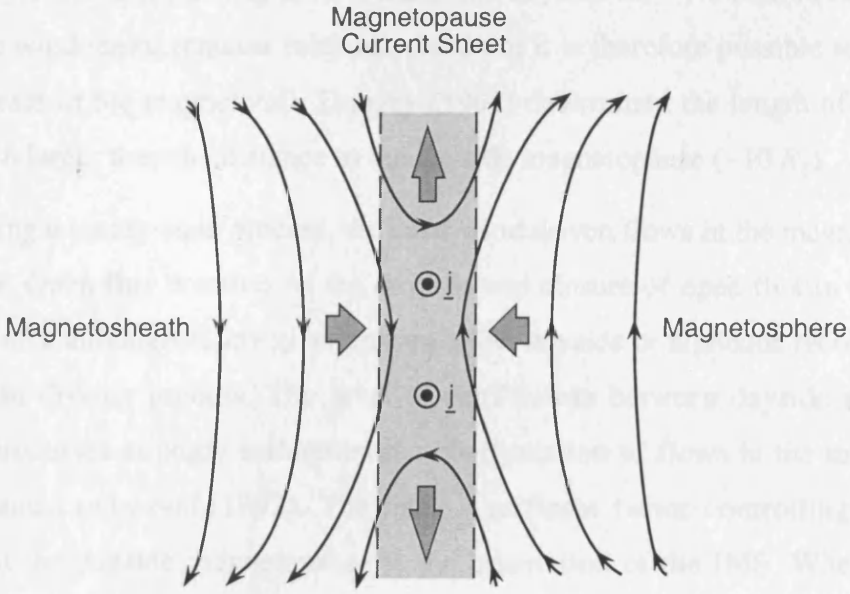

Figure 1.4. Magnetic reconnection at the magnetopause current sheet. In the current sheet (*light shading*) current density is directed out of the page (*dotted cirlces*). *Solid arrowed lines* represent magnetic field lines and the large arrows show the direction of the plasma motion

IMF whilst the other end remains in the Earth's polar region. The three most important consequences of this open magnetospheric configuration are as follows:

i. As open field lines are transported tailward by the solar wind flow, momentum is transferred efficiently between the solar wind and the magnetosphere.

ii. Open flux tubes enable the direct transfer of particles across the boundary between the magnetosphere and the solar wind

iii. As the newly reconnected field lines contract along the boundary from the reconnection site, the plasma population on these field lines will be accelerated and heated.

The tailward transportation of open field lines by the solar wind during periods of southward IMF initiates a cyclical flow pattern within the magnetosphere first suggested by Dungey (1961) and often referred to as the *Dungey cycle*. In this description open field lines connected to the Earth's polar regions are carried tailward by the solar wind flow (Figure 1.5). As the field is stretched out on the nightside, the near-Earth portion of the field sinks toward the centre of the magnetotail and eventually reconnects via another X-type field arrangement. Tailward of this location, the "disconnected" field and plasma is carried off into the solar wind. Earthward of this, the reconnected field lines in the tail move Sunward and the cycle repeats. The overall flow pattern is that of open flux tubes moving antisunward over the poles and closed flux tubes returning through the central magnetosphere. Typically the cycle time of this system is ~6-12 hours during which a field line is open and being stretched downtail for ~2-4 hours and closed and flowing back towards the dayside for ~4-8 hours (Cowley, 1993). Since the solar wind speed remains relatively constant it is therefore possible to estimate the approximate scale of the magnetotail; Dungey (1961) determined the length of the tail to be ~1000 R_E, much larger than the distance to the dayside magnetopause (~10 R_E).

Rather than being a steady-state process, the solar wind driven flows in the magnetosphere are highly variable. Open flux creation on the dayside and closure of open flux in the tail is, on average, in balance although at any given instant either dayside or nightside reconnection may be the dominant driving process. The level of equilibrium between dayside and nightside reconnection processes strongly influences the configuration of flows in the magnetosphere (e.g. Cowley and Lockwood, 1992). The most significant factor controlling the level of reconnection at the dayside magnetopause is the orientation of the IMF. When the IMF is southward (i.e. oppositely directed to the Earth's equatorial magnetic field) the rate of reconnection is largest and this drives large magnetospheric flows. One might naïvely imagine that when the IMF is oriented northward (i.e. aligned parallel to the Earth's

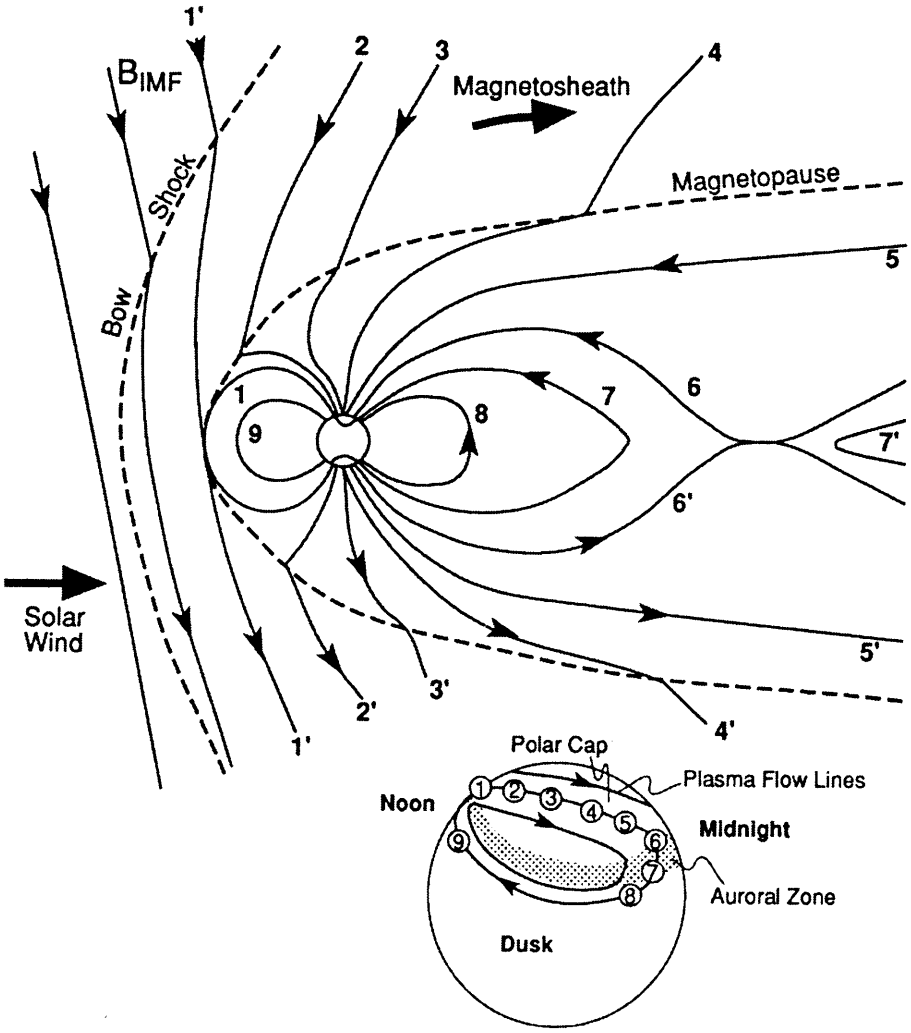

Figure 1.5. The convective flow of plasma in the magnetosphere due to magnetic reconnection. The *numbered field lines* indicate the evolution of a newly reconnected field line (1′) as it is transported tailward before undergoing reconnection (field lines 6 and 6′) at an X-line in the tail. The inset presents the location of the northern hemisphere ionospheric footprint of numbered field lines and the resulting plasma flows; antisunward flows in the polar cap and a return flow at lower latitudes (from Hughes, 1995).

equatorial magnetic field) reconnection would cease entirely. This, however, is not necessarily true. Figure 1.6a presents the case when the IMF is oriented northward but with a component in the Earth/Sun direction. In this configuration the magnetic field geometry is such that some reconnection may occur at the lobes of the magnetosphere (e.g. Cowley, 2000). Finally, the component of the IMF in dusk/dawn direction has important implications for magnetospheric flows as demonstrated in Figure 1.6b. Following reconnection, magnetic tension will tend to pull newly reconnected field lines in opposite directions in each hemisphere, setting up asymmetric flows in the magnetosphere (e.g. Heppner and Maynard, 1987; Cowley and Lockwood, 1992).

Nightside reconnection also contributes to the overall flow pattern, however reconnection on the nightside tends to occur in bursts corresponding to periods of high geomagnetic and auroral disturbance known as *substorms* (Akasofu, 1964; Elphinstone *et al.*, 1996). The exact nature of magnetospheric substorms and the processes that trigger them are not clearly understood at present, however, and several contemporary descriptions and models will be discussed more fully in Chapter 2.

In addition to reconnection there are other processes by which momentum is transferred from the solar wind to the magnetosphere. For example, solar wind particles travelling close to the magnetopause may be scattered across the boundary through a variety of mechanisms (e.g. plasma waves) and carry with them their anti-sunward directed momentum. This leads to the tailward transportation of closed magnetic flux tubes which later return towards the Earth in a convective cycle analogous to that which arises due to reconnection. The viscous and reconnection coupling processes generally occur simultaneously although the contribution made by each process is dependent upon prevailing magnetospheric conditions. Observations have shown that viscous coupling remains weak and relatively steady whereas coupling through reconnection, although highly variable as discussed earlier, is a very efficient driver of solar wind flows (Cowley, 1993). Therefore viscous coupling can be considered most significant during quiet periods (i.e. when the IMF points north) with reconnection driven flows dominating at other times.

1.3 The ionosphere

One of the most significant consequences of the incidence of solar radiation upon the atmosphere of the Earth is the ionisation of neutral gas particles in the atmosphere. Between altitudes of 60-600 km the ionisation gives rise to a plasma concentration sufficient to exert

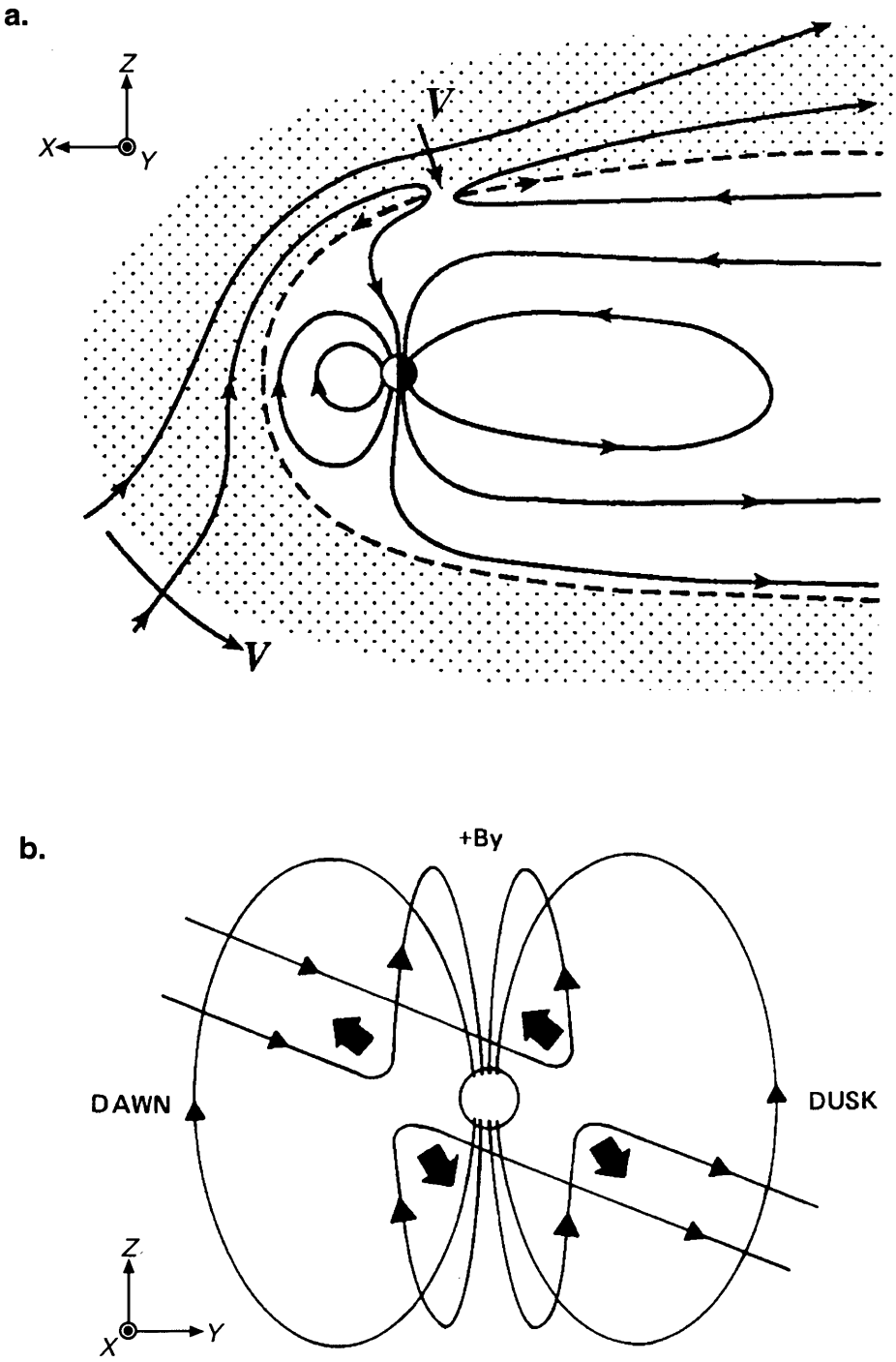

Figure 1.6. a A schematic showing the fields (*solid arrowed lines*) and flows (*labelled V*) expected for single-lobe reconnection for an IMF with positive *Z*, positive *Y*, and negative *X* components. Reconnection in the northern lobe has resulted in open field lines being draped over the dayside before being swept into the tail by the magnetosheath flow (from Cowley, 2000). **b** The configurations of newly reconnected field lines due to southward IMF with a positive *Y* component. The *short broad arrows* indicate the direction in which magnetic tension will tend to distort the field lines (from Hughes, 1995).

an influence on the propagation of radio waves. This region of the atmosphere is known as the *ionosphere* and it acts as the interface between the fully ionised magnetospheric plasma and the neutral atmosphere. The physics of the ionosphere has been the subject of research by scientists world-wide for almost a century and there are many texts on the subject, e.g. Rishbeth and Garriott (1969) and Kelley (1989).

1.3.1 The structure of the ionosphere

Various factors such as production, loss, transport and recombination cause the plasma concentration in the ionosphere to be non-uniform with respect to altitude. Also the position of the Sun in the sky relative to the zenith influences plasma densities at any given time giving rise to substantial seasonal and diurnal variations. Chapman (1931a,b) simply described the variation in ion production with altitude in terms of the amount of radiative energy absorbed by the neutral particle population. Because the rate of ionisation depends upon the solar radiation intensity (which increases with height) and the density of the neutral atmosphere (which decreases with height) there will clearly be an altitude at which ion production for any given species reaches a maximum. The resulting ion production functions are known as *Chapman production functions* and the layers of maximum ion concentration are referred to as *Chapman layers*. In reality the structure of the Earth's ionosphere is more complicated than that of the Chapman layer description. For example, Chapman theory fails to take into account the effects of complex atmospheric chemistry and auroral electron and particle precipitation at high latitudes.

Below an altitude of ~100 km the atmosphere is mixed by turbulence and is of roughly constant composition. Above this altitude solar far-UV and X-rays heat the gas to ~1000 K (Figure 1.7). The increase of temperature with height causes the atmosphere to become more stable and as rapid mixing ceases the atmosphere becomes stratified due to gravity with the concentration of each species decreasing exponentially with altitude according to mass. The exact ion composition depends upon that of the neutral atmosphere however the most notable regions are the *D-region* (below 90 km); the *E-region* (90-150 km), chiefly composed of singly-charged molecular ions such as O_2^+ and NO^+; the *F-region* (150-900 km), dominated by singly-charged oxygen atoms O^+; and the *protonosphere* populated mainly by H^+ (protons) and He^+ (Kelley, 1989). Typical daytime and nighttime ionospheric plasma density profiles are presented in Figure 1.7.

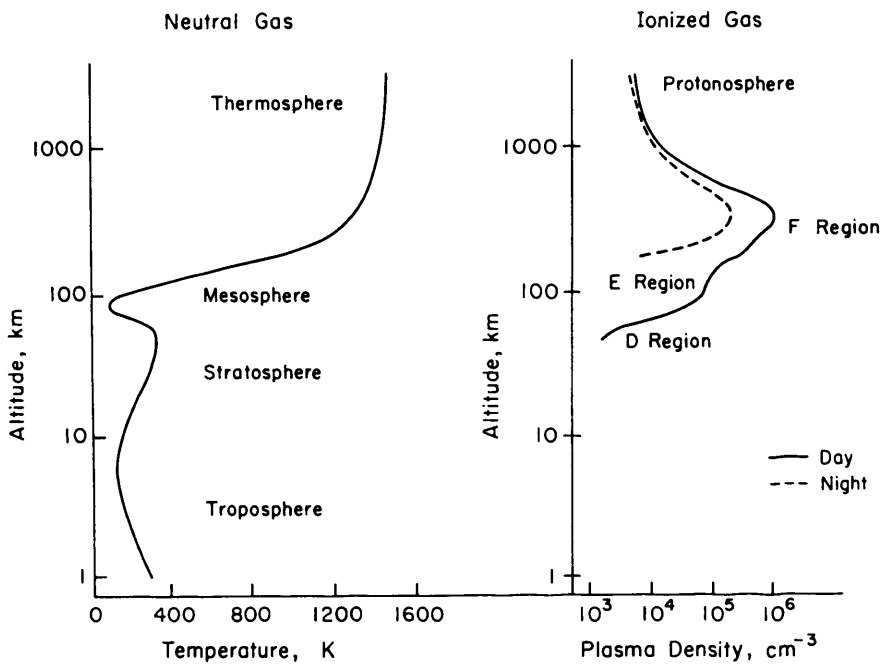

Figure 1.7. Typical profiles of neutral atmospheric temperature and ionospheric plasma density (day and night). The designation of appropriate layers are indicated (from Kelley, 1989).

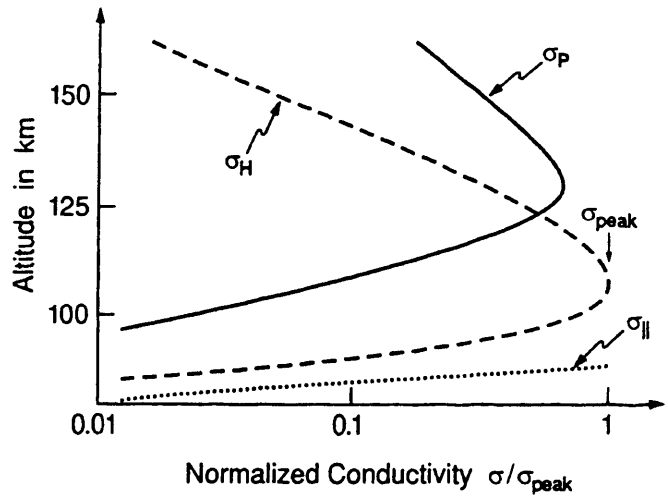

Figure 1.8. Height profiles of normalised conductivities (from Baumjohann and Treumann, 1997)

1.3.2 Ionospheric currents and conductivity

Most significantly, the partial ionisation of the Earth's atmosphere implies that electrical currents are able to flow in the ionosphere. In the lower ionosphere abundant collisions between particles from the plasma and the neutral atmosphere in the presence of the terrestrial magnetic field and electric fields of magnetospheric origin lead to a finite anisotropic conductivity tensor. Conductivity is therefore discussed in terms of three tensor elements; the *Pedersen conductivity* (σ_P), the *Hall conductivity* (σ_H), and the *parallel conductivity* ($\sigma_{||}$). These will be more rigorously discussed in Chapter 2 but the three elements can be summarised as follows. The Pedersen conductivity governs the Pedersen current in the direction of that part of the local electric field normal to the magnetic field. The Hall conductivity controls the Hall current directed orthogonal to both electric and magnetic field. Finally, the parallel conductivity determines the *field-aligned current* (FAC) driven by the electric field component parallel to the magnetic field. Due to the variation in atmospheric composition and density as a function of altitude each element of the ionospheric conductivity tensor peaks at a different height as indicated in Figure 1.8.

1.3.3 Magnetosphere-Ionosphere coupling and the aurora

An implication of the "open" magnetosphere as discussed in section 1.2.3 is that solar wind driven convection in the magnetosphere is communicated to the ionosphere and drives a twin-vortex pattern of flows at high latitudes as depicted in Figure 1.5. This twin-vortex pattern lies in the polar cap and auroral zones, superimposed upon the co-rotation of the ionosphere and is an important mechanism by which ionised plasma is transported between the dayside and nightside ionosphere. Furthermore, magnetospheric plasma is able to precipitate down magnetic field lines into the ionosphere providing a further source of energy input, creating additional ionisation and influencing ionospheric conductivity. The most conspicuous consequence of this precipitation is the high-latitude emission of visible light produced by collisions between precipitating energetic electrons and neutral atmosphere particles. Collisions impart energy to the neutral particles causing them to enter an excited state, emitting a photon as they fall back to the ground state. This emission occurs across a wide wavelength range including visible and ultraviolet (UV) and is known as the *aurora*. Optical aurora are most commonly coloured green corresponding to the transition of states of atomic oxygen at altitudes between 100 and 200 km, emitting light at a wavelength of 557.7 nm (the *auroral green line*). At higher altitudes red emissions due to atomic oxygen at 630.0 nm (the *auroral red line*) are sometimes observed. The aurora is visible in both the

northern and southern hemispheres (termed the *Aurora Borealis* and *Aurora Australis* respectively) in belts known as the *auroral ovals* surrounding the magnetic poles at latitudes of ~70°. Within the auroral ovals, aurora are generally observed as thin bands extending in the east-west direction know as *auroral arcs* although there are many classes of more complex aurora. Auroral forms are usually associated with upward directed FACs (corresponding to downward precipitating electrons) and some examples of this type will be studied later in this thesis.

1.4 Summary

As the solar wind flows out from the sun, carrying with it the interplanetary magnetic field, the terrestrial magnetic field behaves as an obstacle around which the solar wind must flow. The Earth's magnetic field defines a cavity in the solar known as the *magnetosphere* and existing within this cavity is a complex system of plasma flows, currents and electric fields. Figure 1.9 presents a schematic representation of the Earth's magnetosphere summarising many of the features discussed in this chapter. In addition, incident solar radiation leads to the partial ionisation of the Earth's atmosphere forming the *ionosphere*. The ionosphere is sufficiently conductive to sustain current systems driven by the magnetosphere and magnetosphere-ionosphere interactions can result in both large and small scale phenomena.

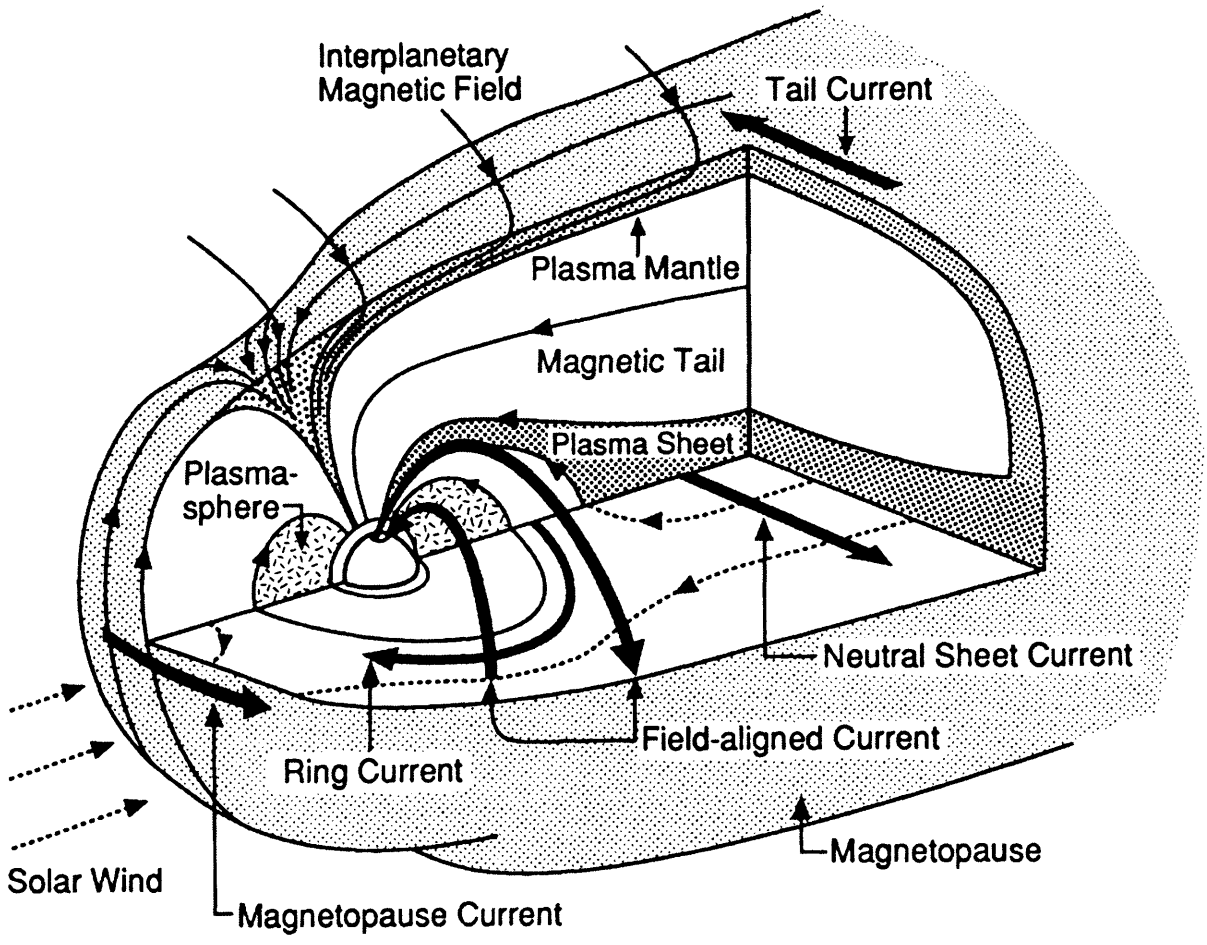

Figure 1.9. A schematic view of the Earth's magnetosphere indicating principal currents, fields and plasma regions (from Russell, 1995).

CHAPTER 2

Fundamental ionospheric and magnetospheric electrodynamics

2.1 Introduction

In the previous chapter, the concept of the ionosphere as an electrically conducting medium was introduced. In this chapter, the basic electrodynamic properties and the coupling of the ionosphere and the magnetosphere are discussed in more detail. Whilst the electrical conductivity of the solar wind may be approximated to a near-infinite scalar, the existence of a strong magnetic field and abundant collisional processes in the Earth's atmosphere imply increased complexity in the conductive nature of the lower ionosphere. The overall configuration of the magnetosphere leads to a network of field-aligned magnetospheric currents that flow both away from and towards the Earth, closing through the ionosphere. It is ionospheric conductivity that determines the ability of the imposed electric fields to drive currents, and hence flows, in the ionosphere and, to some degree, the magnetosphere.

Some of the most significant magnetospheric perturbations to be imposed upon the ionosphere arise due to magnetospheric substorms – the explosive release of energy stored in the magnetotail. The physical processes that give rise to substorms and the mechanisms that govern their evolution remain unclear and are currently the focus of research and debate world-wide. Therefore, descriptions of several key substorm models are included in this chapter and the particular merits of each discussed.

2.2 Ionospheric conductivity

2.2.1 Conductivity of an unmagnetised plasma

The equation of motion for a charged particle (charge q, mass m) under the action of Coulomb and Lorentz forces due to magnetic ($\mathbf{B}$) and electric ($\mathbf{E}$) fields in a collisional environment is presented in Eq. (2.1). Assuming that the collision partners (in reality neutral atmospheric atoms and molecules) move with velocity $\mathbf{u}$ and charged particles move with velocity $\mathbf{v}$ we have

$$m\frac{d\mathbf{v}}{dt} = q(\mathbf{E} + \mathbf{v} \times \mathbf{B}) - m\nu_c(\mathbf{v} - \mathbf{u}) \tag{2.1}$$

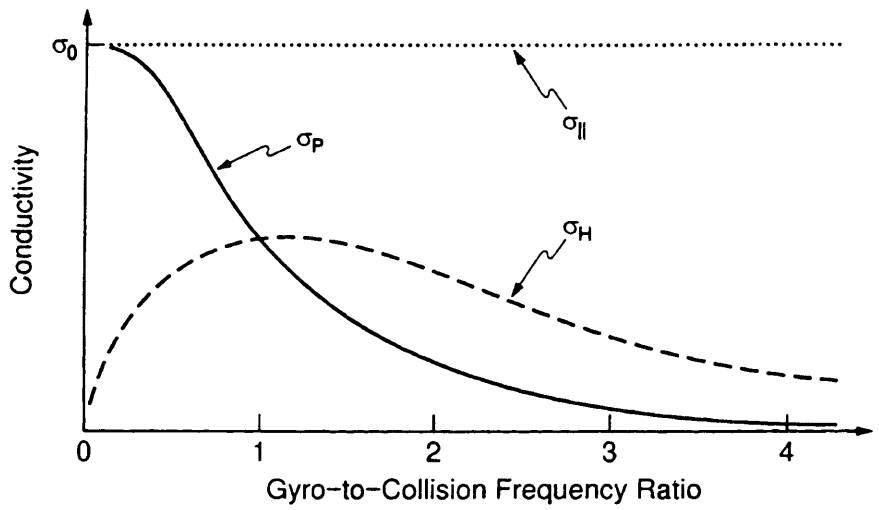

Figure 2.1. The dependence of the three ionospheric conductivity tensor elements on the ratio between gyrofrequency and collision frequency (from Baumjohann and Treumann, 1997).

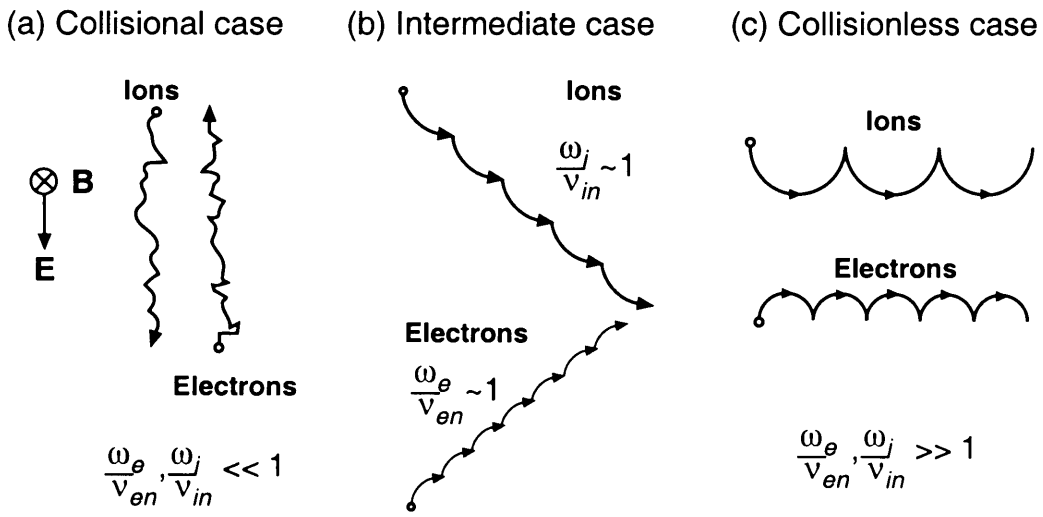

Figure 2.2. Electron and ion motion due to perpendicular electric and magnetic fields in various collisional environments.

The collision term on the right hand side describes momentum lost through collisions occurring at frequency ν_c.

For the moment, consider an unmagnetised plasma in a steady-state, where all electrons move with velocity $\mathbf{v_e}$ and all collision partners (ions in the case of a fully ionised or neutrals in a partially ionised plasma) remain at rest. Eq. (2.1) reduces to

$$-e\mathbf{E} = m_e \nu_c \mathbf{v}_e \tag{2.2}$$

where m_e is the electron mass and e the electronic charge. At this stage, it is useful to define the *mobility*, μ, of a charged particle as the drift velocity per unit electric field which for electrons is given by

$$\mu = \frac{\mathbf{v}_e}{\mathbf{E}} = -\frac{e}{m_e \nu_c} \tag{2.3}$$

where $\mathbf{v_e}$ and $\mathbf{E}$ indicate velocity and electric field magnitudes respectively. Note that in this case the mobility has a negative value since electrons will be driven in the direction opposite to the electric field. If there are n_e electrons in motion with respect to the ions, they constitute a flow of current described by

$$\mathbf{j} = -n_e e \mathbf{v}_e = -n_e e \mu \mathbf{E} \tag{2.4}$$

Alternatively, this relationship can be expressed as

$$\mathbf{j} = \sigma_0 \mathbf{E} \tag{2.5}$$

where σ_0 is the *plasma conductivity* and is defined as

$$\sigma_0 = \frac{n_e e^2}{m_e \nu_c} \tag{2.6}$$

2.2.2 Conductivity of a magnetised plasma

In the magnetised case, plasma may move with velocity $\boldsymbol{v}$ across the magnetic field $\mathbf{B}$. It is therefore necessary to incorporate a $\mathbf{v} \times \mathbf{B}$ electric field into Eq. (2.5), hence

$$\mathbf{j} = \sigma_0 (\mathbf{E} + \mathbf{v} \times \mathbf{B}) \tag{2.7}$$

Eq. (2.7) is simply a generalised form of *Ohm's law* and is valid in fully ionised plasmas where the collision frequency is low and the conductivity can be considered to be near-infinite. However, in a collisional plasma such as that of the lower ionosphere, the presence of a magnetic field leads to significant anisotropy in the plasma conductivity. In order to take

this into account let us first consider the equation of motion in the steady-state case where electrons move with velocity $\mathbf{v}_e$ and the collision partners remain at rest. Eq. (2.1) yields

$$\mathbf{E} + \mathbf{v}_e \times \mathbf{B} = -\frac{m_e \nu_c}{e}\mathbf{v}_e \tag{2.8}$$

By substituting for the definition of σ_0 and using Eq. (2.4) to express $\mathbf{v}_e$ in terms of current we obtain

$$\mathbf{j} = \sigma_0 \mathbf{E} - \frac{\sigma_0}{n_e e}\mathbf{j} \times \mathbf{B} \tag{2.9}$$

A frequently used parameter in plasma physics is the *gyrofrequency* or *cyclotron frequency*, ω_g. This is a measure of the frequency with which a charged particle rotates about the guiding centre of its motion, for instance the frequency with which a charged particle spirals around a magnetic field line as it travels along it. It is defined as

$$\omega_g = \frac{qB}{m} \tag{2.10}$$

It should be noted that the gyrofrequency is dependent only on the charge (q) and mass (m) of the particle and the magnetic field strength (B). It is independent of particle velocity but oppositely charged particles rotate in opposite directions. Assuming that the magnetic field in our magnetised plasma is oriented along the z axis of an arbitrary Cartesian co-ordinate system and taking into account the definition of the gyrofrequency we obtain

$$\begin{aligned} j_x &= \sigma_0 E_x + \frac{\omega_{ge}}{\nu_c} j_y \\ j_y &= \sigma_0 E_y - \frac{\omega_{ge}}{\nu_c} j_x \\ j_z &= \sigma_0 E_z \end{aligned} \tag{2.11}$$

By combining the first two equations to eliminate j_y from the first and j_x from the second equation we arrive at

$$\begin{aligned} j_x &= \frac{\nu_c^2}{\nu_c^2 + \omega_{ge}^2}\sigma_0 E_x + \frac{\omega_{ge}\nu_c}{\nu_c^2 + \omega_{ge}^2}\sigma_0 E_y \\ j_y &= \frac{\nu_c^2}{\nu_c^2 + \omega_{ge}^2}\sigma_0 E_y - \frac{\omega_{ge}\nu_c}{\nu_c^2 + \omega_{ge}^2}\sigma_0 E_x \\ j_z &= \sigma_0 E_z \end{aligned} \tag{2.12}$$

Which can be expressed in matrix notation as

$$\mathbf{j} = \sigma \cdot \mathbf{E} \tag{2.13}$$

where

$$\sigma = \begin{pmatrix} \sigma_P & -\sigma_H & 0 \\ \sigma_H & \sigma_P & 0 \\ 0 & 0 & \sigma_{\|} \end{pmatrix} \tag{2.14}$$

and the tensor elements are given by

$$\begin{aligned} \sigma_P &= \frac{\nu_c^2}{\nu_c^2 + \omega_{ge}^2}\sigma_0 \\ \sigma_H &= -\frac{\omega_{ge}\nu_c}{\nu_c^2 + \omega_{ge}^2}\sigma_0 \\ \sigma_{\|} &= \sigma_0 = \frac{n_e e^2}{m_e \nu_c} \end{aligned} \tag{2.15}$$

As mentioned in Chapter 1, the tensor element σ_P is known as *Pedersen conductivity* and controls the *Pedersen current* in the direction of that part of the electric field, $\mathbf{E}_\perp$, which is orthogonal to the magnetic field. The *Hall conductivity*, σ_P, governs the *Hall current* directed perpendicular to both the electric and magnetic fields (in the $-\mathbf{E}\times\mathbf{B}$ direction). The *field-aligned current* is determined by the *parallel conductivity*, $\sigma_{\|}$, driven by the parallel electric field component, $\mathbf{E}_{\|}$. It should be noted that the parallel electric field is equal to the plasma conductivity in the unmagnetised case as shown in Eq. (2.6).

If the magnetic field is oriented at an arbitrary angle to the axis of the chosen co-ordinate system, Eq. (2.13) can be re-written in the form

$$\mathbf{j} = \sigma_{\|}\mathbf{E}_{\|} + \sigma_P\mathbf{E}_\perp - \sigma_H(\mathbf{E}_\perp \times \mathbf{B})/B \tag{2.16}$$

In the Earth's ionosphere both ions and electrons undergo scattering and collisions with neutral particles, therefore the *ion-neutral collision frequency*, ν_{in}, gives rise to currents governed by the same equations as current carried by the electrons. Consequently Eq. (2.16) is still valid if an ion contribution is added to the electron conductivity tensor elements given in Eq. (2.15). Assuming that the terrestrial ionosphere is composed of a single ion species, ion conductivities are found by replacing ν_c with ν_{en} and ν_{in} for electrons and ions respectively and including the *ion gyrofrequency*, ω_{gi}, where appropriate giving

$$\sigma_P = \left(\frac{\nu_{en}}{\nu_{en}^2 + \omega_{ge}^2} + \frac{m_e}{m_i} \frac{\nu_{in}}{\nu_{in}^2 + \omega_{gi}^2} \right) \frac{n_e e^2}{m_e}$$

$$\sigma_H = \left(\frac{\omega_{ge}}{\nu_{en}^2 + \omega_{ge}^2} + \frac{m_e}{m_i} \frac{\omega_{gi}}{\nu_{in}^2 + \omega_{gi}^2} \right) \frac{n_e e^2}{m_e} \tag{2.17}$$

$$\sigma_{\|} = \sigma_0 = \left(\frac{1}{\nu_{en}} + \frac{m_e}{m_i} \frac{1}{\nu_{in}} \right) \frac{n_e e^2}{m_e}$$

Because the terrestrial ionosphere is composed of many ion species, it is generally necessary to sum the ion contributions over all species. Figure 2.1 presents the dependence of each of the conductivities on the ratio of gyrofrequency to collision frequency and the height profiles of each conductivity tensor element are presented in Figure 1.8. The trajectories of ions and electrons in perpendicular magnetic and electric fields that give rise to these anisotropic conductivity tensor elements are shown schematically in Figure 2.2. For $|\omega_x| << \nu_{nx}$ (where x represents either ions or electrons) the Pedersen conductivity dominates since the plasma particles are scattered in the direction of the electric field before they can gyrate about the magnetic field (Figure 2.2a). In the case of $|\omega_x| >> \nu_{nx}$, plasma particles can undergo $\mathbf{E} \times \mathbf{B}$ drift for many gyrocycles before scattering occurs and Hall conductivity is dominant (Figure 2.2c). The plasma conductivity is most anisotropic when $|\omega_x| \approx \nu_{nx}$ in which case plasma particles are scattered approximately once per gyrocycle and the resultant motion is a combination of $\mathbf{E} \times \mathbf{B}$ drift and movement along the transverse electric field. Under this regime both Pedersen and Hall conductivities are of comparable significance and on average the plasma moves at 45° to both the $\mathbf{E} \times \mathbf{B}$ and transverse electric field direction (Figure 2.2b).

2.3 Large-scale ionospheric electrodynamics

2.3.1 High-latitude ionospheric convection

Magnetic field lines are transported tailward in the magnetosphere by the motion of the solar wind as discussed in section 1.2.3 either as a result of magnetic reconnection on the dayside or by viscous coupling through the magnetopause. Ionospheric plasma that is tied to the footprint of these field lines is dragged from the dayside across the polar cap as shown in Figure 1.5. As open flux is moved into the flanks of the magnetotail, newly closed field lines flow sunward at lower latitudes completing the magnetospheric convection cycle whilst ionospheric plasma tied to the footprint of these field lines is transported toward the dayside.

This "stirring" effect results in the formation of a twin-cell convection pattern in the polar ionosphere.

The ionospheric convection can also be interpreted as an electric potential pattern. From basic electromagnetic theory (e.g. Baumjohann and Treumann, 1997) it can be shown that the guiding centre drift of a charged particle subject to non-parallel electric and magnetic fields, the so-called $\boldsymbol{E} \times \boldsymbol{B}$ *drift*, is given by

$$\mathbf{v} = \frac{\mathbf{E} \times \mathbf{B}}{B^2} \tag{2.17}$$

Electromagnetic theory defines electric field as the negative gradient of electric potential, ϕ. By substituting this definition into Eq. (2.17) we obtain

$$\mathbf{v} = -(\nabla\phi \times \mathbf{B})/B^2 \tag{2.18}$$

The gradient of the electric potential, $\nabla\phi$, is perpendicular to the contours of constant potential. Since the $\mathbf{E} \times \mathbf{B}$ drift is perpendicular to both $\nabla\phi$ and $\mathbf{B}$, the convection streamlines are also equipotential contours. The implication is that particles will drift along the equipotential contours therefore drawing equipotential contours and drawing $\mathbf{E} \times \mathbf{B}$ drift streamlines for the plasma can be considered to be equivalent. This equipotential is equivalent to an ionospheric electric field directed toward dusk in the polar cap as shown in Figure 2.3. Inside the northern hemisphere duskside auroral oval the electric field is directed toward the pole and in the dawnside auroral oval the field is directed toward the equator.

2.3.2 The auroral electrojets

Abundant energetic particle precipitation at high latitudes causes significant ionisation of the atmosphere. This ionisation leads to enhanced ionospheric conductivity within a ring-shaped region offset from the magnetic pole toward magnetic midnight by ~5° known as the *auroral oval* (Feldstein and Starkov, 1967; Holzworth and Meng, 1975). Consequently, high-latitude ionospheric currents termed *auroral electrojets* are concentrated within the auroral oval. The auroral electrojets carry a current of ~10^6 A (Baumjohann and Treumann, 1997) yet they are located only ~100 km above the surface of the Earth. Currents of this magnitude flowing in such close proximity to the ground cause the largest ground magnetic disturbances of any currents in the Earth's environment. Typically, the ground disturbances are ~100-1000 nT in magnitude and are due to Hall currents (Figure 2.4) although during periods of extreme activity the perturbations may reach ~4000 nT (~5% of the geomagnetic field at high-latitudes).

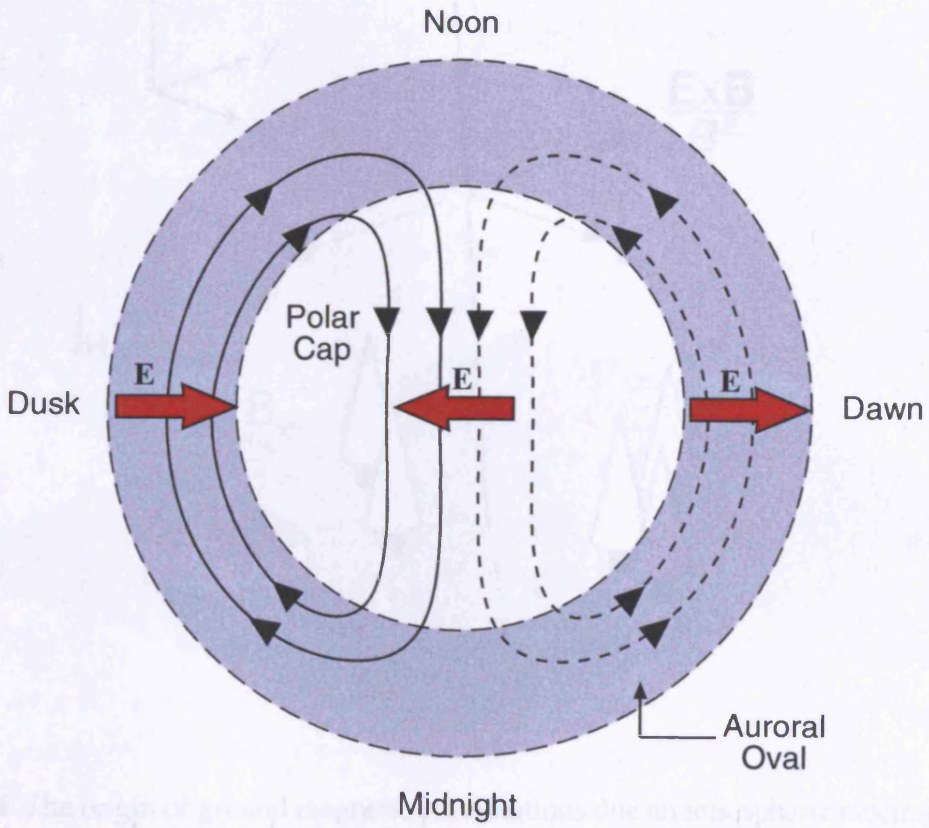

Figure 2.3. Convection electric fields in the high latitude ionosphere indicating electric potential contours/plasma streamlines. On the dusk side ionospheric plasma streamlines are represented by *solid arrowed lines*. On the dawn side, equivalent contours of constant electric potential are shown by *dashed lines*. *Large red arrows* indicate the direction of principal electric fields.

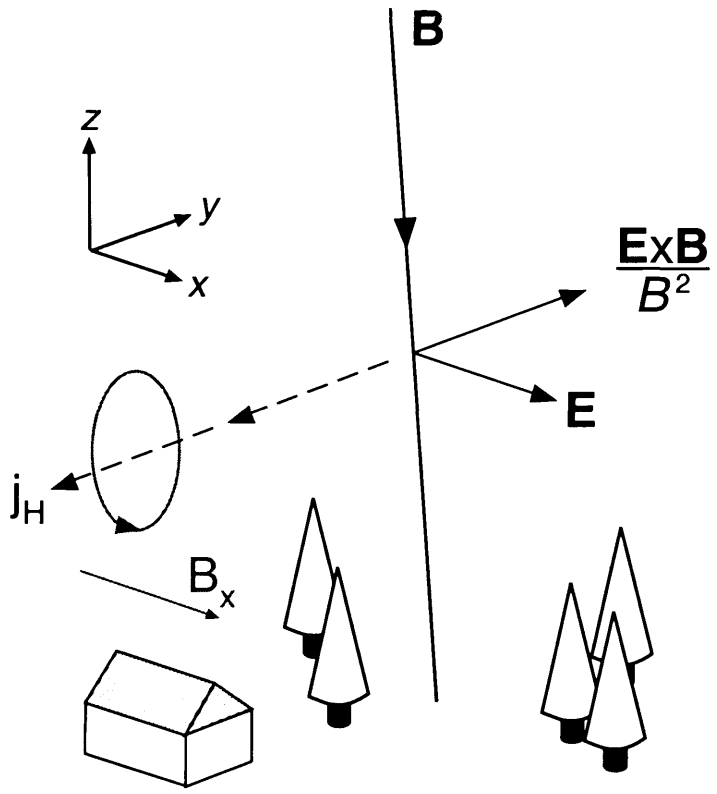

Figure 2.4. The origin of ground magnetic perturbations due an ionospheric electrojet in the E-region. A near-vertical magnetic field, **B**, and an electric field, **E**, directed along the positive *x*-axis results in an **ExB** drift of electrons in the positive *y*-direction (ions are constrained by collisions). The resultant Hall current induces a magnetic field around the y-axis indicated in the figure by *a dark grey loop*. Observed by an instrument located on the ground this magnetic field is oriented in the positive *x*-direction as shown by a *dark grey arrow*.

Depending on their energy, pitch angle and charge, magnetospheric particles that drift towards and around the Earth precipitate in different local time sectors thus enhancing the ionospheric conductivity above the level due to solar radiation ionisation. The typical pattern of conductivity in the auroral oval is shown in Figure 2.5a. Conductivities are weakest in the noon sector and strongest in the midnight sector where Pedersen and Hall conductivities are typically 7-10 S and 10-20 S respectively (Baumjohann and Treumann, 1997).

Overall, the electric field structure within the auroral oval is consistent with the large-scale electric field pattern that results from the plasma convection pattern in the high-latitude ionosphere as discussed in the previous section, although in reality it is slightly more complicated. The auroral zone field electric field is directed poleward in the afternoon and early evening sector, equatorward in the postmidnight and morning sector and rotates from north over west to south in the pre-midnight sector (Figure 2.5b). The region in which the electric field rotates is known as the *Harang discontinuity*. This rotation arises as a result of a weak polarisation electric field directed from midnight to noon that has its origin in the charge build up that occurs at the boundary of the highly conducting auroral zone and the polar cap.

Figure 2.5c presents a schematic view of the *eastward* and *westward electrojets*. The electrojets are Hall currents originating from downward field-aligned current sheets in the noon sector. The current sheet density is lowest in the noon sector and increases toward midnight due to the increasing Hall conductance in the auroral oval. The eastward electrojet is located in the afternoon sector and flows toward midnight, terminating in the vicinity of the Harang discontinuity where it diverts poleward combining with the westward electrojet. The westward electrojet flows through the morning sector and typically crosses local midnight into the evening sector along the poleward boundary of the auroral oval. In the evening sector both the eastward and westward electrojets diverge as upward FACs.

The overall pattern of Pedersen and field-aligned currents in the auroral oval is shown in Figure 2.5d. Sheets of FAC in the poleward half of the auroral oval known as *Region-1 currents* (Iijima and Potemra, 1978) connect with sheets of FAC in the equatorward half of the auroral oval (*Region-2 currents*) via ionospheric Pedersen currents. In the eastward electrojet region the Pedersen currents flow poleward connecting downward and upward FAC sheets in the equatorward and poleward halves of the auroral zone respectively. In the westward electrojet region the Pedersen currents provide current closure connecting downward and upward FAC sheets in the poleward and equatorward halves of the auroral

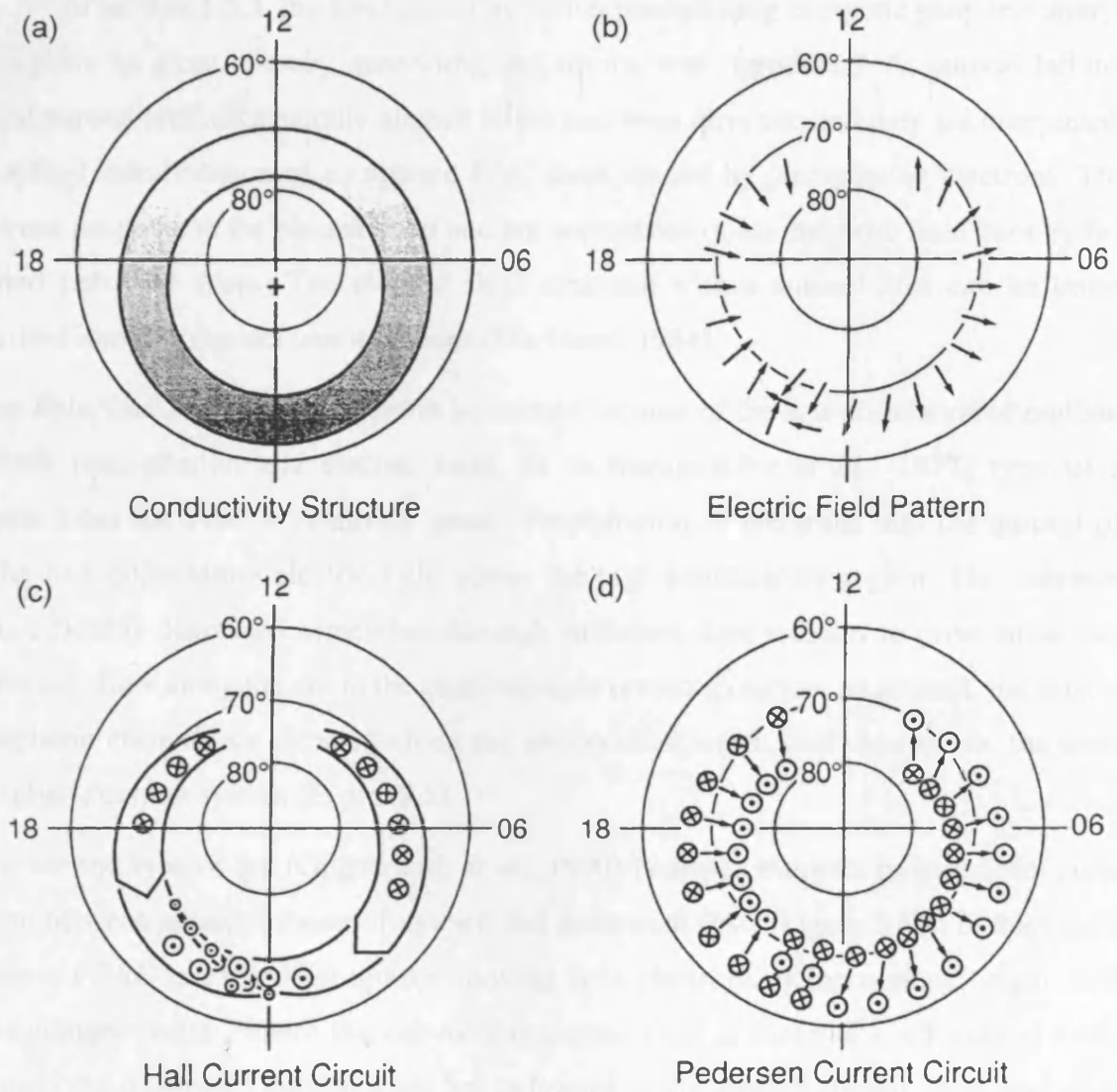

Figure 2.5. An overview of the electrodynamic properties of the auroral oval and the auroral electrojets (from Baumjohann and Treumann, 1997)

zone respectively. In the Harang discontinuity region the evening and morning side Pedersen currents overlap resulting in three sheets of FAC.

2.3.3 Auroral arc associated electric fields

In section 1.3.3, the mechanism by which precipitating energetic particles cause the atmosphere to glow, thereby generating the aurora, was introduced. At auroral latitudes, optical auroral arcs are generally aligned in the east-west direction and they are interpreted as the optical manifestation of an upward FAC sheet carried by precipitating electrons. These electrons originate in the plasma sheet and are accelerated down magnetic field lines by field-aligned potential drops. The electric field structure within auroral arcs can be broadly classified into two distinct configurations (Marklund, 1984).

In the *Polarisation* or *Anti-correlation* (so named because of the anti-correlation of regions of electron precipitation and electric field, de la Beaujardière *et al.*, 1977) type of arc (Figure 2.6a) the FAC is relatively small. Precipitation of electrons into the auroral oval results in a polarisation electric field across the high conductivity region. The convection electric field is depressed somewhat although sufficient field remains to drive an eastward (westward) flow along the arc in the post-midnight (evening) sector. As a result, the principal ionospheric currents are directed along the arc contributing to, and closing via, the overall ionospheric current system (Figure 2.5).

In the second type of arc (Opgenoorth *et al.*, 1990) Pedersen currents provide local current closure between adjacent sheets of upward and downward FAC (Figure 2.6b). In this case the downward FAC is carried by upward-moving cold electrons of ionospheric origin. In the post-midnight sector (where the convection electric field is directed southward at auroral latitudes) the downward current sheet lies poleward of the upward current sheet leading to a narrow (10-100 km) region of enhanced southward electric field poleward of the principal precipitation region. This enhanced electric field drives eastward flows slightly poleward of the optical arc. In the evening sector the convection electric field is directed poleward and the downward FAC lies equatorward of the upward FAC. This arrangement gives rise to Pedersen currents that enhance the poleward electric field in a narrow belt equatorward of the electron precipitation region. The enhanced field results in westward plasma flows equatorward of the optical arc.

The processes by which auroral arcs are formed are the focus of much research (e.g. Akasofu and Kan, 1985; Goertz, 1981). However, it is sometimes useful to consider the two types of

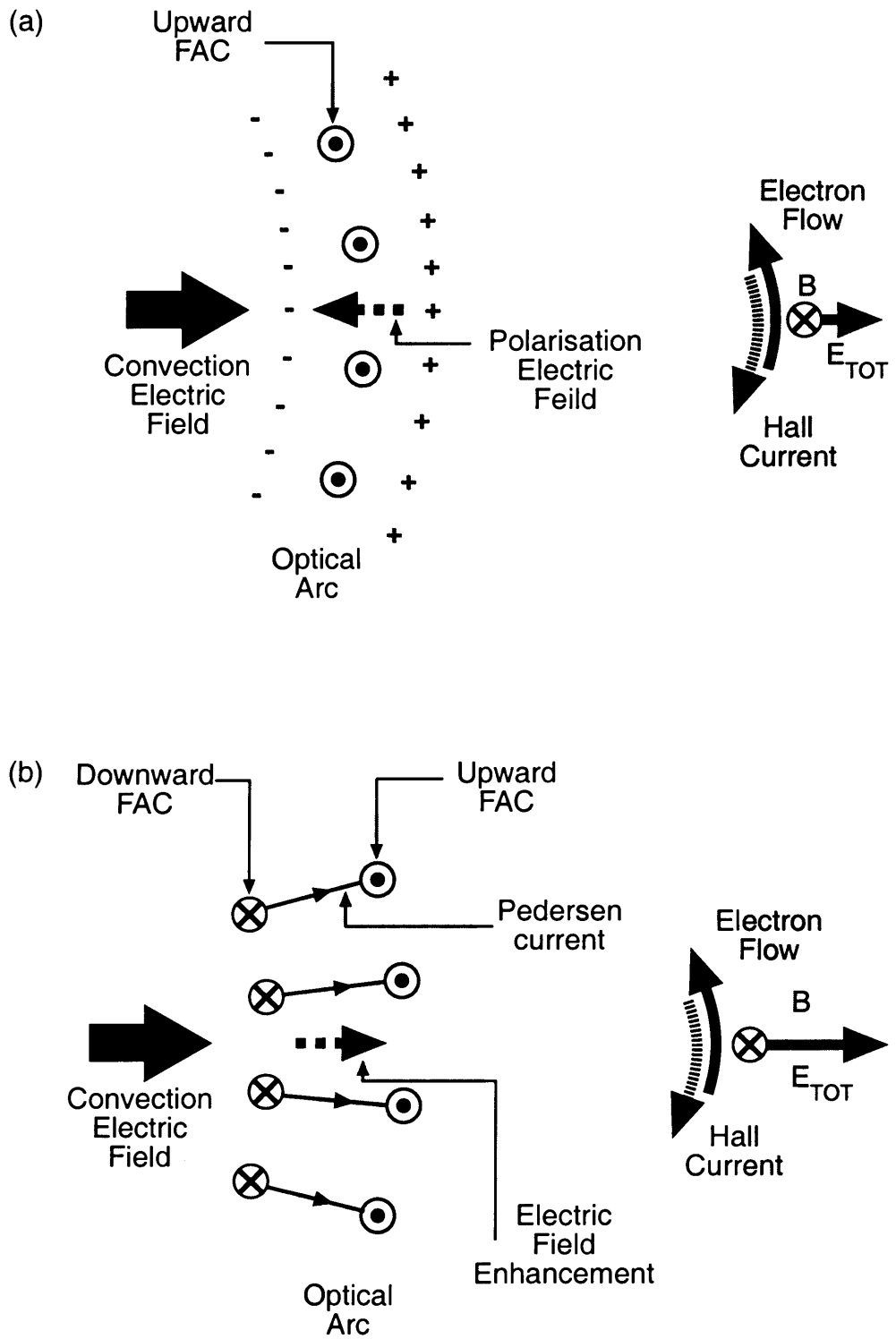

Figure 2.6. a Polarisation or Anti-correlation type post-midnight auroral arc. Although the dipolarisation electric field across the arc suppresses the convection electric field slightly (*left-hand figure*) the resultant field is sufficiently strong to drive current along the arc (*right-hand figure*). The principal current flows along the arc and closes via the ionospheric current system depicted in Figure 2.5c; **b** In the arc structure proposed by Opgenoorth *et al.* (1990) a downward FAC sheet lying outside the optical arc connects via Pedersen currents to the upward FAC sheet associated with the arc. The configuration for a post-midnight arc (downward FAC located poleward of upward FAC) is shown in the *left-hand figure*. The resulting enhancement of the convection electric field at the poleward boundary of the optical arc drives eastward flows in a narrow belt along the boundary (*right-hand figure*).

arc introduced above in terms of the strength of the generating currents (i.e. with the second type of arc forming as an evolutionary consequence of the first). It is therefore reasonable to assume that arcs may arise with intermediate electrodynamic configurations.

2.4 Magnetospheric substorms

Although on average the quantity of magnetic reconnection that takes place on the dayside and on the nightside must be balanced, there is no requirement for the instantaneous rates of reconnection to match. The amount of reconnection that occurs at the dayside magnetopause depends amongst other parameters upon the velocity of the solar wind and the orientation of the IMF, of which the latter is particularly variable. The obvious implication is that there are periods, particularly when the IMF is directed southward, during which significant amounts of terrestrial magnetic flux are reconnected and transported tailward. Conversely, intervals occur during which dayside reconnection is reduced to very low level and the tailward motion of open field is dramatically reduced. Of all the flux transported into the tail, only a fraction is instantaneously reconnected and convected back toward the dayside (Rostoker *et al.*, 1987 and references therein). The remaining flux is added to the tail lobes causing the magnetic flux density to increase. This stored energy is eventually released in an explosive fashion and the magnetosphere undergoes rapid reconfiguration. It is this process of gradual energy storage and sudden release that is known as a *magnetospheric substorm.*

2.4.1 The development of the substorm concept

Although substorms are now thought to be driven by magnetospheric processes, it was Akasofu (1964) who first used the term substorm to describe sudden and dramatic increases in auroral activity (Figure 2.7). Although no two substorms are exactly alike, Akasofu originally envisaged all substorms as having two distinct phases; the *expansion phase* which lasted ~10-30 min and the *recovery phase* lasting ~2-3 hours. During the first ~5 min of the expansion phase quiet arcs, usually centred near magnetic midnight suddenly brighten (Figure 2.7b). Over the next 5 min (Figure 2.7c) the brightened arcs move poleward creating a *bulge* in the midnight sector. The speed of this poleward expansion depends upon the strength of the substorm. Typical propagation speeds are ~1-2 km s^{-1} although they can be as large as ~3 km s^{-1} during particularly violent substorms. Approximately 10-30 min after the substorm breakup began (Figure 2.7d) the substorm bulge reaches its most poleward location, typically ~70°,~75°, or ~80° magnetic latitude depending on whether the substorm was weak, moderate, or intense. During this period the arcs within the bulge are very active. In the

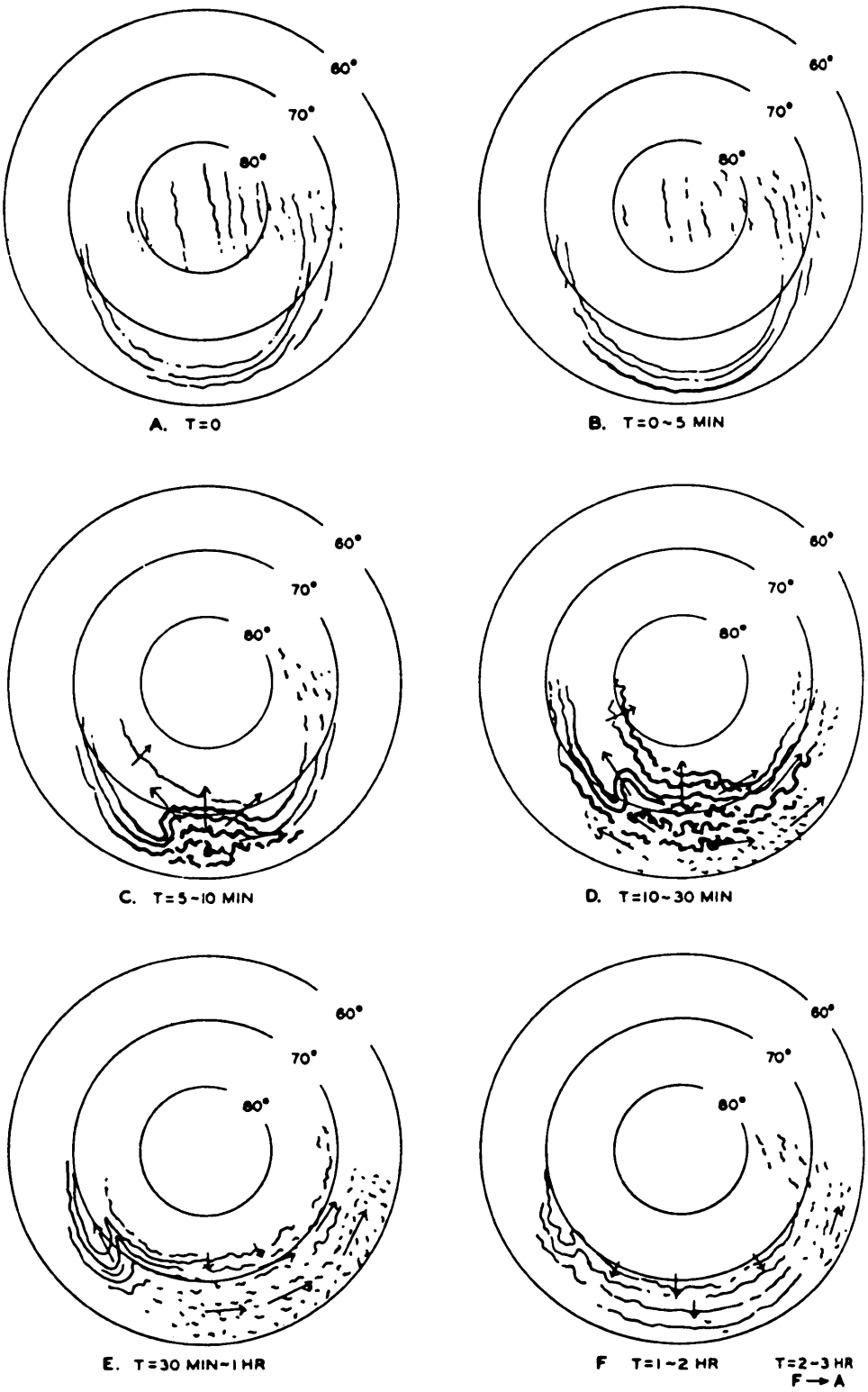

Figure 2.7. Time series schematic illustrations of the auroral development during a substorm (**a**→**f**) based on all-sky camera observations. In each diagram, the view is from above the north geomagnetic pole (located in the centre of the concentric circles) and the sun is located toward the top of the diagram (from Akasofu, 1964).

evening sector arcs begin to fold and propagate westward due to the poleward expansion of the bulge resulting in what is known as the *westward travelling surge*. The propagation speed of the westward travelling surge varies depending upon the intensity of the substorm but speeds of ~0.2-2 km s^{-1} are typical. During the recovery phase, lasting ~2 hours, there is equatorward motion of arcs over a wide range of latitudes and longitudes and the aurora in the westward sector becomes faint (Figures 2.7e and f). Gradually all east-west motion ceases and the brightness of auroral arcs is reduced considerably as the auroral oval returns to conditions that are broadly similar to those prevailing prior to substorm expansion phase onset.

Despite presenting detailed observations of the large-scale development of auroral substorms, Akasofu (1964) made no suggestions as to the driving processes responsible. Indeed, for several years the common view was that the substorm began with the auroral breakup and consisted of only two phases (e.g. Feldstein and Starkov, 1967; Akasofu, 1968). McPherron (1970) was among the first to suggest the concept of a *growth phase* in the magnetosphere that precedes the auroral breakup. It was proposed that during the growth phase, enhanced magnetospheric convection lead to the addition of open magnetic flux to the tail. This view was supported by observations prior to substorms of the dayside magnetopause moving Earthward (presumably due to reconnection processes) when the IMF turned southward (Aubry *et al.*, 1970). Walker *et al.* (1976) observed that magnetotail field lines became stretched prior to substorm onset and Baker *et al.* (1978) found preferentially field-aligned electron distributions at geosynchronous orbit for 30-90 min prior to the majority of substorms. In time the growth phase became an integral component of substorm studies based on magnetospheric observations.

Even though it is now generally agreed that addition of flux to the magnetotail results in a build-up of energy that is released rapidly during the substorm expansion phase (e.g. Elphinstone *et al.*,1996; Baker *et al.*, 1996; Rostoker, 1996), the exact mechanism, triggering factors and in particular the location of expansion phase onset in the magnetosphere remain the subjects of active debate (e.g. Lui *et al.*, 2000). Several models have emerged which attempt to describe the substorm process in a manner consistent with observations. Unfortunately, to date no single model has been proposed that satisfactorily explains all observed ionospheric and magnetospheric behaviour during substorms. Several leading substorm models and their respective merits are discussed in the following sections.

2.4.2 Phenomenological models of magnetospheric substorms

A consequence of magnetic reconnection is the direct application of the interplanetary electric field to the Earth's ionosphere. Furthermore, divergences in this electric field or discontinuities in the ionospheric conductivity will result in field-aligned currents. Perreault and Akasofu (1978) introduced the *driven model* of substorms in order to explain the high correlation between current sensitive magnetic indices and solar wind activity. A southward turning of the IMF enhances the coupling of the solar wind electric field to the ionosphere and hence the strength of ionospheric currents. In order to explain the sudden enhancement in auroral activity during the substorm expansion phase Akasofu (1979, 1980, 1981) suggested that an outward FAC located near midnight develops a field-aligned potential drop when the current density exceeds a critical value. This potential drop accelerates electrons downward, increasing the current and ionospheric conductivity. If the applied electric field is to remain constant then the FAC must increase in order to balance the enhanced conductivity, further enhancing the field-aligned potential drop. Akasofu proposed that it was this instability that corresponded to the substorm expansion phase, however no significance was placed upon the delays between the onset of dayside and nightside reconnection and the magnetospheric reconfiguration that such a delay would imply.

Rostoker and Eastman (1987) proposed another reconnection model of substorms known as the *boundary-layer dynamics (BLD) model.* Observations indicate that fast plasma flows in the central plasma sheet of the magnetotail at ~20 R_E are most frequently directed Earthward (Eastman *et al.*, 1985) and this was interpreted by Rostoker and Eastman as evidence that the source of the substorm expansion was distant from the Earth. The model relied upon a magnetic field model in which the high-latitude dusk convection reversal boundary is mapped to the same topological feature in the magnetosphere as the Harang discontinuity near magnetic midnight. The convection reversal boundary maps to the inner edge of *the low-latitude boundary layer* (LLBL) on the duskside of the plasma sheet implying, by continuity of mapping, that the Harang discontinuity at midnight mapped to a location close to the distant *neutral* or *X-line*. The expansion phase was explained in terms of the sudden onset of reconnection at this distant X-line causing energised plasma to rapidly flow Earthward, enhancing the velocity shear at the inner edge of the LLBL. This velocity shear would become unstable due to the Kelvin-Helmholtz instability causing portions of the boundary layer to fold, particularly on the duskside; on the dawnside of the plasma sheet FACs flow out of the velocity shear and into the centre of vortices on the duskside. Unfortunately, the BLD model is based upon a magnetic field model that is now known to be incorrect (e.g. Fairfield

and Mead, 1975). Instead of mapping to the distant X-line (~100-200 R_E), the Harang discontinuity maps close to synchronous orbit (6.7 R_E). Furthermore, the BLD model fails to correctly explain the location of tailward flow and southward magnetic field in the plasma sheet which are most frequently observed at midnight.

The *thermal-catastrophe model* proposed by Smith *et al.* (1986) and Goertz and Smith (1989) depends upon surface-wave perturbations on the tail magnetopause to transport energy into the magnetotail rather than magnetic reconnection. Wave energy propagates into the plasma-sheet boundary layer and is absorbed by field lines for which the natural resonant frequencies match the incident frequencies. The absorbed energy heats the plasma, which then convects into the central plasma sheet and eventually earthward. The substorm growth phase corresponds to an increase in the intensity of compressional waves crossing the lobes. More and more energy is absorbed by the boundary layer which, for a given level of convection, leads to an increase in plasma temperature. Since the efficiency of the resonant-wave absorption process is dependent on the plasma temperature, there exists a critical temperature at which the boundary layer becomes totally opaque and all incident wave energy is absorbed. At this temperature, convection is unable to maintain an equilibrium and the plasma temperature rises explosively. The plasma sheet is forced to reconfigure to a geometry appropriate to the elevated temperature. At higher temperatures the opacity of the boundary layer falls and convection is once again able to carry off the energy deposited by the waves. The adjustment of the boundary layer state from one temperature to another at constant energy, the so-called thermal-catastrophe, corresponds to the substorm expansion phase. However, despite attempts to correlate wave power in the lobes with substorm activity, evidence of a connection that would support the thermal-catastrophe model is far from compelling (e.g. Henderson and Murphree, 1995).

2.4.3 The near-Earth neutral-line model

Arguably the best-developed of all phenomenological models is *the Near-Earth Neutral Line (NENL) model* (McPherron *et al.*, 1973; Russell and McPherron, 1973), indeed some proponents of the NENL model would claim that the substorm problem is now largely solved (e.g. Baker *et al.*, 1999). This model concentrates on providing an internally-consistent-explanation for most magnetospheric phenomena. Consequently, in its original form the NENL model describes far and mid-tail substorm processes better than inner magnetosphere ($\leq$10 R_E) and ionospheric dynamics although recent modifications have gone far to address many of the model's deficiencies.

In the NENL model the substorm growth phase begins with a southward turning of the IMF. As reconnection begins at the dayside magnetopause and newly-opened flux is carried into the tail, the cross-section of the dayside magnetosphere is reduced whereas on the nightside the addition of flux to the lobes causes the tail to expand outward. This flaring of the magnetosphere (Figure 2.8) increases the angle of attack of the solar wind to the magnetosphere increasing the pressure exerted on the magnetopause. The increased pressure must be balanced by increased magnetic pressure within the tail lobes and this increased lobe pressure is transmitted to the plasma sheet, causing it to thin.

As the growth phase progresses, the near-Earth current sheet becomes thinner and much more intense. Much of the magnetic flux normally crossing this region is forced to cross the magnetic equatorial plane at greater radial distances and the field becomes very weak and tail-like (Kokubun and McPherron, 1981; Baker and Pulkkinen, 1991). The reduction in closed flux on the dayside is apparent in the ionosphere as an increase in polar-cap size as the auroral electrojets move equatorward and become more intense. Figure 2.9 presents a series of schematics showing the magnetotail reconfiguration during the course of a magnetospheric substorm. Panel ① indicates the magnetospheric configuration during the growth phase.

Obviously, the redistribution of magnetic flux described above cannot continue indefinitely. Eventually, there would be no closed flux crossing the nightside equatorial plane and the plasma sheet would thin to the scale of an ion gyroradius. Alternatively, the dayside magnetopause would be eroded entirely as reconnection strips off closed field lines and transports them to the tail. Before this situation arises, a global instability develops that allows closed field lines to return to the dayside and in the NENL model this instability is the onset of reconnection.

When some portion of the current sheet reaches an appropriate threshold, magnetic reconnection begins spontaneously at an X-line of limited azimuthal extent located at the centre of the current sheet (panel ②) at a distance of ~20-30 R_E from the Earth. In the NENL model it is the onset of reconnection of closed field lines that signifies the onset of the substorm expansion phase. This reconnection creates shorter closed field lines that move Earthward from the X-line and loops of magnetic flux around an "O-line" positioned tailward of the new X-line. Within the plasma sheet, plasma flows vertically into the X-line and then out horizontally.

Of all the models discussed so far, a feature unique to the NENL model is the creation of this *plasmoid*, or bubble of closed field lines surrounding the O-line, that is ejected from the

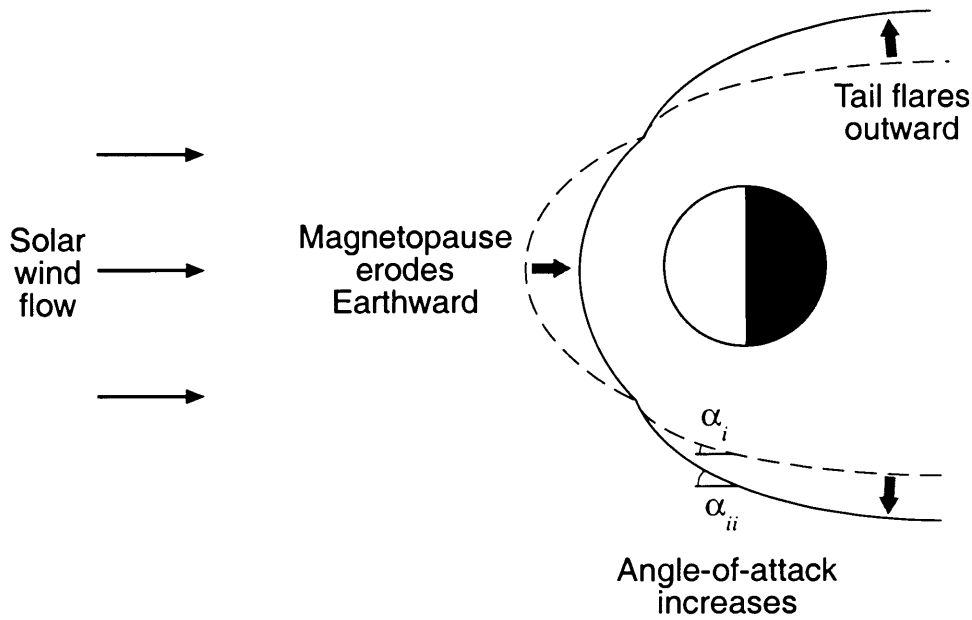

Figure 2.8. The change in profile of the near-Earth magnetosphere in the noon-midnight meridian due to a southward turning of the IMF. The *dashed* (*solid*) *line* represents the profile prior to (after) the southward turning. The heavy arrows show the motion of the magnetopause due to the IMF reorientation. α_i and α_{ii} represent the solar wind angle-of-attack prior to and following the southward turning respectively.

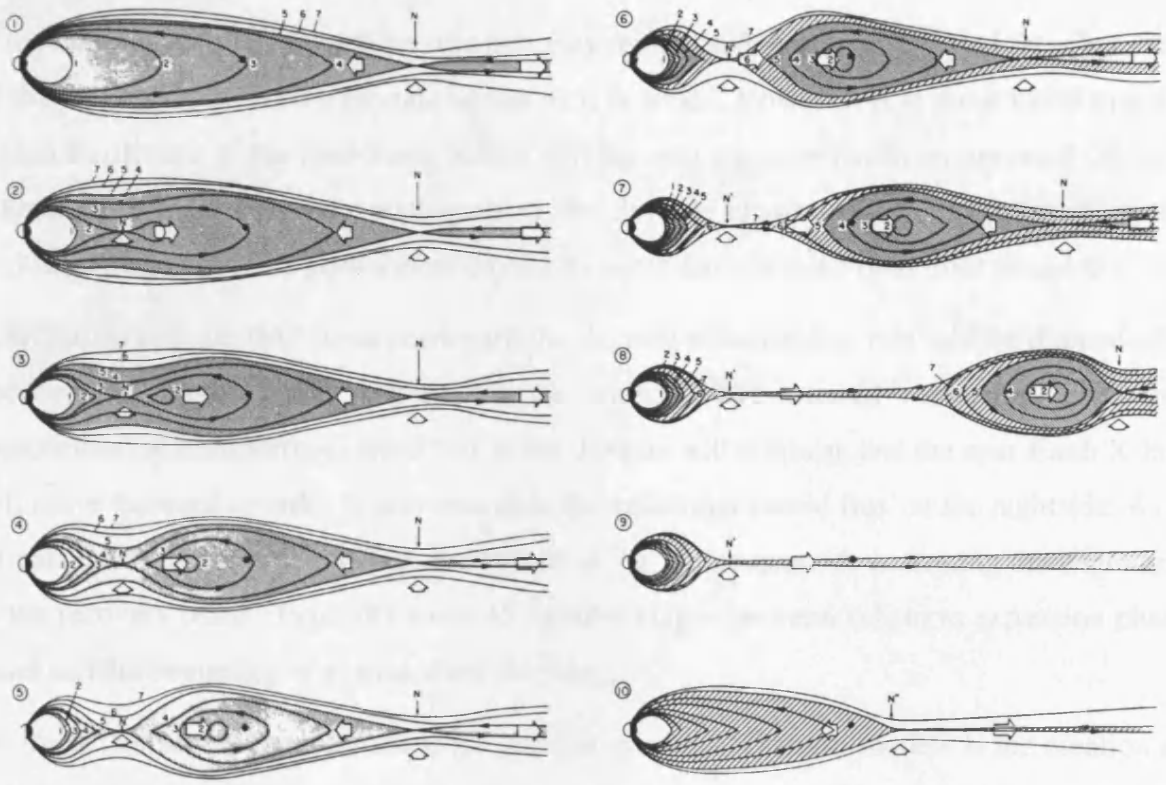

Figure 2.9. Schematic representation of the evolution of the magneotail in the noon-midnight meridian plane during a magnetospheric substorm. Magnetic fields are represented by *black lines* and plasma flows by *white arrows*. The location of the the distant neutral line is indicated by the letter *N*. The *shaded areas* represents the plasma sheet which contains the closed field lines 1, 2, 3, 4 and is bounded by the "last closed field line" 5. Field lines 6 and 7 are in the lobe, outside the plasma sheet (from Hones, 1984).

plasma sheet during the expansion phase. As reconnection continues at the NENL, the structure of closed magnetic loops expands (panels ③ & ④) until the last closed field-line of pre-substorm plasma sheet is pinched off by reconnection (panel ⑤). Within 5-15 min of the onset of reconnection at the NENL the plasma sheet tailward of the X-line is a free plasmoid, no longer magnetically attached to the Earth. The plasmoid accelerates tailward under the influence of pre-existing plasma pressure gradients and of lobe field lines which reconnect after its detachment and contract tailward (panels ⑥, ⑦ & ⑧).

If the IMF remains southward the situation may remain stable provided closed flux flows out of the dipolar region to the dayside as fast as it is added. However, it is more likely that the region Earthward of the near-Earth X-line will become congested with reconnected (closed) nightside flux. In a manner analogous to the dayside erosion of the magnetosphere the nightside magnetosphere grows more dipolar by accretion of closed field lines (Panel ⑩).

Alternatively, if the IMF turns northward the dayside reconnection rate will be dramatically reduced and reconnection may even cease entirely. The internal convection processes responsible for transporting closed flux to the dayside will diminish and the near-Earth X-line will move tailward in order to accommodate the additional closed flux on the nightside. As it retreats tailward, the plasma sheet Earthward of the X-line expands indicating the beginning of the recovery phase. Typically some 45 minutes elapse between substorm expansion phase onset and the beginning of plasma sheet recovery.

An important ionospheric consequence implicit in many substorm models is the creation of *Substorm Current Wedge (SCW)* (Figure 2.10). In the original NENL model it was proposed that the formation of an azimuthally limited near-Earth neutral-line causes a reduction in the net current flowing across the tail in the meridian of the X-line. To maintain current continuity, the original cross-tail current is diverted along field lines connecting each end of the X-line to the ionosphere, closing via the *substorm electrojet*. Earthward-flowing plasma occupies a narrow channel with strong flow-shears located at the channel edges. The sense of the shears is such that more current is diverted into the growing SCW. As the flow nears the Earth it is slowed and the embedded field compressed by the strong field of the inner magnetosphere. As the Earthward flow channel develops the plasma polarises creating a dawn-to-dusk (westward) electric field across the flow channel and the electric field propagates to the ionosphere as an Alfvén wave. This wave is manifested in high-latitude ground magnetometer data as Pi2 pulsations (Rostoker *et al.*, 1980). When the E-field reaches the ionosphere it initiates equatorward plasma flow which is subsequently retarded by inertia

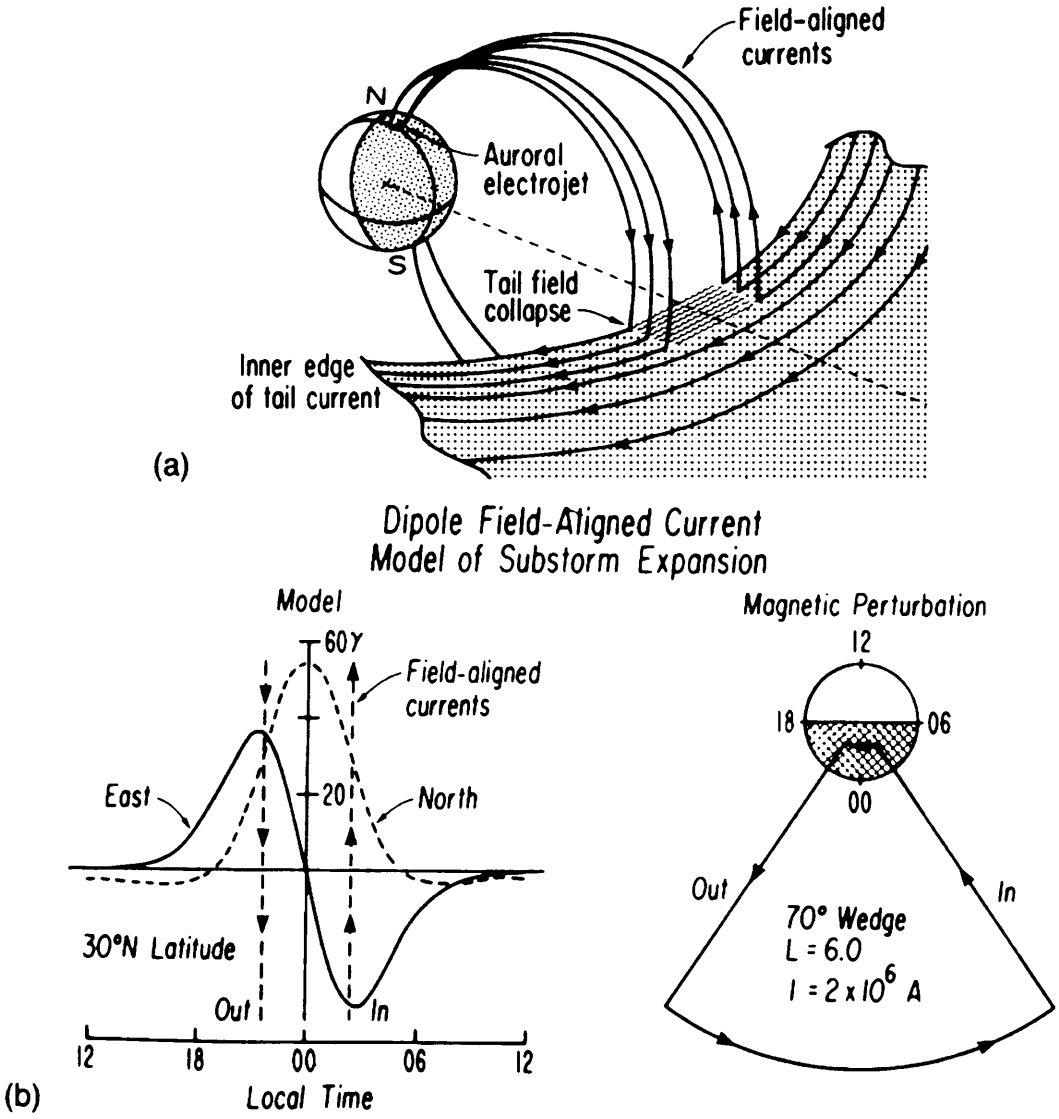

Figure 2.10. a A simplified representation of the diversion of the inner edge of the tail current to form the substorm current wedge; **b** The expected mid-latitude magnetic perturbation due to the SCW equivalent current system (*left panel*) and an equivalent current system which, when added to the tail current, models the diversion (*right panel*) (from Clauer and McPherron, 1974).

and the E-field is mostly reflected. As a result, the initial wave reverberates between the plasma sheet and the ionosphere several times eventually establishing the DC current necessary to drive the equatorward flow against ionospheric resistance.

The turbulent plasma population tailward of the interface between dipolar and tail-like field precipitates into the ionosphere creating the unstructured aurora of the auroral bulge with the interface corresponding to the poleward edge of the bulge. As Earthward flow in the tail adds flux to the dipolar field region the interface moves tailward causing the ionospheric location of the precipitation region to expand poleward. Within the auroral bulge, ionospheric conductivity is enhanced relative to the surrounding ionosphere with strong conductivity gradients located at the latitudinal edges of the bulge. The westward electric field generated by high-velocity Earthward flow projects into the region of enhanced conductivity driving westward Pedersen currents and northward Hall currents in the ionosphere.

Whilst the poleward motion of the auroral bulge can be explained relatively convincingly by the NENL model in the incarnation presented here there are difficulties in reconciling the predicted location of bright emission with observations of the initial auroral substorm brightening occurring at the equatorward edge of the auroral oval. This, and other inconsistencies, between the model and observations have lead some to conclude that the NENL model does not accurately describe the substorm process.

2.4.4 The current-sheet disruption model

Observations of the magnetosphere just beyond synchronous orbit during magnetospheric substorms made by the AMPTE *CCE* spacecraft have been interpreted as conflicting with a near-Earth neutral-line geometry because of inconsistencies in particle and field signatures (Takahashi *et al.*, 1987; Lui *et al.*, 1988). In order to take these new observations into account, Lui (1991) suggested that instabilities in the current sheet were responsible for substorm expansion phase onset and proposed a new substorm model, the *Current-sheet disruption* model (Figure 2.11).

In the current-sheet disruption model, it is proposed that a thin, inner-magnetosphere current sheet develops during the growth phase for the same reasons as in the NENL model. As it thins, non-adiabatic ions and electrons stream across the current sheet in opposite directions and interact via the kinetic cross-field-streaming instability to produce lower-hybrid waves (Lui *et al.*, 1990). Simultaneously, the density gradient at the boundary of the plasma sheet drives the lower-hybrid-drift instability. These two types of waves lead to an anomalous

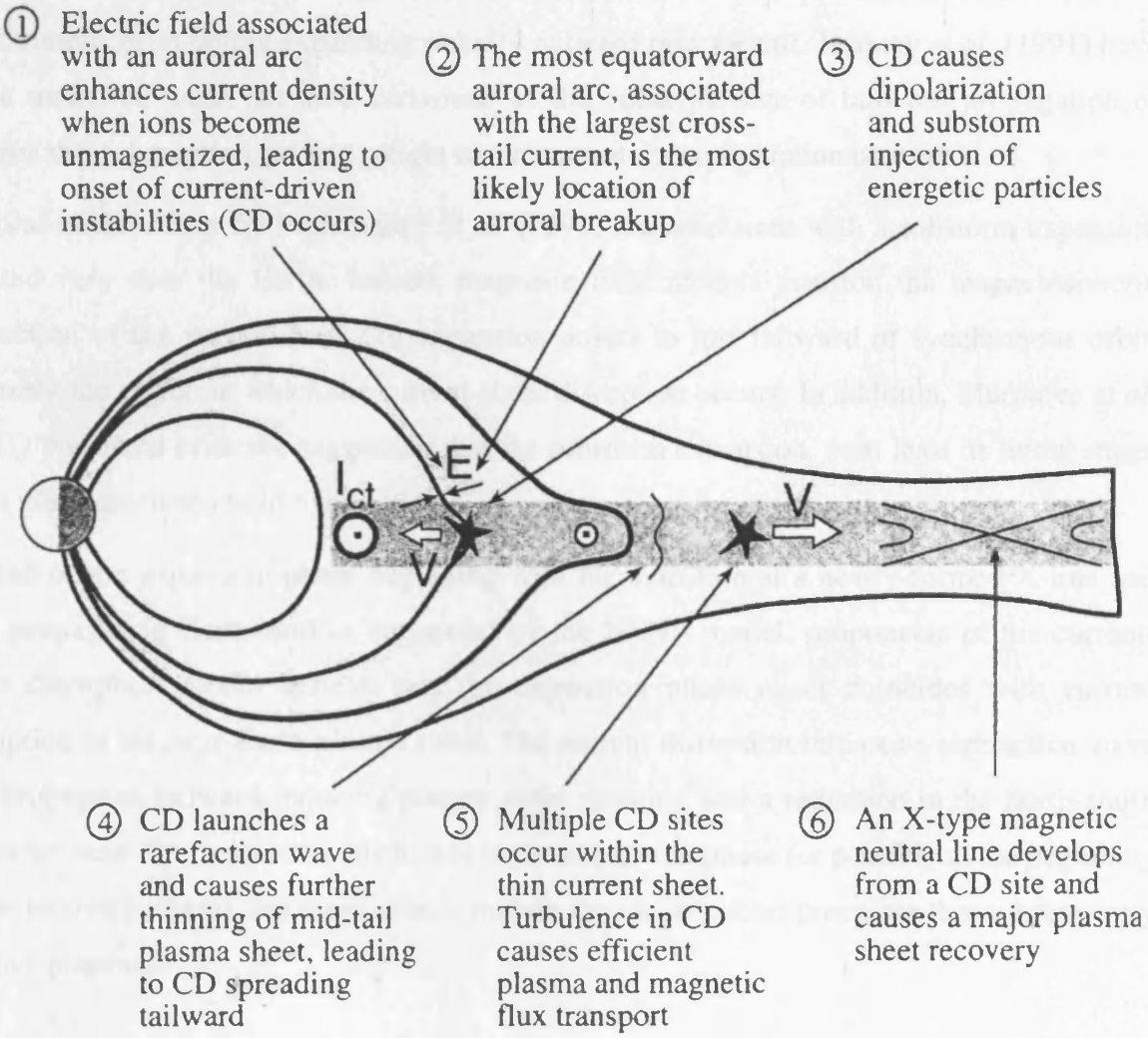

Figure 2.11. The sequence of events that occur during a magnetospheric substorm onset and expansion as described by the current disprution model (from Lui *et al.*, 2000).

resistance in the plasma sheet which disrupts the current flowing across the tail and diverting it along field lines, particularly those of the SCW.

The most significant difference between the NENL model and the current-sheet disruption model is the initial location and subsequent propagation of the substorm expansion. Multi-spacecraft observations of delays in substorm-related field reconfigurations in the tail lobes (Lopez and Lui, 1990) indicate that the current sheet disruption is initiated close to synchronous orbit before expanding radially outward into the tail. Jacquey *et al.* (1991) have since modelled these tail-lobe variations as the consequences of tailward propagation of current sheet disruption, adding weight to the current-sheet disruption concept.

Auroral observations by Elphinstone *et al.* (1991) are consistent with a substorm expansion located very near the Earth. Indeed, magnetic field models position the magnetospheric projection of the auroral oval and expansion onsets to just tailward of synchronous orbit, probably the region in which the current-sheet disruption occurs. In addition, Murphree *et al.* (1991) presented evidence suggesting that the substorm expansion, or at least its initial stage, takes place on closed field lines.

Instead of the expansion phase beginning with reconnection at a newly-formed X-line and then propagating Earthward as suggested by the NENL model, proponents of the current-sheet disruption model believe that the expansion phase onset coincides with current disruption in the near-Earth plasma sheet. The current disruption initiates a rarefaction wave that propagates tailward inducing plasma sheet thinning and a reduction in the north-south magnetic field. Crucially, it is much later in the expansion phase (or possibly at the beginning of the recovery phase) that these effects initiate the reconnection processes that subsequently create a plasmoid.

2.4.5 Recent developments in substorm models

In recent years, advocates of the NENL model have attempted to reconcile the inconsistencies between the model and observations. Measurements made by the *Geotail* spacecraft have been interpreted as confirmation of the existence of a NENL during substorms, typically located between 20-30 R_E (Baumjohann *et al.*, 1999). However, by far the most significant adaptation of the NENL model of magnetospheric substorms has been the re-evaluation of the nature of the reconnection processes at the NENL. Whilst it was earlier thought that the NENL was a large-scale, relatively stable phenomenon, observations of intermittent high-speed Earthward flows between 10-20 R_E known as *Bursty Bulk Flows (BBFs)* (e.g.

Angelopoulos *et al.*, 1992; 1996; Baumjohann *et al.*, 1990) suggest that reconnection at the NENL also occurs in an intermittent and bursty fashion, possibly at a localised X-line. What is more, it appears that near-Earth reconnection is frequently restricted to the plasma sheet, i.e. closed field lines, and it is only during major substorms that lobe field lines are reconnected at the near-Earth neutral line.

As the fast flows generated by reconnection at the near-Earth X-line arrive at the inner magnetosphere, the strongly dipolar field they encounter causes deceleration. This braking and the increasing plasma pressure gradients that build-up as plasma is transported Earthward by the BBFs results in the generation of a dawnward cross-tail current, the diversion of the originally duskward neutral sheet current through the auroral ionosphere, dipolarisation of the field and thus the establishment of the SCW just tailward of synchronous orbit. The build-up of the SCW will be associated with Pi2 pulsations (Shiokawa *et al.*, 1998) and it has been suggested that the stresses imposed upon on the field lines during braking will generate FACs and, thus, brightening of the aurora (Haerendel, 1992). The inclusion of bursty bulk flows and flow braking by the inner magnetosphere is a cornerstone of the current near-Earth neutral line model as summarised in Figure 2.12. It differs from the original NENL model presented in section 2.4.3 in which the auroral breakup and SCW were tied to a near-Earth X-line, a concept to which many had strong objections. In its current form the NENL model is able to describe the typical ionospheric signatures of substorm onset in terms of the braking of Earthward flow, resolving many of the original model's shortcomings.

2.5 Summary

In this chapter the electrodynamics of the magnetosphere-ionosphere system have been discussed in detail ranging from the fundamental properties of the ionospheric plasma that lead to an anisotropic conductivity tensor to the large-scale reconfigurations that occur in the magnetosphere during substorms. Probably the most important consequence of the interaction between the ionosphere and magnetosphere in the context of this thesis is the potential to derive information regarding magnetospheric processes from observations of ionospheric phenomena. Clearly the ionospheric electric fields, currents, and flows presented in Figures 2.3, 2.5, and 2.7 will be influenced by the overlying magnetospheric processes discussed in Section 2.4. Whilst spacecraft are able to provide excellent *in-situ* observations of the magnetosphere, the fundamental nature of their orbits introduce many spatial/temporal ambiguities. Furthermore, the high cost of construction, launch and operation severely limits the number of spacecraft missions active at any given time to a handful. By employing the

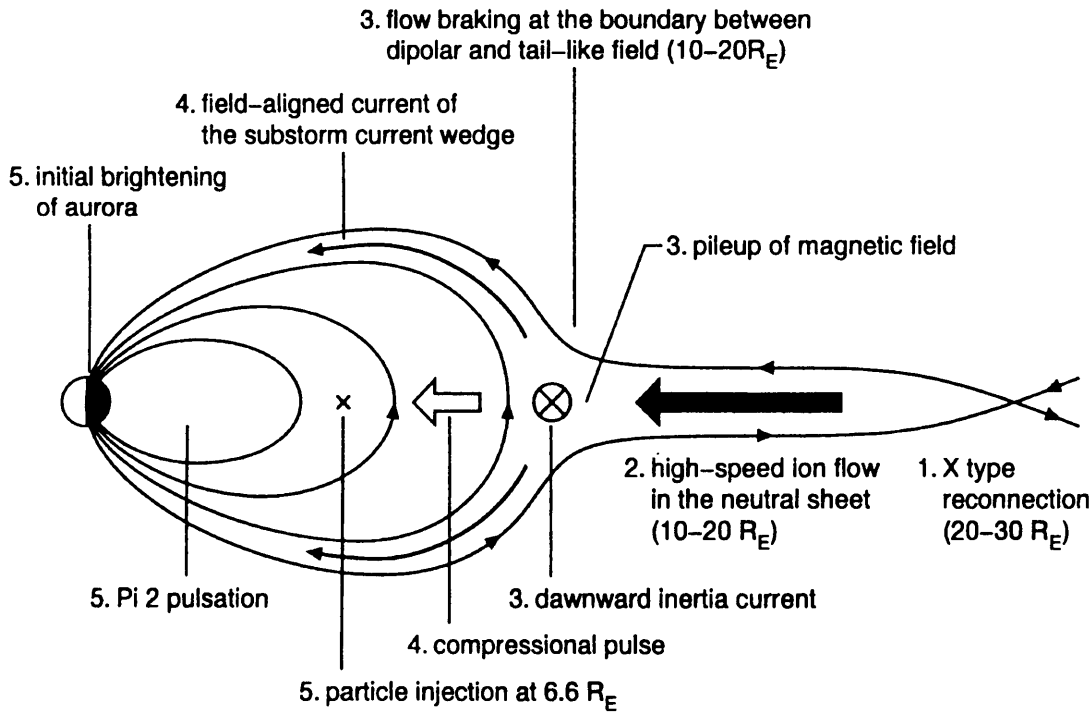

Figure 2.12. The proposed model of substorm current wedge formation during the initial stage of the substorm expansion phase as described by the revised NENL model. The number preceding each comment indicates the order of occurrence (from Shiokawa *et al.*, 1998).

wealth of ground-based geophysical observatories currently available to study ionospheric features it is possible to infer information regarding the structure and evolution of the magnetosphere on a routine basis. The physical principles and experimental techniques associated with several such ground-based instruments are discussed in the next chapter.

CHAPTER 3

Ionospheric diagnostic instruments

3.1 Introduction

In order to undertake simultaneous observations of the high-latitude auroral region over a wide range of magnetic local times, extended networks of instruments are required. In some cases, single institutions deploy entire arrays of instruments in order to provide detailed coverage over a particular region. This is often the case with arrays of ground-magnetometers since individual magnetometers are relatively inexpensive. Conversely, there are occasions when the cost of deploying and operating more than one or two instruments proves to be prohibitive and several institutions collaborate, each deploying a small number of instrument of a common type and sharing data. The SuperDARN radar network (Greenwald *et al.*, 1995) is a particularly good example of this kind of international collaboration. Finally, some projects (for example the European Incoherent Scatter (EISCAT) radar system) are so ambitious that to reach fruition they must be underwritten by the funding bodies of several countries. However, it is worth bearing in mind that in general, as the unit cost of an instrument increases then so does its capabilities. For instance, although the cost of a single magnetometer is a tiny fraction of the cost of, for example, a modern incoherent scatter radar facility, the magnetometer makes a point measurement of a single physical parameter whereas the radar is able to observe a host of parameters and infer many more.

This chapter describes the instrumentation employed to make observations of the magnetospheric and ionospheric phenomena discussed in this thesis and the physical principles by which they operate.

3.2 Radio wave diagnosis of the ionosphere

3.2.1 The development of radar

The practical applications of radio waves to make observations of the reflecting layers of the ionosphere were first recognised in the 1920s (e.g. Breit and Tuve, 1925; 1926). In 1935 Watson Watt lead a team of British scientists studying the problem of detecting aircraft using radio waves. Working from an Air Ministry station on the East Coast of England Watt's team experimented with pulses of radio waves and by the end of 1935 they

had succeeded in obtaining radio reflections from aircraft. By the outbreak of the Second World War in 1939 the first operational radar system in the world had been deployed. This system was called Chain Home and stations were capable of detecting aircraft within a range of around 200 km. By 1940 the U.S. Navy had introduced the word *radar*, a derivation of *radio detection and ranging,* to describe such equipment.

During the war, the Chain Home system operating in the high frequency range between 3-30 MHz was occasionally troubled by what operators named "*n*th-time-around" clutter. It had been known since the experiments of Marconi in 1901 that radio waves could be transmitted beyond the horizon because of the signals he transmitted from Cornwall to Newfoundland. With the verification of the existence of the ionosphere by Appleton and Barnett (1925a, b), Marconi's transatlantic communications could be explained in terms of the propagation of a wave refracting in the ionosphere and curving over the horizon. The early radar engineers knew that *n*th-time-around clutter was a consequence of radio wave diversion by the ionosphere causing the signal to travel unusually long distances and began to consider how this unwanted propagation effect could be exploited to their advantage.

From the early experiments with long-range propagation of radio waves, two types of high-frequency *over-the-horizon (OTH)* radar have emerged. *Surface-wave* (or ground-wave) radars are predominantly monostatic systems that rely upon the surface-wave propagation mode (e.g. Rishbeth and Garriott, 1969) to look over the nearby horizon and are most useful out to ranges of up to ~400 km. Radars that employ the ionospheric propagation mode to achieve an OTH capability are known as *skywave radars*. Skywave radars are usually bistatic and rely upon the refraction of high frequency radio waves in the ionosphere to transmit signals to very long ranges (~4000 km), sometimes in a forward scatter mode to a receiver beyond the target.

Since the middle of the last century, radar has become more and more a feature of everyday life with a plethora of civilian applications emerging. As this thesis testifies, radars have also made a significant contribution to the scientific understanding of the geospace environment that surrounds the Earth (e.g. Rodger, 1999).

3.2.2 Radio wave propagation in the ionosphere

The effect of the ionosphere on an electromagnetic wave depends upon, amongst other parameters, the frequency of the wave. The dispersion relation for electromagnetic waves travelling at an arbitrary propagation angle through an isotropic, magnetised plasma is

expressed by the *Appleton-Hartree equation* (e.g. Hargreaves, 1979). This equation describes the refractive index (n) for the propagation of radio waves (of angular frequency, ω) through a plasma.

$$n^2 = (\mu - i\chi)^2 = 1 - \frac{X}{1 - iZ - \frac{Y_T^2}{2(1 - X - iZ)} \pm \left[\frac{Y_T^4}{4(1 - X - iZ)^2} + Y_L^2 \right]^{1/2}} \tag{3.1}$$

where $X = \omega_P^2/\omega^2$, $Y = \omega_e/\omega$ and $X = \nu/\omega$. The subscripts T and L denote the transverse and longitudinal components of the magnetic field relative to the direction of propagation. The plasma angular frequency (the typical oscillation frequency in an ionised plasma), electron angular gyrofrequency and the collision frequency between the electrons and neutrals are represented by ω_P, ω_e and ν respectively. The refractive index has both real and imaginary parts represented by μ and χ respectively. The complex nature of the refractive index for a radio wave propagating through the ionosphere is a result of the plasma behaving as a lossy dielectric.

The Appleton-Hartree equation predicts that Very High Frequency (VHF) radio waves (30-300 MHz) propagate in an essentially rectilinear fashion. In reality VHF radio waves only undergo refraction during large and rapid changes in ionospheric refractive index such as those associated with strong auroral arcs (Prikryl and Cogger, 1992). In comparison, High Frequency (HF) radio waves (3-30 MHz) are typically subject to significant levels of refraction in the ionosphere. Furthermore, an HF radio wave incident on the ionosphere may undergo sufficient refraction to be effectively reflected downward from the ionosphere when Snell's Law is satisfied:

$$n = \sin\theta \tag{3.2}$$

where θ is the angle between the k vector of the incident radio wave and the normal to the plane of reflection.

Another important implication of the Appleton-Hartree equation is the relationship between plasma frequency and electron concentration. Radio waves will be reflected from the region of the ionosphere where the frequency of the wave matches that of the local plasma frequency. This effect is exploited by ionosondes that sound the ionosphere, usually with vertical incidence radio waves, in order to map the altitude of various ionospheric layers as a function of frequency.

3.2.3 Ionospheric irregularities

Coherent-scatter radars rely upon the existence of non-thermal electron concentration perturbations or *irregularities* in the ionosphere from which radio waves can be backscattered. It is therefore appropriate to describe the processes that create these irregularities before considering the operational principles of coherent-scatter radars. The ionospheric irregularities of significance to this thesis are created by two mechanisms; the *two-stream instability* (Farley, 1963; Buneman, 1963) and the *gradient-drift instability* (Ossakow and Chaturverdi, 1979). A brief descriptions of the mechanism by which both types of irregularity are generated are presented here although rigorous decriptions of irregularities can be found in various texts covering ionospherc physics (e.g. Kelley, 1989).

The two-stream instability, often referred to as the *Farley-Buneman instability*, occurs only in the E-region where the concentration of neutral particles is relatively large compared to that at higher altitudes. Collisions with the abundant neutral particles (which to the first order remain stationary) constrain the E-region ion population as discussed in section 2.2. Meanwhile, electrons move under the $\mathbf{E}\times\mathbf{B}$ drift, flowing through the ions and neutrals at velocities which can exceed 2000 m s^{-1}. It is this differential flow of ions and electrons that drives the two-stream instability. The instabilities created have a phase speed close to the local ion accoustic speed, which is approximately 350-600 m s^{-1} at an altitude of 110 km, dependent on the electron drift speed (Robinson, 1986).

The gradient-drift instability is generated by electron concentration gradients in both the E and F-regions. Unlike two-stream instabilities which are sound-speed limited, there is no upper or lower velocity threshold governing the motion of gradient-drift instabilities which are therefore free to move at the $\mathbf{E}\times\mathbf{B}$ drift velocity.

Farley (1963) and Buneman (1963) used fluid and kinetic approaches respectively in order to derive linear dispersion relations for plasma waves. It is usual to represent the amplitude (Φ) of a plasma wave in terms of an exponential function containing time (t) varying and space ($\mathbf{r}$) terms as:

$$\Phi(\mathbf{r},t) = \Phi_0 e^{-\mathrm{i}(\omega+\mathrm{i}\alpha)t} e^{\mathrm{i}\mathbf{k}\cdot\mathbf{r}} \tag{3.3}$$

Where ω and α are the real and imaginary parts of the wave frequency and represent the angular frequency and the growth rate of the wave respectively. The wave vector is indicated by $\mathbf{k}$. Linear theory (e.g. Sudan *et al.*, 1973) can be used to find expressions for these parameters:

$$\omega = \frac{\mathbf{k} \cdot \mathbf{V_D}}{(1+\Psi)} \tag{3.4}$$

$$\alpha = \frac{\Psi}{(1+\Psi)}\left(\frac{\omega^2 - k^2 C_S^2}{\nu_i} + \frac{\Omega_e \omega}{\nu_e k L}\right) \tag{3.5}$$

where

$$\Psi = \frac{\nu_e \nu_i}{\Omega_e \Omega_i}\left(1 + \frac{\Omega_e^2 \sin^2 \delta}{\nu_e^2}\right) \tag{3.6}$$

and the ion-acoustic speed is given by

$$C_S = \left(\frac{\gamma_e T_e + \gamma_i T_i}{m_i}\right)^{1/2} \tag{3.7}$$

In Eq. (3.4) - (3.7), the symbols have the following meanings:

$\mathbf{V_D}$	plasma drift velocity
ν_X	frequency of collisions between species x and neutral particles
Ω_X	gyrofrequency of species x
T_X	temperature of species x
γ_X	specific heat ratio of species x
m_I	ion mass
L	concentration gradient scale length
δ	magnetic aspect angle (angle between irregularity wave vector and the magnetic field direction)

with subscripts "*i*" and "*e*" referring to ions and electrons respectively.

Equations (3.4) and (3.5) describe both two-stream and gradient-drift waves. Of particular significance is the relation between the growth of a plasma wave and the magnetic aspect angle between the wave vector and magnetic field direction. When the aspect angle is large the force required to drive the waves is greater than when the aspect angle is small. As a result, irregularity wave fronts align themselves parallel to the local magnetic field while the plasma waves move perpendicular to the magnetic field (Haldoupis, 1988).

In the absence of an electron concentration gradient, $L \rightarrow \infty$ and Eq. (3.5) reduces to the growth rate of the two-stream instability. Linear theory predicts that two-stream instabilities will be created at phase speeds approaching the ion-acoustic speed when the plasma drift speed satisfies the condition:

$$V_D \cos\theta \geq C_S(1+\Psi) \tag{3.8}$$

where θ is the angle between the plasma drift velocity and the direction of propagation of the irregularity.

The generation mechanism for the gradient-drift instability is presented schematically in Figure 3.1. In this idealised case, vertical magnetic and horizontal electric fields permeate the ionospheric plasma approximating the conditions at high latitudes. There is also an electron concentration gradient of which a component lies in the horizontal direction parallel to the electric field. In this situation, any inhomogeneities that arise in the electron concentration will result in the creation of polarisation electric fields that further perturb the concentration distribution in the direction of the electron concentration gradient (Figure 3.1b). As the perturbation grows, electron-depleted regions move along the concentration gradient toward denser regions and electron-dense regions move toward regions of electron rarefication (Figure 3.1c). Due to the configuration of the electron concentration gradient and the electric and magnetic fields, this region of the ionosphere is unstable to electron concentration fluctuations. Had the electron concentration gradient contained a component in the direction opposite to the ambient electric field, high electron concentration plasma would drift into higher concentration regions, stabilising the concentration fluctuations.

3.2.4 The principles of coherent scatter

As discussed in the previous section, non-thermal electron concentration irregularities arise in the ionosphere and, in general, these irregularities align themselves parallel to the ambient magnetic field. Electromagnetic radiation incident normally upon planes of irregularities will scatter and constructively interfere if the separation between the planes is equal to an integer multiple of half the wavelength of the transmitted wave. This process is analogous to Bragg scattering of X-rays from the layers of a crystal lattice, a commonly employed technique in crystallography. For an arbitrary scattering angle (θ), the separation of the irregularities behaving as scatter planes, d, is given by

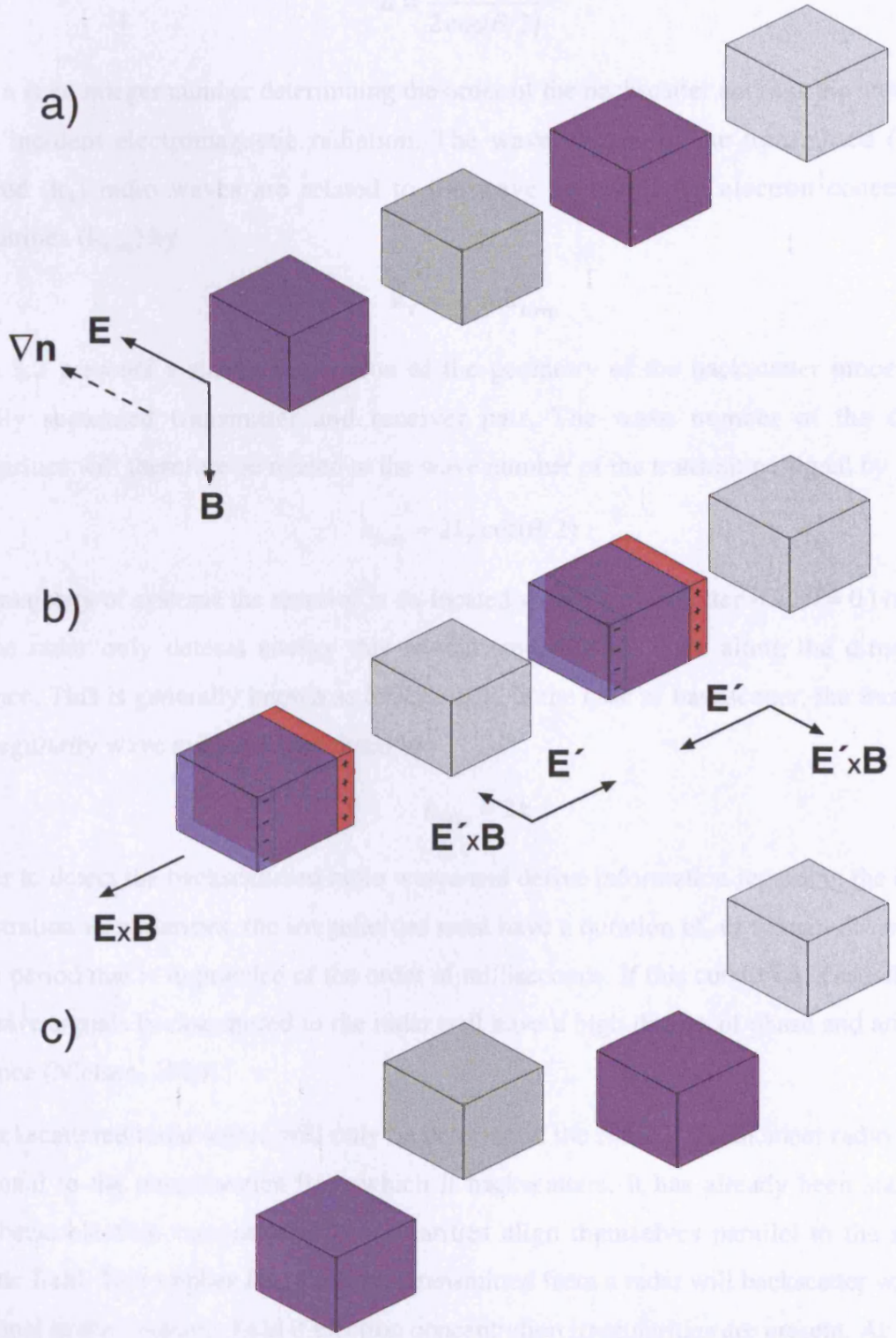

Figure 3.1. Schematic representation of the growth of the gradient-drift instability. **a** Four arbitrary volumes of ionospheric plasma which are subject to a vertical magnetic field **B** and a horizontal electric field **E**. In addition, there exists an electron density gradient (**∇n**) which has a component in the horizontal plane indicated by a *dashed arrow*. Two of the volumes (*shaded dark blue*) have slightly increased electron concentrations; **b** Since the mobility of electrons (*blue*) is higher than that of ions (*red*), **ExB** drifting of the electrons perturbs the plasma and sets up polarisation electric fields (**E´**) which in turn introduce additional drifts **c.** The natural perturbation continues to grow as the electron density irregularities drift due to the local density gradient.

$$d = \frac{n\lambda}{2\cos(\theta/2)} \tag{3.9}$$

where n is an integer number determining the order of the backscatter and λ is the wavelength of the incident electromagnetic radiation. The wave vectors of the transmitted ($\mathbf{k}_T$) and scattered ($\mathbf{k}_S$) radio waves are related to the wave vector of the electron concentration irregularities ($\mathbf{k}_{Irreg}$) by

$$\mathbf{k}_T = \mathbf{k}_S + \mathbf{k}_{Irreg} \tag{3.10}$$

Figure 3.2 presents a simple illustration of the geometry of the backscatter process for a spatially separated transmitter and receiver pair. The wave number of the detected irregularities will therefore be related to the wave number of the transmitted signal by

$$k_{Irreg} = 2k_T \cos(\theta/2) \tag{3.11}$$

In the majority of systems the receiver is co-located with the transmitter (i.e. $\theta = 0$) implying that the radar only detects energy that is scattered directly back along the direction of incidence. This is generally known as *backscatter*. In the case of backscatter, the transmitted and irregularity wave numbers are related by

$$k_{Irreg} = 2k_t \tag{3.12}$$

In order to detect the backscattered radio waves and derive information regarding the electron concentration irregularities, the irregularities must have a duration of, or remain *coherent* for, a finite period that is in practice of the order of milliseconds. If this condition is satisfied then successive signals backscattered to the radar will have a high degree of phase and amplitude coherence (Nielsen, 1989).

The backscattered radar signal will only be detected at the radar if the incident radio wave is orthogonal to the irregularities from which it backscatters. It has already been stated that ionospheric electron concentration irregularities align themselves parallel to the ambient magnetic field. This implies that the signal transmitted from a radar will backscatter when it is orthogonal to the magnetic field if electron concentration irregularities are present. At low and mid-latitudes this orthogonality condition is relatively easy to satisfy with a VHF system since radio waves transmitted by the radar propagate in a near-rectilinear manner as indicated in Figure 3.3 (a and b). This is not the case at high latitudes where the Earth's magnetic field is almost vertical as shown in Figure 3.3c. High frequency radars exploit the refraction of radio waves propagating through the ionosphere in order to circumvent this limitation. At HF frequencies, non-vertical incidence radio waves will tend to refract Earthward, increasing the

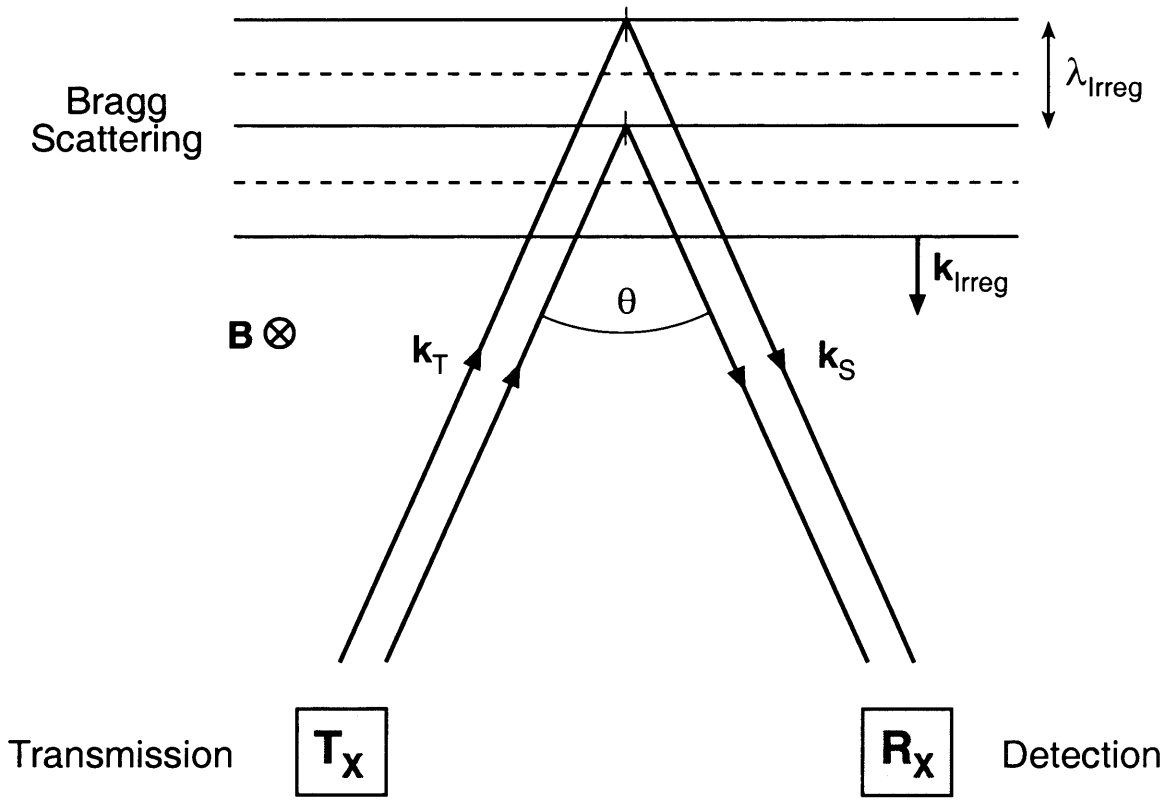

Figure 3.2. A simplified schematic of the geometry germane to the coherent scatter technique.

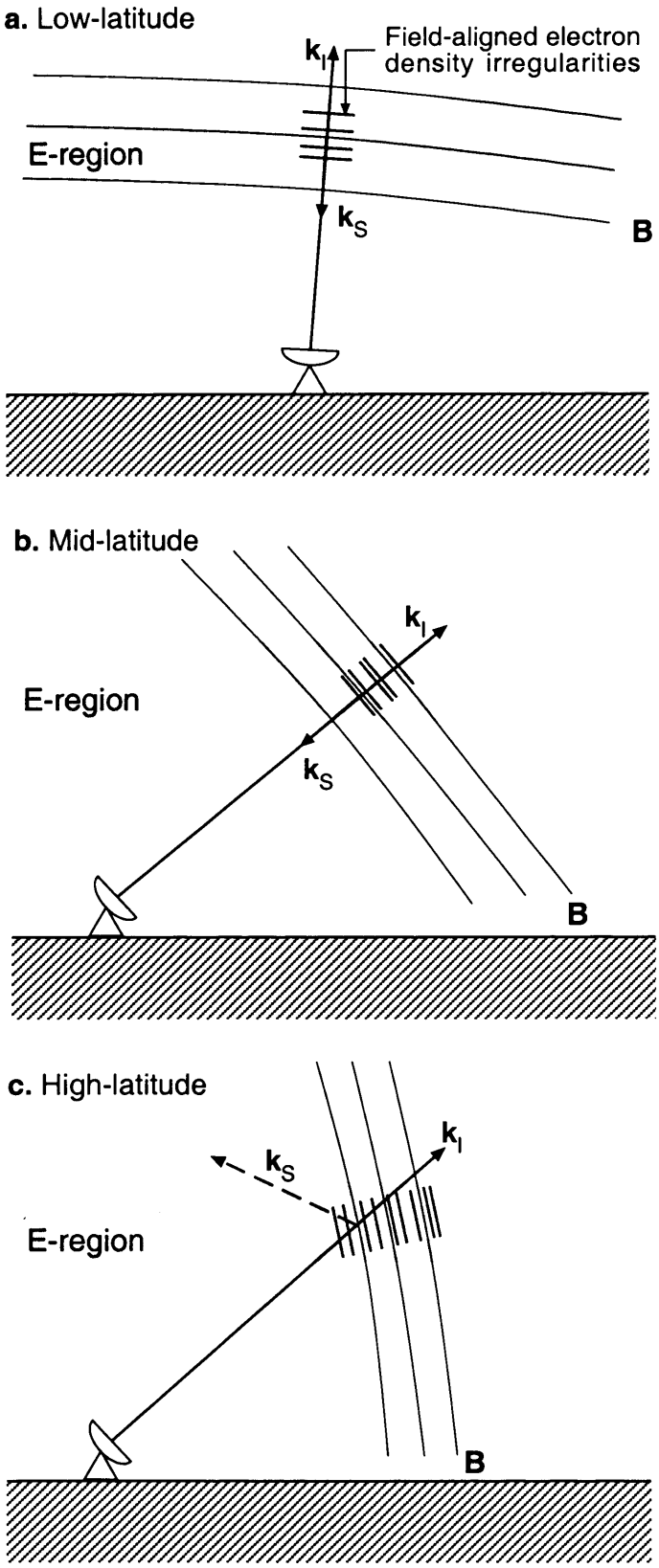

Figure 3.3. The scattering geometry for a VHF coherent scatter radar for E-region electron density irregularities at (**a**) low, (**b**) mid, and (**c**) high-latitudes. In each panel, the incident wave vector is indicated by an *arrowed line* and labelled $\mathbf{k}_I$. In both the low and mid-latitude cases the incident wave is orthogonal to field-aligned electron density irregularities and a fraction of the signal is backscattered toward the radar (the backscattered wave vector is labelled $\mathbf{k}_S$). In the high-latitude case, the incident signal does not satisfy the orthogonality condition required for backscatter and the radar signal is scattered into space as indicated by the *dashed arrow*.

likelihood of satisfying the requirement of orthogonality as presented in Figure 3.4. Furthermore, whilst VHF systems generally scatter from E-region irregularities, the enhanced electron concentration in the F-region increases the degree of refraction and therefore the likelihood of F-region backscatter, however the transition to HF frequencies is not without its drawbacks. Although the Earthward refraction of HF radio waves implies extended range and over-the-horizon capability, the position of the backscatter region is more ambiguous and absorption of the radar signal in the D-region is commonplace (Milan *et al.*, 1996).

3.3 Coherent-scatter radars

Later chapters of this thesis will include data from both HF and VHF coherent-scatter radars. Of the coherent-scatter systems deployed during recent years, the majority operate in a broadly similar manner. In order to provide a lucid description of the relevant techniques, descriptions of two currently operating radar systems (one HF and one VHF) will be presented as examples.

3.3.1 CUTLASS

The Co-operative UK Twin-Located Auroral Sounding System (CUTLASS) comprises a pair of identical HF coherent-scatter radars located in Þykkvibær (63.8°N, 20.3°W), Iceland and Hankasalmi (62.3°N, 26.6°E), Finland (Figure 3.5). The CUTLASS radars are deployed and operated by the University of Leicester and jointly funded by UK Particle Physics and Astronomy Research Council (PPARC), the Finnish Meteorological Institute (FMI) and the Swedish Institute of Space Physics. Each radar is frequency agile, capable of operating in the 8-20 MHz range although in practice backscatter is most frequently observed at frequencies between 10-13 MHz. The main array of each CUTLASS radar consists of 16 log-periodic antennas with both transmit and receive capability. In addition to the main array, each radar includes an interferometer array of 4 antennas with receive capability only. The antennas in each array are phased in relationship to one another in order to create an antenna pattern in which the maximum gain has one of 16 azimuthal pointing directions. In effect, each radar forms a beam that can be electronically steered to any of 16 pointing directions, each one separated by ~3.24° and distributed symmetrically about the radar boresites of –12° and 30° for the Finland and Iceland radars respectively.

CUTLASS employs a highly flexible radar control program to define the operational characteristics of each radar. Figure 3.6 presents the fields-of-view of the CUTLASS radars whilst operating in standard scan mode. In this mode each of the 16 beams is sounded for

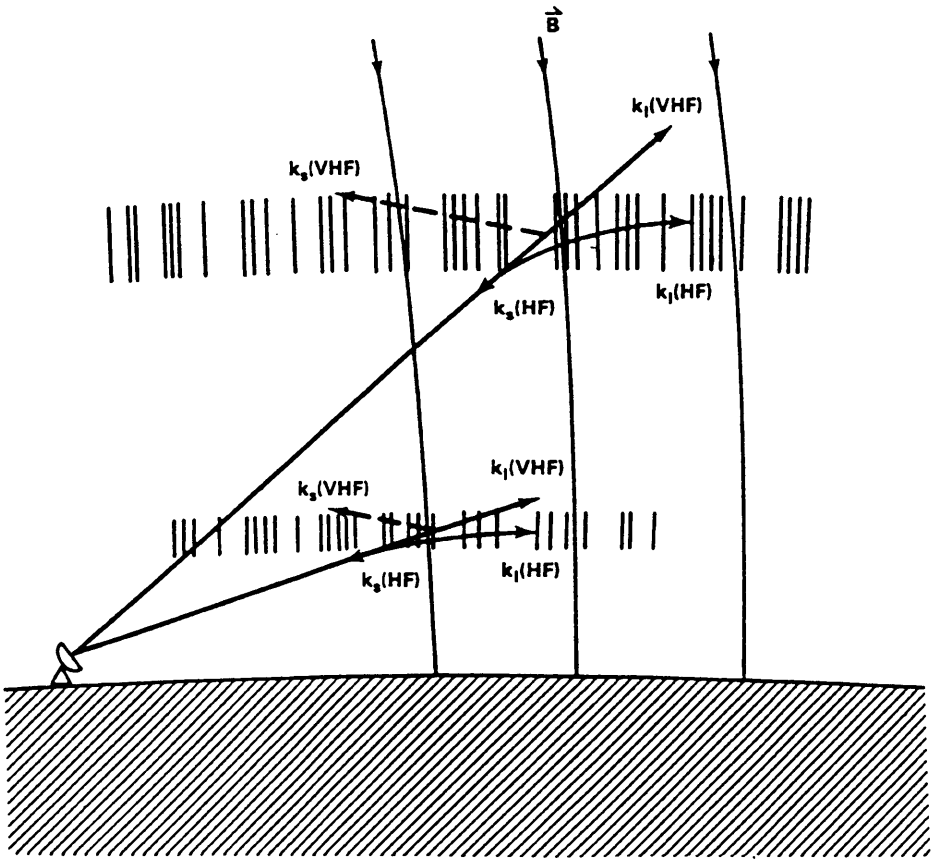

Figure 3.4. A comparison of the propagation and scattering by ionospheric electron density irregularities of VHF and HF radio waves at high-latitudes. Incident wave vectors are labelled $\mathbf{k}_I(x)$ and scattered wave vectors $\mathbf{k}_S(x)$ where x can represent either VHF or HF waves. In the example, the presented VHF waves scatter into space from both the E and F-regions whilst HF signals refract sufficiently to coherently backscatter from the field-aligned irregularities and return to the radar (from Greenwald *et al.*, 1995).

Figure 3.5. The CUTLASS Finland (top) and Iceland (bottom) radars. The four antennas of the interferometer array and equipment building that contains the transmitters and control computers are clearly visible at the Iceland site whilst they are hidden by trees at the Finland site (Photographs provided by E. Chris Thomas, University of Leicester).

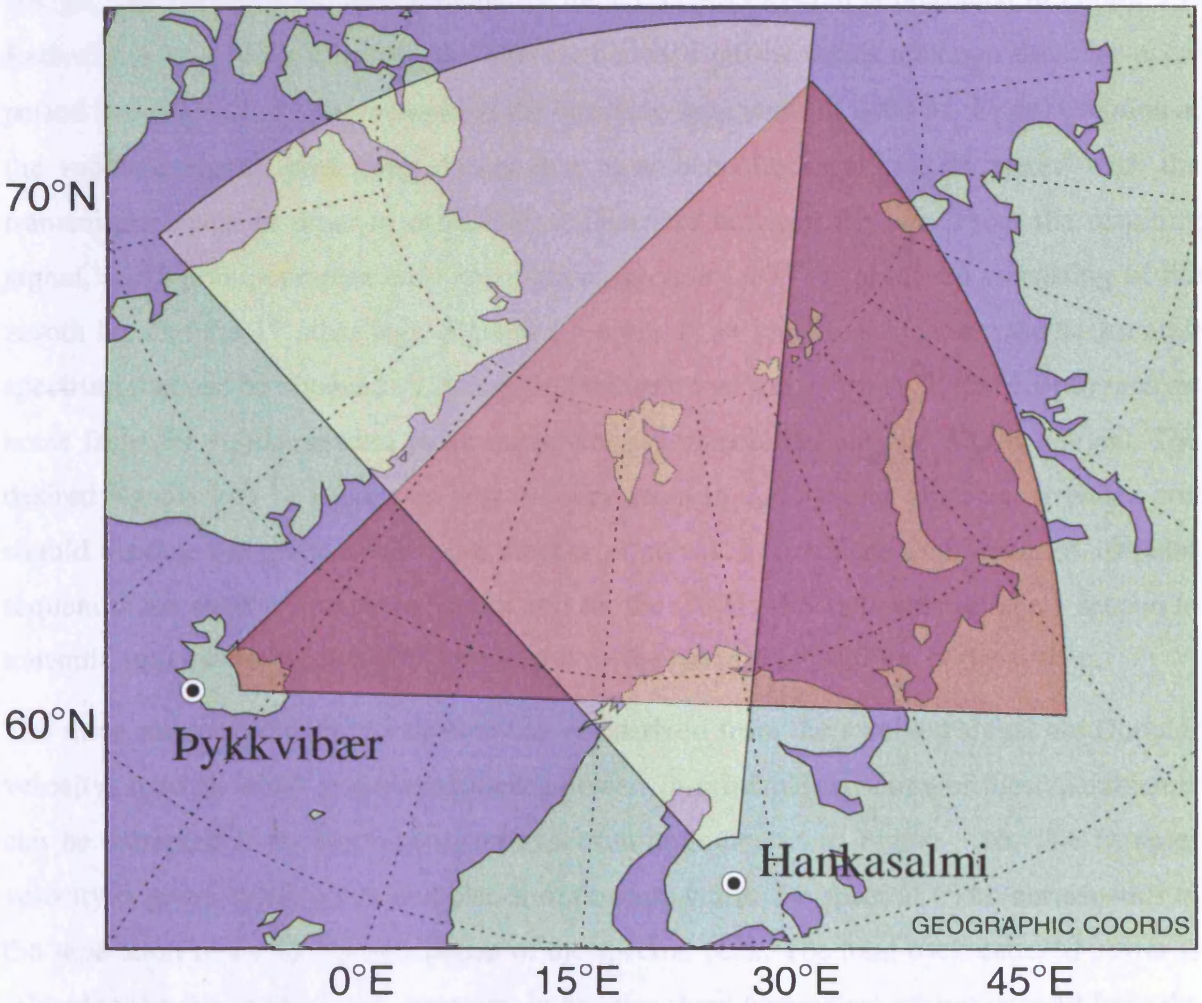

Figure 3.6. The fields-of-view of the CUTLASS Finland (*yellow shading*) and Iceland (*red shading*) radars.

either 3 or 7 s producing a full 16-beam scan covering ~50° in azimuth every 1 or 2 minutes. Ordinarily, 75 range gates of length 45 km are sampled from each beam with a lag to the first gate of 180 km. As a result, in standard scan mode each CUTLASS radar has the potential to make observations to a range greater than 3500 km, encompassing an area in excess of 3×10^6 km^2. The radars are fully automated and operate 24 hours a day, 365 days a year excepting maintenance periods or equipment failures.

The CUTLASS radars transmit a pulse sequence that comprises 7 individual pulses of length 300 μs. The normal scan pulse scheme for the CUTLASS system is presented in Figure 3.7. Rather than remaining constant, the interval between pulses varies although the inter-pulse period is always an integer multiple of the basic lag separation of 2400 μs. Upon reception at the radar, a signal containing pulses that have been backscattered is mixed with the transmitted signal in order to extract the differences between the two. From the resulting signal, an 18 point, complex *auto-correlation function* (ACF) is produced consisting of the zeroth lag and the 17 other lags. Figures 3.8 presents an idealised ACF and the backscatter spectrum that can be obtained by taking the Fourier transform of the ACF. In order to remove noise from the signal, several pulse sequences are transmitted and the ACF averaged. The desired signals will be correlated whereas any noise in the signal will be uncorrelated and should average out given a sufficient number of pulses. In practice, a minimum of 10 pulse sequences are required to remove noise and for the CUTLASS radars these take 1 second to transmit, imposing a fundamental lower limit on the temporal resolution of the system.

The three most significant parameters that are derived from the received signal are Doppler velocity, spectral width and backscattered power. In principle, all three of these parameters can be extracted from the backscatter spectrum as indicated in Figure 3.8b. The Doppler velocity is given by the mean Doppler-shift position whilst the spectral width corresponds to the separation of the half power points of the spectral peak. The total backscattered power is related to the area beneath the spectrum. In practice these parameters are not derived from the spectrum since the peak is defined by only a small number of points from the original 18 lag ACF. Consequently, the poor resolution of the spectral peak leads to unacceptably large uncertainties is the derived parameters.

Instead, the three parameters discussed above are determined by direct analysis of the full ACF. In order to obtain the Doppler velocity, a least-squares fit is applied to the difference in phase between the real and imaginary components as function of lag (effectively a measure of the phase velocity, $d\phi/dt$). Spectral width is determined by studying the decay of the ACF

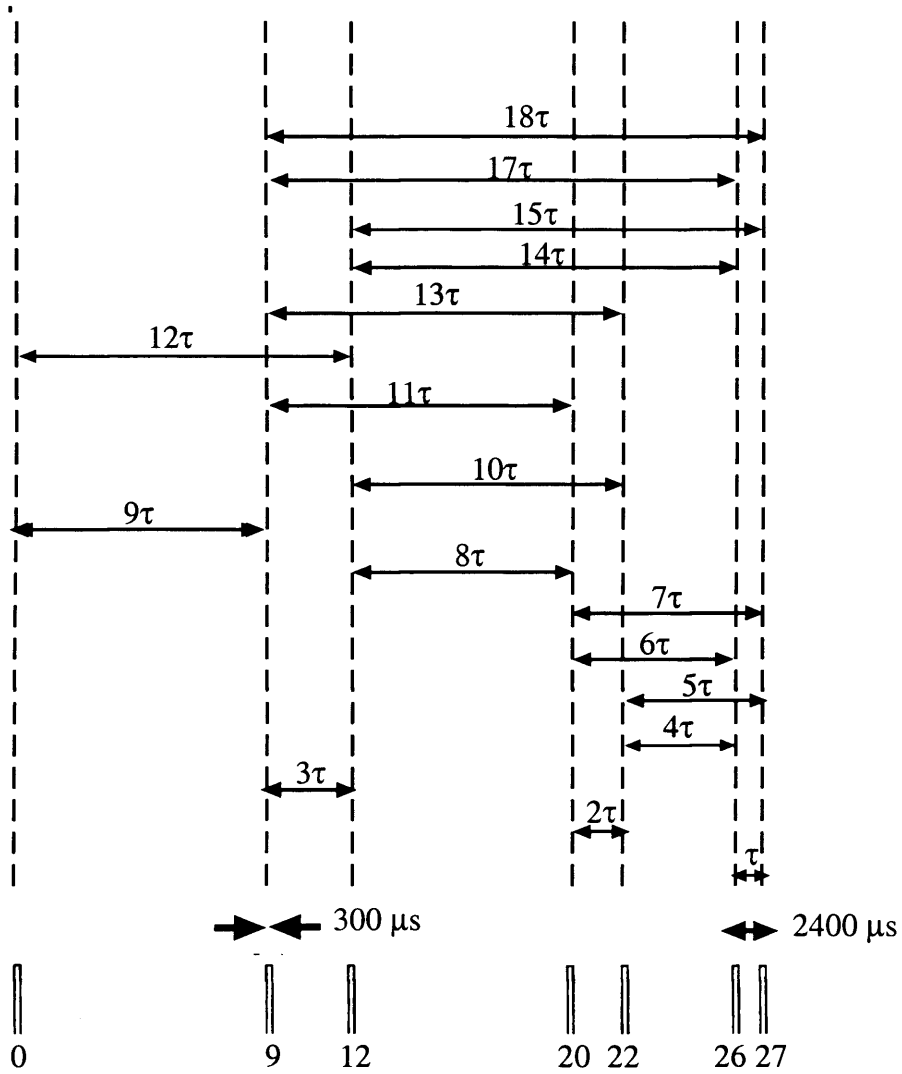

Figure 3.7. The normal scan pulse scheme for the CUTLASS radars. The sequence is made up of seven individual pulses, each of length 300 μs and the basic lag separation is 2400 μs. An 18 lag ACF is calculated, consisting of the zeroth lag and 17 other unique lags as indicated above, all of which are multiples of the basic lag separation, τ (from Provan, 1998).

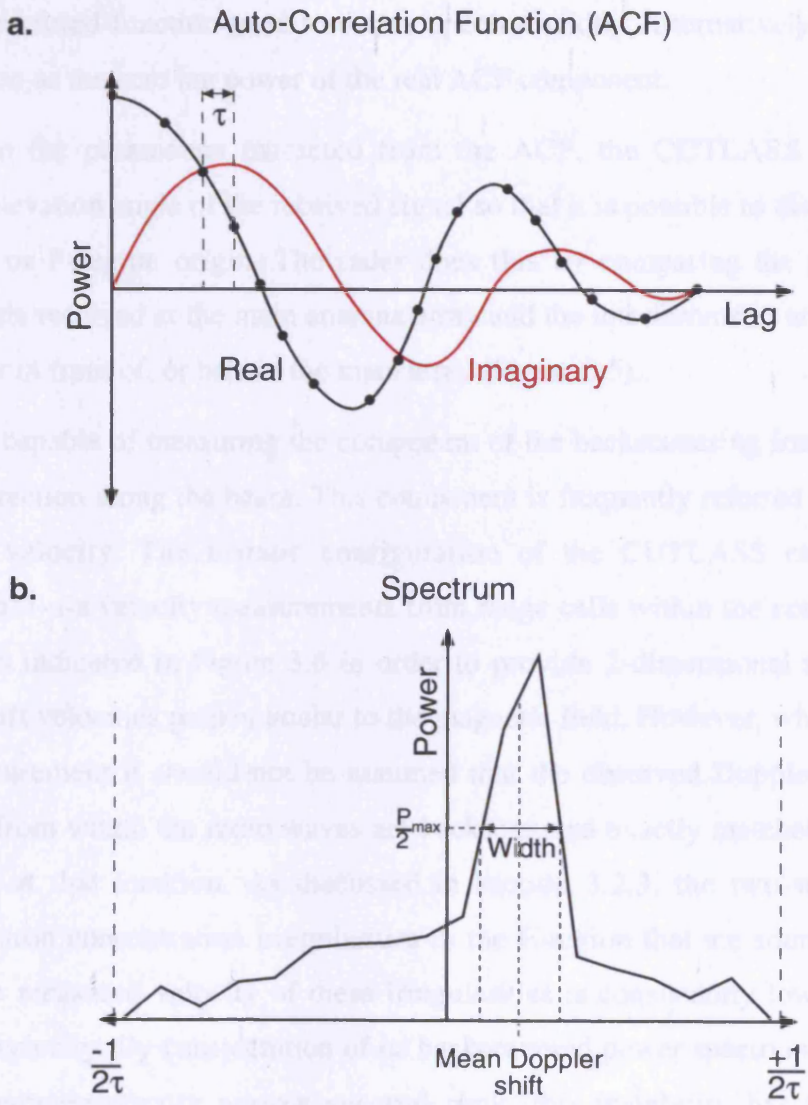

Figure 3.8. **a** The real and imaginary parts of an idealised backscatter autocorrelation function; **b** The backscatter spectrum obtained by taking the Fourier transformation of the ACF. Possible techniques to determine the spectral width and mean Doppler velocity directly from the spectrum are also indicated.

modulus in order to quantify the signal decorrelation time-scale. An assumed function is fitted to the modulus (either an exponential or Gaussian) from which the spectral width is then derived. Data presented in this thesis employ the exponential fit since this is found to be the optimum fit for most ACFs (Villain *et al.*, 1987). Finally, the backscattered power may be determined by two methods. The most frequently used approach is to calculate the intercept at zero lag of the fitted function used to derive spectral width. Alternatively, the power may simply be taken as the zero lag power of the real ACF component.

In addition to the parameters extracted from the ACF, the CUTLASS radars routinely measure the elevation angle of the received signal so that it is possible to distinguish between signals of E or F-region origin. The radar does this by comparing the phase difference between signals received at the main antenna array and the interferometer array located some distance either in front of, or behind the main array (Figure 3.5).

Each radar is capable of measuring the component of the backscattering irregularity velocity only in the direction along the beam. This component is frequently referred to as the line-of-sight (l-o-s) velocity. The bistatic configuration of the CUTLASS radars allows the combination of l-o-s velocity measurements from range cells within the common volume of the two radars indicated in Figure 3.6 in order to provide 2-dimensional measurements of irregularity drift velocities perpendicular to the magnetic field. However, when studying l-o-s velocity measurement it should not be assumed that the observed Doppler velocity of the irregularities from which the radio waves are backscattered exactly matches the ionospheric drift velocity at that location. As discussed in section 3.2.3, the two-stream instability generates electron concentration irregularities in the E-region that are sound-speed limited. Therefore, the measured velocity of these irregularities is consistently lower that the local electron drift velocity. By consideration of its backscattered power spectrum, which typically displays a characteristically narrow spectral peak, this instability has been defined as producing Type I irregularities (Bowles *et al.*, 1960). On the other hand, the gradient drift instability is not subject to an upper or lower velocity threshold and it is assumed that the irregularities move with the local $\mathbf{E} \times \mathbf{B}$ drift velocity. This implies that irregularities resulting from the gradient-drift instability are an accurate reflection of the ionospheric plasma convection speed (Greenwald *et al.*, 1985). Cohen and Bowles (1967) defined Type II irregularities as being a consequence of gradient-drift instabilities in the E and F-regions. The peak of the backscattered power spectrum from Type II irregularities is broader than for Type I suggesting that they occur in more turbulent regions of the ionosphere.

In operation, the CUTLASS radars receive backscattered radio waves from a variety of sources. Figure 3.9 presents a schematic of the propagation modes that can result in a backscattered signal being detected at the radar. Backscatter is usually denoted by the number of times ground scatter or *hops* have occurred and the ionospheric region through which the signal has propagated. For instance a 1F mode has only made 1 hop travelling through the F-region before backscattering from the ground whereas a 2F mode has been reflected from the ground and makes a subsequent hop. Ionospheric scatter is assumed to have originated half-way between points of ground scatter. Therefore, the 1/2E mode represents a signal that has been directly backscattered to the radar without being scattered from the ground.

It is possible to differentiate between signals that have been backscattered from the gound or the ionosphere by studying the 3 parameters derived from the ACF. Ground backscatter is generally powerful with a low Doppler velocity. Furthermore, signals backscattered from the ground do not decorrelate rapidly (i.e. they have an exceptionally narrow spectral width). A signal is generally assumed to have originated from ground scatter if the magnitude of the measured velocity is less than 50 m s^{-1} and the spectral width less than 50 m s^{-1}.

3.3.2 SuperDARN

In addition to operating as a stand-alone experiment, CUTLASS forms the easternmost pair of radars of the Super Dual Auroral Radar Network (Greenwald *et al.*, 1995). SuperDARN is an international chain of near-identical coherent HF radars intended to study the large-scale plasma motion due to the ionospheric convection electric field (section 2.3.1) and currently comprises 14 operational radars of which 8 are located in the northern hemisphere and 6 in the southern hemisphere as shown in Figure 3.10 and listed in Appendix A. In addition, a ninth northern hemisphere radar is currently awaiting deployment. In general, radars operate in pairs in order to provide common volumes from which 2-dimensional flows can be derived. The scheduling of the operational modes is dealt with centrally in order to most efficiently exploit the radars and an agreement between the organisations responsible for each radar ensures that data are freely distributed between SuperDARN member institutions.

The first SuperDARN radar was deployed in 1983 at Goose Bay in Canada by the Johns Hopkins University Applied Physics Laboratory (Greenwald *et al.*, 1985). Since then, many aspects of radar construction and operation have evolved considerably. For example, the proliferation of the internet has enabled cheap and relatively reliable access to the majority of

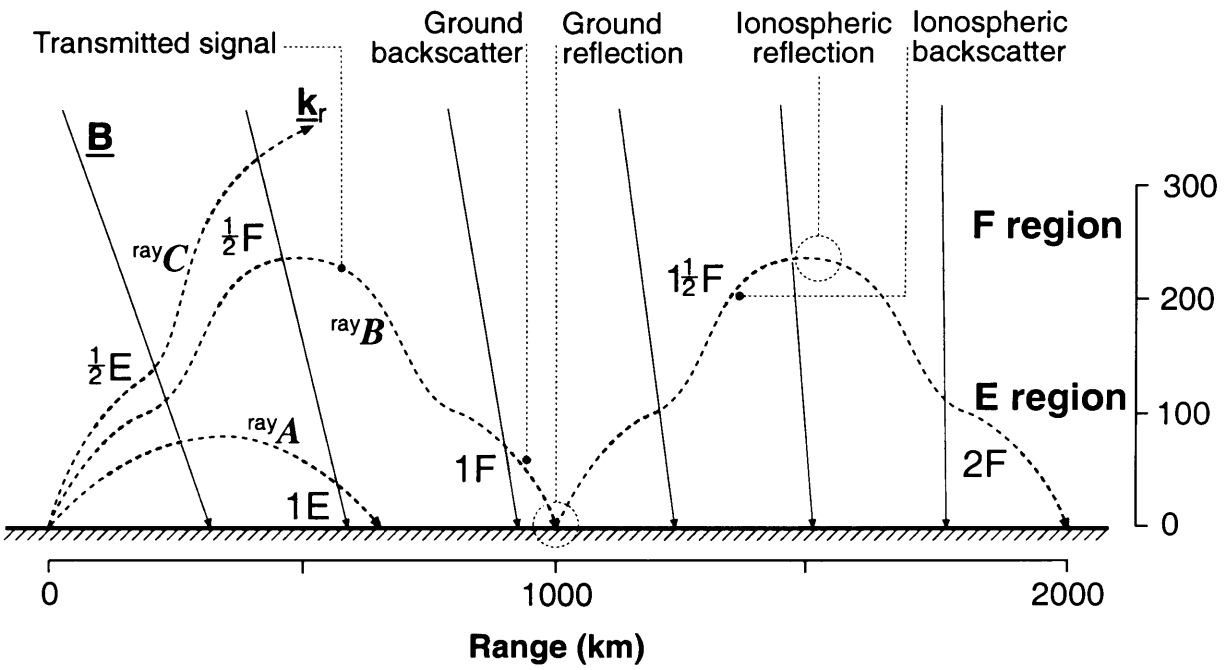

Figure 3.9. A schematic illustration presenting some of the possible modes of propagation and the regions from which backscatter can occur. The stated ranges and altitudes are approximate and depend on ionospheric conditions. Three example rays are indicated: ***A*** E-region mode; ***B*** F-region mode producing both far and near-range scatter; ***C*** a ray that penetrates the ionosphere (from Milan *et al.*, 1997).

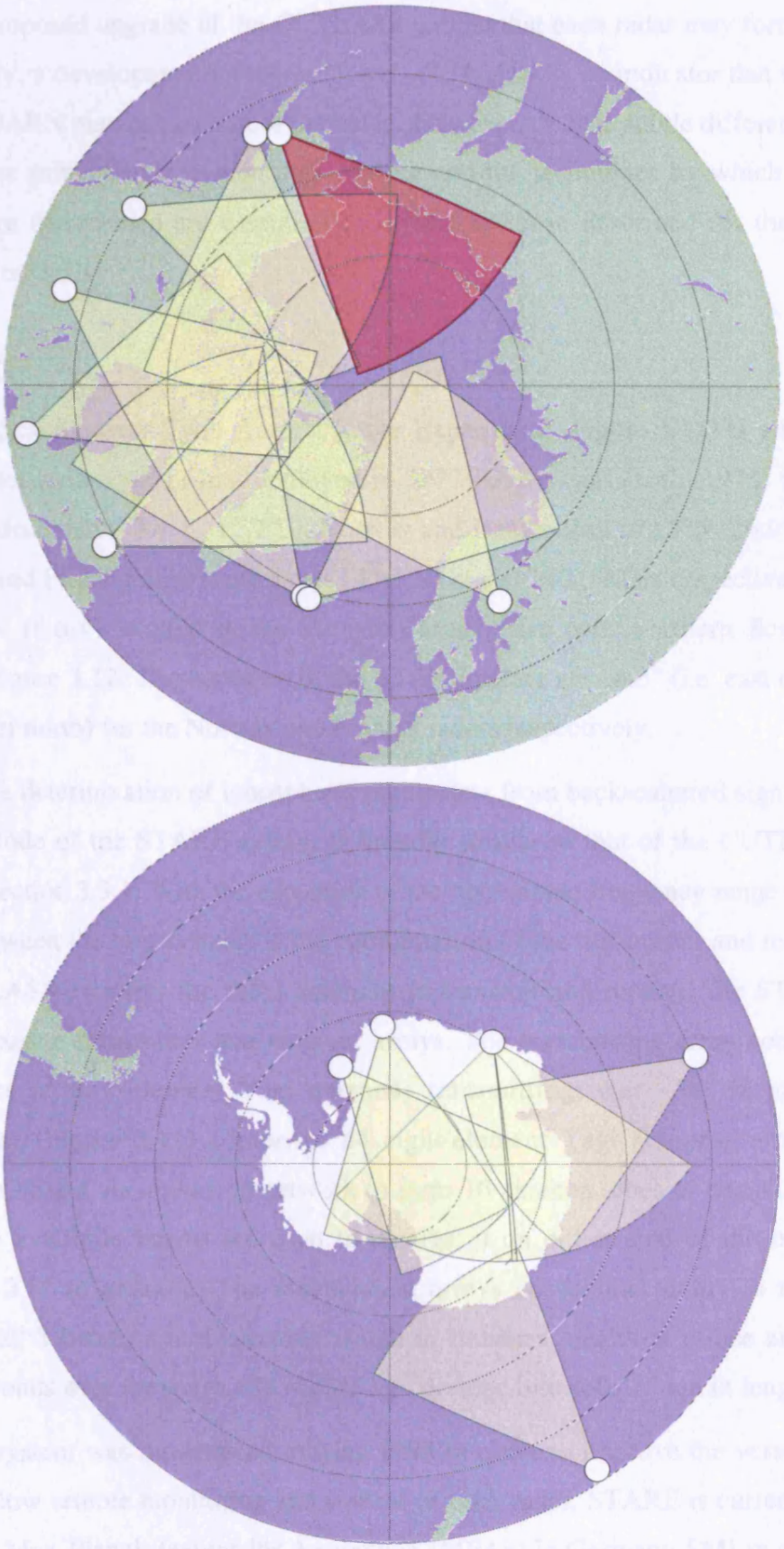

Figure 3.10. The locations and fields-of-view of northern and southern hemisphere SuperDARN radars. Operational radars are shown in *yellow* and proposed radars in *red*.

SuperDARN radars allowing the real-time recovery of data and full remote control of the radars. The proposed upgrade of the CUTLASS pair so that each radar may form two beams simultaneously, a development known as *Stereo-CUTLASS*, is an indicator that the evolution of the SuperDARN network continues unabated. However, despite subtle differences between each radar, the principles by which they operate and the techniques by which geophysical parameters are determined are essentially identical to those described for the CUTLASS radars in section 3.3.1.

3.3.3 STARE

The Scandinavian Twin Auroral Radar Experiment (Figure 3.11) is a bistatic VHF coherent-scatter radar system first deployed in 1977 (Greenwald *et al.*, 1978) with stations located in Midtsandan (63.4°N, 10.7°E), Norway and Hankasalmi (62.3°N, 26.9°E), Finland. The Norway and Finland radars operate at 143.8 MHz and 140.0 MHz respectively with their fields-of-view (f-o-v) located in the E-region ionosphere over northern Scandinavia as indicated in Figure 3.12. The boresites of the STARE radars are 26.3° (i.e. east of north) and –15.5° (west of north) for the Norway and Finland radars respectively.

In terms of the determination of ionospheric parameters from backscattered signal ACFs, the operational mode of the STARE system is broadly similar to that of the CUTLASS radars described in section 3.3.1. With the exception of the operational frequency range the principal difference between the two systems is the configuration of the transmitter and receiver array. Whilst CUTLASS employs the same antennas to transmit and receive, the STARE radars each have separate transmitter and receiver arrays. The transmitting array consists of two vertical stacks of four-element Yagi antennas transmitting over ~58° in azimuth. The receiving array (Figure 3.11) comprises 64 eight-element Yagi antennas arranged in 16 vertical stacks linked via a phasing network to form 16 antenna lobes or beams. In practice, only 8 of the available beams are used to receive, 4 on either side of the boresite each separated by 3.6° in azimuth. The independent arrays confer the ability to transmit and receive over all 8 beams simultaneously which in standard operation utilise an integration time of 20 seconds over the range 495 – 1245 km, divided into cells 15 km in length.

The STARE system was modernised in May 1998 in order to improve the versatility of the system and allow remote monitoring and control of each radar. STARE is currently operated jointly by the Max-Planck-Institut für Aeronomie (MPAe) in Germany FMI in collaboration with ELAB (University of Trondheim) in Norway.

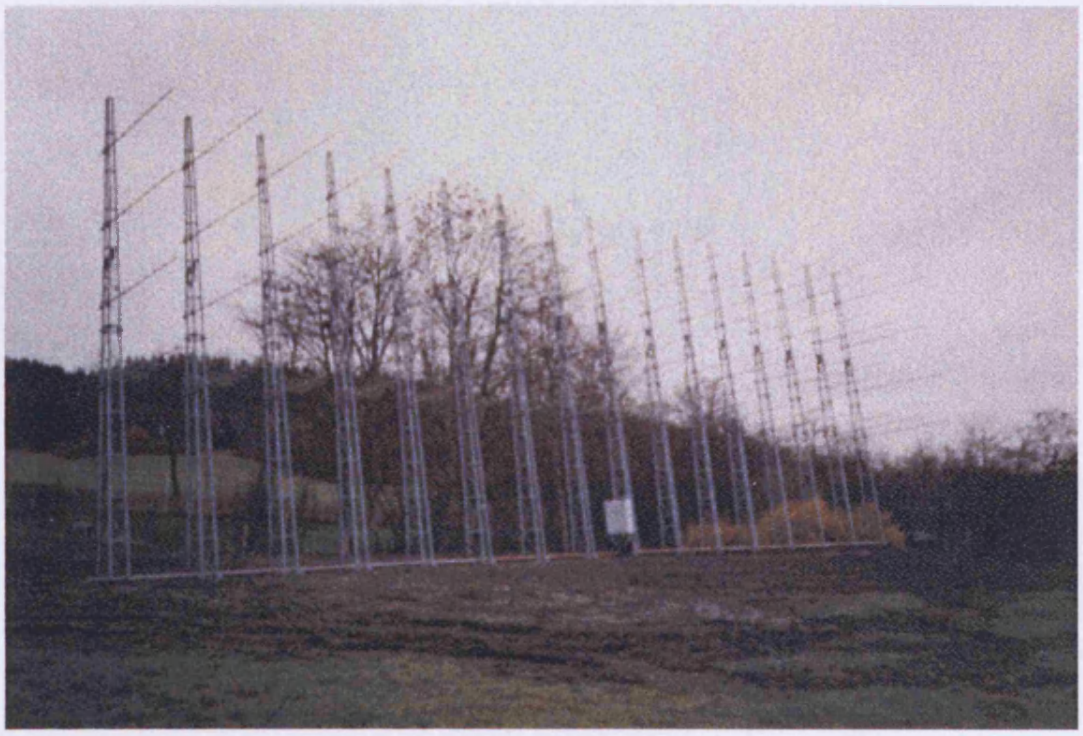

Figure 3.11. The receiver array of the STARE radar located in Midtsandan, Norway.

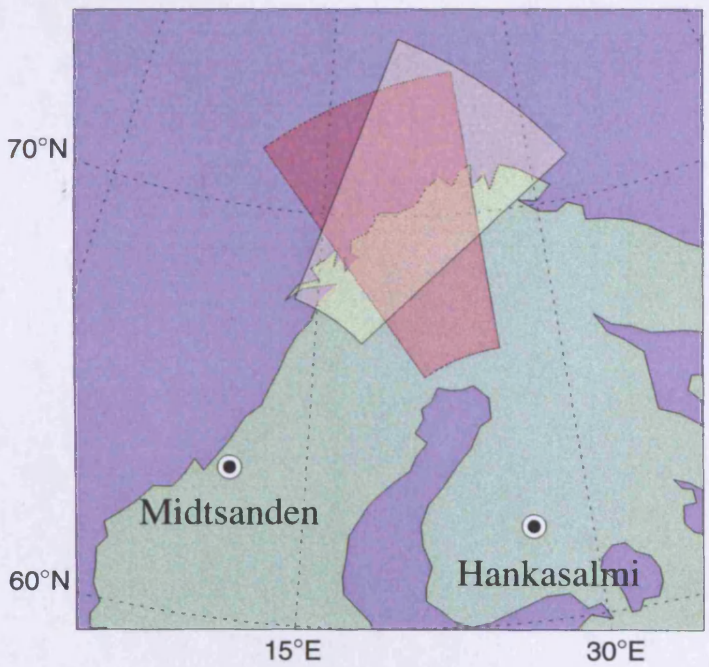

Figure 3.12. The locations and fields-of-view of the STARE radars.

3.4 Incoherent-scatter radars

Although the majority of radar data presented in this thesis originate from coherent-scatter systems, some incoherent-scatter radar observations are included. It is therefore appropriate to provide a brief account of the technique and the radar system employed.

3.4.1 Incoherent-scatter theory

The scattering of electromagnetic radiation from a single electron was first proposed by J. J. Thomson (1906) who demonstrated that the scattering cross-section was related to the classical radius of the electron. It was not until 1958 that the sensitivity of radar equipment had advanced sufficiently to measure radio waves backscattered from incoherent sources. The first practical measurements of an incoherent-scatter spectrum were made by Bowles (1958) at Long Branch, Illinois using a 6 MW transmitter operating at a frequency of 41 MHz. It had been predicted by Gordon (1958) that the spectrum would have a Doppler shift due to the bulk motion of ionospheric electrons and a width related to their thermal velocities however the measured spectral width was considerably narrower than expected. The cause for this discrepancy was explained in a clutch of papers published in quick succession (e.g. Dougherty and Farley, 1960; Fejer, 1960; Hagfors, 1961).

The electrostatic forces within a plasma are such that ions tend to form a shielding layer around each electron. The effectiveness of this shielding layer is influenced by the interplay between random thermal energy and the electrostatic potential of each species and is described by the *Debye Length*, D, given by

$$D = \left(\frac{\varepsilon_0 k T_e}{N_e e^2} \right)^{1/2} \approx 69 \left(\frac{T_e}{N_e} \right)^{1/2} \tag{3.13}$$

where ε_0 is the permittivity of free space, k is the Boltzmann constant, e is the charge of an electron and T_e and N_e are the electron temperature and number density respectively. Eq. (3.13) implies that the Debye length of ionospheric plasma will vary with altitude since both T_e and N_e are altitude dependent. Furthermore, the Debye length is influenced by solar activity, season, time of day and geographic location with values ranging from ~0.3 cm at the F-region peak to ~6cm in the lower E-region. If the wavelength of the radio wave incident upon the plasma is smaller than the Debye length then true incoherent or electron-dominated scatter of the kind suggested by J. J. Thomson will occur and the backscattered power spectrum will have the wide bandwidth predicted by Gordon (1958).

If the wavelength of the radar signal is comparable, or larger than, the Debye length then scattering occurs via a different process. Through electrostatic coupling, random thermal motion of the electrons within the plasma generate longitudinal oscillations known as *ion-acoustic* and *electron-acoustic waves.* These waves result in electron concentration fluctuations from which the incident signals backscatter. Of course, this implies that incoherent-scatter is in fact not truly incoherent at all. Rather than obtaining true Thomson scatter from individual charge carriers, the signal is scattered by the thermal wave mode which has the required wavelength to satisfy the Bragg condition for the sounding radar wave. Rather than being a disadvantage, the almost coherent nature of the "incoherent-scatter" technique is a positive benefit. If the scatter had actually been incoherent-scatter from electrons then the shape of the backscattered power spectrum would have yielded information regarding the electron concentration (from the total returned power), electron temperature (from the spectral width) and the bulk plasma velocity (from the mean Doppler shift). Since the scatter is quasi-coherent from ion-acoustic waves, the properties of which change in response to the characteristics of the ions as well as the electrons, information regarding the ion population can be determined also. The incoherent-scatter technique will therefore yield three further parameters namely the ion temperature, ion composition and ion-neutral collision frequency. In addition to the parameters that may be measured directly, a host of parameters may be inferred from incoherent scatter observations. A list of parameters that can be measured or derived using the incoherent scatter technique is presented in Table 3.1.

3.4.2 EISCAT

The European Incoherent Scatter radar system (e.g. Rishbeth and Williams, 1985) can trace its origins to the URSI meeting held in Ottawa in 1969 at which time the concept of a sophisticated incoherent-scatter radar system located at high-latitude was first suggested. By 1975, an agreement had been signed creating the EISCAT Scientific Association which was to be based in Kiruna, Sweden. Under this agreement France, Germany and the UK each contributed 25% of the capital and operating costs whilst Norway, Sweden and Finland jointly contributed the remaining 25%. Operations began in 1981 with the commissioning of a tristatic UHF system which was supplemented in the summer of 1984 by a monostatic VHF radar located in Tromsø, Norway (Figure 3.13). In recent years, Japan has joined the EISCAT Scientific Association and the radar system has been enhanced by the completion of the EISCAT Svalbard Radar (ESR) project (Wannberg *et al.*, 1997) which now comprises two UHF incoherent-scatter radars.

Directly measured parameters	**Derived indirectly**
Electron density, N_e	Electric field, E
Electron temperature, T_e	Hall conductivity, σ_H
Ion temperature, T_I *	Hall current, J_H
Ion composition, m_I	Pedersen conductivity, σ_P
Ion velocity, v_I *	Pedersen current, J_P
Electron velocity, v_e *	Joule heating
Ion-neutral collision frequency, ν_{in}	Neutral temperature, T_n
Photoelectron flux	Neutral density, N_n
Electric current density, $\mathbf{J} = N_e(v_e - v_i)$ *	Neutral velocity, v_n

Table 3.1. List of a measured and derived parameters obtained from the incoherent scatter technique. Parameters labelled with an asterisk cannot be determined fully using a monostatic system. In that case, only the line-of-sight component of the parameter will be measured.

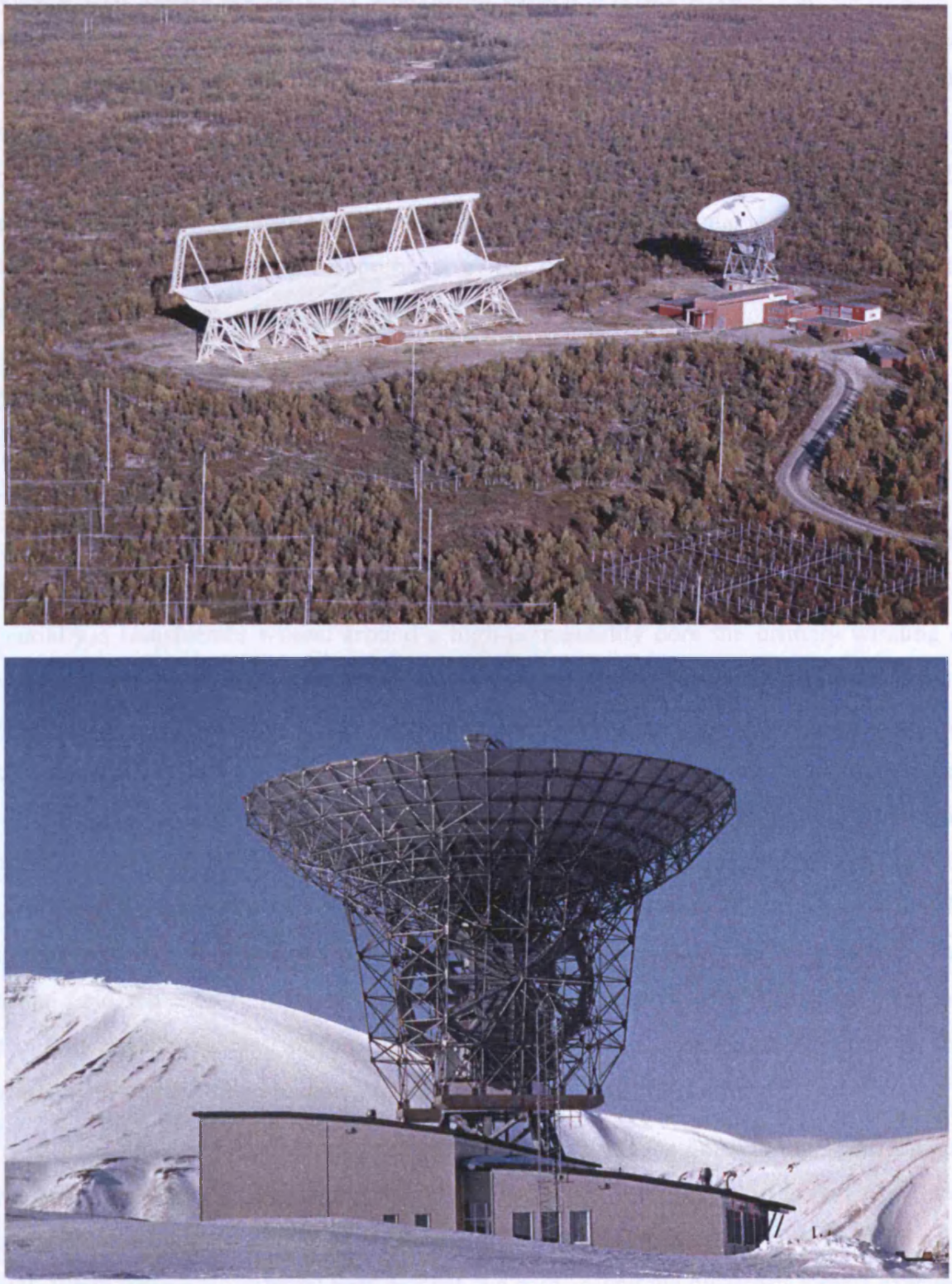

Figure 3.13. (*Top panel*) The EISCAT site at Ramfjordmoen near Tromsø, Norway. The VHF antenna is on the left and the 32 m UHF antenna is on the right, adjacent to the buildings that contain the transmitters and control equipment. (*Lower panel*) The buildings and 32 m steerable antenna of the ESR at Longyearbyen, Svalbard (Photographs courtesy of EISCAT).

The locations and configurations of the EISCAT radars are summarised in Table 3.2. The mainland UHF radars are currently undergoing extensive refurbishment with the upgraded system expected to begin operations by the autumn of 2000. The EISCAT radars are operated irregularly but frequently on a campaign basis with experimental personnel augmenting the permanent EISCAT staff at each site as required. The choice of radars and the mode in which each radar operates may be modified to satisfy the scientific requirements of any particular experimental campaign. There are currently far too many experimental configurations of the EISCAT system to present a comprehensive list, therefore a description of the relevant experiments will be presented as appropriate in later chapters.

3.5 Magnetic field observations

3.5.1 The measurement of magnetic fields

The instrument most commonly adopted to measure magnetic field vectors is the *fluxgate magnetometer*. The element of this instrument that is sensitive to magnetic fields is essentially a transformer wound around a high-permeability core the primary winding of which is driven by high frequency (~kHz) alternating current. The strength of the driving current and the permeability of the core are chosen so that the core saturates on each half cycle. A secondary or *sense* winding measures a time-varying voltage due to the input signal. In the special case of no external magnetic fields, the output reaches saturation at the same threshold value both half-cycles of the driving signal. This is illustrated in Figure 3.14a for a fluxgate magnetometer the core of which has a linear hysteresis curve (i.e. a core in which the resultant magnetic field is directly proportional to the applied field). In the presence of an external field, the core-field reaches saturation in one half-cycle sooner than in the other and the output signal becomes asymmetric as a result, as shown in Figure 3.14b. It is this asymmetry that is exploited to determine the ambient magnetic field strength.

In reality, in order to increase the sensitivity of fluxgate magnetometers high-permeability cores are often used. For high-permeability materials, the hysteresis curve is very non-linear (i.e. a loop) and the output signal is highly distorted, containing many harmonics of the input signal. When there is no external field present, the path around the hysteresis loop is executed in a symmetric manner. For this case it can be shown that only odd harmonics of the driving frequency are present in the output signal. In the presence of an external field, the asymmetry of the field saturation introduces even harmonics to the output signal. The amplitude and

Station	Location	Antenna	Freq (MHz)	Peak Tx Power (MW)	Mean Tx Power (MW)
Tromsø, Norway UHF	69.6°N 19.2°E	32 m steerable paraboloid (transmit/receive)	931.5 (928.5)	1.3 (2.6)	0.16 (0.65)
Kiruna, Sweden UHF	67.9°N 20.4°E	32 m steerable paraboloid (receive only)	931.5 (928.5)		
Sodankylä, Finland UHF	67.4°N 26.7°E	32 m steerable paraboloid (receive only)	931.5 (928.5)		
Tromsø, Norway VHF	69.6°N 19.2°E	120 m x 40 m fixed azimuth parabolic cylinder (transmit/receive)	224	3	0.37
Longyearbyen, Svalbard UHF	78.1°N 16.0°E	32 m steerable paraboloid (transmit/receive)	500	1	0.25
Longyearbyen, Svalbard UHF	78.1°N 16.0°E	42 m fixed paraboloid (transmit/receive)	500	1	0.25

Table 3.2. The geographic locations, antenna configurations and transmitter characteristics of the EISCAT radars. The values quoted reflect realistic operational system parameters over recent years rather than the original design specification. The expected capabilities of the UHF system following refurbishment during the summer of 2000 are enclosed in brackets.

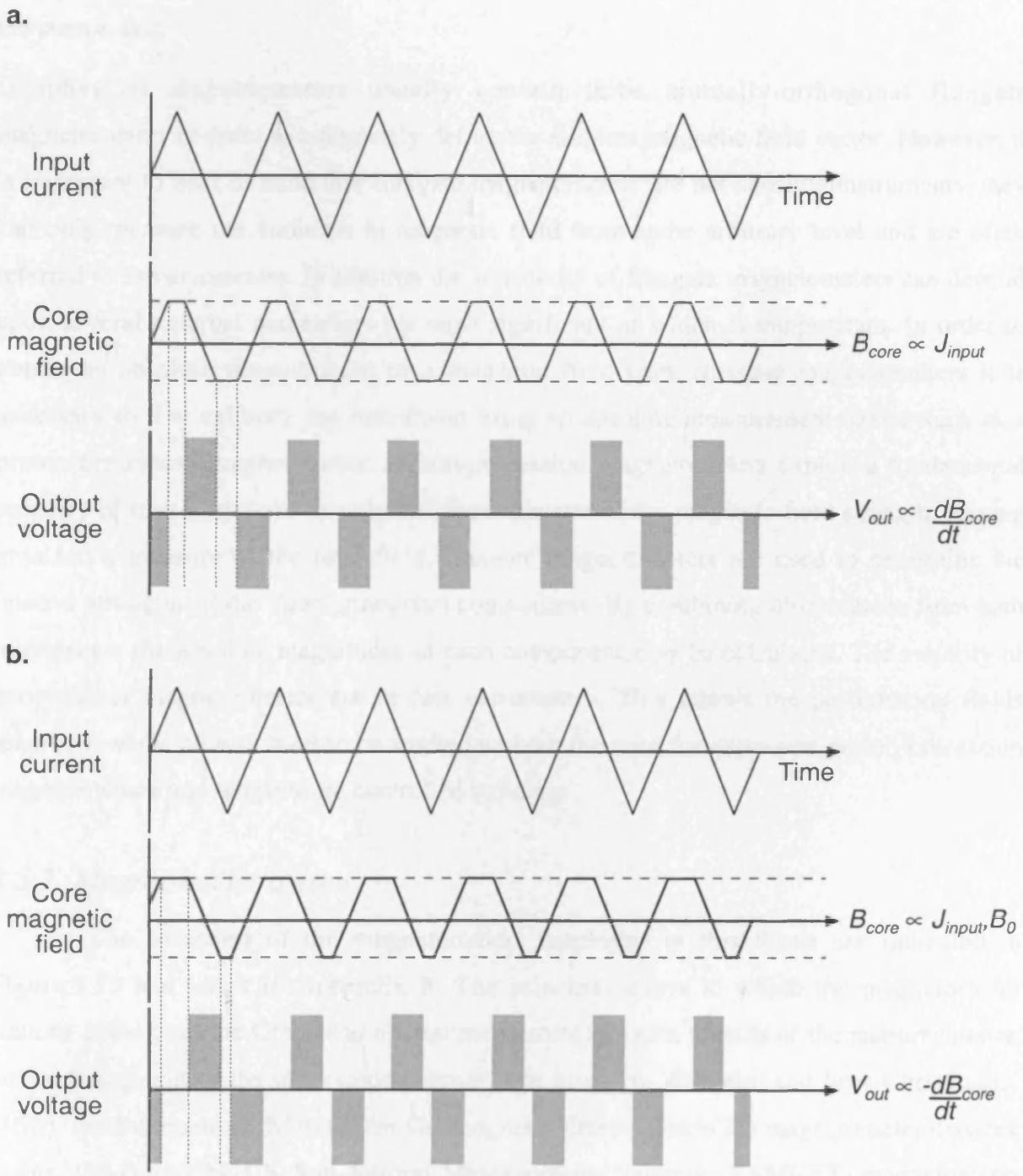

Figure 3.14. A schematic representation of the operating principles of a fluxgate magnetometer. **a** In the presence of no external field, the magnetic field within the core is saturated symmetrically during each half-cycle of the driving signal. The output from the sensing coil is therefore made up of equally spaced pulses; **b** When an external field is applied the total magnetic field within the core is the sum of the fields produced by the driving current and the background field. The core field therefore saturates earlier in one half-cycle than the other. As a result the sensing coil output pulses are spaced asymmetrically. The degree of asymmetry therefore contains information regarding the background magnetic field.

phase of all even harmonics are proportional to the magnitude and direction of the field along the sensor axis.

Geophysical magnetometers usually contain three mutually-orthogonal fluxgate magnetometers in order to completely define the ambient magnetic field vector. However, it is important to bear in mind that fluxgate magnetometers are not absolute instruments, they can only measure the variation in magnetic field from some arbitrary level and are often referred to as *variometers*. In addition the sensitivity of fluxgate magnetometers can depend upon several external parameters the most significant of which is temperature. In order to obtain an absolute measurement of a magnetic field from fluxgate magnetometers it is necessary to first calibrate the instrument using an absolute measurement device such as a proton-precession magnetometer. Proton-precession magnetometers exploit a fundamental property of matter to make an unbiased measurement of the magnetic field strength. Having obtained a measure of the total field, fluxgate magnetometers are used to determine the relative strengths of the three orthogonal components. By combining observations from both instruments the absolute magnitudes of each component may be calculated. The majority of geophysical magnetometers are in fact variometers. This allows the perturbation fields relative to some chosen level to be studied without the need for expensive proton-precession magnetometers and temperature controlled buildings.

3.5.2 Magnetometer arrays

The locations of the magnetometers employed in this thesis are indicated in Figure 3.15 and listed in Appendix B. The principal arrays to which the magnetometer stations belong are the Greenland coastal magnetometer chain (details of the instrumentation and a description of the observatories have been given by Wilhjelm and Friis-Christensen, 1976), the International Monitor for Geomagnetic Effects (IMAGE) magnetometer network (Lühr, 1994) and the UK Sub-Auroral Magnetometer Network (SAMNET) magnetometer array (Yeoman *et al.*, 1990b). In addition, data from the Jan Mayen magnetometer deployed by the Tromsø Auroral Observatory and the Iceland magnetometers deployed by the National Institute for Polar Research (Sato *et al.*, 1984) have been used.

The measurements of magnetic field these instruments provide relate to perturbation magnetic fields rather than absolute measurements of the local magnetic field strength. Although the co-ordinate systems used to measure the magnetic field vector at each station differs between networks, all magnetic field observations presented in this thesis are presented in a common

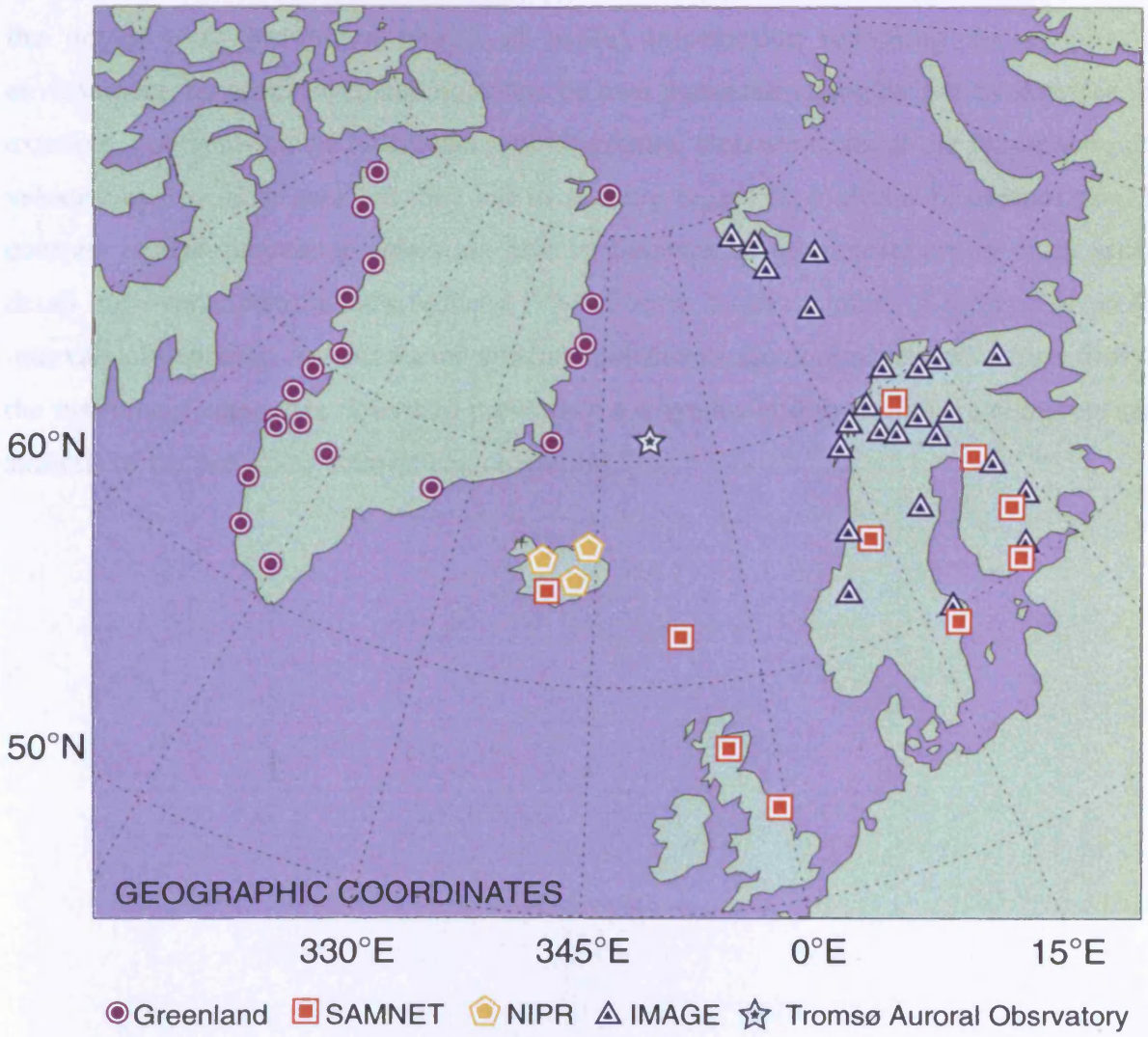

Figure 3.15. The locations of ground magnetometers employed in this thesis.

co-ordinate system. In this system the X, Y, and Z components are aligned to geographic north, geographic east, and vertically downward respectively. The temporal resolution of magnetometer data presented in this thesis varies between 1 and 20 s depending upon the array by which the data was recorded.

3.6 Summary

In this chapter a wide range of diagnostic instruments appropriate to the study of the ionosphere have been described. When considered independently, each type of instrument has the potential to provide a wealth of useful information regarding the geophysical environment, however each technique has its own particular strengths and weaknesses. For example, coherent-scatter radars can provide routine measurements of the ionospheric drift velocity over a large area but they tell us nothing regarding ionospheric composition. By contrast incoherent-scatter radars are able to characterise the ionosphere in much greater detail but over a significantly reduced field-of-view. Later chapters of thesis will present intervals of particular interest during which simultaneous measurements drawn from many of the instrument categories described previously are synthesised to facilitate a comprehensive analysis of the prevailing ionospheric conditions.

CHAPTER 4

CUTLASS HF radar observations of high latitude azimuthally propagating vortical currents in the nightside ionosphere during magnetospheric substorms.

Observations, analysis and discussion of several high-latitude ionospheric phenomena are presented in this and subsequent chapters. Chapter 4 will investigate vortical ionospheric flows that have frequently been observed to propagate azimuthally in the nightside ionosphere during the expansion phase by the CUTLASS HF radars. Although similar small-scale flows have previously been observed in the dayside ionosphere this is the first comprehensive study of the structure and occurrence of such features and their association with magnetospheric substorms. The first simultaneous HF and VHF coherent-scatter radar observations of auroral omega bands, a class of auroral from often associated with the substorm recovery phase, are presented in Chapter 5 and an amended description of the electric and magnetic field structure proposed. Finally, the large-scale evolution of high-latitude ionospheric flows due to a reconfiguration of the interplanetary magnetic field during the recovery phase of an isolated substorm is investigated in Chapter 6. The material contained within Chapter 4 originally appeared in Wild and Yeoman (2000) and elements of it are contained in Yeoman and Wild, (1998; 2000) while Chapter 5 appeared originally in Wild *et al.* (2000).

4.1 Introduction

As discussed in Chapter 2, the study of highly time-dependent ionospheric electric fields that arise as a result of the substorm process and their coupling with magnetospheric source regions remains an area of lively discussion and debate. Previously, rapid ionospheric flow variations between 50 and 1000 m s^{-1} have been observed within localised electrojet features over the timescale of a few minutes (Morelli *et al.*, 1995) and these flows are usually associated with large increases (~500%) in ionospheric conductance. The extended f-o-v and high-time resolution of HF radars makes them particularly suitable for investigating large-scale ionospheric flow dynamics over short time-scales (~10 s), especially in the regions of high conductivity and low electric field at the location of substorm onset where a drop out in E-region backscatter (due to the E-Region VHF radar instrumental threshold effect

discussed in section 3.2.3) has thwarted previous VHF radar studies (e.g. Baumjohann *et al.*, 1981).

Using the CUTLASS Finland radar in a non-standard high-time resolution (~14 s) mode, Yeoman and Lühr (1997) observed pulses of equatorward flow exceeding ~600 m s^{-1} during the expansion phase of an interval of high-latitude substorm activity. The extent of the enhanced flow regions within the f-o-v of the CUTLASS radar was 400-500 km in longitude and 300-400 km in latitude, with a duration of ~5 min and a repetition period of ~8 min. By incorporating the ground magnetic perturbations observed by an extended magnetometer network, the transient features were interpreted as being due to ionospheric current vortices associated with field aligned current pairs propagating azimuthally west-to-east through the f-o-v of an almost meridionally-aligned beam. In the past, both coherent and incoherent-scatter radars have been employed to study similar propagating vortical ionospheric flows such as auroral Ω-bands in the substorm recovery phase (e.g. Lühr and Schlegel, 1994) and dayside travelling convection vortex events (e.g. Lühr *et al.*, 1996) although the relatively short lifetimes of the substorm expansion phase phenomena observed by Yeoman and Lühr (1997) specifically required high-time resolution observations. Subsequently, Yeoman *et al.* (1998) employed measurements from the *Geotail* spacecraft to associate the propagating ionospheric convection features with a dawnward perturbation and dipolarization of the magnetic field in the postmidnight sector of the geomagnetic tail.

In this chapter, similar bipolar signatures of transient convection features have been identified in observations made by the CUTLASS Iceland radar. By employing an almost azimuthally pointing beam operating in a high-time resolution mode (~14 s) it is possible to clearly observe the azimuthal motion of regions of intense l-o-s ionospheric flow velocity ($\leq$ 800 m s^{-1}) as they propagate either away from, or toward, the radar at speeds $\leq$2000 m s^{-1}. Case-studies from two intervals of substorm activity are presented in order to demonstrate the radar signatures of the ionospheric flows that arise due *to azimuthally propagating vortical currents* (APVCs). Measurements from ground magnetometers have also been included in order to study the characteristic perturbations in the local magnetic field. Finally, by performing a statistical study of all available CUTLASS high-time resolution data the relationship between APVC occurrence and substorm phase is examined.

4.2 Instrumentation

Figure 4.1 presents the locations of the instrumentation referred to in this chapter relative to an Altitude Adjusted Corrected GeoMagnetic co-ordinate (AACGM) system (Baker and Wing, 1989). Ionospheric convection velocities are provided by the CUTLASS radars described in section 3.3.1. The high-time resolution measurements required for this study have been obtained using a technique first employed by Pinnock *et al.* (1995) in order to study the ionospheric footprint of the cusp. In general, rather than dwelling on each radar beam for 3 or 7 s in the sequence 0, 1, 2, 3, ...,15 the scan pattern is of the form *n*, 1, *n*, 2, *n*, 3, ..., *n*, 15 allowing measurements to made in beam direction *n* at an enhanced temporal resolution (6 or 14 s) whilst still making observations over the entire f-o-v, albeit at a reduced temporal resolution (2 or 4 min).

As discussed in section 3.5.2, all magnetic field observations have been made by fluxgate magnetometers and data have been presented in a common co-ordinate system where *X*, *Y* and *Z* components have directions geographic north, geographic east and vertically downwards respectively. Each magnetometer station is designated by a three-letter code derived from the station's location as indicated in Figure 4.1 and listed in Appendix B.

4.3 APVC case study: 27th August 1996

4.3.1 Ground-based magnetometer observations

Figure 4.2 presents *X* and *Y* component magnetograms from a selection of stations of the Greenland coastal, NIPR, IMAGE and SAMNET arrays during the interval 01–04 UT on 27th August 1996 (hereafter referred to as *Interval 1*). The lowest panels have been bandpass filtered between 20 and 120 s in order to display Pi2 pulsations and provide a reference time for the substorm onsets (Rostoker *et al.*, 1980). Commencing at 01:42 UT NAQ and HUS observed a sudden decrease in the *X* component (≤100 nT in ~5 min) whilst GML simultaneously observed Pi2 pulsations which then decayed in amplitude over the following 10 min. A negative disturbance in the magnetic field *X* component is a typical indicator of substorm expansion phase onset (e.g. Akasofu *et al.*, 1965). This negative perturbation is a consequence of the increased southward magnetic field observed at the ground due to the enhancement of the westward electrojet associated with the westward travelling surge (Chapter 2). In general, large-scale disturbances were not observed by high latitude IMAGE or Greenland magnetometers although low-amplitude, high-frequency oscillations were present. At 01:42 the magnetic local times of NAQ, HUS, OUJ and GML were 23:32, 01:32,

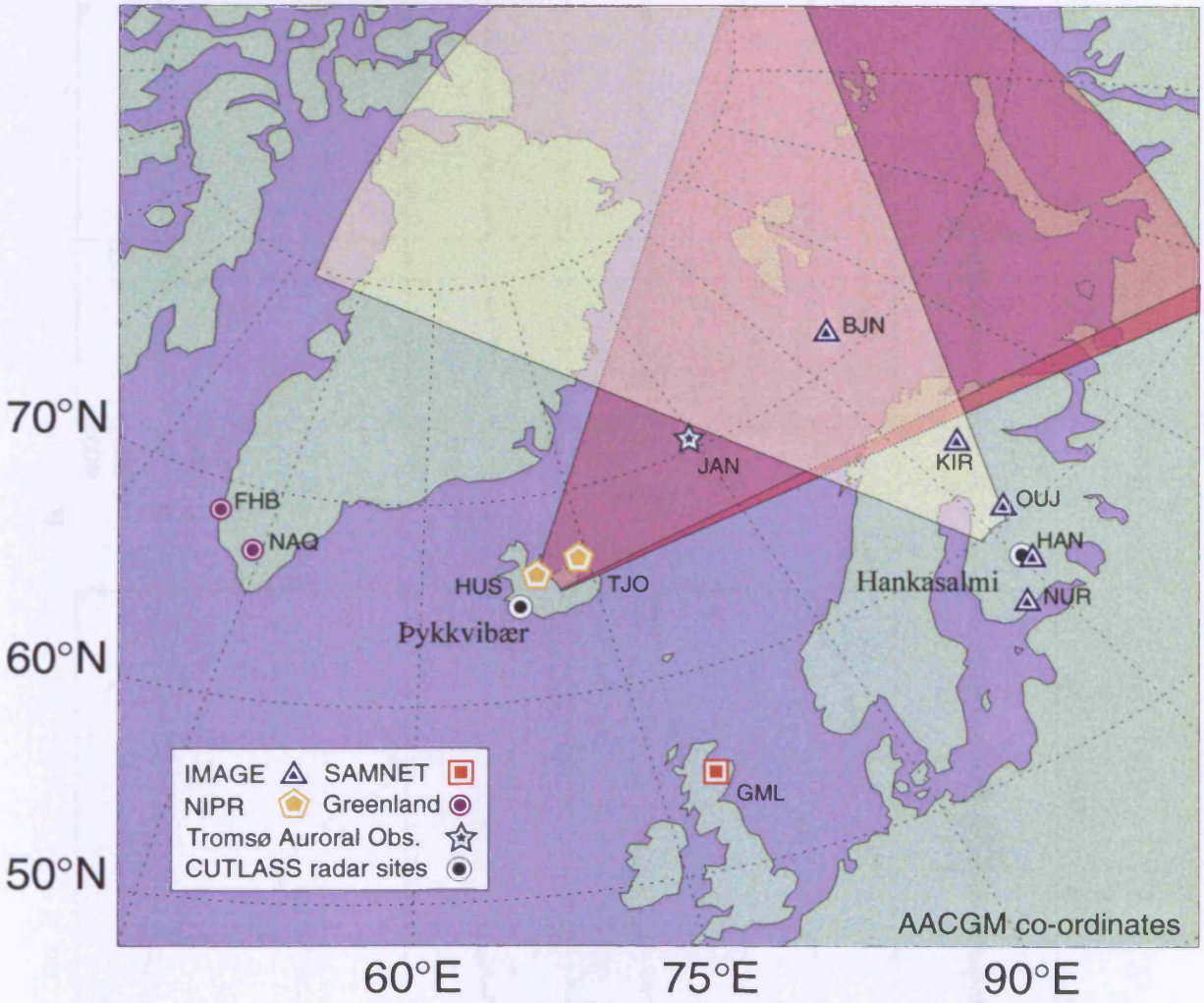

Figure 4.1. The locations of the fields-of-view of the CUTLASS Finland (*yellow shading*) and Iceland (*red shading*) radars. Beam 15 of the Iceland radar is indicated by *dark red shading*. An AACGM coordinate grid has been overlaid and also displayed are the locations of magnetometer stations from the IMAGE, NIPR, SAMNET, Greenland coastal and Tromsø Auroral Observatory arrays.

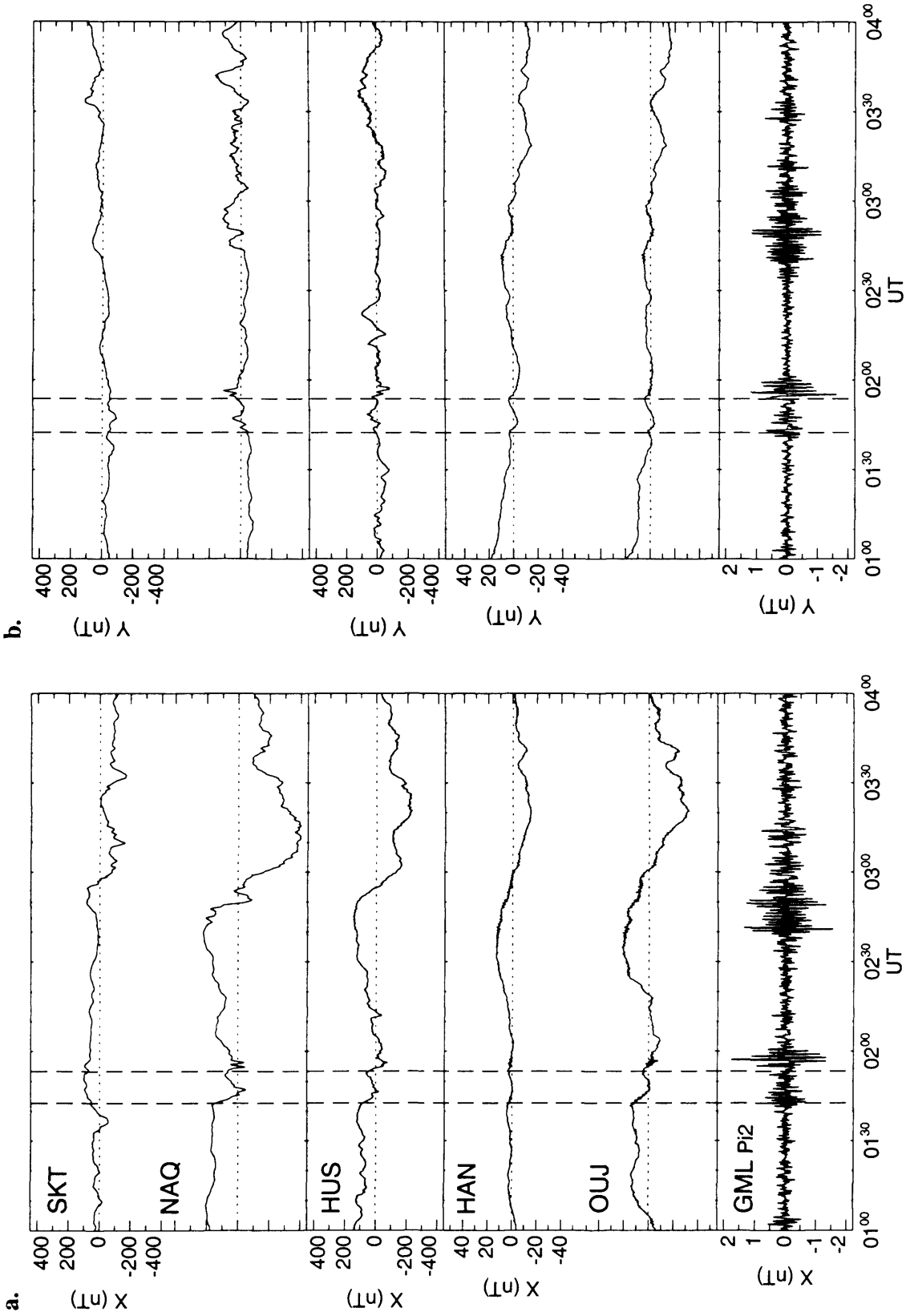

Figure 4.2. Ground magnetograms recorded during the interval 01-04 UT on 27th August 1996 from the Greenland coastal array *(top panel)*, the NIPR Iceland array *(second panel)*, and the IMAGE array *(third panel)*. A bandpass filtered (200–20 s) trace from the GML magnetometer of the SAMNET array is also included *(bottom panel)*. Substorm expansion phase onset/intensifications described in the text are indicated with *dashed vertical lines*. **a** *X* components; **b** *Y* components.

04:06 and 01:12 respectively. A subsequent substorm onset/intensification at 01:53 UT was characterised by a further decrease in *X* component magnetic field at NAQ and HUS and was accompanied by mid-latitude Pi2 pulsations. This second onset/intensification also imposed no significant perturbations on the magnetic field observed in the high latitude Scandinavian sector (both onsets are indicated in Figure 4.2 by dashed vertical lines). For approximately 30 min after 02:00 UT the *X* component of the magnetic field appears to recover to a level comparable to that prior to the substorm activity at 01:42 UT. During this interval, at 02:10 UT there is a sharp reduction in the *X* component measured at HUS. As the *X* component is going negative the *Y* component observed at these stations first increases, then decreases and then increases once more before recovering to a pre-disturbance level. No mid-latitude Pi2 pulsations were observed to accompany this activity, the maximum *X* component disturbance amplitude was ~100 nT and the *Y* component ~150 nT. At 02:40 UT Pi2 pulsations were observed at GML after which *X* component negative bays began to form first at NAQ and subsequently at HUS and OUL, dominating the remainder of the interval presented.

4.3.2 Radar measurements of ionospheric convection

The l-o-s convection velocities observed by the CUTLASS Iceland radar between 00-04 UT on 27th August 1996 are presented in Figure 4.3a. The near-azimuthal orientation of beam 15 implies that observations are made over a large range of magnetic longitudes (~50°) but a relatively small range of magnetic latitudes (~6°) in comparison to other beams. Line-of-sight Doppler velocities are therefore colour-coded and plotted as a function of universal time and magnetic longitude. During this interval the radar was scanning over half of the possible f-o-v only (beams 8-15), returning to beam 15 every other beam. The dwell time on each beam was 7 s resulting in a resolution of 14 s on beam 15 and scan of half of the f-o-v every 2 min. Shortly after the 01:53 UT expansion phase onset/intensification there was a significant reduction in the amount of backscattered signal observed by the radar which remained for ~15 min. During this period the motion of ionospheric irregularities outside of the reduced scatter region was suppressed (approximately 100 m s^{-1}) in comparison to the flows that occurred prior to substorm onset (~±500 m s^{-1}). At 02:23 UT a short-lived region of intense flow (≥600 m s^{-1}) directed toward the radar was observed at ~75° magnetic longitude with a duration ~2 min. This was immediately followed by a region of oppositely directed flow of almost equal magnitude that propagated ~6° in longitude down-range (i.e. eastward) from the radar over the subsequent 6 min. This is equivalent to an eastward propagation

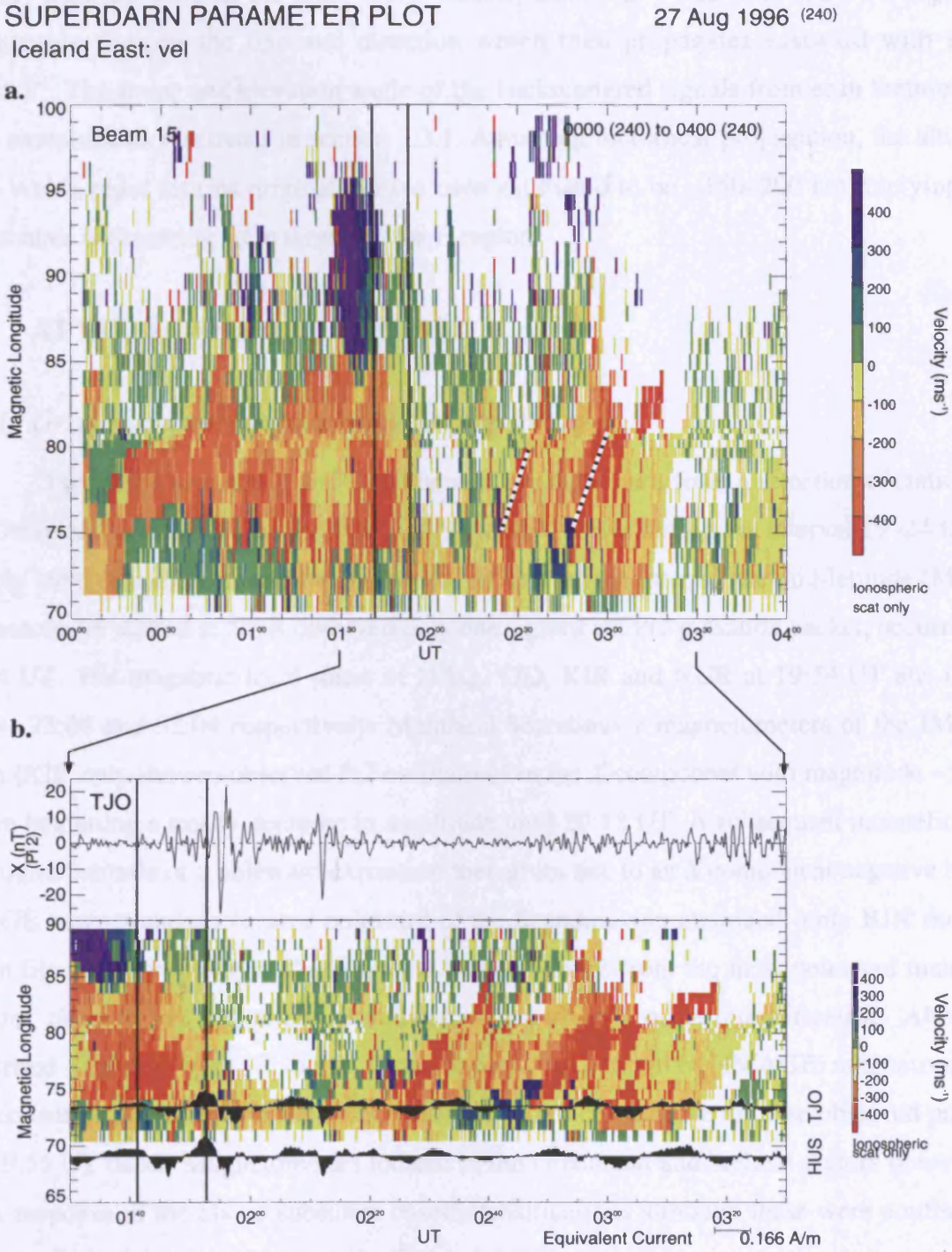

Figure 4.3. a Line-of-sight velocities from beam 15 of the CUTLASS Iceland radar as a function of magnetic longitude and universal time during (UT) the interval 00–04 UT on 27th August 1996. Positive Doppler velocities are towards the radar (approximately westward directed) and negative Doppler velocities are away from the radar (approximately eastward directed). Both of the features discuessed in the text are indicated with a *dashed line*; **b** Expanded view of the interval 01:30-03:30 UT for magnetic longitudes 65°-90°. Overlaid at appropriate magnetic longitudes are longitudinal components of equivalent current vectors derived from ground magnetometer data (see text). The *upper panel* displays *X* component magnetic field from TJO, bandpass filtered between 200–20 s in order to display Pi2 pulsations. In both figures substorm expansion phase onset/intensifications identified from ground magnetometer observations discussed in the text are indicated by *solid vertical lines*.

velocity of approximately 850 m s^{-1}. At 02:46 UT a similar feature was observed: flow initially directed towards the radar (l-o-s velocity ≤600 ms^{-1}) was followed by a region of comparable flow in the opposite direction which then propagates eastward with speed ~1 km s^{-1}. The range and elevation angle of the backscattered signals from each feature have been examined as discussed in section 3.3.1. Assuming rectilinear propagation, the altitudes from which radar returns originated have been estimated to be ~150–200 km implying that backscatter is occurring from targets in the F-region.

4.4 APVC case study: 1st July 1998

4.4.1 Ground-based magnetometer observations

Figure 4.4 presents *X* and *Y* component magnetograms from a selection of stations of the Greenland coastal, NIPR, IMAGE and SAMNET arrays during the interval 19–24 UT on 1st July 1998 (hereafter referred to as *Interval 2*). During the interval the mid-latitude IMAGE magnetometer station at NUR observed only one significant Pi2 pulsation packet, occurring at 19:54 UT. The magnetic local times of NAQ, TJO, KIR and NUR at 19:54 UT are 17:44, 19:44, 22:04 and 22:04 respectively. Mainland Scandinavia magnetometers of the IMAGE chain (KIR only shown) observed Pi2 oscillations in the *X* component with magnitude ~50 nT before beginning a steady decrease in amplitude until 20:18 UT. A subsequent intensification at a higher latitude or a poleward expansion then gives rise to an *X* component negative bay at IMAGE magnetometers located poleward of the Scandinavian mainland (only BJN shown). When filtered appropriately, *X* component magnetograms from the most poleward mainland stations observe Pi2 pulsations simultaneously with this onset/intensification. Although disturbed slightly, both *X* and *Y* components measured by IMAGE magnetometers subsequently recovered over the next 3 hours to values comparable to those observed prior to the 19:55 UT onset. Magnetometers located in the Greenland and Iceland sectors observed a weak response to the above substorm onset/intensifications although these were confined to the lower latitude stations presented in Figure 4.4.

At 20:58 UT, and later at 21:16 UT, increased activity and Pi2 pulsations (not shown) observed by Iceland sector and Jan Mayen (JAN) magnetometers indicate further substorm activity, this time centred further west than the earlier events. As this interval concludes both the *X* and *Y* magnetic field components become more quiescent.

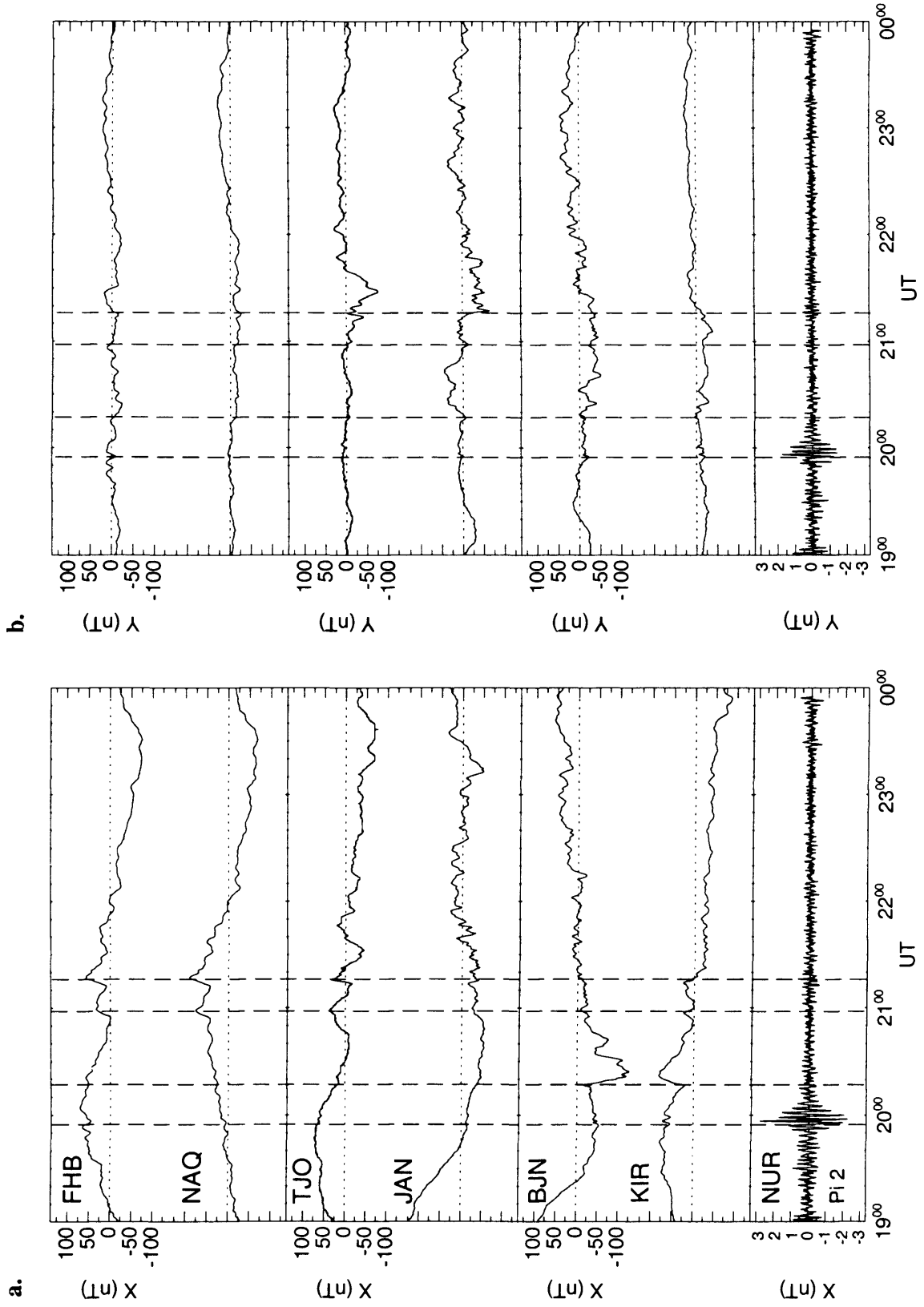

Figure 4.4. Ground magnetograms from the Greenland coastal array *(top panel)*, the Jan Mayen and NIPR Tjornes magnetometers *(second panel)*, and the IMAGE array *(third panel)* for the interval 19–00 UT on 1st July 1998. A bandpass filtered (200–20 s) trace from the NUR magnetometer of the IMAGE array is also included *(bottom panel)*. The substorm expansion phase onsets described in the text are indicated with *dashed vertical lines*; **a** *X* components; **b** *Y* components.

4.4.2 Radar measurements of ionospheric convection

During the interval 1900–2400 UT on 1st July 1998, the ionospheric l-o-s flow velocities observed by beam 15 of the CUTLASS Iceland radar were predominantly directed east-to-west (Figure 4.5a). Throughout the interval presented, the radar was operating in a high-time resolution mode returning to beam 15 every other beam and dwelling for 2 s on each beam. An area of backscatter with l-o-s flow velocity ~1000 ms^{-1} extending over magnetic longitudes 81°-86° was observed for ~25 min prior to the onset at 19:54 UT. This is interpreted as a region of enhanced electric field associated with the expanding auroral oval as it moves into the radar beam (Lewis *et al.*, 1997). For ~100 min, beginning at the time of onset (19:54 UT), the amount of backscattered signal between 81°-86° magnetic longitude was substantially reduced excepting the interval associated with the onset/intensifications observed in ground magnetometer measurements between 20:55–21:15 UT during which flows ~1000 m s^{-1} were once again observed. After 21:40 UT ionospheric backscatter was observed out to magnetic longitudes ~86° until the end of the interval. At 22:30 UT, a region of flow whose l-o-s velocity component is directed towards the radar (~1000 m s^{-1}) began to propagate from east-to-west, spanning magnetic longitudes ~88°-81° in approximately 7 min, equivalent to a propagation velocity ~800 m s^{-1} (this propagating region is highlighted by a dashed line in Figure 4.5b). During the following hour, similar regions of intense flow (~1000 m s^{-1}) directed towards the radar and propagating in a roughly east-to-west direction at ~600 m s^{-1} are observed at 22:47, 22:56, 23:12 and 23:26 UT.

4.5 Discussion of case studies

The observations during the intervals presented in sections 4.3 and 4.4 occur in both the pre- and post-midnight sectors and in both cases the observed structures propagate azimuthally away from local midnight. Furthermore, in general westward propagating structures in the pre-midnight sector contain westward-directed flow and eastward propagating structures in the post-midnight sector contain eastward-directed flow. During interval 1 the features were first observed at similar MLTs as the onset region before propagating eastward. The longitudinal separation between the observed APVC and the onset region during interval 2 was larger and there was a greater delay between the first indicators of substorm activity and the radar observations of vortical flows. As a consequence, the causal relationship between individual substorm onsets and observed APVCs during interval 2 is difficult to determine. In order to characterise APVC structure and investigate the relationship to substorms more fully, observations drawn from approximately 1000 hours of

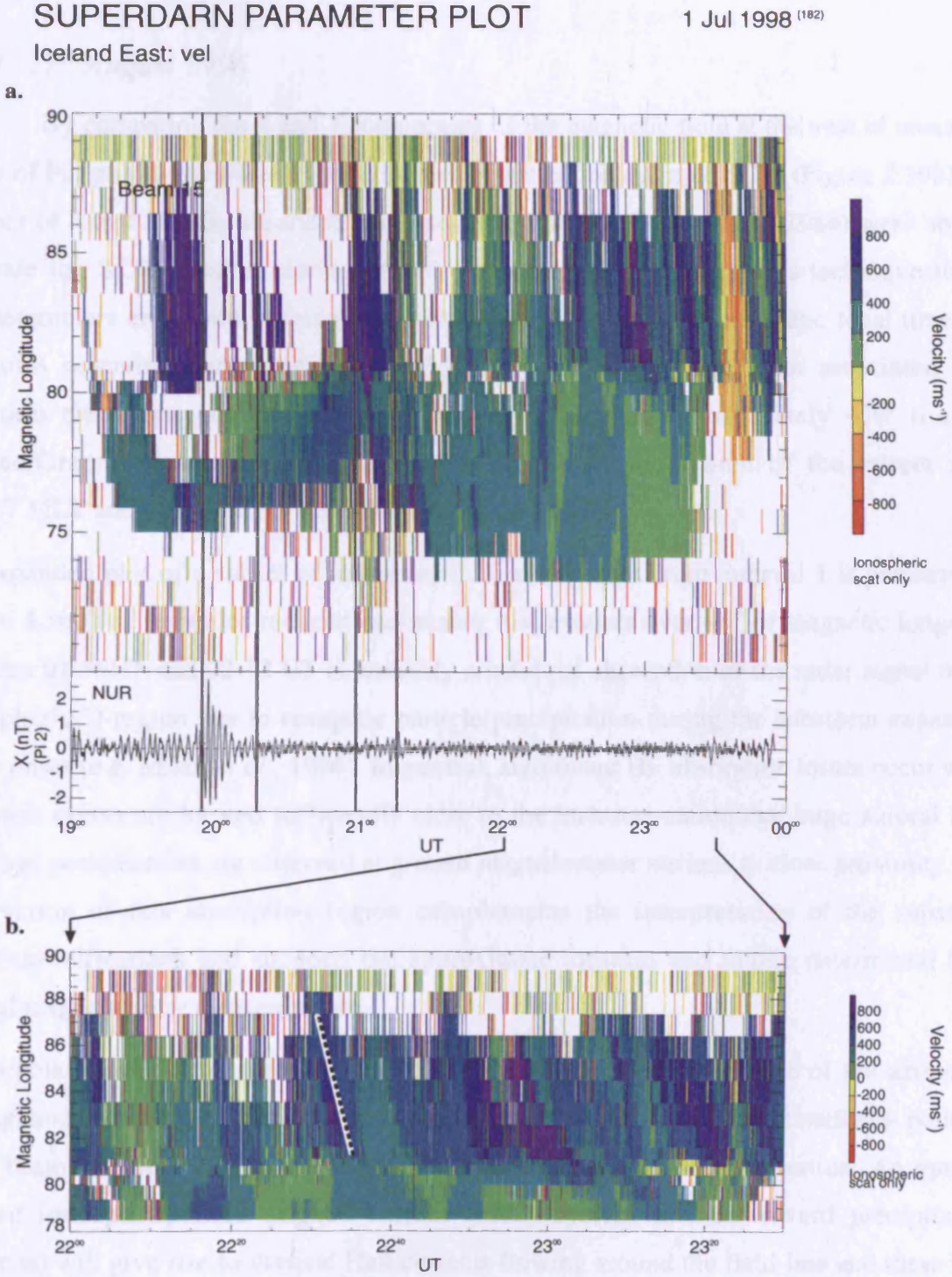

Figure 4.5. **a** Line-of-sight velocities from beam 15 of the CUTLASS Iceland radar as a function of magnetic longitude and time during the interval 19–24 UT on 1st July 1998. The *lower panel* contains magnetic field *X* component data recorded at NUR and bandpass filtered between 200–20 s in order to present Pi2 pulsations; **b** Expanded view of the interval 22:00–23:30 UT for magnetic longitudes 78-90. For clarity, the propagating vortical current feature first observed at 22:30 UT is highlighted with a *dashed line*. In both figures substorm expansion phase onset/intensifications identified from ground magnetometer observations discussed in the text are indicated by *solid vertical lines*.

high-time resolution, nightside radar measurements have been employed to perform a statistical analysis of APVC behaviour (section 4.6).

4.5.1 27th August 1996

By comparing the *X* and *Y* components of the magnetic field at the time of onset and decay of Pi2 pulsations with the perturbations expected for a simple SCW (Figure 2.10b) at a number of longitudinally separated magnetometer stations, Lester *et al.* (1984) were able to estimate the SCW location during several substorms. By applying this technique to the magnetometers employed in this study with coverage ~5 hours of magnetic local time, the substorm onset/intensifications at 01:42 UT and 01:53 UT have been associated with substorm electrojets occurring at a magnetic longitude of approximately ~70° (i.e. the Iceland/Greenland sector). This implies the magnetic local time of the onsets were ~01:37 MLT and ~01:48 MLT respectively (±00:30 MLT).

An expanded plot of a subset of ionospheric l-o-s velocities from interval 1 is presented in Figure 4.3b. The region of reduced backscatter that extends over ~6° of magnetic longitude between 01:56UT and 02:12 UT is probably a result of absorption of the radar signal in the ionospheric D-region due to energetic particle precipitation during the substorm expansion phase onset (e.g. Milan *et al.,* 1996). In general, significant HF absorption losses occur when substorm events are located sufficiently close to the instrumentation that large auroral zone electrojet perturbations are observed at ground magnetometer stations in close proximity. The observation of this absorption region complements the interpretation of the substorm onset/intensifications and supports the approximate location and timing determined from ground magnetometer measurements.

The bipolar flow first observed at 02:23 UT is a characteristic signature of the azimuthal propagation by a vortical flow structure through the f-o-v of an almost azimuthally pointing radar beam. Figure 4.6a presents a schematic diagram of such a configuration. An upward aligned ionospheric field aligned current (FAC) system (i.e. downward precipitating electrons) will give rise to vortical Hall currents flowing around the field-line and these Hall currents are manifested as variations in the ionospheric flow observed by the radar. As the flow vortex moves in the beam, the l-o-s velocity component is first directed toward the radar (colour-coded blue in Figure 4.3). Continued propagation through the beam causes the observed l-o-s velocity component to reverse direction (colour-coded red in Figure 4.3). If the propagation path of the APVC is approximately aligned with the radar beam then this flow

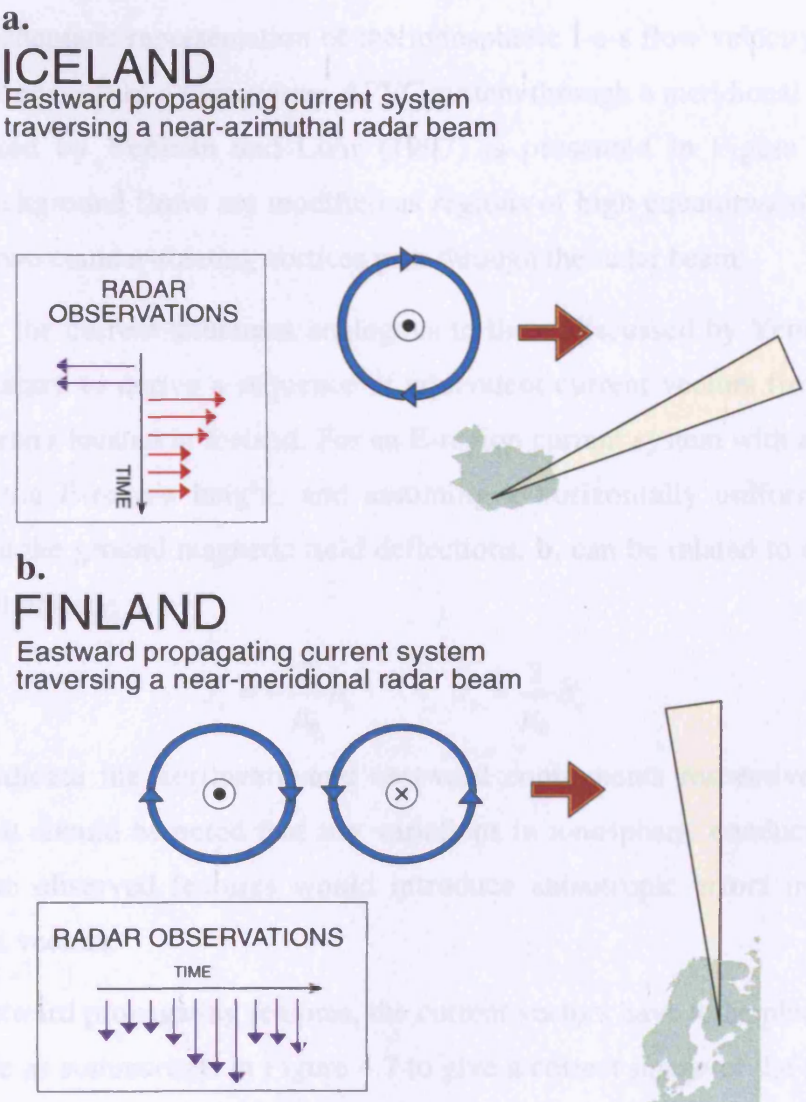

Figure 4.6. A schematic interpretation of observed l-o-s ionospheric flow velocities that result from the passage of vortical flows due to Hall currents circulating around field aligned currents through the f-o-v of an azimuthally pointing beam (**a**) and a meridionally pointing beam (**b**). In **a**, an eastward background flow is first reversed and then enhance by the motion of the vortical flow structure. In **b**, an equator ward background flow is suppressed, enhanced and suppressed again by the presented vortical flow systems.

region may be observed to move down-range from the radar over time, as is the case in the interval presented in Figure 4.3. An APVC with similar structure is observed at 02:46 UT. Both APVCs were characterised by peak ionospheric flows of approximately ±600 m s^{-1}, eastward propagation speed of ~850 m s^{-1} and were observable within the f-o-v of the radar for ~10 min. A schematic representation of the ionospheric l-o-s flow velocity observations resulting from the passage of a twin-vortex APVC system through a meridional pointing radar beam as discussed by Yeoman and Lühr (1997) is presented in Figure 4.6b. In this configuration, background flows are modified as regions of high equatorward flow velocity located between two counter-rotating vortices pass through the radar beam.

In order to study the current structures analogous to those discussed by Yeoman and Lühr (1997) it is necessary to derive a sequence of equivalent current vectors from each of the NIPR magnetometers located in Iceland. For an E-region current system with a spatial extent of greater than the E-region height, and assuming a horizontally uniform ionospheric conductivity, then the ground magnetic field deflections, **b**, can be related to an ionospheric equivalent current density, **J**, by

$$J_x = -\frac{2}{\mu_0} b_y \qquad J_y = \frac{2}{\mu_0} b_x \tag{4.1}$$

where x and y indicate the northward and eastward components respectively (Lühr and Schlegel, 1994). It should be noted that any variations in ionospheric conductivity over the scale sizes of the observed features would introduce anisotropic errors in the deduced equivalent current vectors.

In the case of eastward propagating features, the current vectors have to be plotted against an inverted timescale as summarised in Figure 4.7 to give a correct image of the spatial current distribution (e.g. Lühr and Schlegel, 1994). The longitudinal distribution of the various observations necessitates the inclusion of time offsets in equivalent currents derived from each magnetometer station in order that the azimuthal motion of the APVCs is correctly taken into account. For example, a feature propagating eastward with azimuthal velocity ~850 m s^{-1} will be observed at HUS ~460 s before entering beam 15 of the Iceland radar, and at TJO ~230 s before arriving in beam 15.

The 2-dimensional equivalent current vectors derived from HUS and TJO magnetometer data are presented as a function of magnetic latitude in Figure 4.8. The time offsets discussed above have been applied to the derived current vector time-series in order to take into account the longitudinal separation of the two stations and allow direct comparisons between the

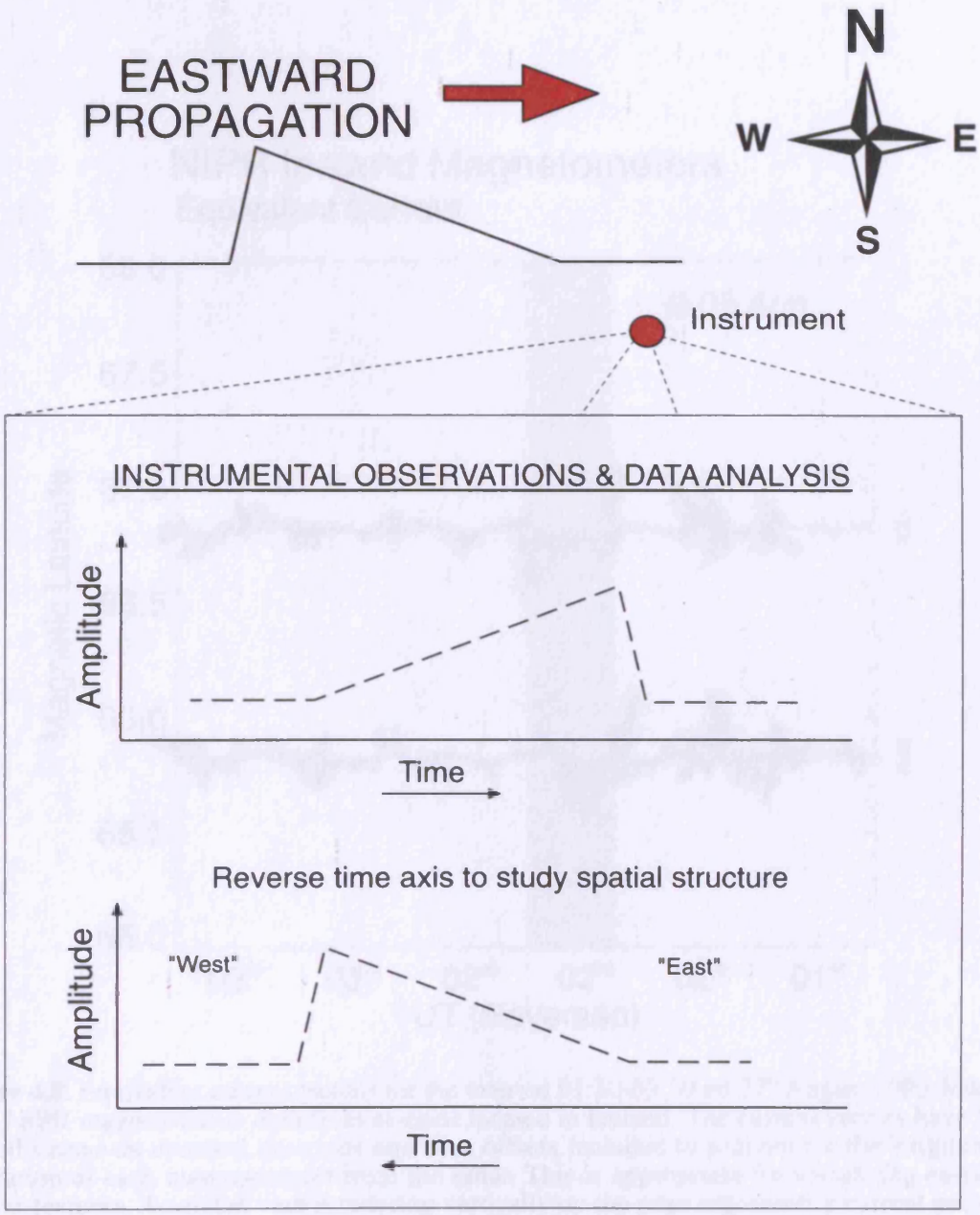

Figure 4.7. The technique employed to extract information regarding the spatial distribution of an arbitrary parameter within an eastward moving structure from a time-series of observations. Assuming that the spatial distribution within the feature under investigation remains constant during the period of observation, the instrument will record the profile indicated. By reversing the time axis the spatial variation of an eastward moving structure is revealed.

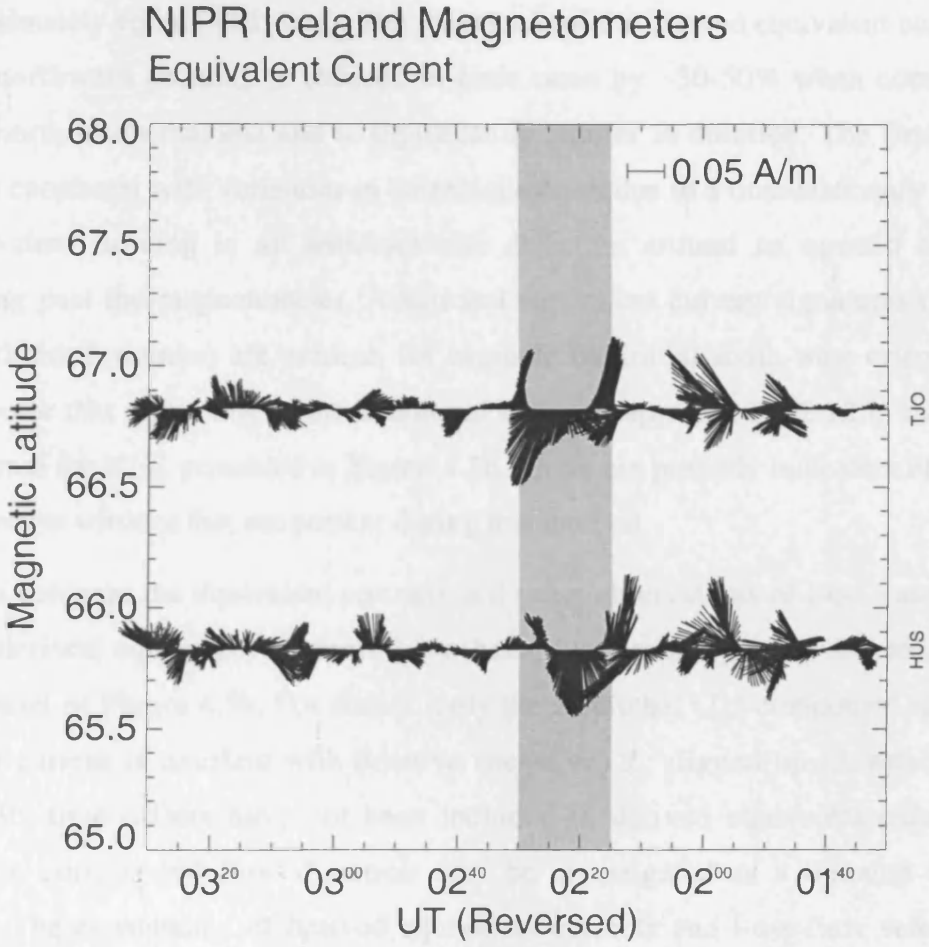

Figure 4.8. Equivalent current pattern for the interval 01:30-03:30 on 27th August 1996 deduced from NIPR magnetometer data from stations located in Iceland. The current vectors have been plotted versus an inverted time axis and time offsets included to account for the longitudinal separation of each magnetometer from the radar. This is appropriate for visualising eastward current features. A current vector pointing vertically up the page represents a current pointing towards the pole (i.e. +ve J_X, *aligned up the page*, +ve J_y *aligned to the right*). The interval associated with the bipolar l-o-s Doppler velocity signature described in the text is *shaded*.

observed APVC current signatures. Although highly dynamic throughout the interval, during the period 02:15-02:30 UT there is a clear intensification in the equivalent current strength. At both stations the equivalent current orients poleward at ~02:15 UT and rotates through the southward direction in a clockwise sense before returning briefly to a northward pointing at ~02:30 UT. The equivalent current strength throughout this rotation is strongest during the initial northward pointing and subsequent southward pointing at which time the magnitudes are approximately equal (~0.1 A/m). The magnitude of the derived equivalent currents during the final northward pointing is reduced in both cases by ~30-50% when compared to the previous north/south maxima and is significantly shorter in duration. The first north-south rotation is consistent with variations in current direction due to a time-stationary vortical Hall current system flowing in an anticlockwise direction around an upward aligned FAC propagating past the magnetometer. Additional equivalent current signatures to the classic north-south-north rotation are evident, for example the initial south-west orientation of the current vector that arises due to the additional structure apparent at 02:12 in the time-series magnetogram for HUS presented in Figure 4.2b. These are possibly indicators of further, less defined current vortices that are present during this interval.

In order to compare the equivalent currents and radar observations of l-o-s ionospheric flow velocity, derived equivalent currents have been superimposed upon the longitude-time-velocity panel of Figure 4.3b. For clarity, only the azimuthal (J_y,) component of the derived equivalent current is overlaid with positive (negative) J_y aligned up (down) the page. In Figure 4.3b, time offsets have not been included in derived equivalent currents so that variation in current and flow direction may be investigated as a function of time and longitude. The consistency of derived equivalent currents and l-o-s flow velocity data as shown in Figure 4.3b during the passage of the main feature (02:15-02:30 UT) supports the interpretation of a significant vortical Hall current system flowing around an upward FAC. Westward directed ionospheric flows (towards the radar, colour coded blue), are associated with eastward directed currents (pointing up the page) and vice versa. It is possible that the subsequent south-north rotation of the currents could be associated with a downward FAC propagating behind the upward FAC (as suggested in Figure 4.6b) but this region of downward FAC is less well defined in its magnetic signature. Also, there is no evidence in the l-o-s velocity observations of a second counter-rotating flow vortex immediately after the passage of the upward FAC. The bipolar l-o-s velocity signature observed by the radar at 02:46 UT appears not to have any significant associated equivalent current signature. Radar observations of this feature first occur at a magnetic longitude of 71° and appear to extend

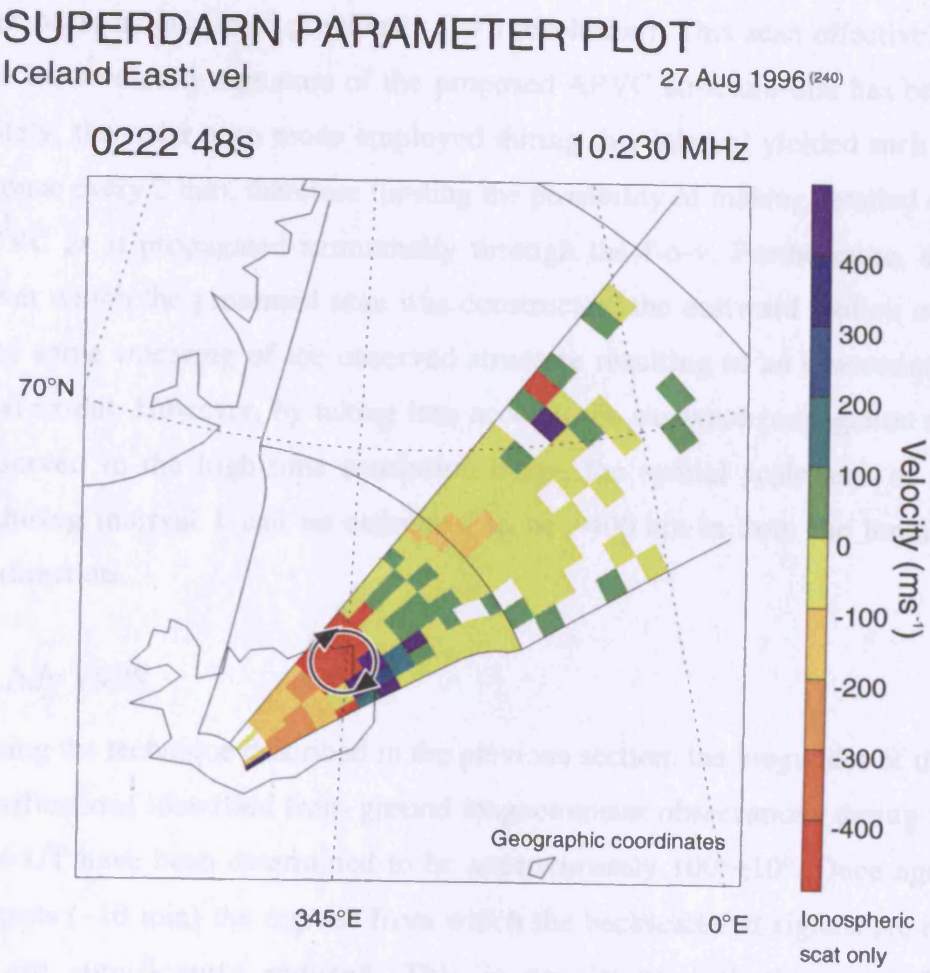

Figure 4.9. A scan of half of the f-o-v of the CUTLASS Iceland radar obtained at 02:22:48 UT on 27th August 1996. The expected vortical flows due to Hall currents flowing around an upward FAC are indicated. Such a flow at the location shown is consistent with the l-o-s Doppler velocities measured by the radar.

slightly further east that the previous APVC. It is therefore conceivable that this particular APVC system occurred far enough eastwards within the f-o-v of the radar that its influence within the region of coverage of the magnetometers presented was negligible.

An indication of the 2-D structure of the APVC can be obtained from the 8-beam scan of the Þykkvibær radar. Figure 4.9 presents a spatial distribution of l-o-s Doppler velocities derived from such a scan which encompasses half of the f-o-v. The high-time resolution beam (beam 15) is located on the extreme right of the f-o-v when viewed from the radar and is sampled every other beam as discussed previously (14 s resolution). This scan effectively illustrates the bipolar l-o-s velocity signature of the proposed APVC structure that has been overlaid. Unfortunately, the radar scan mode employed during this interval yielded such a half f-o-v scan only once every 2 min, therefore limiting the possibility of making detailed observations of the APVC as it propagated azimuthally through the f-o-v. Furthermore, during the 2 minutes over which the presented scan was constructed, the eastward motion of the APVC will lead to some smearing of the observed structure resulting in an overestimation of the longitudinal extent. However, by taking into account the eastward propagation speed of the APVC observed in the high-time resolution beam, the spatial scale size of the APVCs observed during interval 1 can be estimated to be ~400 km in both the longitudinal and latitudinal direction.

4.5.2 1st July 1998

Using the technique described in the previous section, the longitudes of the substorm onset/intensifications identified from ground magnetometer observations during the interval 19:54-21:16 UT have been determined to be approximately 100°±10°. Once again, shortly after the onsets (~10 min) the regions from which the backscattered signals are received by the radar are significantly reduced. This is consistent with the expansion of the onset/intensification region and the associated energetic particle precipitation into the f-o-v of the radar resulting in the absorption of the radar signal within the ionospheric D-region (Milan *et al.*, 1996).

At 22:30 UT (approximately 75 min after the final onset/intensification) an APVC was observed to propagate over longitudes 88°-81° over a period of ~7 min, equivalent to a westward propagation speed of ~800 m s^{-1}. Within this region of flow a peak l-o-s ionospheric flow velocity of ~1200 m s^{-1} directed towards the radar was observed. For clarity, the motion of this APVC has been indicated in Figure 4.5b by a dashed line. During the interval

Universal Time	Longitudinal extent (±1°)	Phase speed along beam 15 (±50 m s^{-1})	Peak l-o-s ionospheric flow velocity (±100 m s^{-1})
22:30	7°	-830	1200
22:47	5°	-820	1200
22:56	5°	-620	1200
23:12	6°	-420	900
23:26	6°	-1060	900

Table 4.1. Longitudinal extent, azimuthal propagation speed and peak ionospheric l-o-s velocities for APVC events observed by the CUTLASS Iceland radar during the interval 22:00-23:30 UT on 1st July 1998 (as shown in Figure 4.5).

presented in Figure 4.5b four subsequent APVC systems are observed to propagate from east to west and these are detailed in Table 4.1. The spatial scales of the APVC systems observed during this interval have been determined by studying the reduced-time resolution scans over all beams in use (in this case 16). All the APVCs were of comparable dimensions being of the order 400 km in the latitudinal direction and 500 km in the longitudinal direction and the lifetimes of these events within the f-o-v of the radar varies between 6 and 10 min. Clearly, both the spatial scales and lifetimes of the APVCs in interval 2 are consistent with those observed during interval 1. However, in contrast to the vortices observed during interval 1, there are no clear bipolar signatures associated with each APVC system as it propagates through the radar beam. During the interval presented in Figure 4.5b there are significant background flows ≥ 400 m s^{-1} in the westward direction in the region through which the APVCs are observed to pass. Assuming a background flow of 400 m s^{-1} aligned parallel to contours of constant geomagnetic latitude, the vortical features in the data may be highlighted by subtracting the component of this velocity in the radar look direction for each beam and range. Using this technique (data not shown) it is possible to identify regions of suppressed westward flows located poleward of the enhanced westward flows presented in Figure 4.5. It has therefore been concluded that although a bipolar signature is not observed, the suppression and enhancement of the background flow is consistent with a vortical flow imposed upon a strong background. Furthermore, the location of the suppressed westward flow poleward of the enhanced westward flow is consistent with the clockwise vortical flow pattern associated with an upward FAC.

During this interval no significant vortical currents were revealed by ionospheric equivalent currents derived from ground magnetometer records. Radar observations place the observed features at magnetic latitudes ~68° and propagating westward from magnetic longitudes ~88°-81°, a region that is poorly covered by ground magnetometer stations (see Figure 4.1). It is concluded that by the time they were expected to have arrived at the NIPR Iceland magnetometers the APVCs had dwindled to such extent that no significant perturbations due to the derived ionospheric equivalent current were observed.

The case-studies discussed in this section present observations of vortical current structures propagating both eastward and westward through the high-latitude ionosphere, all of which occurred during periods of substorm activity. The next section presents a statistical study of many such events in order to determine the occurrence frequency, location and flow characteristics of APVCs and their relationship to substorm phase.

4.6 Statistical analysis of APVC observations

Between the commissioning of the Finland radar (February 1995) and August 1998, CUTLASS has been operational for ~29,000 hours and of these the radars have been operating in high-time resolution modes in the nightside for ~1000 hours. However, of this dataset only ~600 hours contains useful backscatter data. By examining these intervals of high-time resolution data for indications of high speed (>400 m s^{-1}) ionospheric flow regions that propagate rapidly (>500 m s^{-1}) in a predominantly azimuthal direction through the f-o-v of either of the CUTLASS radars, 25 examples of azimuthally propagating vortical currents have been identified during this period. The timing of these events relative to substorm expansion phase onset was estimated by comparison with observations of mid-latitude Pi2 pulsations drawn from the ground magnetometer arrays listed in Appendix B. From this it has been estimated that that the average occurrence rate of APVC events is ~1 per day compared to an average substorm occurrence rate of ~4 per day reported by Borovsky *et al.* (1993), drawing on observations of over 1000 substorms. In addition, the difficulty in obtaining useful backscatter observations using HF instruments during substorms due to absorption as discussed by Milan *et al.*, (1996) implies that the APVC occurrence rate is likely to be underestimated. When all the events are studied only ~20% of the APVCs observed were isolated occurrences. During an interval of substorm activity it is much more common to observe a sequence of several APVCs. Of those events that occurred during a period in which more than one APVC was observed, ~50% occurred within 30 min of the previous/subsequent APVC. By comparing the radar observation time of each event with the time of substorm onset/intensification determined from ground magnetometer measurements, a histogram of occurrence relative to onset/intensification has been constructed (Figure 4.10). Approximately 50% of APVCs observed occurred within the first hour after expansion phase onset and over 90% occurred within 2 hours. In only one case was an APVC observed in a quiet period preceding a substorm (the APVC leading the substorm by 16 min). The mean magnitudes of several parameters associated with the APVC structures observed are presented in Table 4.2. In both interval 1 and interval 2 several APVCs were observed during the period of substorm activity. The ionospheric signatures of substorms are most commonly observed around local magnetic midnight however during interval 1 the signatures are located further dawnward at ~01:37 MLT and ~01:48 MLT. The mean MLT of substorms occurring during this study is ~24 MLT with individual substorms observed over the range 22-02 MLT. Therefore, the particular MLT of substorm onsets during any given interval are not interpreted as being significant to the occurrence of APVCs. All of the flows interpreted as APVCs have been

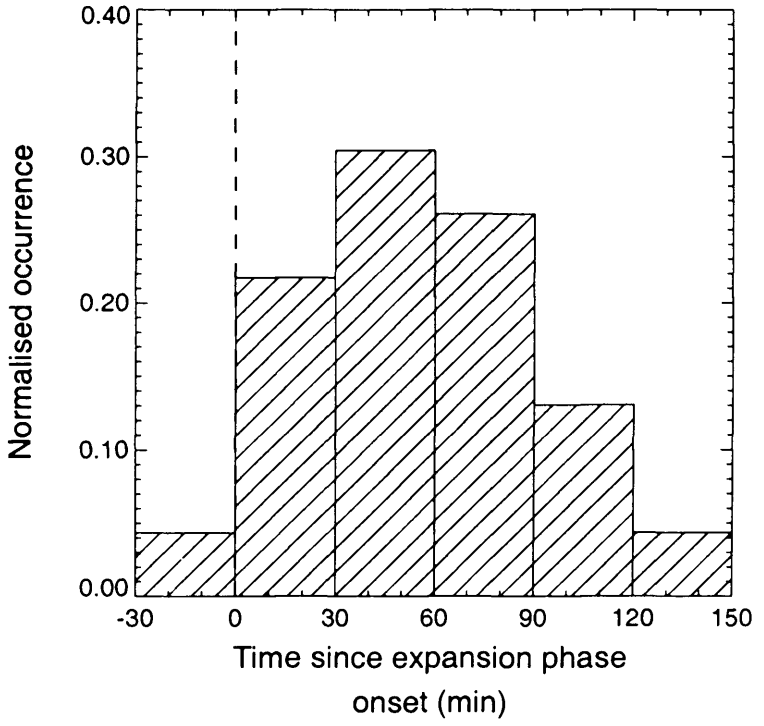

Figure 4.10. A histogram presenting the normalised occurrence rate of azimuthally propagating vortical current systems observed by CUTLASS relative to magnetospheric substorm onset/intensification time. *The dashed vertical* line represents the moment of substorm onset.

Parameter	Mean magnitude
l-o-s convection velocity	900 m s^{-1} (±500 m s^{-1})
azimuthal propagation velocity	780 m s^{-1}(±700 m s^{-1})
spatial extent	300 km (lat) x 400 km (lon) (±100 km)
observed magnetic latitude	65.5°
K_P index	3

Table 4.2. Mean magnitudes of various characteristics of the 25 observed azimuthally propagating vortical current features. Where approproiate, figures in brackets indicate the variation in the magnitude of the parameter.

consistent with upward FACs and in no cases were the anticlockwise flows expected to be associated with downward FACs observed. Clearly, both upward and downward FACs are required in order to facilitate current closure through the ionosphere although the observations in this study yielded no information regarding the location of downward FACs with respect to the APVCs. However, it is possible that the highly structured electron precipitation associated with upward FACs is leading to a preferential selection of radar observations of upward FACs. Finally, the longitudinal separation between the observed location of each APVC within the field of view of the radar and the region of expansion phase onset/intensification with which it has been associated is presented in Figure 4.11 as a function of the azimuthal propagation velocity. Although there appears to be no direct relationship between longitudinal separation and propagation velocity there is an obvious trend that events that occur to the east of the onset region propagate eastward and vice-versa.

4.7 Discussion

The CUTLASS observations presented indicate that APVC systems frequently propagate in an azimuthal direction away from the region of substorm onset/intensification, outside of the substorm expansion bulge as presented in Figure 4.12. However, their rapid propagation speeds and relatively short lifetimes within the f-o-v of any particular radar imply that high-time resolution observations (~few seconds) are required and these are not routinely implemented. From the small sample of observations of this phenomenon available it appears that APVCs propagate not only eastward, as first described by Yeoman and Lühr (1997), but also westward, in both cases moving away from the region of substorm onset. In this respect, the APVCs described are analogous to dayside *travelling convection vortices* (TCVs) which have been observed to propagate westward through the morning sector at speeds of several kilometres per second (e.g. Glassmeier, 1992; Lühr *et al.*, 1996). TCVs are usually described as pairs of anti-parallel field-aligned currents closing in the ionosphere and are most commonly observed in the morning hours between 08-10 MLT. The study of TCVs by Lühr *et al.* (1993) included observations of the perturbations to equivalent currents derived from ground magnetometer data that are very similar to those presented in Figures 4.3b and 4.8. The TCV twin-vortices observed in that study were inferred to have dimensions of ~1000 km and 2000 km in the latitudinal and longitudinal directions respectively, somewhat larger than the APVC structures observed in the current study.

Yeoman *et al.*, (1998) observed a series of APVCs propagating through the f-o-v of the CUTLASS Finland radar with durations ~5 min and repetition period ~8 min. The overall

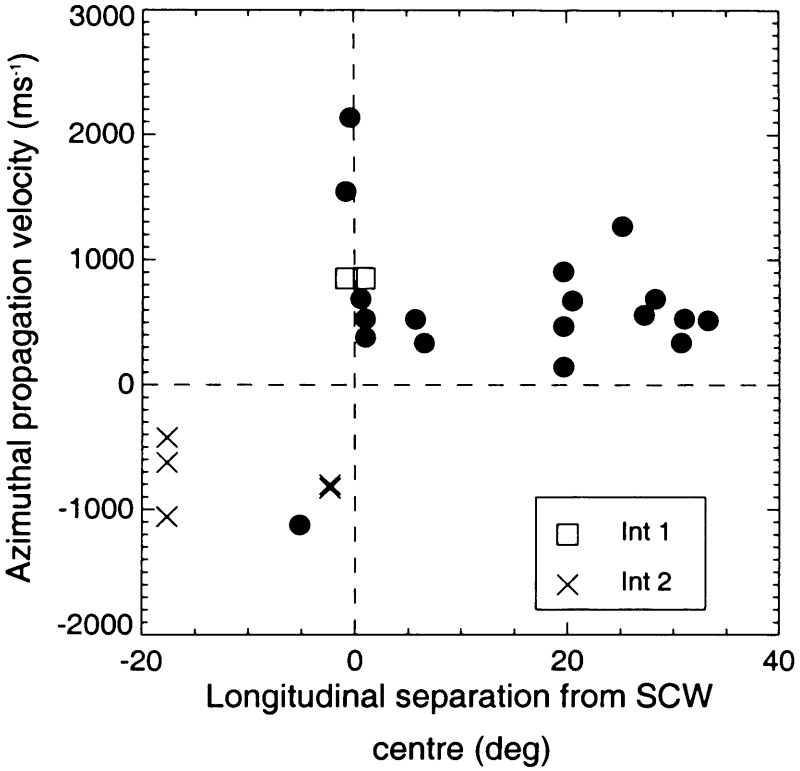

Fig 4.11. The relationship between azimuthal propagation velocity of APVC events and the longitudinal separation from the region of substorm onset/intensification. Positive velocities indicate eastward propagation. The events discussed in the text are denoted by squares (interval 1) and crosses (interval 2).

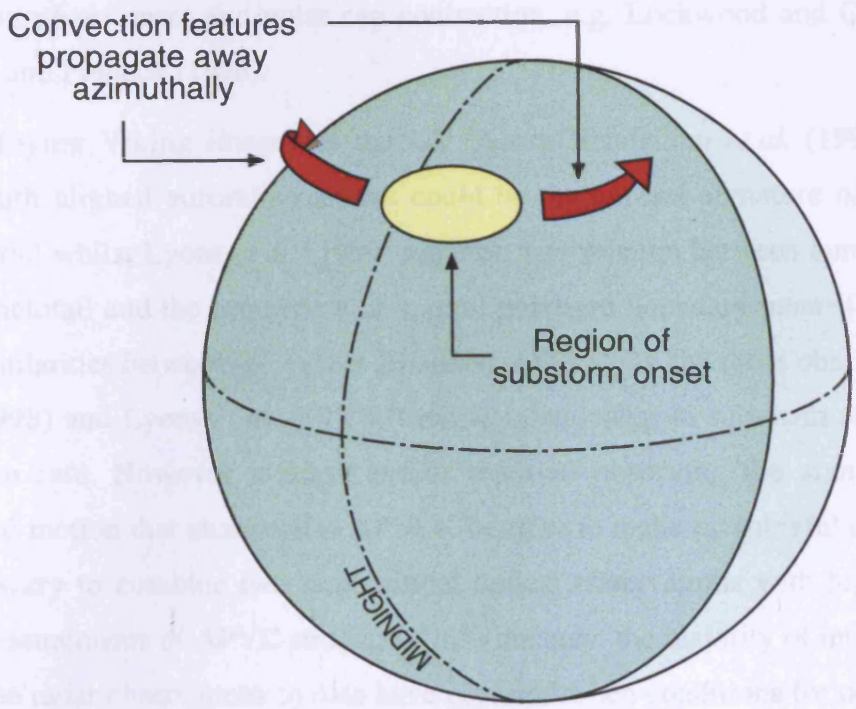

Figure 4.12. A schematic representation of the propagation of the observed APVCs away from the region of substorm onset/intensification.

morphology of the APVCs was very similar to the ionospheric twin-vortex signature that arises as a result of flux transfer events occurring at the dayside magnetopause (Lockwood *et al.*, 1990) and it was proposed that source mechanism of these events may be transient reconnection at the NENL. It was further suggested that the azimuthal flows were the inner magnetosphere response to the resulting Earthward plasma flows (BBFs), a supposition supported by *in-situ* observations of the magnetosphere made by the *Geotail* spacecraft. If the APVCs studied in this paper and by Yeoman *et al.* (1998) are signatures of transient reconnection at the NENL then observations up to 150 min after substorm onset are certainly unexpected and the single observation of an APVC prior to an onset remains unexplained. However, previous authors have observed delays ~30 min between substorm expansion phase onset and polar cap contraction, e.g. Lockwood and Cowley (1992) and Yeoman and Pinnock (1996).

By employing Viking images of the UV aurora Henderson *et al.* (1998) suggested that north-south aligned auroral structures could be the auroral signature of BBFs within the magnetotail whilst Lyons *et al.* (1999) reported a correlation between bursty flow activity in the magnetotail and the occurrence of auroral poleward boundary intensifications. There are many similarities between the events discussed in this study and those observed by Henderson *et al.* (1998) and Lyons *et al.* (1999), such as relationship to substorm phase, duration and repetition rate. However, neither author reported observing the significant systematic azimuthal motion that characterise APVCs. In order to make meaningful comparisons it will be necessary to combine two-dimensional optical observations with high-time resolution radar measurements of APVC structure. Unfortunately, the majority of intervals of high-time resolution radar observations to date have occurred when conditions for optical observations were unsuitable and the optical characterisation of APVCs remains an area for future study.

4.8 Summary

During the period February 1995 to August 1998, the CUTLASS radars periodically operated in non-standard modes that provided enhanced resolution measurements of l-o-s ionospheric Doppler velocities in specific beam directions whilst still taking sufficient measurements over the entire field of view in order to facilitate studies of ionospheric plasma flow velocities over 4 X 10^6 km^2. When operating in such a mode, short-lived (~min) regions of intense l-o-s velocities (~500 m s^{-1}) were frequently observed to propagate in an almost azimuthal direction, often with a characteristic bipolar flow variation occurring over timescales of the order of minutes. The azimuthal propagation speed of these regions varied

between ~300–2000 m s^{-1} and the regions of intense flow are often associated with strong perturbations in the magnetic field recorded at the ground. Analysis indicates that these perturbations are the electric and magnetic field signatures of ionospheric Hall current vortices of scale-sizes ~400 km, flowing around field-aligned currents flowing out of the ionosphere.

By studying ground magnetometer data during the intervals in which azimuthally propagating vortical current (APVC) systems are observed it has been possible to determine the approximate location of any substorm activity during that interval. In all the cases studied, APVCs were observed within 150 min after a substorm expansion phase onset/intensification and in one case 16 min prior to onset. Furthermore, comparisons of the propagation velocity of APVCs and the location of substorm onset/intensification have revealed that although azimuthal propagation velocity does not appear to be directly related to the distance from the substorm onset, the direction of propagation is generally away from the ionospheric region of onset.

The conclusions drawn from the case study of a single APVC event by Yeoman and Lühr (1997) and the subsequent analysis of magnetotail structure during the same event (Yeoman *et al.*, 1998) have been augmented by the inclusion of observations spanning more than three years. Yeoman *et al.* (1998) and Nakamura *et al.* (1999) have reported high-speed Earthward flows or BBFs in the magnetotail undergoing deceleration and azimuthal diversion in the near-Earth region. However, in order to more fully characterise any relationship with these flows and APVCs and allow comparisons to be made with other phenomena associated with BBFs such as north-south aligned auroral structures and poleward boundary intensifications it will be necessary to undertake a period of co-ordinated observations using not only high-time resolution ionospheric radars but optical instruments with a two-dimensional imaging capability and further *in-situ* spacecraft observations in the magnetosphere.

CHAPTER 5

Multi-instrument observations of the electric and magnetic field structure of omega bands

5.1 Introduction

Omega bands are a distinct class of auroral form that generally occur in the morning sector during the recovery phase of magnetospheric substorm (Akasofu, 1974; Saito, 1978; Rostoker and Barichello, 1980). They are characterised by bright regions extending from the poleward boundary of the aurora separated by a dark region that loosely resembles an inverted Greek letter Ω. In many cases the bright protruding regions, originally described as "torches" by Akasofu and Kimball (1964), also resemble the letter Ω and the term "omega band" is often used to describe auroral features with either characteristic. Two examples that clearly demonstrate the broad range of auroral structures that are classified as omega bands are presented in Figure 5.1. Whereas the omega band in Figure 5.1a appears to have been created by the distortion of a narrow auroral arc, those presented in Figure 5.1b adhere more to the classification offered above, namely alternative bright and dark protrusions at the poleward boundary of the auroral oval. Differences in the extent of the bright emissions south of the poleward auroral boundary should also be noted. For instance, although the area bounded by the auroral loop situated in the top-left corner of Figure 5.1a contains regions of bright emission, a significant dark patch remains. This is in contrast to the almost uniform emission equatorward of the omega bands presented in Figure 5.1b.

Omega bands have been observed to propagate in the eastward direction at velocities ~1 km s^{-1} (Lühr and Schlegel, 1994) and have also been observed in both hemispheres simultaneously (Mravlag *et al.*, 1991). As they travel eastward, the spatial structure of omega bands remains relatively unchanged and observations of omega bands are usually accompanied by azimuthal component magnetic disturbances. Studies by various authors (Saito, 1978; Kawasaki and Rostoker, 1979; Opgenoorth *et al.*, 1983; Buchert *et al.*, 1988) have concluded that the observation of a Ps6 pulsation (period ~4-40 min) implies the existence of an auroral omega band. In addition, previous authors have linked Ps6 pulsations to the propagation of vortical Hall currents associated with field-aligned currents (e.g. Lühr and Schlegel, 1994), although the mechanism by which these FACs arise is still uncertain.

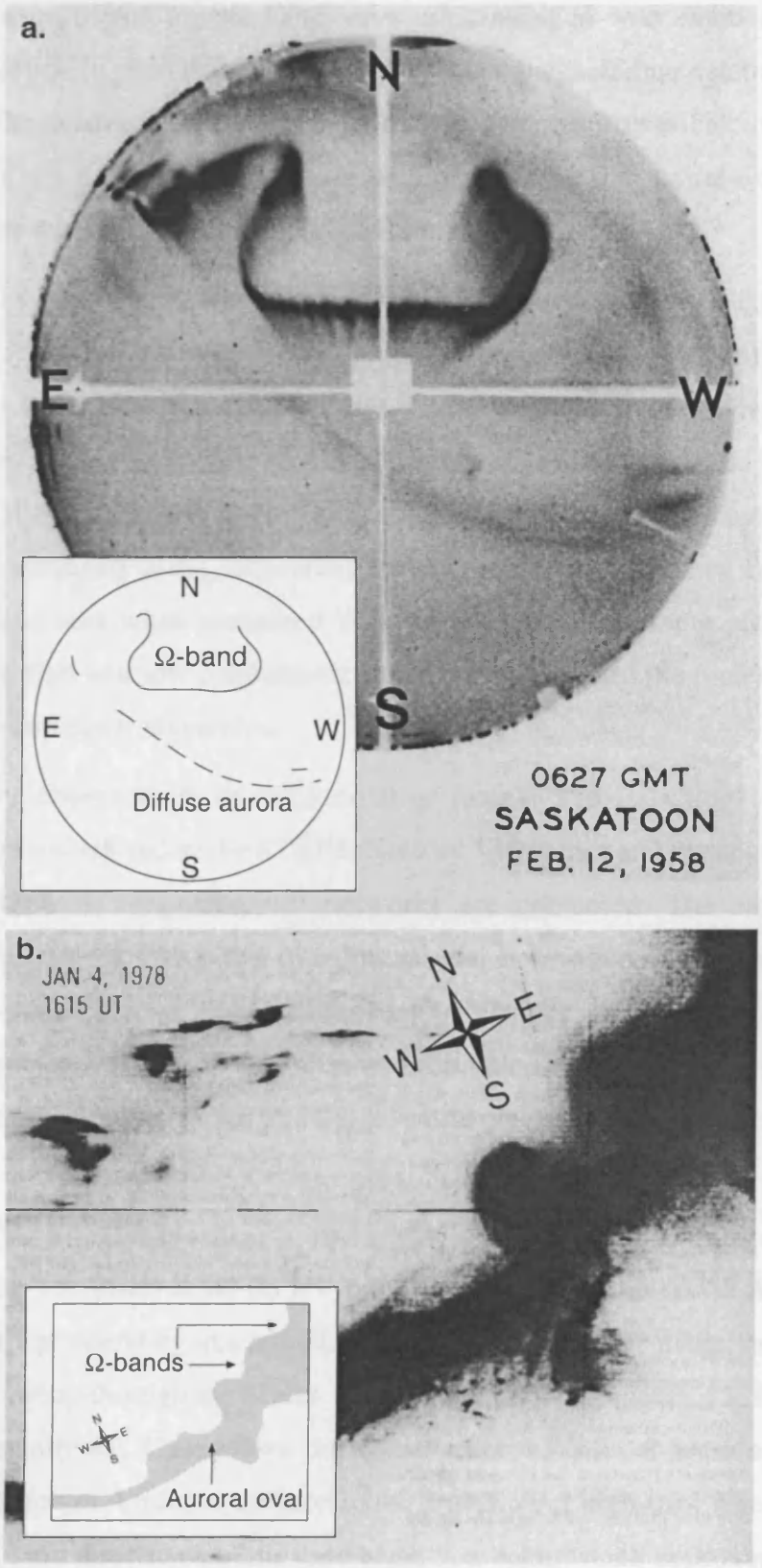

Figure 5.1. a An all-sky-camera (ASC) image of an auroral omega band above Saskatoon, Canada (from Akasofu and Kimball, 1964). In this negative image the dark areas represent the regions of brightest visible emissions. North is toward the top of the image and east toward the left. The location of the omega band is highlighted in the inset; **b** A broad-band visible auroral image taken by a Defense Meteorological Satellite Program (DMSP) spacecraft from low Earth orbit (from Lyons and Walterscheid, 1985). In this negative image, north is approximately directed toward the top of the image. Omega band locations are indicated in the inset.

The stable nature of the omega band structure combined with rapid propagation in the azimuthal direction implies that extended networks of magnetometer stations are particularly suitable for the study of this phenomenon. Equivalent currents calculated from ground magnetometer stations reveal much information regarding the spatial extent of the auroral features and the current systems contained within them.

Furthermore, by combining observations of ionospheric flow made by HF and VHF coherent-scatter radars (effectively a measure of ionospheric electric field strength) and magnetic field measurements from ground magnetometers within the radar field-of-view, it is possible to make estimates of the ionospheric Hall conductance at several key points inside the region of interest. Whilst this technique does not readily yield absolute measurements of conductance such as those obtained using incoherent scatter radars, the estimates can be made over a greatly extended area when compared with the incoherent scatter approach. The resulting distribution of high and low conductance contributes further to the understanding of omega band structure and electrodynamics.

In this chapter observations of an interval of intense Ps6 pulsations undertaken by the CUTLASS Finland HF radar, the STARE Norway VHF radar and elements of the Greenland coastal and IMAGE magnetometer networks are presented. The simultaneous multi-instrument observations facilitate a two-dimensional description of the omega bands in terms of magnetic perturbations, FACs, ionospheric electric fields, Hall conductances and equivalent currents. Finally, various proposed formation mechanisms are considered and the relationship between omega bands and the substorm phases are discussed.

5.2 Instrumentation

During the interval 00-08 UT on 11th May 1998, the CUTLASS Finland radar (section 3.3.1) was operating in a non-standard scan mode. In this mode, rather than the usual anticlockwise sweep through the beams 15, 14, 13,..., 0 the sequence 15, 9, 14, 9, 13, 9,...,1, 9, 0, 9 was employed. This allows the construction of full 16-beam scans at a reduced temporal resolution of 4 min, in addition to the provision of high-time resolution data (~14 s) along a single look direction (in this case beam 9, a beam which approximately overlies the main meridional chain of the IMAGE magnetometer array (section 3.5.2)). The CUTLASS Iceland radar was operating in a similar mode during this interval providing one high-time resolution beam (beam 15) in addition to reduced temporal resolution scans of the entire field-of-view. Although backscattered power from approximately 8° of magnetic latitude over a

period of a least 5 hours was observed by the Finland radar, no significant backscatter was observed in the same region by the Iceland radar during this interval.

Both radars of the STARE system (section 3.3.3) were also operational during the interval of interest making measurements of E-region backscattered power and irregularity l-o-s phase velocity at 20 s resolution. Although it is in principle possible to derive E-region ionospheric flow velocities perpendicular to the magnetic field by combining velocity measurements from the overlapping region of the two fields-of-view of the STARE radars (~2.3 x 10^5 km^2), during this interval significant backscattered power was measured at one radar only (Norway).

The locations of the instruments discussed in this chapter in addition to the fields-of-view of the radars employed are summarised in Figure 5.2.

5.3 Observations of omega bands

5.3.1 Ground magnetometer response

Figure 5.3 presents the *X* and *Y* components of the local magnetic field measured at several stations of the IMAGE magnetometer array and the Jan Mayen (JAN) magnetometer of the Tromsø Auroral Observatory. These elements of the IMAGE array are located at magnetic local times (MLT) approximated by MLT≈UT+2 and Jan Mayen is located at MLT≈UT+1. Beginning at approximately 01:50 UT, a series of at least five Ps6 wave-cycles with periods of approximately 18 minutes are clear in the *Y* component magnetograms from the SOR, TRO, AND and KIL stations. Less intense pulsations are also observed at BJN. Oscillations of comparable magnitudes and periods are also apparent in the *X* component measured at all of the IMAGE stations shown. These pulsations are not observed at JAN although both *X* and *Y* components are disturbed throughout the interval. At stations where the pulsations are most pronounced (e.g. TRO) the first positive deviation in the *Y* component is significantly smaller than during later pulsations. Subsequently, the *Y* component oscillations lead the *X* component oscillations in phase (*Y* component becomes more positive as the *X* component becomes more negative and vice-versa). The maximum amplitude of the *Y* component oscillations at TRO occurs at around 02:20 UT with a peak-to-peak value ~150 nT. The delay between each pulsation being observed at SOR after being observed at AND suggest that the structures are propagating in an eastward direction over the Scandinavian sector with a longitudinal speed ~0.75 km s^{-1}. Furthermore, comparing the Ps6 pulsation train at SOR and AND at geographic longitudes of 22.22° and 16.03° respectively, it is clear that

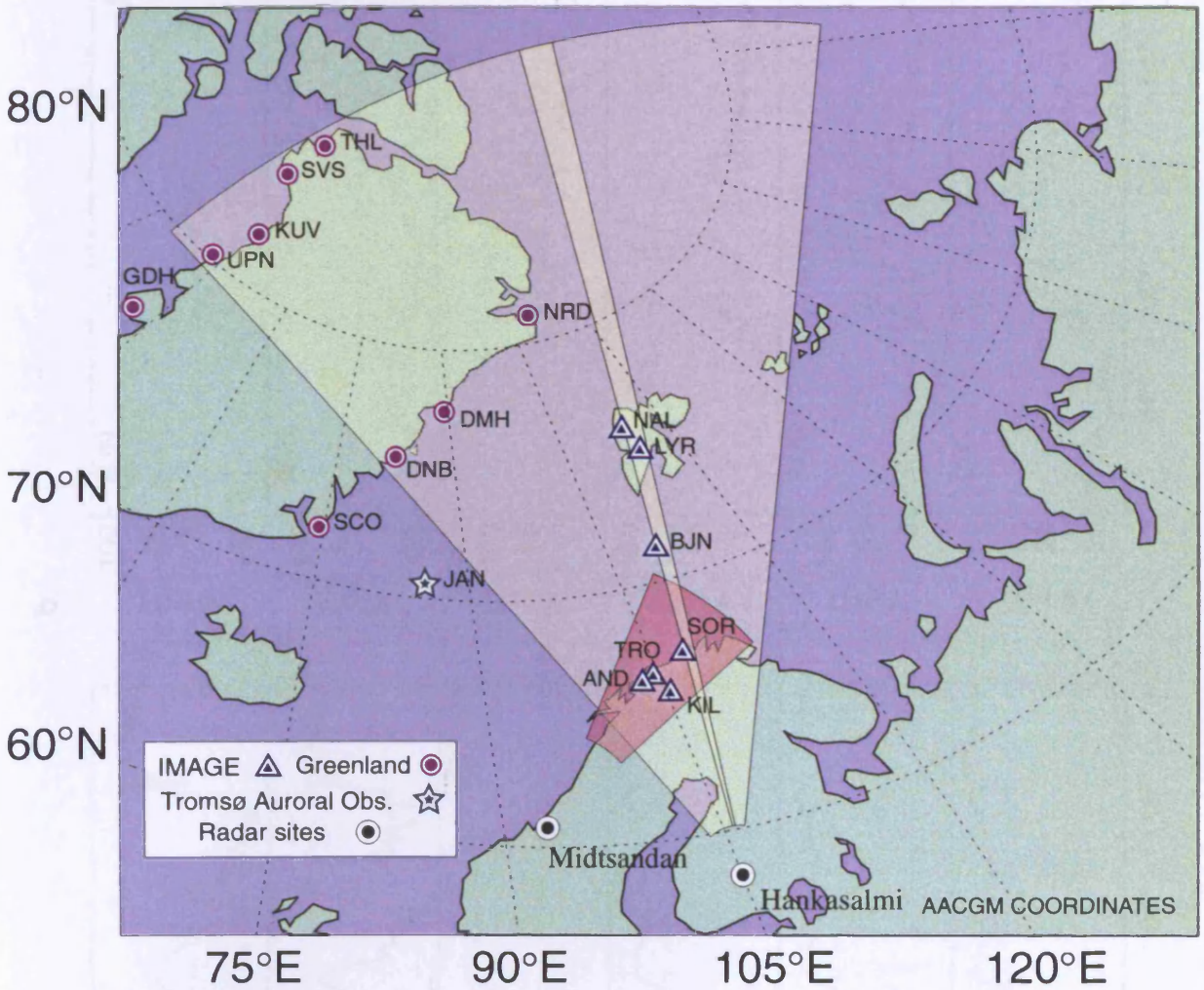

Figure 5.2. The locations of the fields-of-view of the CUTLASS Finland (*yellow shading*), and STARE Norway (*red shading*) radars and elements of the IMAGE and Greenland magnetometer networks. Beam 9 of CUTLASS Finland which is sampled at a high rate is indicated by *dark yellow shading*.

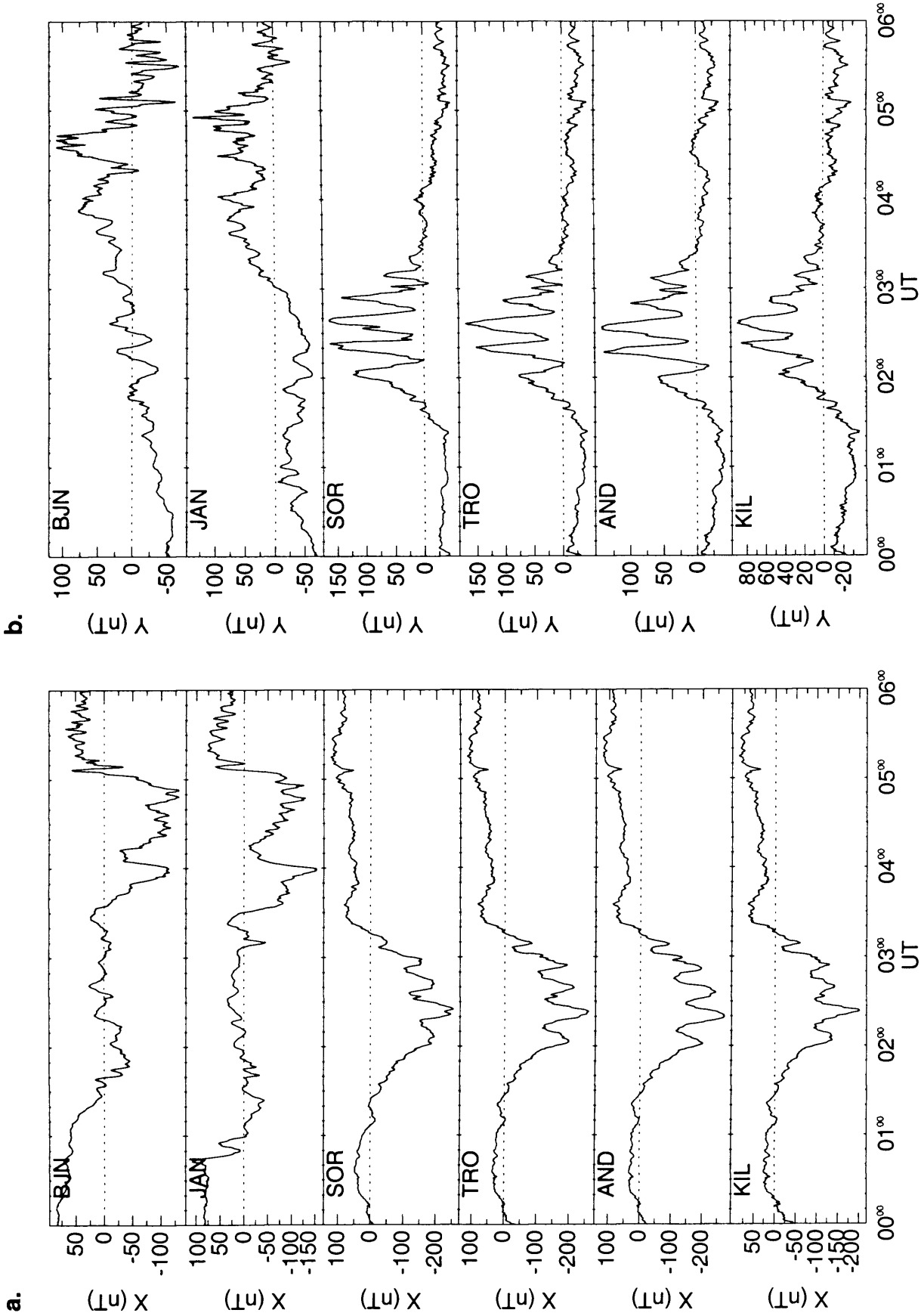

Figure 5.3. Ground magnetograms from the IMAGE array and Tromsø Auroral Observatory magnetometer located at Jan Mayen for the period 00-06 UT on 11th May 1998; **a** *X* components; **b** *Y* components. Stations are presented in descending magnetic latitude from top to bottom.

ionospheric structures that gives rise to the pulsations are coherent over the timescale of at least tens of minutes.

Observations from a selection of high-latitude magnetometers of the Greenland east-coast chain are shown in Figure 5.4. At 23:08 UT (~20:50 MLT) on 10th May 1998 slight magnetic perturbations are observed at several stations of the Greenland array accompanied by faint Pi2 pulsations, typical signatures of a *pseudobreakup* (Koskinen *et al.*, 1993). Pseudobreakups are usually defined as events that are broadly similar to a substorm onset (characterised by short lifetime, extreme localisation and weak magnetic perturbations on the ground) but do not develop into a full-blown substorm expansive phase. At 00:12 UT on 11th May (~22:00 MLT) a negative bay is observed in the *X* component at NAQ and FHB, a feature indicative of intensification of a westward current and the onset of the expansion phase of a magnetospheric substorm. By 00:43 UT (~22:30 MLT) this onset has expanded poleward to SKT. Further intensifications of negative bays observed at SKT at 01:35, 0150 and 03:05 UT (23:20, 23:35 and 00:50 MLT respectively) suggesting subsequent high-latitude substorm onset/intensifications. *X* component data have been filtered between 200 and 20 s in order to study Pi2 pulsations (SKT only shown) and provide a reference time for the substorm onsets (Rostoker *et al.*, 1980) and these are indicated in Figure 5.4 by vertical lines. In addition, the majority of IMAGE magnetometers observed a significant substorm onset/intensification at 23:30 UT on the previous day (10th May 1998, not shown).

5.3.2 Radar measurements of ionospheric convection

The line-of-sight (l-o-s) ionospheric convection velocities observed by the STARE Norway and CUTLASS Finland radars between 01:30-03:30 UT on 11th May 1998 are presented in Figure 5.5. Prior to 01:50 UT a background flow with poleward component ≤120 m s^{-1} was observed between magnetic latitudes 65°-75° by the CUTLASS radar (Figure 5.5a). At ~01:53 UT a region of intense poleward flow ~600 m s^{-1} developed at ~71° magnetic latitude and drifted ~2° poleward over the following 5 min. This is immediately followed by a region of equatorward flow of velocity ~240 m s^{-1} propagating polewards over a similar timescale and latitudinal extent. Beginning at 02:00 UT, a region of poleward flow ~600 m s^{-1} is observed over approximately 1.5° of magnetic latitude with the equatorward boundary located at ~68°. This region was observed to move in a poleward direction at a rate of approximately 3° in 10 min and was again followed by a region of weaker (~240 m s^{-1}) equatorward flow. Regions of comparable strong poleward then weak equatorward flow, always propagating away from the radar, are then observed with a repetition period ~18 min.

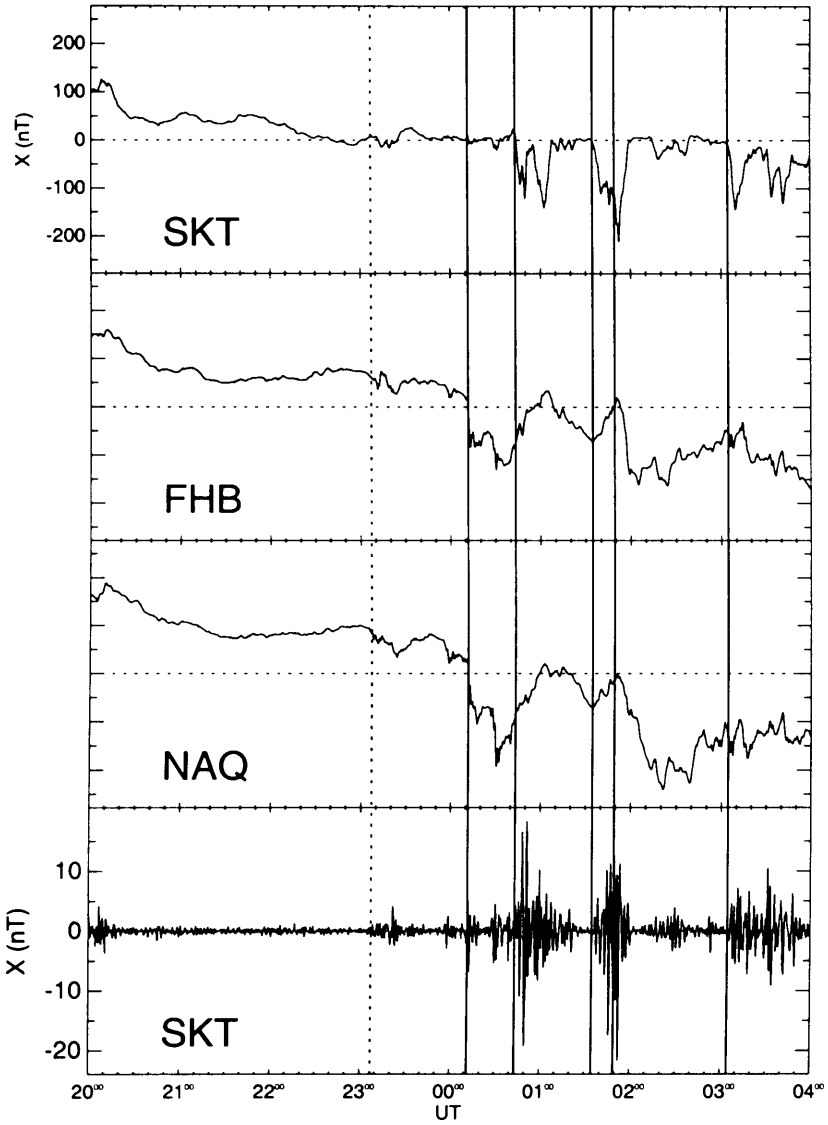

Figure 5.4. Ground magnetograms from the Greenland array. *X* component magnetograms from a subset of west coast stations for the interval 20:00 UT 10th May – 04:00 UT 11th May 1998 are displayed. A bandpass filtered (200–20 s) trace from SKT is included in the *bottom panel*. Substorm expansion phase onset/intensifications are marked with *solid vertical lines*. The *dashed vertical line* at 23:08 UT indicates a pseudobreakup.

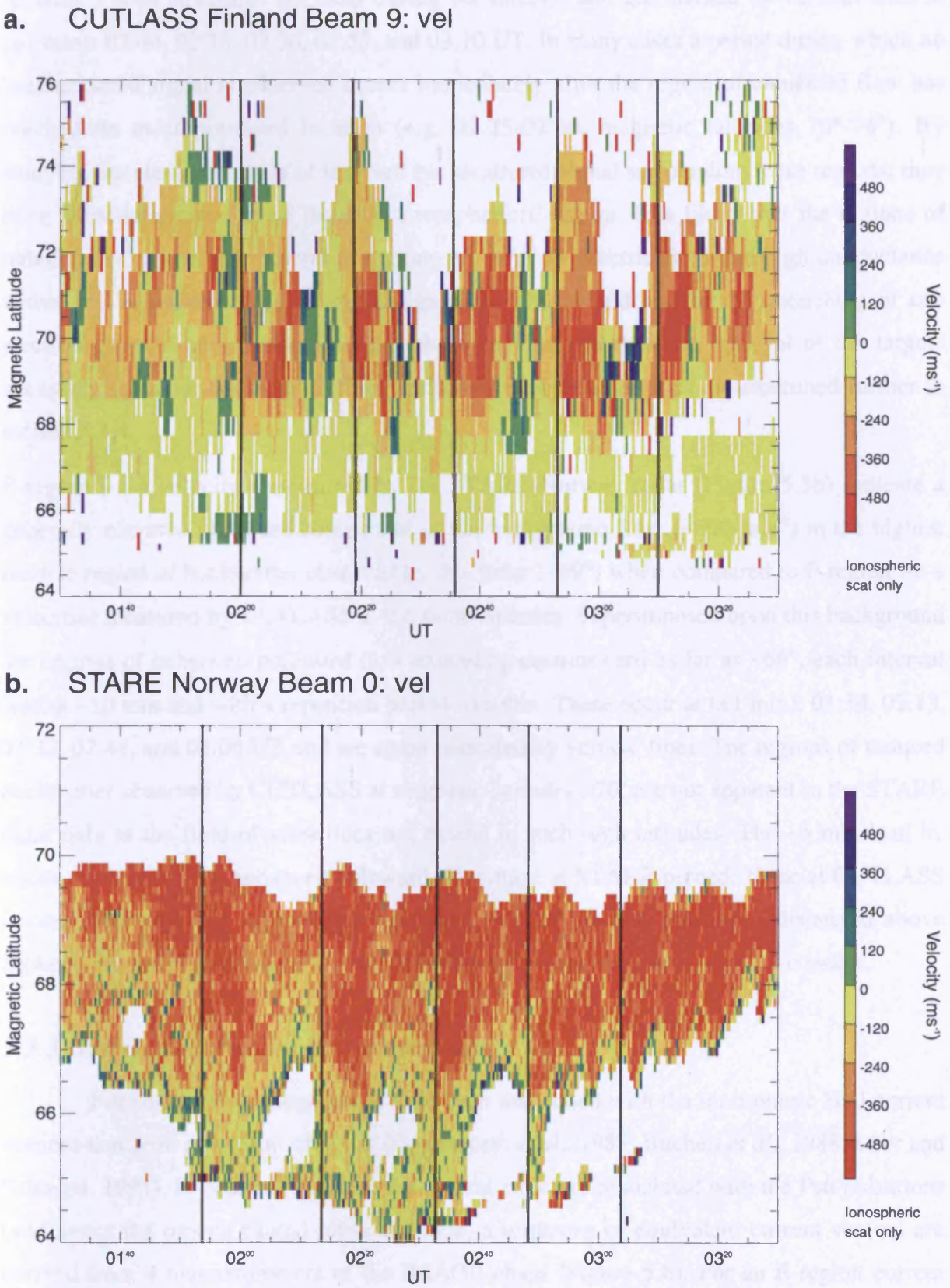

Figure 5.5. a Line-of-sight velocities from beam 9 of the CUTLASS Finland radar as a function of magnetic latitude and time, showing dynamic ionospheric features associated with the auroral omega bands. Positive Doppler velocities are towards the radar (equatorward) and negative Doppler velocities are away from the radar (poleward). The timing of omega band observations are highlighted with *vertical lines*; **b** STARE Norway line-of-sight velocities measured by beam 0 as a function of magnetic latitude and time.

At least 5 such structures are clear during the interval and are marked by vertical lines at (±1 min): 02:00, 02:18, 02:36, 02:53, and 03:10 UT. In many cases a period during which no backscattered signal is observed occurs immediately after the region of enhanced flow has reached its most poleward location (e.g. 02:25-02:40, magnetic latitudes 70°-74°). By studying the elevation angle of received backscattered signal surrounding these regions, they have been determined to be from the ionospheric F-region. It is likely that the regions of reduced backscatter correspond to regions of very low electric field and high conductance within the luminous tongue of the omega band. This would lead to the quenching of any electron concentration irregularities in these regions and thus the removal of the targets necessary for radar backscatter. The conductances in these regions are examined further in section 5.3.4.

E-region l-o-s velocities measured by the STARE Norway radar (Figure 5.5b) indicate a generally elevated poleward component of the background flow (~600 m s^{-1}) in the highest latitude region of backscatter observed by this radar (~69°) when compared to F-region l-o-s velocities measured by CUTLASS at the same latitudes. Superimposed upon this background are regions of enhanced poleward flow extending equatorward as far as ~66°, each interval lasting ~10 min and with a repetition period ~18 min. These occur at (±1 min): 01:54, 02:13, 02:32, 02:48, and 03:04 UT and are again indicated by vertical lines. The regions of reduced backscatter observed by CUTLASS at magnetic latitudes ≥70° are not apparent in the STARE radar data as the field-of-view does not extend to such high latitudes. The ~5 min lead by which observations of enhanced poleward flow made at STARE precede those at CUTLASS is consistent with the azimuthal propagation time of the Ps6 pulsations discussed above between ground magnetometers located beneath the presented beams of the two radars.

5.3.3 Derived equivalent current features

For some time, omega bands have been associated with the ionospheric Hall current vortices that arise as a result of FACs (Opgenoorth *et al.*, 1983; Buchert *et al.*, 1988; Lühr and Schlegel, 1994). In order to visualise the current structure associated with the Ps6 pulsations (and hence the omega bands) presented here, a sequence of equivalent current vectors are derived from 4 magnetometers of the IMAGE chain (Figure 5.6). For an E-region current system with a spatial extent of greater than the E-region height, and assuming a horizontally uniform ionospheric conductivity, then the ground magnetic field deflections, b, can be related to an ionospheric equivalent current density, J, by Eq. (4.1). Since the omega bands appear to move eastward in a time-stationary manner, according to the observed propagation

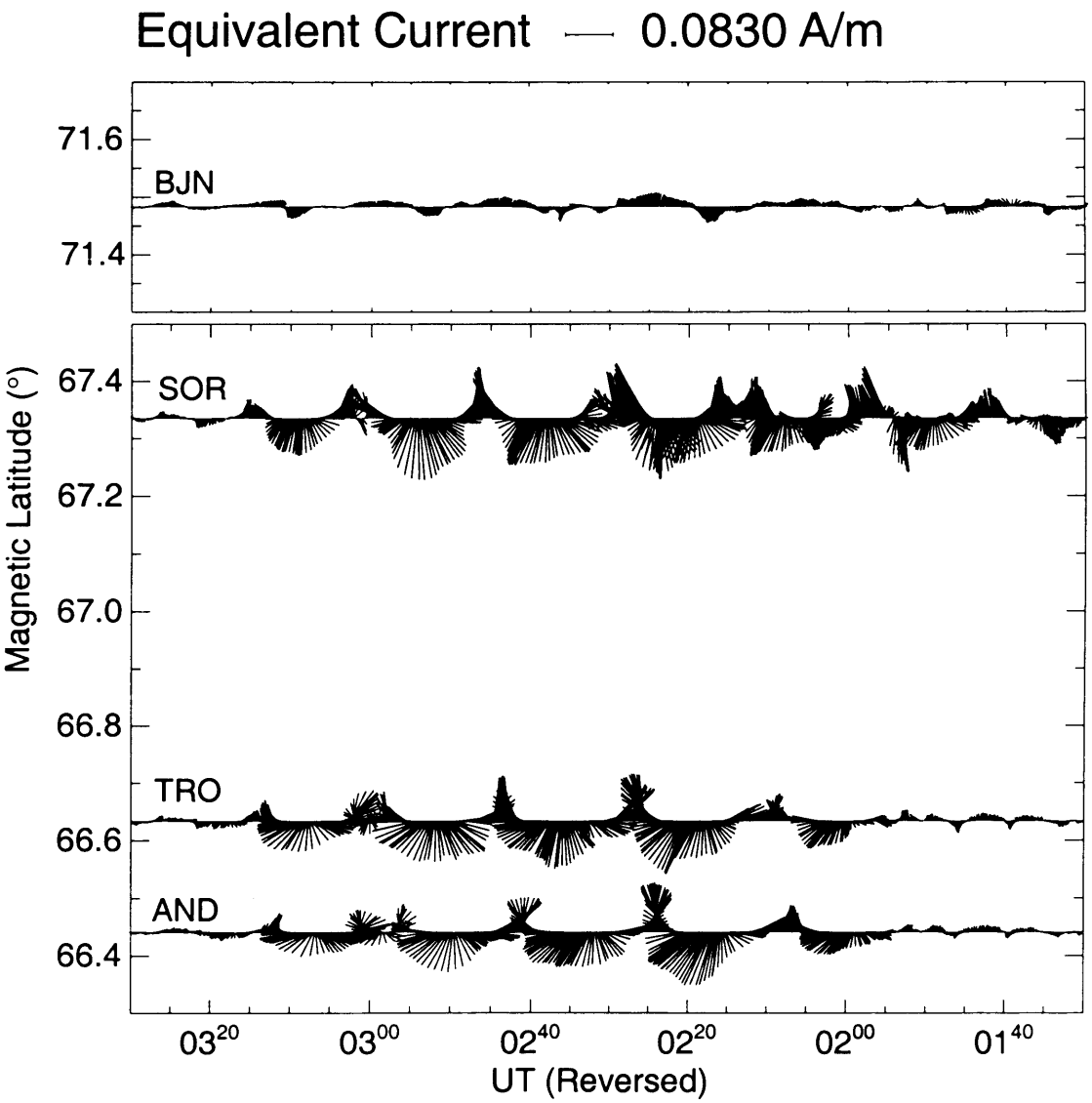

Figure 5.6. Equivalent current patterns deduced from IMAGE magnetometer data. The current vectors have been plotted against a reversed time axis. This is appropriate for visualising eastward moving features. The AND, TRO and BJN time series have been shifted by +350, +180 and -60 s respectively to account for the propagation delay between those magnetometers and SOR.

delay in the magnetometer data, the current vectors have to be plotted against an inverted timescale to give a correct image of the spatial current distribution (see Figure 4.7). So that direct comparisons can be made between the current distributions at various latitudes, time offsets appropriate for the propagation delay between each longitudinally-separated station have been incorporated (60, 180 and 350 s for BJN, TRO and AND respectively). These offsets are consistent with the time taken for each omega band to travel longitudinally between the observing magnetometer and beam 9 of the CUTLASS radar at the speed calculated in section 5.3.1. During the interval presented at least 5 pairs of vortices are observed. Each pair of vortices is associated with a region of upward and a region of downward FAC where each FAC generates a Hall current of anticlockwise and clockwise sense respectively – characteristic features of auroral omega bands. As the series of current pairs propagate eastward over the Scandinavian mainland magnetometers (Figure 5.6, lower panel), the measured equivalent current vectors rotate in a clockwise direction indicating that the current system is located poleward of SOR, TRO and AND. In the region between each upward/downward FAC pair, the equivalent current will be directed in an approximately equatorward direction. From Figure 5.6 the equivalent current direction at SOR, TRO and AND can be seen to achieve an equatorward pointing direction (vertically downward in figure) at the following times (±1 min): 02:04, 02:20, 02:38, 02:55, and 03:08 UT. The equivalent currents derived at BJN are significantly weaker and rotate in an anticlockwise direction with similar periodicity (~18 min) implying that the observed current system is located equatorward of that station, i.e. in the region between SOR and BJN. It is just this region that is contained within the fields of view of the CUTLASS and STARE radars.

5.3.4 Derived ionospheric Hall conductances

It is possible to further examine the variation of ionospheric conductance due to the passage of the omega bands observed during this interval by combining the measured ionospheric flow speed (which is related to one component of the horizontal electric field as indicated in Figure 2.4) and the derived equivalent current intensity at the ground. As the equivalent Hall currents J_H are related to the ionospheric electric field, E, and hence the plasma convection velocity, v, via the height integrated Hall conductance, Σ_H, by

$$J_H = \Sigma_H E = \Sigma_H vB \tag{5.1}$$

where B is the magnetic field strength. In the present experimental arrangement an estimate of the Hall conductance may be estimated from Lühr *et al.* (1993, 1996):

$$\Sigma_H \approx -\frac{2}{\mu_0}\frac{b_y}{v_x B}. \tag{5.2}$$

The l-o-s velocities measured by the radar are assumed to have been made along a near-meridional beam direction implying

$$v_{l-o-s} \approx v_x \tag{5.3}$$

and b_y is simply the component of the observed magnetic field in the Y direction. In order to emphasise the fluctuations in the ionospheric Hall conductances that result from omega band passage over a given location, magnetic field data have been filtered between 1200 and 300 seconds. The background magnetic field is determined by applying low pass filter (1200 s) to the original magnetic field data. This background field is then added to the filtered data to provide a time-series of magnetic field observations which although filtered, still contains information regarding the background level of the magnetic field. Finally, the absolute value of magnetic field from the quiet period prior to the Ps6 pulsations is subtracted from the resulting time series effectively removing the quiet time, internal and ring current magnetic field variations. What remains is the magnetic field due to the enhanced electrojet and omega band structures. In the interests of consistency l-o-s velocity data have been filtered similarly although there is no requirement to subtract the background from these absolute measurements. Figure 5.7 presents the parameters used to calculate Σ_H employing data from the SOR magnetometer and CUTLASS Finland (beam 9, range gate 16). Magnetic field and l-o-s velocities are processed in the manner described above (centre 2 panels). A suitable offset (75 s) has been added to the B_y time-series to account for the slight longitudinal separation of SOR and the chosen range gate in the high-time resolution beam of the radar. The calculated Hall conductance is insensitive to the uncertainties in this offset (± 20%) as this uncertainty is small compared to the lifetime of each pulsation (~20 min). Equivalent currents derived from SOR and BJN are overlaid at appropriate latitudes on the Range-Time-Velocity (RTV) plot (lower panel). Finally, the calculated Hall conductance is presented (top panel). All panels are plotted against a common reversed timescale in order to visualise the spatial structure of the omega bands. Once again, it should be noted that this technique assumes a spatially uniform ionospheric conductivity. Any spatial gradients in conductivity would introduce errors into the technique employed to determine ionospheric equivalent currents. Most notably, the resulting overestimation of ionospheric Hall currents would lead to the overestimation of the derived ionospheric Hall conductance.

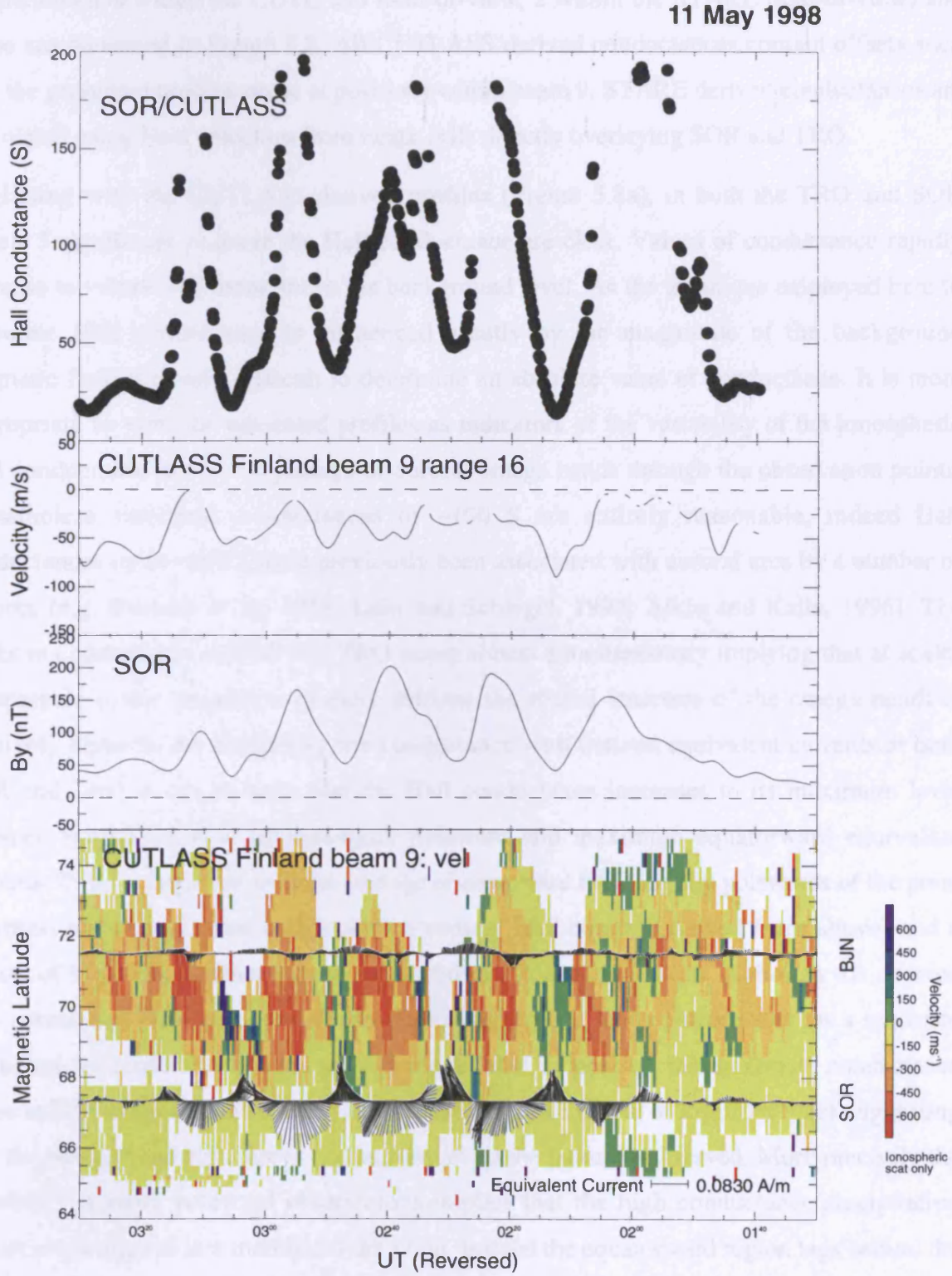

Figure 5.7. Line-of-sight velocities from beam 9 of the CUTLASS Finland radar as a function of magnetic latitude and time (*bottom panel*). Equivalent current patterns deduced from SOR and BJN are overlaid at appropriate latitudes. Filtered magnetometer *Y* component data from SOR and filtered l-o-s velocity data from CUTLASS beam 9, range 16 are also presented (*centre panels*). Estimated ionospheric Hall conductances, derived from magnetometer and l-o-s velocity data are displayed in the *top panel* (see text for description). All panels are plotted against a common reversed time axis in order to correctly visualise the spatial structure of eastward propagating features.

Conductance time-series have been calculated for 5 magnetometer/radar pairs (3 magnetometers within the CUTLASS field-of-view, 2 within the STARE field-of-view) and these are presented in Figure 5.8. All CUTLASS derived conductances contain offsets such that the presented profiles occur at positions within beam 9. STARE derived conductances are calculated using l-o-s velocities from range cells directly overlaying SOR and TRO.

Beginning with the CUTLASS derived profiles (Figure 5.8a), in both the TRO and SOR panels 5 significant peaks in the Hall conductance are clear. Values of conductance rapidly increase to values ~10 times above the background level. As the technique employed here to calculate Hall conductance is influenced greatly by the magnitude of the background magnetic field it is very difficult to determine an absolute value of conductance. It is more appropriate to view the presented profiles as indicators of the variability of the ionospheric Hall conductance due to the passage of auroral omega bands through the observation points. Nonetheless sustained conductances of ~100 S are entirely reasonable, indeed Hall conductances up to ~200 S have previously been associated with auroral arcs by a number of authors (e.g. Buchert *et al.,* 1988; Lühr and Schlegel, 1994; Aikio and Kaila, 1996). The peaks in conductance at SOR and TRO occur almost simultaneously implying that at scales comparable to the separation of these stations the spatial structure of the omega bands is relatively uniform. By comparing the conductance with derived equivalent currents at both SOR and TRO it can be seen that the Hall conductance increases to its maximum level between the observation of maximum poleward and maximum equatorward equivalent currents. This is consistent with the passage of an upward FAC slightly polewards of the point of observation creating an anticlockwise vortical Hall current (viewed from above) and a region of high conductance due to enhanced electron precipitation. Although the derived conductances at BJN are not as clearly defined as those at lower latitude stations a sequence of successive peaks and troughs are still identifiable. In general, the maximum conductance value at BJN is substantially lower and is observed prior to that at lower latitudes suggesting that the omega band structure is not uniform at all the latitudes observed. More precisely the "leading" of more poleward observations implies that the high conductance/precipitation region is not aligned in a meridional direction. Instead the equatorward region lags behind the poleward by some distance (~ 200 km in the longitudinal direction) as the whole structure propagates eastwards.

Similar conductance signatures of multiple omega band passage are apparent in STARE derived conductances (Figure 5.8b). All 5 omega bands are clearly contained within the STARE/SOR observations. Within the range gate overlaying TRO, no l-o-s velocity

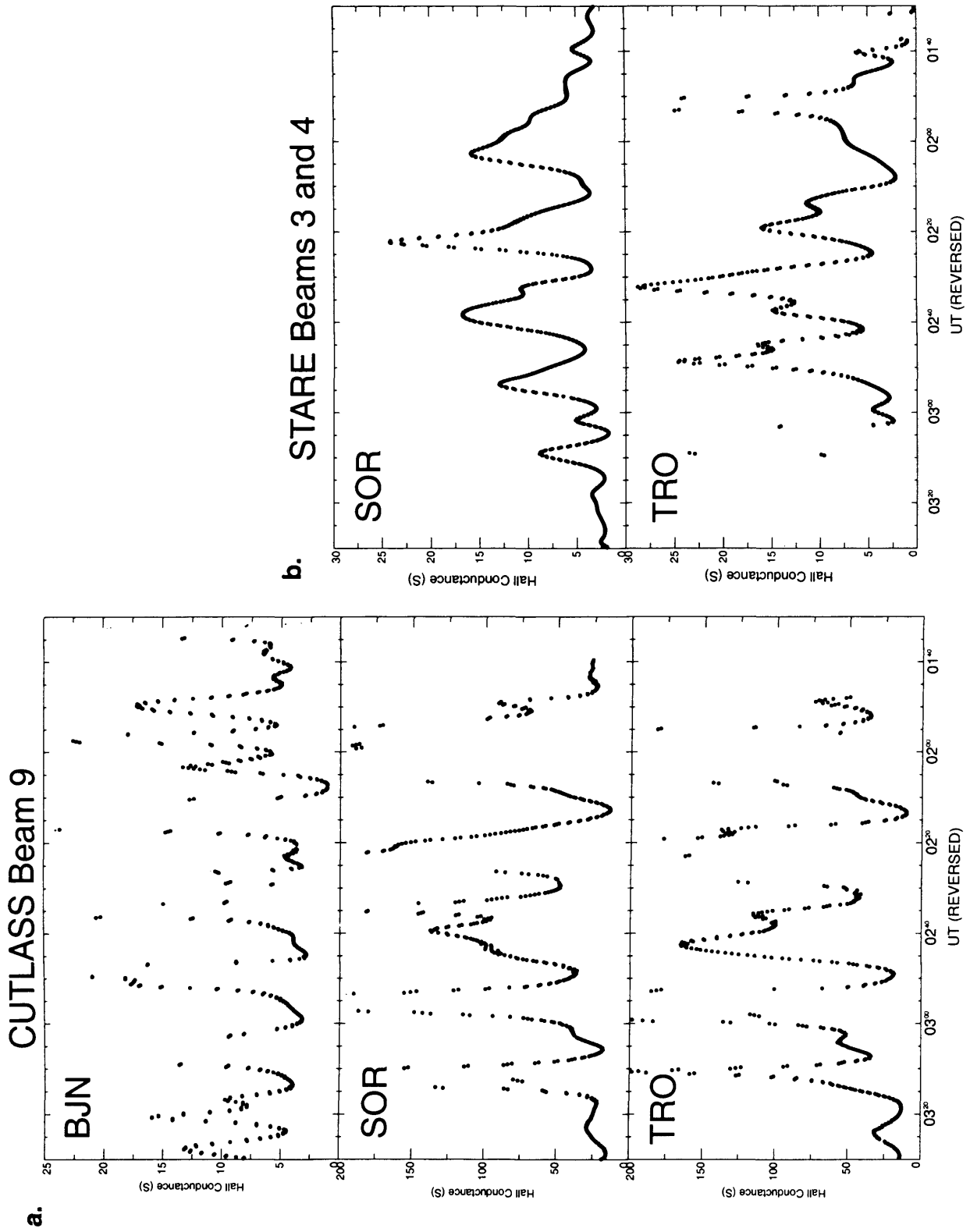

Figure 5.8. a Ionospheric Hall conductances derived from CUTLASS beam 9, l-o-s velocities and IMAGE magnetometer data. Presented are BJN (*top panel*), SOR (*centre panel*), and TRO (*bottom panel*). **b,** Ionospheric Hall conductances derived from STARE beam 4 and SOR (*top panel*) and STARE beam 3 and TRO (*bottom panel*). BJN, SOR and TRO are located at magnetic latitudes of 71.3°, 67.1° and 66.4° respectively. CUTLASS derived profiles are directly comparable as all l-o-s velocities are drawn from a single beam whereas STARE derived profiles represent simultaneous measurements from two separate locations (see text for description). Conductance scales are not uniform for all panels.

measurements were made after ~03:15 UT although 4 significant conductance intensifications were observed prior to this time. It should be noted that conductances calculated from the STARE beams selected are a factor ~5 smaller than CUTLASS derived conductances. The selection of beams within the STARE field-of-view that closely overlay SOR and TRO rather than the beam that is most closely aligned to a meridional direction implies that Eq. (5.3) is no longer accurate as the l-o-s velocities will be contaminated with the zonal component of the ionospheric flow. Examination of STARE beam 0 (azimuth ~13°) reveals that l-o-s velocities in a near-meridional direction are ~4 times smaller than those measured in beams 3 and 4. Also, the poleward component of velocity, v_x, measured by STARE is likely to be underestimated due to sound-speed limiting effects (Robinson, 1986). Furthermore, the use of l-o-s velocities from multiple beams introduces a temporal offset between each beam's estimated conductance profile. It is therefore reasonable to assume that the suppressed conductances and dispersed timings deduced from STARE l-o-s velocities are artificially distorted due to viewing angle geometry. Once the relevant geometrical issues have been resolved, conductance magnitudes derived from CUTLASS and STARE are in approximate agreement although direct E-region/F-region comparisons are not straightforward. Nevertheless the location of regions of elevated Hall conductance at SOR and TRO derived from CUTLASS and STARE are approximately co-located.

5.4 Discussion

5.4.1 Omega band structure

The observations and interpretation presented so far have been employed to construct a schematic representation of the structure of an auroral omega band (Figure 5.9 a). Measurements of ionospheric electric field, equivalent currents and derived conductances are combined to infer the optical and current structure of the omega band, associating high conductance with high auroral luminosity. In general the peak of conductance is located on the westward side of the enhanced conductance region that relates to the auroral projection. Highly luminous, high conductance regions are associated with upward FACs (Akasofu, 1981; Opgenoorth *et al.*, 1983), which in this case are located near the poleward boundary of the auroral oval, and around which vortical Hall currents flow in an anticlockwise sense. These upward FACs occur further towards the east at higher latitudes as indicated by the offset of regions of high conductance at BJN and SOR as shown in Figure 5.8. Outside the high conductance region, downward FACs (associated with clockwise Hall currents) allow

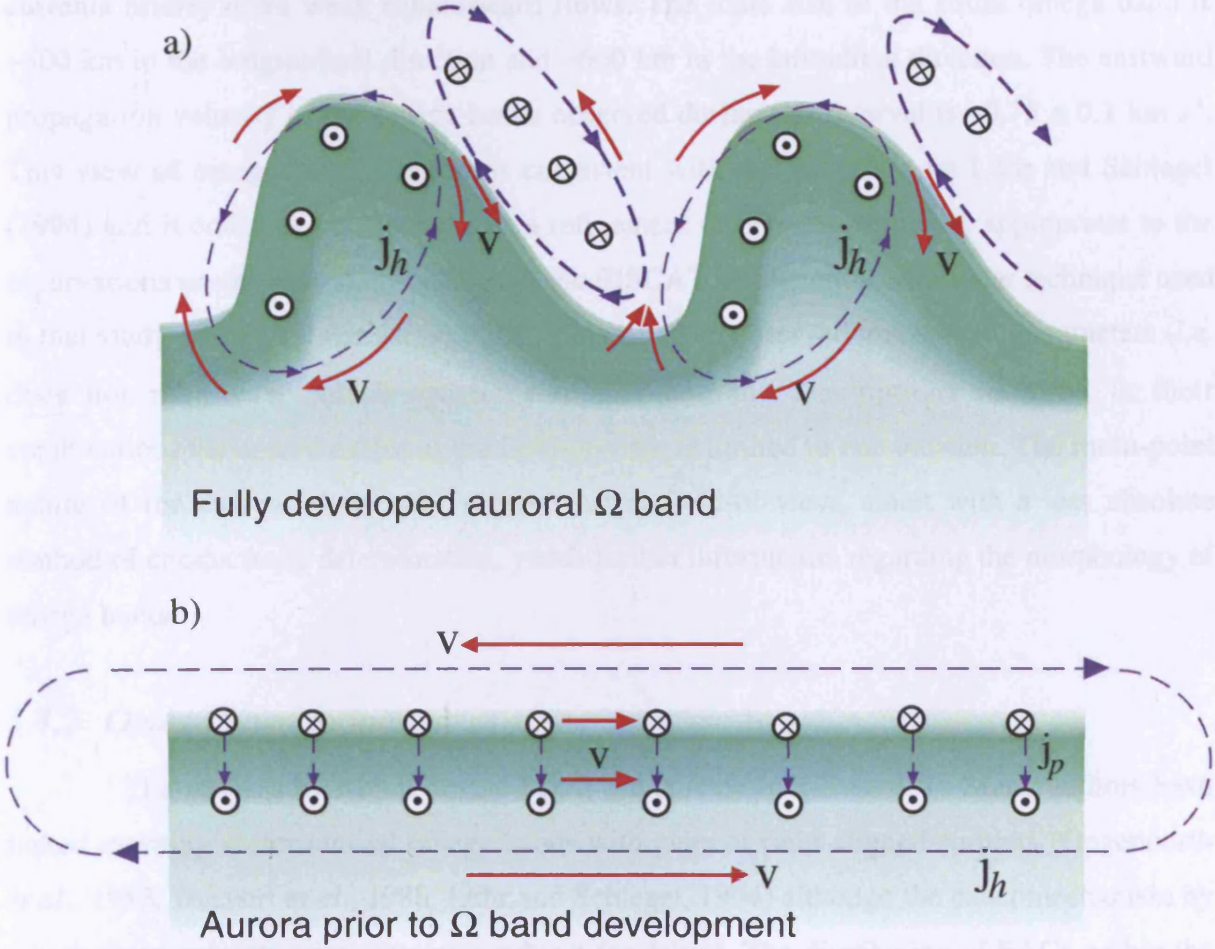

Figure 5.9. a Schematic representation of the auroral omega bands observed on 11th May 1998. In this figure, north is toward the top of the figure and east toward the right. *Green shaded regions* represent bright aurora, *blue dashed lines* indicate ionospheric Hall currents, *red solid arrows* indicate convection flow direction, the length of the line is an indicator of flow strength. Upward FAC (*dotted circles*) and downward FAC (*crossed circles*) are also shown but Pedersen currents have been omitted for clarity; **b** A simplified interpretation of the region 1 – region 2 currents before the advent of instability. Currents, flows and FACs and bright auroral regions are denoted as in **a**.

current closure through the ionosphere. The resulting equatorward current between the two Hall current systems gives rise to the intense poleward flow observed by the radars. This flow is then shifted to higher latitudes by the distorted poleward boundary of the auroral oval as the next omega band moves in from the west. This region is clearly apparent as a diagonal band of poleward flow in the reversed timescale range-time-intensity plot in Figure 5.7. Finally, just before the high conductance region reaches its maximum poleward extent, vortical Hall currents briefly drive weak equatorward flows. The scale size of the entire omega band is ~500 km in the longitudinal direction and ~600 km in the latitudinal direction. The eastward propagation velocity of the omega bands observed during this interval is ~0.75 ± 0.1 km s^{-1}. This view of omega band structure is consistent with that proposed by Lühr and Schlegel (1994) and it could be considered that a refinement of that description is appropriate to the observations in this case study. Although the EISCAT incoherent scatter radar technique used in that study allows the derivation of Σ_H directly from observed ionospheric parameters (i.e. does not require a radar/magnetometer pair and the assumptions required in their combination) the spatial extent of the field-of-view is limited to one location. The multi-point nature of the current study over a much larger field-of-view, albeit with a less absolute method of conductance determination, yields further information regarding the morphology of omega bands.

5.4.2 Omega band formation

The process by which omega bands are created is still unclear. Many authors have linked morning sector auroral omega bands with pairs of field-aligned currents (Opgenoorth *et al.*, 1983; Buchert *et al.*, 1988; Lühr and Schlegel, 1994) although the exact mechanism by which these currents arise remains a subject for debate. The distribution of FACs within the inferred bright region is not consistent with the expected distribution if omega bands were to form as a result of the interchange instability as proposed by Yamamoto *et al.* (1993; 1997). In that case, upward FAC would be concentrated within the bright region at the eastward boundary of each omega band and downward current just inside the westward boundary (Figure 5.10). Despite the lack of optical observations due to the unsuitable season of the interval presented, the asymmetrical distribution of omega band structure presented here is entirely consistent with optical observations in previous studies (e.g. Snyder and Akasofu, 1974; Opgenoorth *et al.*, 1994). These are characterised by a roughly Ω shaped distortion of the bright poleward boundary of the auroral oval, slightly darker in the central region than at the edge and often "leaning" slightly in the longitudinal direction as is the case in Figure 5.1a.

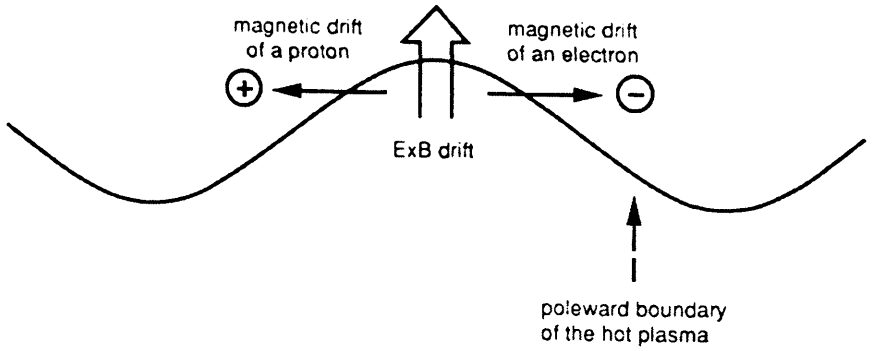

(a)

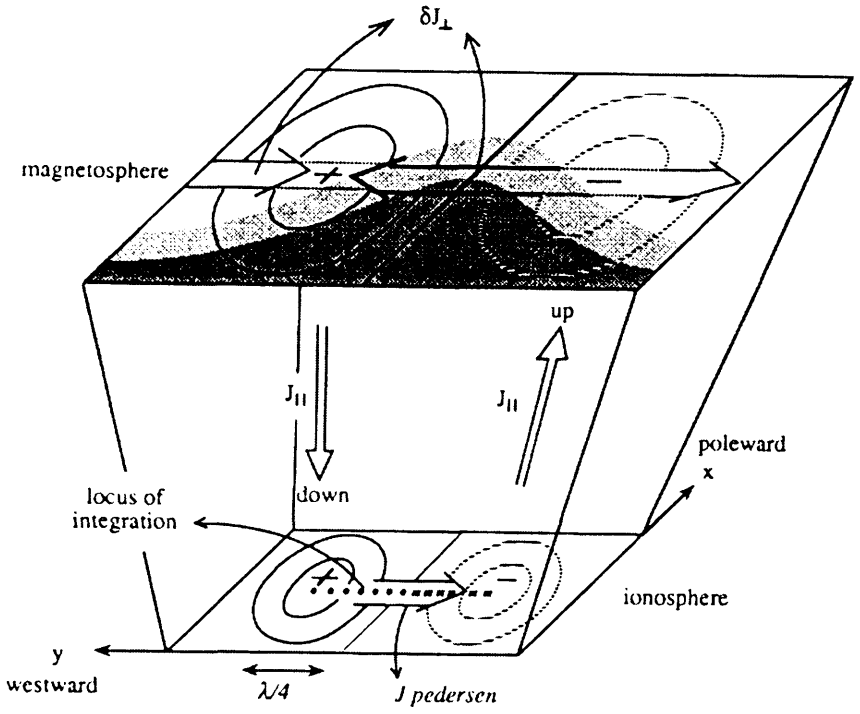

(b)

Figure 5.10. a A schematic illustrating the mechanism for a magnetic-drift induced interchange instability at the location in the magnetosphere that maps to the poleward edge of the auroral oval. Oppositely directed magnetic drifts of hot protons and electrons induce charge separation. The resulting poleward electric field increases the perturbation amplitude; **b** The ionospheric coupling to the magnetospheric interchange instability (from Yamamoto *et al.*, 1993). In this configuration upward FACs are located at the eastern edge of the bright region, contrary to the inferred location of upward FAC within the omega bands observed on 11th May 1998.

Complementary observations of the ultraviolet aurora routinely made by the Ultra-Violet Imager (UVI) instrument on-board the *Polar* spacecraft (Torr *et al.*, 1995) would have proven useful in characterising the spatial structure but these were also unavailable during the interval presented here. The omega bands described here are, however, consistent with the results of a Kelvin-Helmholtz type instability near the poleward boundary of the auroral oval, the mechanism of formation being similar to that of auroral spirals or folds as discussed by Hallinan (1976). In this case a velocity shear would occur near the poleward boundary of the auroral oval in the dawn convection cell where region 1 (downward) and region 2 (upward) FACs lead to Hall currents (opposite in direction to the $\mathbf{E} \times \mathbf{B}$ drifts) as discussed by Fujii *et al.* (1994) and as indicated in Figure 5.9b. It is possible that the presented omega bands have been generated by another instability process but the exact determination of the generation mechanism would require co-ordinated in-situ observations from spacecraft within the appropriate region of the magnetosphere which are unavailable for this interval.

Of particular interest is the relationship of omega bands in the morning sector to substorm phase. Generally observed in the morning hours around 05:00 MLT following substorm activity, it has long been assumed that omega bands are a purely recovery phase phenomenon (Akasofu, 1974; Saito, 1978; Rostoker and Barichello, 1980). The omega bands observed on the morning of 11th May 1998 occurred during a sequence of substorm onset/intensifications that began at 23:30 UT of the previous day (not shown) with subsequent onset/intensifications at 00:43, 01:35, 01:50, and 03:05 UT (Figure 5.4). The onset/intensification of a substorm to the west over Greenland at 01:50 UT and the almost simultaneous observation (within minutes) of auroral omega bands in the morning sector suggests a more subtle mechanism. The concurrent growth of a magnetospheric substorm during the recovery phase of a previous substorm and the link with auroral omega bands in the morning sector has been discussed previously by Pellinen *et al.* (1992). Conventional interpretation suggests that the substorm recovery phase is an interval during which the general level of magnetic disturbance declines to some quiet level. It seems unlikely then that a system that is tending to a more quiescent state would spontaneously generate a series of instabilities such as omega bands in the morning sector. A new substorm onset, acting upon an already disturbed system could intensify the dawn convection cell, already energised by the previous substorm expansion, and thus could have the ability to drive the large-scale downward currents at the poleward edge of the morning sector oval unstable, creating a series of filamentary FACs. A detailed study of IMAGE network *X* component magnetograms reveals a sudden intensification of the negative bay at 01:50 UT observed at many stations simultaneously, regardless of

longitudinal location. This is in contrast with the observations of Ps6 pulsations (omega bands) that follow shortly afterwards which are dispersed in longitude. This implies that that the onset of the bay is a regional response to the onset/intensification (Opgenoorth and Pellinen, 1998) observed at Greenland and the pulsations are due to drifting omega bands that are formed at the new substorm onset. Furthermore, the absence of Ps6 pulsations at JAN (located between the Scandinavian and midnight sectors at 70.3° magnetic latitude) suggests that the observed omega bands have not propagated eastward from the region of substorm onset/intensification but have been created in the morning sector in response to the substorm onset. In order to more fully determine whether or not all omega bands are triggered by an expansion phase onset during the substorm recovery phase, as appears to be the case here, it will be necessary to perform an extensive statistical study of previous omega band intervals and this will be the basis for future research.

5.5 Summary

During the interval 00-08 UT on 11th May 1998, the CUTLASS Finland HF radar was operating in a high-time resolution mode providing 14 s observations of a single beam in an approximately poleward direction. Between 01:30-03:30 UT a series of 5 intervals of flow of latitudinal extent ~1.5° were observed to propagate away from the radar, each lasting for ~10 min with a repetition period ~18 min. The STARE Norway VHF radar operating in a standard scan mode with temporal resolution ~20 s also observed extended regions of poleward flow of similar duration and repetition frequency. The latitudinal extent of the enhanced flow region was consistent with that measured by HF radar although STARE observations preceded those from CUTLASS by ~5 min.

Stations of the IMAGE magnetometer network situated in the Scandinavian sector (~05 MLT) recorded at least 5 intense Ps6 pulsation wave-cycles in both the *X* and *Y* components between 02:00-03:30 UT implying the nearby transit of a series of auroral omega bands. The scale size of these omega bands has been estimated at ~400 km in the longitudinal-direction and ~600 km in the latitudinal. The delay between observing the pulsations at longitudinally separated stations indicates that the eastward propagation of the omega bands is at a speed of ~0.75 km s^{-1}. By studying ionospheric electric fields, ground magnetometer data, derived equivalent currents and derived ionospheric Hall conductances the spatial structure of the observed omega bands has been deduced. The region of elevated conductance has a peak value at the westward edge of each omega band, and appears to be associated with upward FAC (assumed to be downward precipitating electrons). Downward FACs are located outside

of the high conductance regions. The Hall currents that arise as a result of both upward and downward FACs result in strong flows in the region just poleward the auroral boundary between the high conductance regions (inferred to be bright tongues) and weak equatorward flows at the tip of the tongues. This structure is consistent with omega band formation due to a Kelvin-Helmholtz instability near or at the poleward boundary of the auroral oval although observations that would verify this supposition are not available for this interval.

The interval during which the radar observations were made occurred during a period of several magnetospheric substorm onset/intensifications and simultaneously with a new intensification at 01:50 UT observed by the Greenland west coast magnetometer chain located at ~23:35 MLT. It is suggested that the global response to a onset/intensification that occurs during the recovery phase of a previous substorm acts as a trigger causing the downward current at the poleward edge of the auroral oval to the east to become unstable. The series of filamentary FACs that would then result manifest themselves as omega bands at the poleward boundary of the auroral oval.

CHAPTER 6

High-time resolution radar observations of high-latitude flows during the recovery phase of an isolated substorm

6.1 Introduction

Although usually less dramatic than the substorm expansion phase, the recovery phase is nevertheless associated with significant auroral activity, such as morning sector omega bands as discussed in the previous chapter. Ionospheric conditions during the recovery phase are particularly suitable for coherent HF radar observations since extensive areas can be observed at high temporal and spatial resolution without suffering from the serious loss of backscatter associated with expansion phase onset (Milan *et al.*, 1996). As discussed in section 3.4, incoherent-scatter radars are able to provide a wider range of directly measured or inferred ionospheric parameters than coherent-scatter systems although their fields-of-view are, in general, much more restricted. Consequently, coincident coherent and incoherent observations complement each other most favourably, the combination yielding excellent measurements of the overall large-scale ionospheric configuration in addition to detailed ionospheric observations at several key locations.

As discussed in section 2.3.2, auroral displays are most frequently observed within the auroral oval, the annular region that encircles the geomagnetic pole in each hemisphere. It is thought that the nightside auroras occur on closed magnetic field lines (Parks *et al.*, 1984) and that the dark regions poleward of the auroral oval (known as the *polar cap*) corresponds to the ionospheric footprint region of open magnetic field lines (see inset of Figure 1.5). The dimensions of the auroral ovals and the polar caps they encompass vary with geomagnetic activity, with the polar cap size increasing as magnetic activity increases. However, auroral activity is not restricted exclusively to the auroral ovals and both discrete and diffuse auroral forms are sometimes observed far inside the polar cap, often apparently isolated from the auroral oval. Ismail and Meng (1982) classified polar cap auroral arcs into three types: type 1, distinctly sun-aligned polar cap arcs; type 2, morning/evening polar cap arcs that extend from the auroral oval; and type 3, hook-shaped arcs connecting the polar cap arc with the oval arcs. Most of the observations of polar cap aurora have been made during intervals of quiet magnetic conditions, with the majority during periods of northward IMF. *Theta aurora* are a class of transpolar arc first reported by Frank *et al.* (1986) who employed instruments aboard

the Dynamics Explorer 1 and 2 spacecraft (DE-1 and DE-2 respectively) to obtain global auroral images. Theta aurora are characterised as transpolar arcs that are generally sun-aligned and extend continuously from the dayside to nightside sectors of the auroral oval (Figure 6.1a), a pattern reminiscent of the Greek letter θ. The plasma convection associated with the sun-aligned arc is sunward whilst it is antisunward elsewhere in the polar cap, a configuration that Frank and co-authors interpreted as consistent with the four-cell convection pattern expected for B_Z+ and $B_Y \approx 0$ conditions (Figure 6.1b). Hones *et al.* (1989) reported observation of the *horse-collar aurora*, a frequently observed auroral pattern during periods of geomagnetic quiescence. Horse-collar aurora (Figure 6.1c) are usually observed during intervals of northwards IMF and comprise two auroral "bars" extending from the pre and post midnight nightside auroral oval, spanning the polar cap and connecting with the dayside auroral oval near 12 MLT. Birn *et al.* (1991) suggested that the teardrop-shaped polar cap maps to regions of open flux with the brighter bars along its side corresponding to the plasma sheet boundary layers originating from a distant neutral line in the tail. Previous observations also suggest that horse-collar aurora may be a stage in the development of theta-aurora and that the IMF B_Y component influences its configuration (Hones *et al.*,1989).

This chapter presents the findings of a combined coherent/incoherent study of the ionospheric flows associated with the auroral zone and polar cap during the recovery phase of an isolated magnetospheric substorm.

6.2 Instrumentation

A map indicating the locations and fields-of-view of the principal instruments referred to in this chapter is presented in Figure 6.2. Between 00 UT on 20th August 1998 and 00 UT on 25th August 1998, the CUTLASS radars were operating in non-standard scan modes with each radar sounding all 16 available beams at a dwell time of 2 s, in a pattern similar to that described in section 5.2. This provides in one high-time resolution (4 s) beam within each radar's f-o-v (beam 10 in the case of CUTLASS Iceland; beam 9 in the case of CUTLASS Finland) whilst still yielding observations of the entire f-o-v at ~1 min resolution. During the period of interest in this study, no significant backscatter was observed within the region of interest by the Iceland radar, therefore only data from the Finland radar is presented.

For 4 consecutive evenings beginning on 20th August 1998, two EISCAT radars were implementing the UK special program SP-UK-CSUB over 4-hour intervals between 21-01 UT. The EISCAT Svalbard Radar (ESR) located at Longyearbyen was pointing

a.

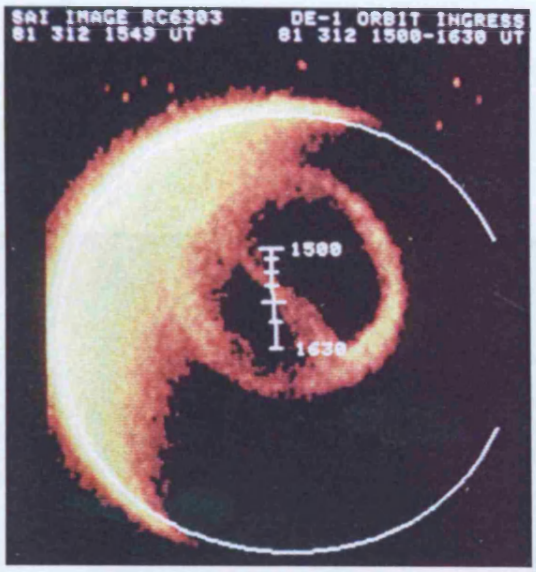

b.

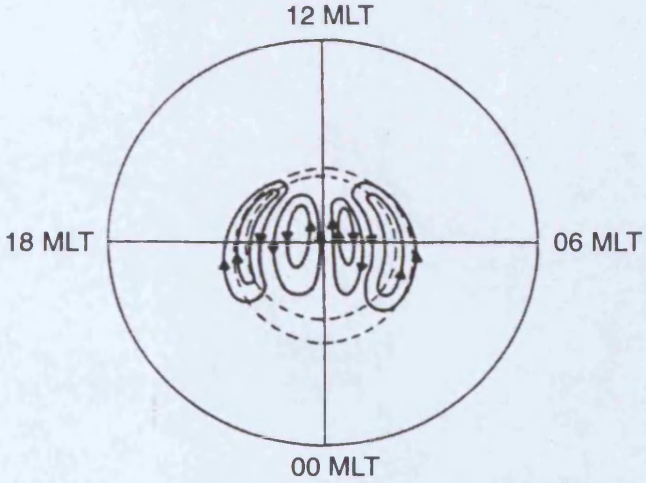

c.

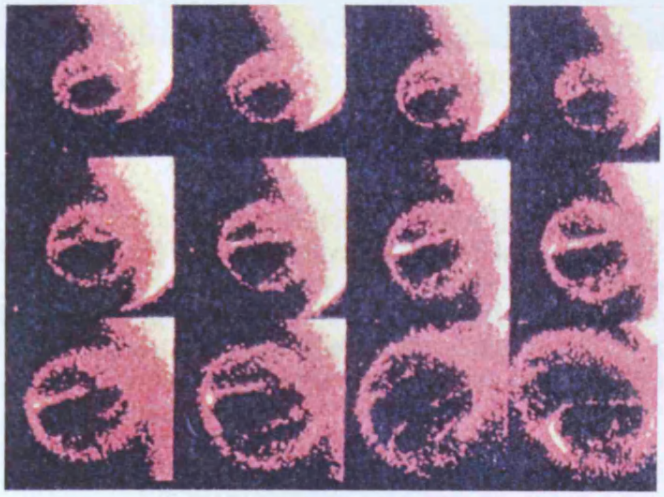

Figure 6.1. a Image of the northern auroral zone and polar cap with theta aurora configuration as seen in atomic oxygen (130.4-135.6 nm) emissions on 8th November 1981. Overlaid is the satellite position mapped to 300 km altitude (from Frank *et al.*, 1986); **b** The 4-cell northern hemisphere convection pattern expected for northward IMF and $B_Y \approx 0$ (from Cowley and Lockwood, 1992); **c** A series of images of atomic oxygen emission in the southern hemisphere auroral oval and polar cap on 9th May 1983. The sequence runs horizontally from *top-left* to *bottom-right* and shows the evolution of a horse-collar aurora that subsequently develops into the theta aurora configuration (from Hones *et al.*, 1989).

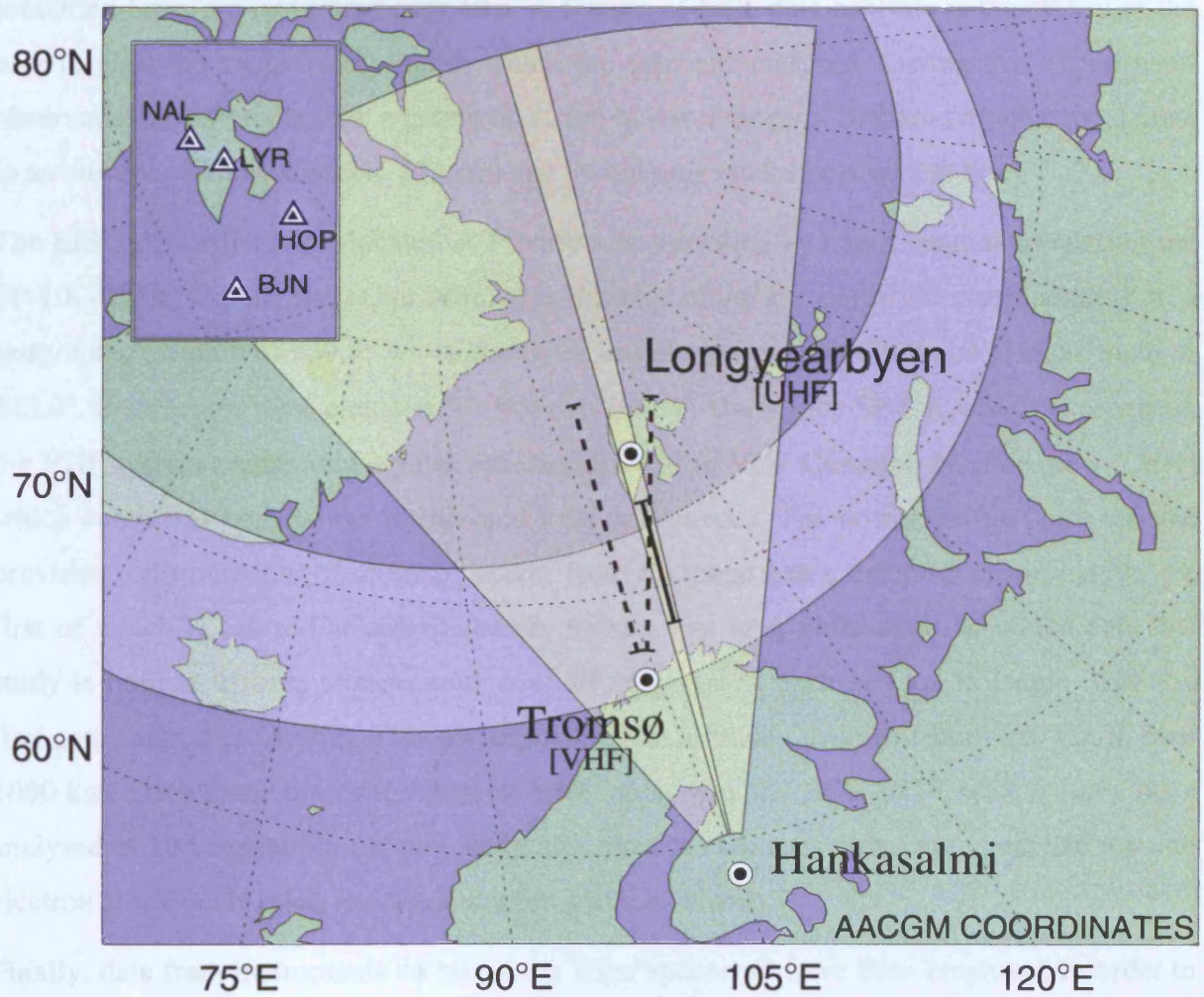

Figure 6.2. The location and field-of-view of the CUTLASS Finland (*yellow shading*) radar. Beam 9 is sampled at a high rate and is indicated by *dark yellow shading*. The beam of the ESR is represented by a *heavy solid black line* and the beams of the EISCAT VHF radar by *heavy dashed black lines*. Radar sites are indicated by *dotted circles*. Overlaid is the statistical location of the auroral oval for K_P=1+ (after Feldstein and Starkov, 1967). The inset presents the locations of IMAGE magnetometers in the region of the Svalbard archipelago.

southward with a geographic azimuth of 161.6° and an elevation of 31.0°. With this orientation the beam of the ESR is directed, at least in azimuth, along beam 9 of the CUTLASS Finland radar. During the SP-UK-CSUB experiment, the ESR was transmitting the GUP0 radar code, a multi-frequency long pulse scheme in which the received signals, as presented here, are integrated over 10 s. A feature of ESR data analysis is the ability of the user to alter the range resolution at which the data are analysed. During this experiment, observations were made with a gating of 12 km below a range of 330 km (which corresponds to an altitude of approximately 175 km) and 36 km range gates beyond 330 km.

The EISCAT VHF system located at Tromsø was operating in a split beam mode during the SP-UK-CSUB experiment. One beam was directed along the boresight corresponding to a geographic azimuth of 359.5° whilst the other was phased westward to point at an azimuth of 345.0°. Both beams were elevated 30° from horizontal. During the SP-UK-CSUB experiment, the VHF system transmitted a pulse scheme identical to VHF Common Programme 4 (CP-4) which comprises both power profile and long pulse codes. The power profile pulse scheme provides measurements of returned power from 83 range gates, each 4.5 km in length, the first of which is centred at approximately 85 km. The long pulse code, to which data this study is limited, affords observations over 20 range gates, each ~65 km in length, with the first gate centred at 533 km. This corresponds to an altitude coverage from ~280 km to over 1000 km. Data from both the Tromsø VHF radar and the ESR UHF system have been analysed at 10 s resolution for this study and provide estimates along each beam of ion and electron temperature, electron concentration and ion velocity.

Finally, data from instruments on board the *Wind* spacecraft have been employed in order to characterise the solar wind and IMF conditions prevailing during the interval under scrutiny. The Magnetic Fields Investigation (MFI) instrument (Lepping *et al.*, 1995) comprises a dual triaxial fluxgate magnetometer in order to make measurement of the IMF in 3 orthogonal directions; the fundamental operation of the MFI instrument is broadly similar to the ground magnetometers described in section 3.5.1. The Solar Wind Experiment (SWE) instrument (Ogilvie *et al.*, 1995) is designed to make measurements of the solar wind particle population in which the spacecraft is immersed. As such the SWE instrument routinely yields information regarding three components of the proton velocity, number density and thermal speed as well as the α-particle/proton ratio. The *Wind* spacecraft was launched on 1st November 1994 and is operated by the United States National Aeronautics and Space Administration (NASA). It was originally intended to observe the solar wind approaching the Earth from a position near the *Lagrangian point L1*, and it is part of the International Solar-

Terrestrial Physics (ISTP) initiative. Since the end of 1998, *Wind's* mission has been extended in order to allow the spacecraft to make *in-situ* measurements of the solar wind at a wider range of locations. The location of the *Wind* spacecraft during the interval presented in this chapter is summarised in Figure 6.3.

6.3 Observations

6.3.1 Interplanetary conditions

Figure 6.4a presents IMF observations made by the MFI instrument on the *Wind* spacecraft during the interval 00 UT on 21st August 1998 and 00 UT on 23rd August 1998. The IMF had been oriented northward for ~20 hours prior to 20:25 UT on 21st August and the IMF B_Y component had been positive for ~4 hours. At 20:25 UT both the B_Y and B_Z components measured at *Wind* abruptly switched polarity indicating the conclusion of a period of quiet solar wind conditions. Figure 6.4b presents the *X* component magnetogram from the IMAGE magnetometer located at Bear Island (BJN). This magnetogram is typical of Scandinavian sector magnetic field observations during the interval with exceptionally quiet conditions prevailing until ~1 hour to midnight on 22nd August.

At 20:25 UT, the solar wind velocity observed at *Wind* was ~300 km s^{-1}. By first considering the propagation time for an element of the solar wind travelling along the GSM *X* axis from the projection of the spacecraft's position to the bow shock and then estimating the propagation time through the magnetosheath using the technique of Khan and Cowley (1999), a propagation delay of ~37 minutes to the subsolar magnetopause is calculated. In fact the solar wind flow speed does not vary more than ±50 km s^{-1} implying that the calculated 37 min delay is appropriate throughout that interval. Assuming an additional 2 min delay for the effect of the IMF reorientation to reach the ionospheric footprint of the subsolar magnetopause and 15 min for the resulting reconfiguration of the ionospheric convection pattern to expand to the nightside (Cowley and Lockwood, 1992), the effects of the southward turning at 20:25 UT would be expected to reach the nightside ionosphere at ~21:19 UT (a total delay of some 54 min). Figure 6.5 presents 6 hours of *Wind* magnetic field observations spanning midnight of 22nd August 1998 that have been adjusted to include this offset. Over the following hours it is possible to broadly classify the IMF into the 4 regimes indicated in Figure 6.5 and summarised in Table 6.1.

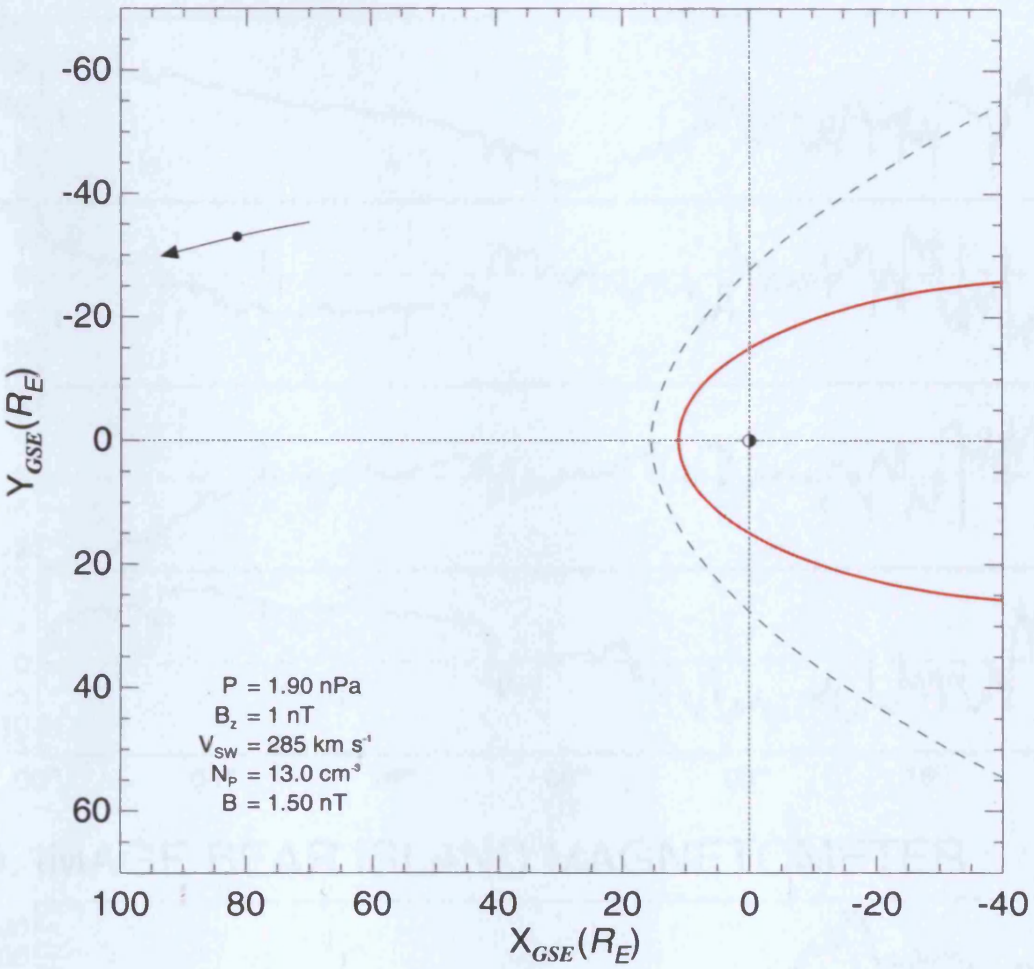

Figure 6.3. The location of the *Wind* spacecraft presented in the *X-Y* plane of a Geocentric Solar Ecliptic (GSE) coordinate frame. In this coordinate system, the *X* direction is directed from the centre of the Earth toward the Sun and the *Y* direction is in the ecliptic plane pointing from the centre of the Earth towards dusk. The *Z* axis makes up the final direction of a right-handed set and is aligned parallel to the ecliptic pole. The spacecraft's motion in the ecliptic (*X-Y)* plane between 00 UT on 21st August 1998 and 00 UT on 23rd August 1998 is indicated by the *solid black arrow*. During this interval the spacecraft was located between 4.5-6.0 R_E below the ecliptic plane. The location of *Wind* at 00:30 UT on 22nd August 1998 is indicated by a *filled black circle*. The approximate positions of the magnetopause and the bow-shock at this time are indicated by *solid red* and *dashed green lines* respectively. These locations of these boundaries have been estimated using the Roelof and Sibeck (1993) model of magnetopause shape and are based upon *in-situ* measurements of the solar wind parameters made by instruments on-board the *Wind* spacecraft (listed).

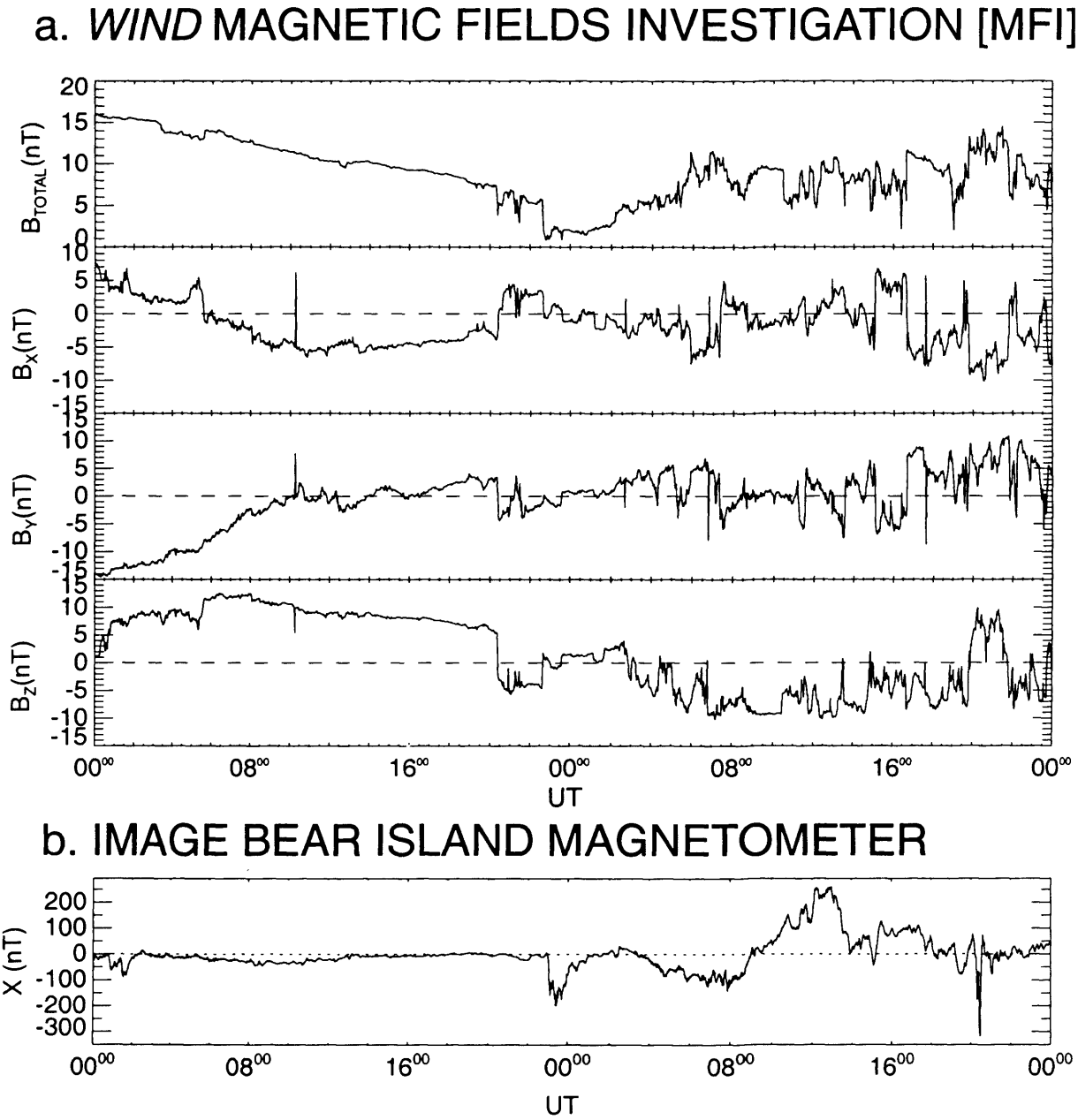

Figure 6.4. a Total and component magnetic field observations made by the MFI instrument on-board the *Wind* spacecraft during the interval 00 UT on 21st August 1998 to 00 UT on 23rd August 1998, presented in Geocentric Solar Magnetospheric (GSM) coordinates. As with the GSE coordinate system the *X* axis points from the centre of the Earth toward the Sun however the *Y* axis is defined to be perpendicular to the Earth's dipole so that the *X*-*Z* plane contains the dipole axis. The positive *Z* axis is chosen to be in the same sense as the northern magnetic pole. This coordinate system is appropriate when studying IMF-terrestrial field interactions; **b** *X* component magnetic field measurements from the Bear Island (BJN) magnetometer of the IMAGE array.

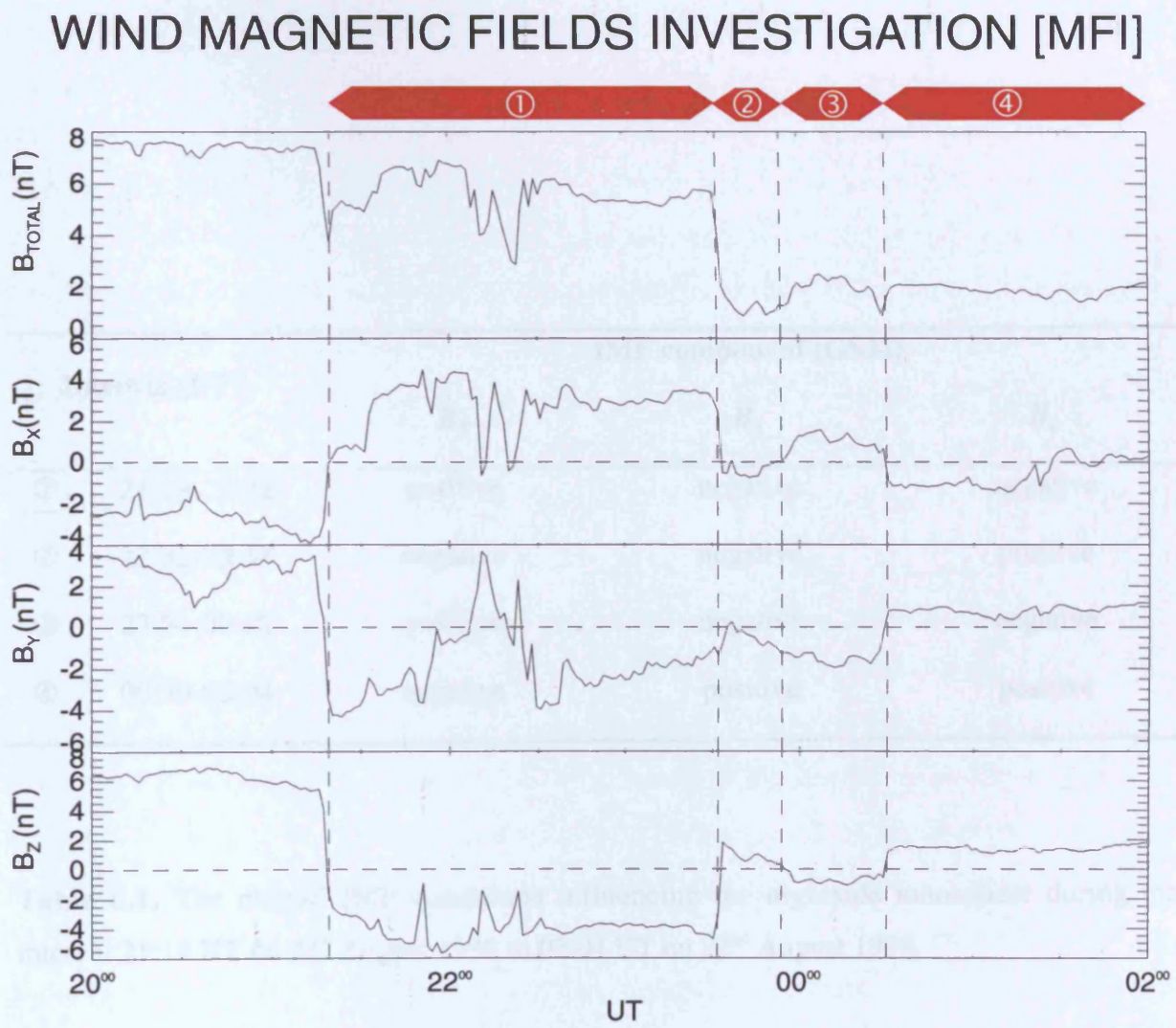

Figure 6.5. Magnetic field observations made by the *Wind* MFI instrument between 20 UT on 21st August 1998 and 02 UT on 22nd August 1998, presented in GSM coordinates. The observations have been offset by 54 min in order to account for the propagation of solar wind effects to the nightside ionosphere as described in section 6.3.1. The evolution of the solar wind during this interval can be broadly divided into the sub-intervals indicated by the *red bars* above the uppermost panel.

Interval (UT)		IMF component (GSM)		
		B_X	B_Y	B_Z
①	21:19-23:32	positive	negative	negative
②	23:32-23:54	negative	negative	positive
③	23:54-00:30	positive	negative	negative
④	00:30-02:04	negative	positive	positive

Table 6.1. The overall IMF conditions influencing the nightside ionosphere during the interval 21:19 UT on 21st August 1998 to 02:04 UT on 22nd August 1998.

6.3.2 Ground-based magnetometer observations

Useful measures of geomagnetic activity are the K and the K_P indices (Bartels, 1949; Bartels and Veldkamp, 1949). Although its derivation is somewhat complex, the K-index is essentially a quasi-logarithmic local index of the 3-hourly range in magnetic activity relative to an assumed quiet-day curve for a single geomagnetic observatory site (a detailed description of its calculation can be found in Rostoker, 1972). It consists of a single-digit ranging from 0 (low activity) to 9 (high activity) for each 3-hour interval of the universal time day. The scale is O to 9 expressed in thirds of a unit, e.g. 5- is 4 2/3, 5 is 5 and 5+ is 5 1/3. The planetary 3-hour-range index, K_P, is the mean standardised K-index from 13 geomagnetic observatories between 44 degrees and 60 degrees northern or southern geomagnetic latitude (listed in Table 6.2). During the 4 3-hour intervals prior to midnight on 22nd August the K_P index had values of 0+, 0, 0, and 2+ with the total K_P value for the day being 8-; an indicator of exceptionally low levels of geomagnetic activity. The K_P value for the first 3-hour interval of 22nd August was 1+.

Figure 6.6 presents magnetic field measurements from five stations of the IMAGE magnetometer array (section 3.5.2) between 20 UT on 21st August 1998 and 02 UT on 22nd August 1998. Unfiltered X, Y, and Z component magnetograms are displayed in addition to a single magnetogram (SOD) that has been bandpass filtered between 200 and 20 s to emphasis Pi2 pulsations. At 22:50 UT on 21st August, a clear Pi2 pulsation burst is observed at mid-latitude magnetometer stations of the IMAGE array followed by a weaker burst at 23:05 UT. The first of these Pi2 bursts coincides with a strong negative bay (~300 nT) in the X component of auroral zone magnetograms, indicating a substorm-enhanced westward electrojet (as discussed in section 4.3.1) and the conclusion of an interval of quiet magnetic conditions. The X component disturbance propagates poleward over the next 30 min reaching BJN at 22:58 UT and HOP at 23:18 UT. The Z component disturbance first observed at 22:50 UT is negative at all mainland Scandinavian stations (of which SOR is northernmost) and positive at locations further poleward, only becoming negative once the westward electrojet has passed overhead during the poleward track indicated by the X component disturbance. Following the disturbance onset at 22:50 UT, two large (~80 nT) positive deviations of the type usually associated with auroral loop and surge features (e.g. Untiedt and Baumjohann, 1993) are observed in mainland Scandinavian Y component magnetograms (SOR and KIL presented) centred at 23:00 UT and 23:08 UT. This marks the beginning of an interval of complex Y component disturbances observed at all stations of the IMAGE chain.

Station		Geomagnetic position		Country
		Lat (°)	Lon (°)	
Sitka	(SIT)	60.0	275.3	USA
Meanook	(MEA)	61.8	301.0	Canada
Lovö	(LOV)	58.1	105.8	Sweden
Ottawa	(OTT)	57.0	351.5	Canada
Fredricksburg	(FRD)	49.6	349.8	USA
Hartland	(HAD)	54.6	79.0	UK
Eskdalemuir	(ESK)	58.5	82.9	UK
Lerwick	(LER)	62.5	88.6	UK
Witteveen	(WIT)	54.1	91.2	Sweden
Wingst	(WNG)	54.6	94.1	Sweden
Brorfelde	(BFE)	52.1	89.8	Denmark
Canberra	(CNB)	-45.6	133.3	Australia
Eyrewell	(EYR)	-50.1	-103.7	New Zealand

Table 6.2. The locations of ground-magnetometer stations that currently contribute to the K_P index.

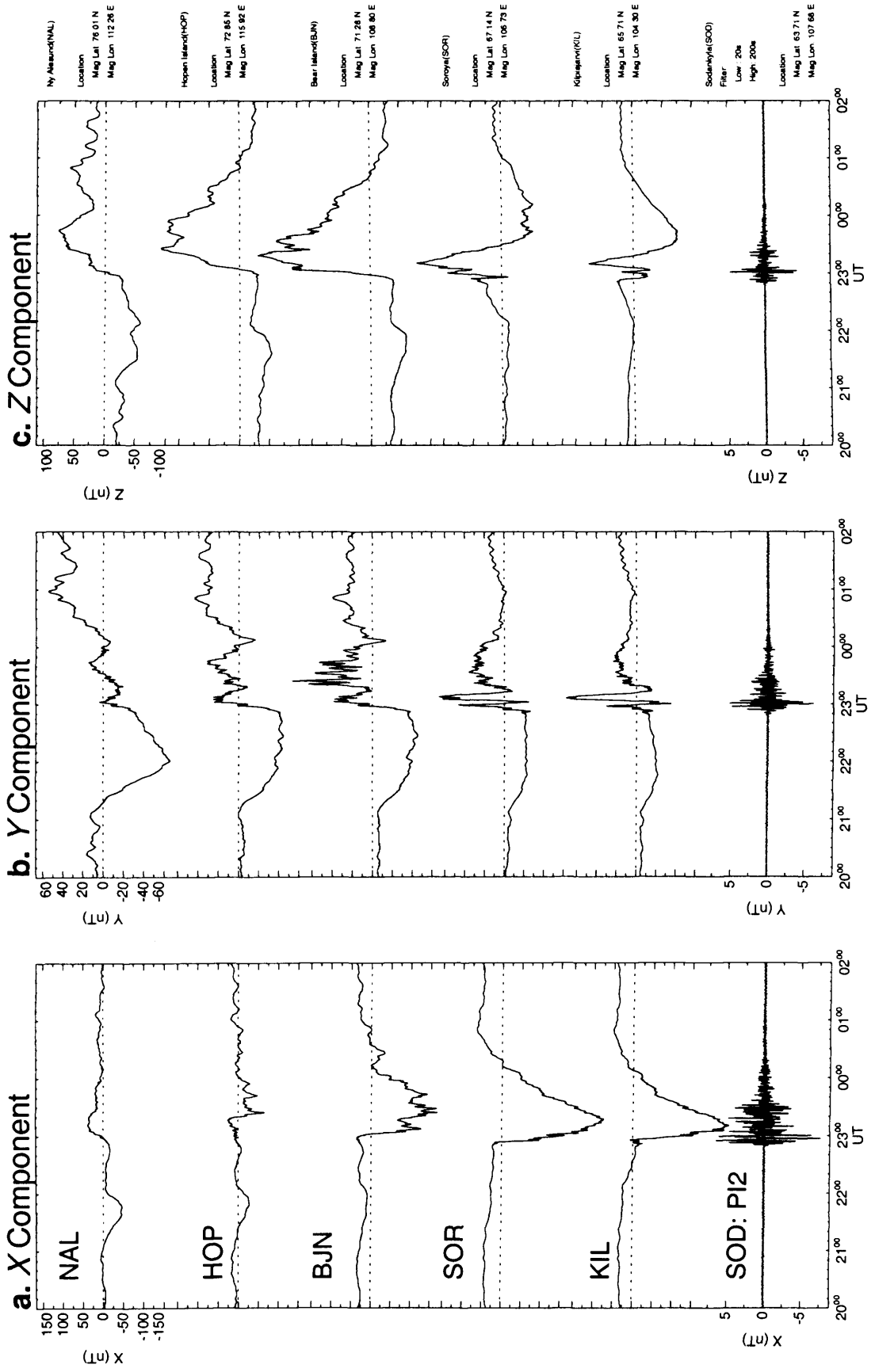

Figure 6.6. Magnetic field data from a selection of stations of the IMAGE magnetometer array for the interval 20 UT (21st August 1998) to 02 UT (22nd August 1998). Unfiltered *X*, *Y*, and *Z* components are presented. The lowest panel of each column displays data from SOD, band pass filtered between 200 and 20 s, in order to emphasise Pi2 pulsation activity.

Although some smaller scale (~50 nT) structure is apparent, all three components of IMAGE ground magnetograms recover toward their pre-onset conditions over the subsequent 2 hours.

6.3.3 HF radar observations of ionospheric flow

Figure 6.7 presents backscattered power and line-of-sight (l-o-s) Doppler velocity measurements from Beam 9 of the Finland radar as a function of magnetic latitude and universal time for the interval 21 UT on 21st August 1998 to 01 UT on 22nd August 1998. At ~21:30 UT the equatorward boundary of HF radar backscatter begins to migrate equatorward, a characteristic that has previously been associated with the substorm growth phase (Lewis *et al.*, 1997). At ~22:50 UT there is a marked reduction in backscatter observed by the CUTLASS Finland radar that extends to over 10° of magnetic latitude by ~23:20 UT. This loss of backscattered signal is frequently observed during the substorm expansion phase and is a result of D-region absorption of the radar signal due to energetic particle precipitation (Milan *et al.*, 1996; Milan *et al.*, 1999).

The complex flows that arise due to the expansion phase onset during this interval are the subject of a study by Yeoman *et al.* (2000) and will therefore not be discussed in detail here. By ~23:45 UT ionospheric backscatter was again observed over a comparable latitudinal range to that prior to onset.

At 00:08 UT, the observed backscatter Doppler velocities over the range of magnetic latitudes 68.5°-74.0° simultaneously reverse with the predominantly equatorward flow (colour-coded green/blue) giving way to predominantly poleward flow (colour-coded yellow/red). At 00:32 UT a region of flow located at ~73° with a l-o-s component directed away from the radar ($\leq$ 800 m s^{-1}) begins to drift poleward and finally extends at least 2° poleward of the existing backscatter boundary. This poleward motion encompasses ~5° over the subsequent 18 min, equivalent to a poleward propagation speed of ~400 m s^{-1}. Ground magnetometers in close proximity to the location of the backscatter feature observed very weak (~10 nT), short-lived perturbations during its poleward motion. At ~00:45 UT, prior to the arrival of this flow region at its most poleward location within the CUTLASS Finland radar's field-of-view, the l-o-s flow velocity between magnetic latitudes 73.5°-75.0° increases from ~200 m s^{-1} to ~500 m s^{-1}.

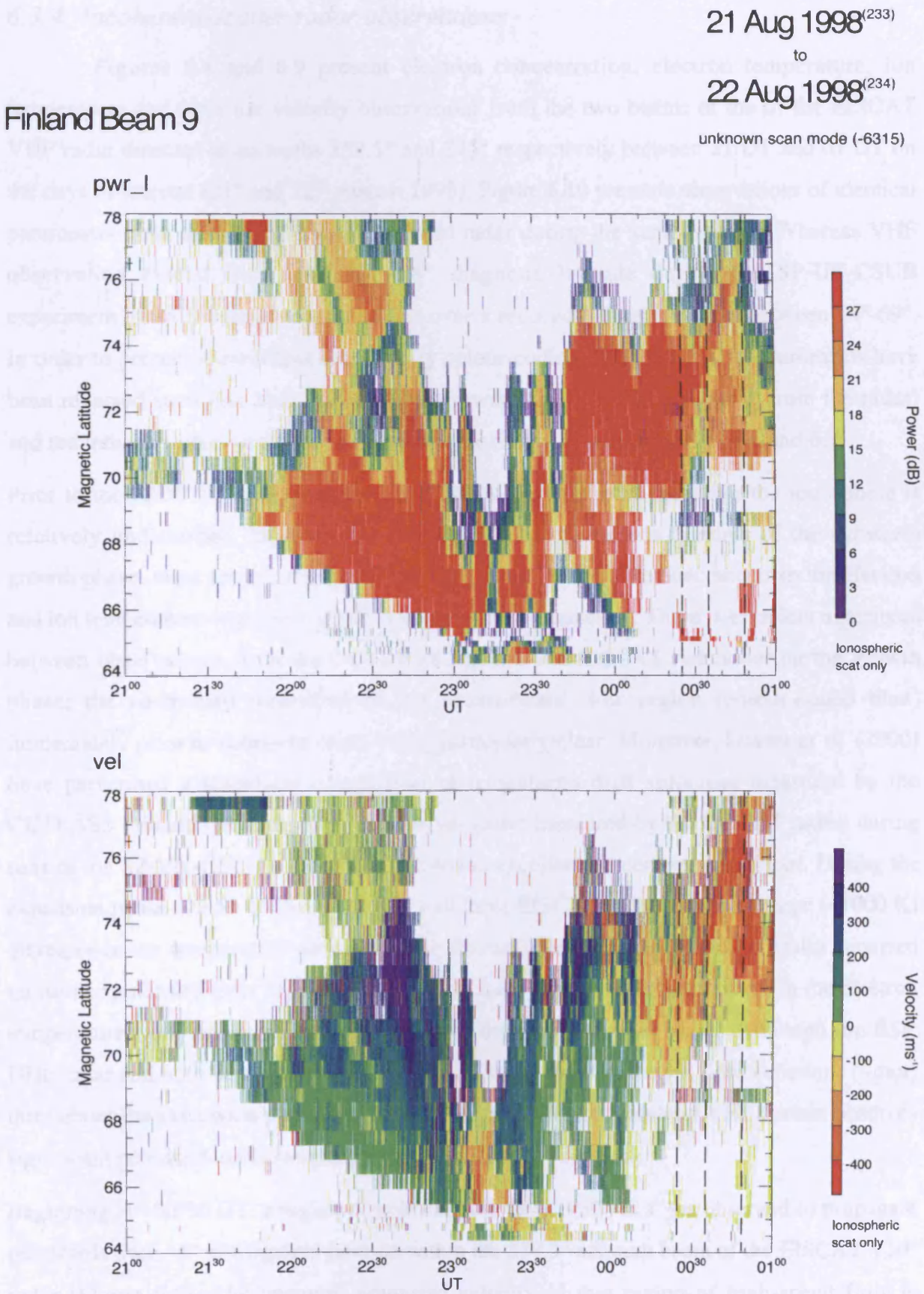

Figure 6.7. Backscatter power (*upper panel*) and line-of-sight Doppler velocity (*lower panel*) measurements from beam 9 of the CUTLASS Finland radar plotted as a function of magnetic latitude and universal time. Doppler velocities are colour-coded such that *red* represents flow away from the radar (approximately poleward) and *blue* represents flow toward the radar (approximately equatorward). *Dashed lines* indicate the CUTLASS Finland scan times referred to in the text.

6.3.4 Incoherent-scatter radar observations

Figures 6.8 and 6.9 present electron concentration, electron temperature, ion temperature and l-o-s ion velocity observations from the two beams of the of the EISCAT VHF radar directed at azimuths 359.5° and 345° respectively between 21 UT and 01 UT on the days of interest (21st and 22nd August 1998). Figure 6.10 presents observations of identical parameters from the UHF EISCAT Svalbard radar during the same interval. Whereas VHF observation extend from ~71° to ~78° magnetic latitude during the SP-UK-CSUB experiment, the ESR made measurements over a reduced latitudinal range between 74°-69°. In order to present a consistent ion velocity colour-coding, ESR velocity measurements have been reversed such that blue indicates equatorward flow (in this case *away* from the radar) and red indicates poleward flow (now *toward* the radar) as in Figures 6.7, 6.8, and 6.9.

Prior to the 22:50 UT substorm onset EISCAT observations suggest that the ionosphere is relatively undisturbed. Equatorward drifting arcs, characteristic features of the substorm growth phase, were observed prior to 22:30 UT manifesting as enhancements in the electron and ion temperature (especially clear in the ESR measurements). There is excellent agreement between observations from the CUTLASS Finland and EISCAT radars during the growth phase; the southward migration of the equatorward flow region (colour-coded blue) immediately prior to substorm onset being particularly clear. Moreover, Davies *et al.* (2000) have performed a statistical comparison of irregularity drift velocities measured by the CUTLASS Finland radar and F-region ion velocities measured by the EISCAT radars during runs of the SP-UK-CSUB experiment and found excellent agreement throughout. During the expansion phase (22:50 UT to ~00:10 UT) all three EISCAT radars observed large (~1000 K) increases in ion temperature although these fluctuations were bursty and generally occurred no further poleward than 73° magnetic latitude. Less structured enhancements in the electron temperature were measured by both beams of the mainland VHF radar. Although the ESR UHF radar and both beams of the EISCAT VHF radar measured rapid flow variations (~min) throughout the expansion phase, only the 359.5° beam of the mainland VHF system observes significant poleward ion flows prior to 00:10 UT on 22nd August.

Beginning at ~00:30 UT, a region of poleward ion flow (~800 m s^{-1}) is observed to propagate polewards over ~5° of magnetic latitude within the 359.5° azimuth beam of the EISCAT VHF radar (Figure 6.8). The apparent poleward velocity of this region of high-speed flow is ~550 m s^{-1}, comparable to the poleward moving feature observed by the CUTLASS Finland radar. This feature is also associated with a depletion in the electron concentration (~50%), a

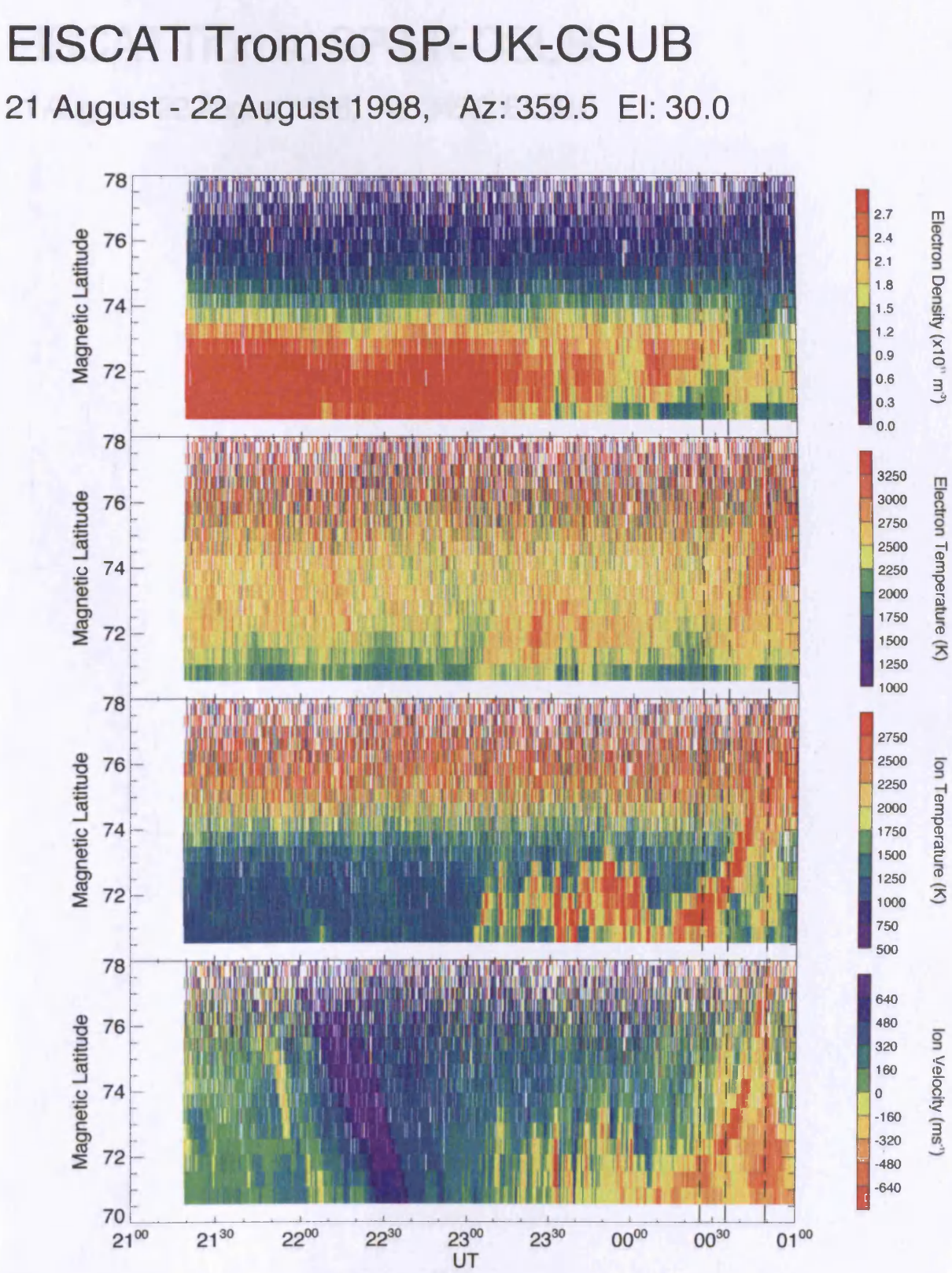

Figure 6.8. Measurements of electron density, electron temperature, ion temperature, and ion velocity made by the 359.5° azimuth beam of the EISCAT VHF radar, plotted as a function of magnetic latitude and universal time. Ion velocity measurements are colour-coded consistently with CUTLASS measurements, i.e. *red* indicates flow away from the radar (approximately poleward) and *blue* represents flow toward the radar (approximately equatorward). *Dashed lines* indicate the CUTLASS Finland scan times referred to in the text.

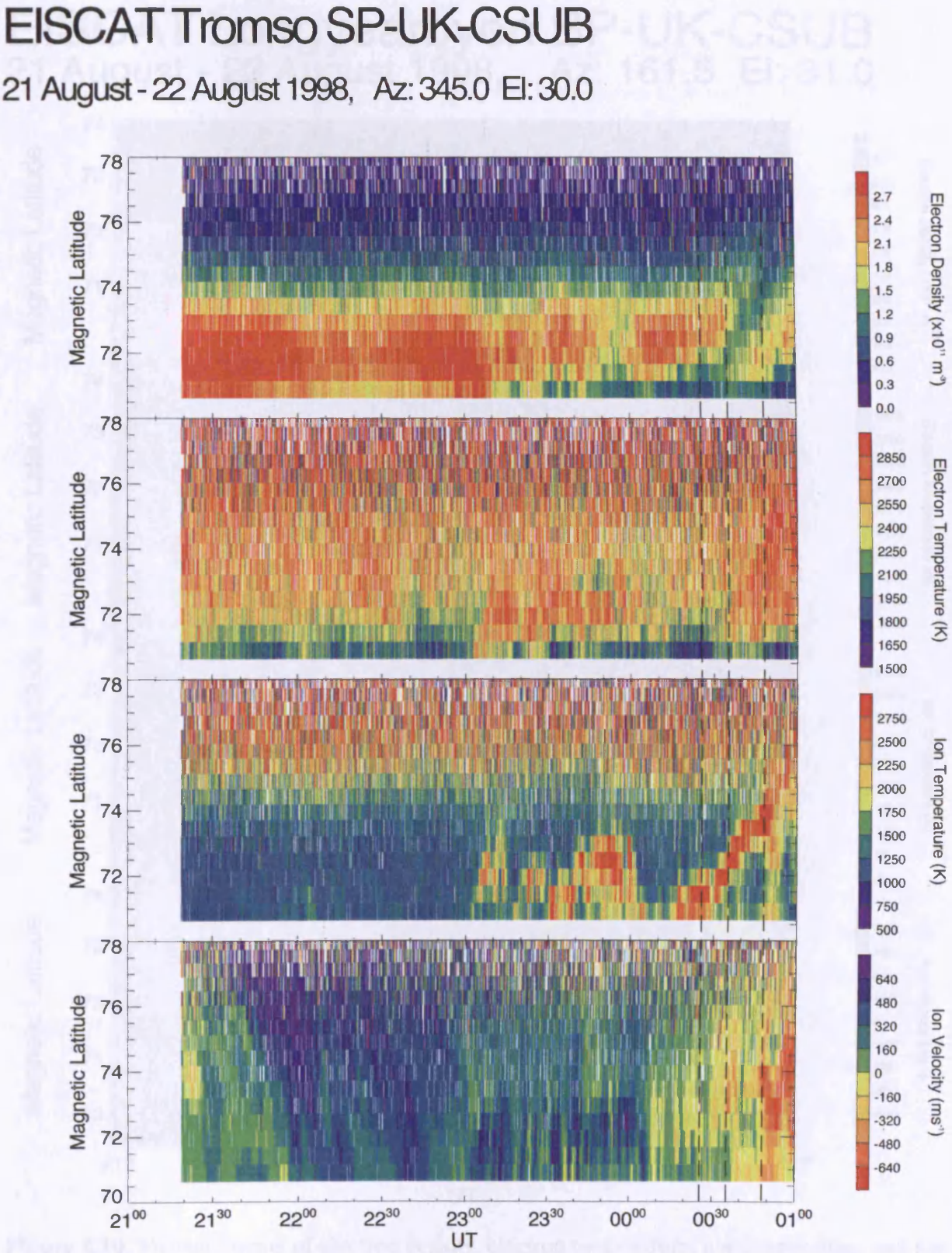

Figure 6.9. Measurements of electron density, electron temperature, ion temperature, and ion velocity made by the 345.0° azimuth beam of the EISCAT VHF radar, plotted as a function of magnetic latitude and universal time. *Dashed lines* indicate the CUTLASS Finland scan times referred to in the text.

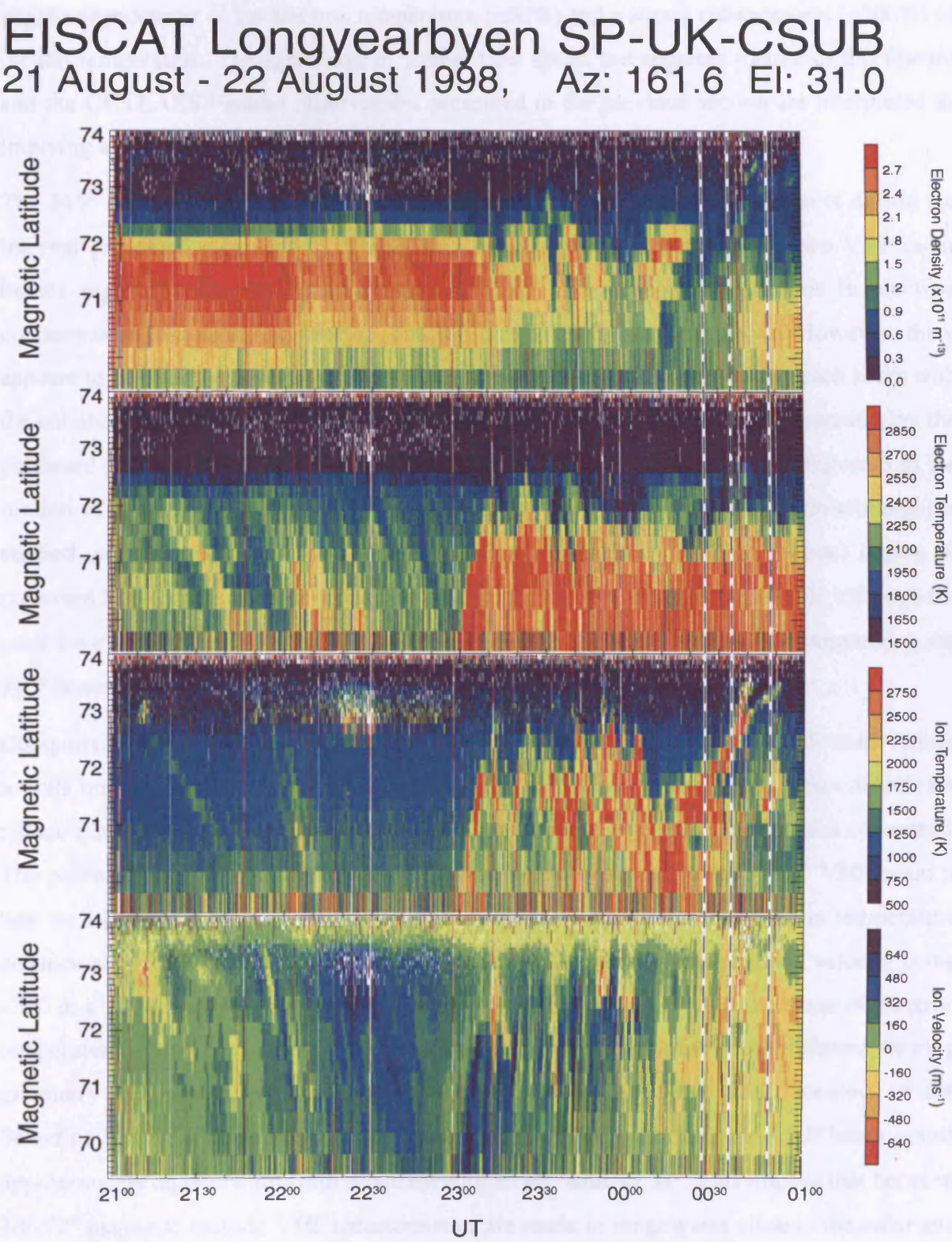

Figure 6.10. Measurements of electron density, electron temperature, ion temperature, and ion velocity made by the UHF EISCAT Svalbard radar (ESR), plotted as a function of magnetic latitude and universal time. In this figure, measurements of ion velocity have been reversed in order to present a colour-coding scheme consistent with other radar measurements. *Blue* represents flow away from the radar (approximately equatorward) and *red* indicates flow toward the radar (approximately poleward). *Dashed lines* indicate the CUTLASS Finland scan times referred to in the text.

slight enhancement of the electron temperature (~50%) and a strong enhancement (~300%) of the ion temperature. The agreement in timing, flow speed and apparent motion of this feature and the CUTLASS Finland observations presented in the previous section are interpreted as implying a simultaneous observation of a single ionospheric feature.

The 345° beam of the EISCAT VHF radar made almost identical measurements during the interval presented (Figure 6.9). There is excellent agreement between the two VHF radar beams regarding the timing and location of the enhancements/depletions in electron concentration, electron temperature, and ion temperature discussed above. However, there appears to be poor agreement between the determination of ion velocity along each beam with the enhancement being much less pronounced in the 345° beam. If instead of considering the poleward propagation of the highest velocity region (coloured bright red in Figure 6.8) the motion of the surrounding, albeit weaker, velocity enhancement (shaded yellow/orange) is studied, some agreement is apparent. In each case, a broad (~2° in latitude) region of poleward flow can be seen to propagate poleward over ~5° of magnetic latitude although the peak l-o-s velocity component is significantly elevated in the 359.5° beam compared to the 345° beam.

Comparison of the ESR data presented in Figure 6.10 with the EISCAT VHF observations reveals broad agreement between the ionospheric parameters under investigation despite the reduced latitudinal coverage and different viewing geometry of the instruments concerned. The poleward motion of the ion velocity enhancement observed in the 359.5° VHF beam is less well defined in the UHF data (Figure 6.10) although the associated ion temperature enhancement remains particularly striking, its apparent poleward propagation velocity being ~300 m s^{-1}. The apparent inconsistencies between UHF and VHF measurements of electron temperature during the interval presented may be explained in terms of the different viewing geometry of the two systems. Whilst the beams of the VHF radar, located on the Scandinavian mainland, point roughly poleward with 30° elevation, the UHF beam points approximately equatorward from Svalbard with an elevation of 31°. This implies that between 70°-72° magnetic latitude VHF measurements are made in range-gates close to the radar and at relatively low altitude (~300 km) whereas UHF measurements are drawn from distant range gates at high altitude (~850 km). Careful comparison of VHF and UHF electron concentration measurements reveals some similarity i.e. equatorward drifting features prior to 23:10 UT followed by generally enhanced electron temperature between 70°-72° although the

measured electron temperature differs significantly in each case due to variations of the measurement altitude.

6.3.5 Two-dimensional ionospheric flow measurements

In order to investigate the ionospheric flow development within the region of backscatter observed by the CUTLASS Finland radar, it is useful to study the series of 16-beam scans generated during the interval. Each scan yields information regarding the l-o-s Doppler velocity over the entire f-o-v of the radar with a temporal resolution ~1 min. Figure 6.11 presents three representative scans during the rapid poleward flow expansion observed in beam 9 of the radar between 00:30 UT-01:00 UT on 22nd August 1998. The timing of these scans has been indicated by dashed lines on Figures 6.7, 6.8, 6.9, and 6.10.

Ideally, simultaneous l-o-s velocity measurements from both radars of the CUTLASS pair would be combined to yield 2-dimensional ionospheric flow velocity measurements perpendicular to the magnetic field but such data are not available during this interval. Instead, estimates of the horizontal flow vector have been calculated using a *beamswinging* technique (Villain *et al.*, 1987; Ruohoniemi *et al.*, 1989). In the beamswinging process (Figure 6.12) it is assumed that there exists a flow component parallel ($V_{||}$) to lines of constant magnetic latitude (known as *L-shells*) that remains constant across the radar scan and that this flow contributes to the measured l-o-s velocity. Since the angle between the radar beam and the L-shell (θ) varies across the f-o-v of the radar, the contribution the L-shell aligned flow makes to the measured l-o-s velocity ($V_{L\text{-}O\text{-}S}$) will also vary across the f-o-v. In fact, a cosine relationship is expected between θ and the component of $V_{||}$ that contributes to $V_{L\text{-}O\text{-}S}$. By plotting θ as a function of $V_{L\text{-}O\text{-}S}$ and fitting a cosine curve to the resulting distribution it is possible to calculate the expected $V_{L\text{-}O\text{-}S}$ when $\theta = 0$, i.e. calculate $V_{||}$. Having arrived at a value for the L-shell aligned flow velocity, $V_{L\text{-}O\text{-}S}$ and $V_{||}$ are combined in order to obtain a 2-dimensional velocity vector.

Two-dimensional, beamswung vectors have been overlaid on the upper panel of each scan in Figure 6.11. Whilst this technique is very useful in cases where bistatic radar measurements are not available, it must be applied with some degree of care. Clearly, the assumption that $V_{||}$. remains constant across the entire f-o-v will not hold if there are deviations from an overall zonal flow with scale-size comparable to the f-o-v of the radar (Freeman *et al.*, 1991; Yeoman *et al.*, 1992). Also, since the estimation of $V_{||}$. relies upon the extrapolation of a

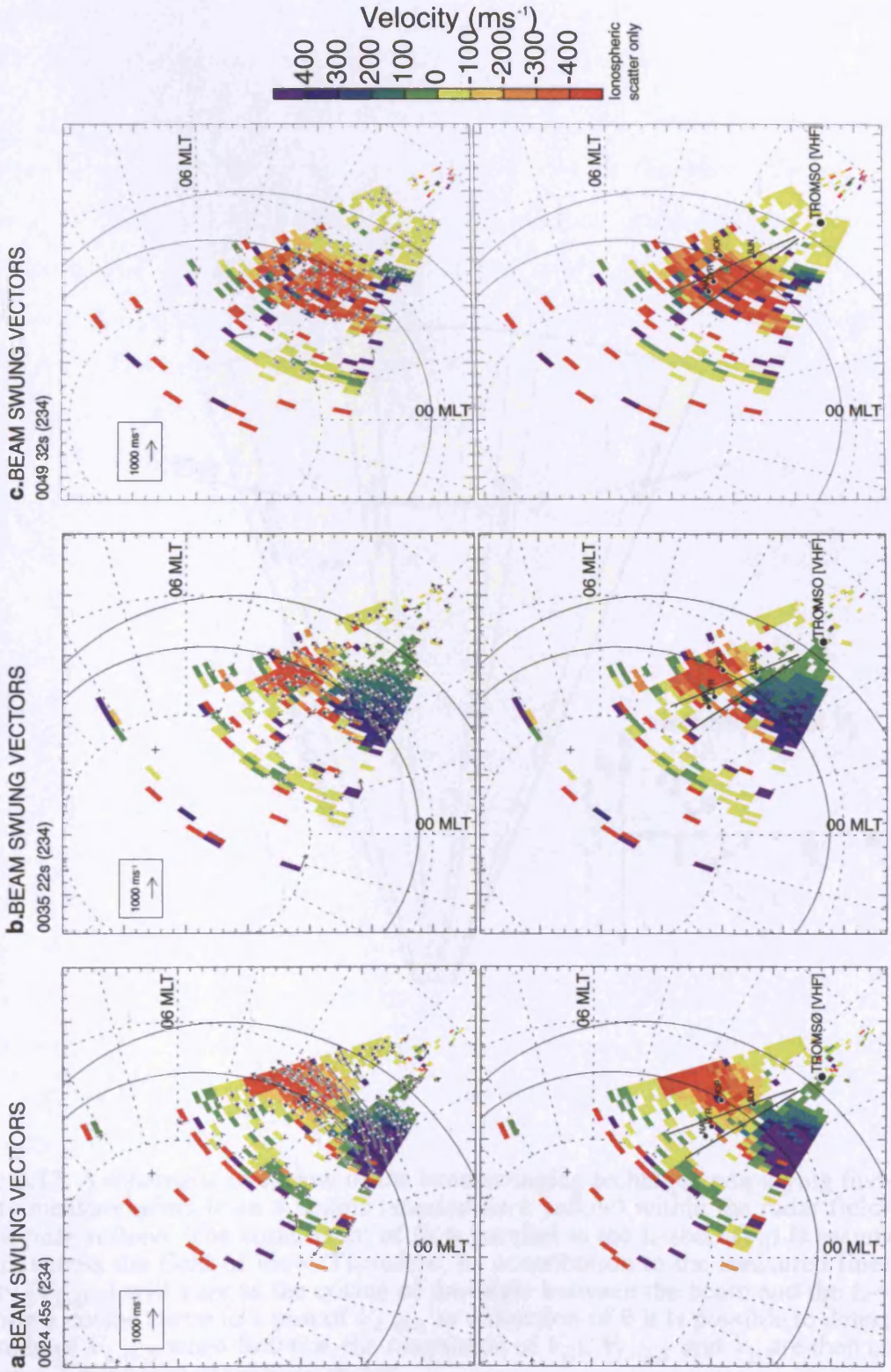

Figure 6.11. Polar projections of 16-beam line-of-sight Doppler velocity scans made by the CUTLASS Finland radar at (**a**) 00:24 UT,(**b**) 00:35 UT, and (**c**) 00:49 UT on 22nd August 1998 (velocity measurements are colour coded as in Figure 6.6). Concentric *dashed circles* represent lines of constant magnetic latitude at 10° increments. Radial dashed lines indicate 1-hour increments of magnetic local time with 00 MLT and 06 MLT labelled in each frame. The location of the geographic pole is indicated in each frame by a *small black cross.* Overlaid is the statistical location of the auroral oval for K_P=1+ (after Feldstein and Starkov, 1967). Beamswung velocity vectors (see text) are superimposed over l-o-s velocity measurements in the *upper frame* of each scan. The locations of the NAL, LYR, HOP, and BJN magnetometers (*black circles*) and both beams of the EISCAT VHF radar (*solid black lines*) are overlaid in the *lower frame* of each scan.

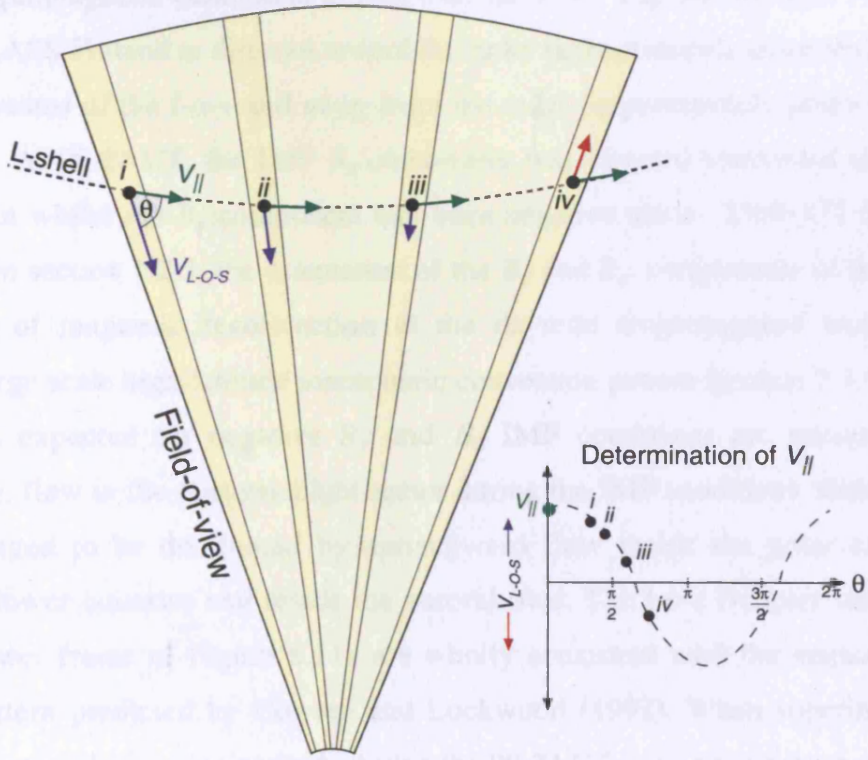

Figure 6.12. A schematic overview of the beamswinging technique employing line-of-sight velocity measurements from 4 beams (*shaded dark yellow*) within the radar field-of-view (*shaded pale yellow*). The component of flow parallel to the L-shell ($V_{||}$) is assumed to be constant across the field of view. Therefore, its contribution to the measured line-of-sight velocity ($V_{L\text{-}O\text{-}S}$) will vary as the cosine of the angle between the beam and the L-shell (θ). By fitting a cosine curve to a plot of $V_{L\text{-}O\text{-}S}$ as a function of θ it is possible to determine the magnitude of $V_{L\text{-}O\text{-}S}$ when θ=0 (i.e. the magnitude of $V_{||}$). $V_{L\text{-}O\text{-}S}$ and $V_{||}$ are then combined to obtain a 2-dimensional velocity vector.

fitted cosine function to observed l-o-s velocities, confidence in the accuracy of the estimated value of $V_{||}$ will increase given more measurements of $V_{L\text{-}O\text{-}S}$ and θ.

At 00:24 UT (Figure 6.11a), the CUTLASS Finland radar observed a broad band of backscatter between 67°-72° of magnetic latitude over all 16 beams corresponding to magnetic local times of ~01:30-04:30 MLT. This band of backscatter was predominantly located within the statistically averaged auroral oval (Feldstein and Starkov, 1967) appropriate to the geomagnetic conditions at that time (K_P=1+). The line-of-sight velocity measured by CUTLASS Finland in directed toward the radar (approximately equatorward) in the most westerly beams of the f-o-v and away from the radar (approximately poleward) in the easterly beams. At 00:24 UT, the IMF B_Z component was directed southward and had been so for ~30 min whilst the B_Y component had been negative since ~23:40 UT (Figure 6.5). As discussed in section 1.2.3, the orientation of the B_Y and B_Z. components of the IMF influence the rate of magnetic reconnection at the dayside magnetopause and, as a consequence, the large scale high-latitude ionospheric convection pattern (section 2.3.1). The high-latitude flows expected for negative B_Y and B_Z IMF conditions are presented in Figure 6.13. Clearly, flow in the post-midnight sector during the IMF conditions observed at 00:24 UT is envisaged to be dominated by antisunward flow inside the polar cap and dawnward flow at lower latitudes and inside the auroral oval. The l-o-s Doppler velocities presented in the lower frame of Figure 6.11a are wholly consistent with the azimuthally-dominated flow pattern predicted by Cowley and Lockwood (1992). When superimposed upon the measurements of l-o-s velocity made during the 00:24 UT scan, beamswung velocity vectors reveal the expected west-east zonal flow within and just poleward of the auroral oval. Furthermore, the beamswinging technique yields estimates of the zonal flow magnitude of approximately 800 m s^{-1}. At this time, the regions in which the strongest poleward l-o-s velocities are observed are located slightly dawnward of the ESR and EISCAT VHF 359.5° beams and the ground magnetometers indicated in Figure 6.11a.

By 00:35 UT (Figure 6.11b) the 359.5° beam of the EISCAT VHF radar has moved into the high poleward l-o-s velocity region located at ~03:30 MLT and observes poleward ion flows of ~800 m s^{-1} at 72.5° magnetic latitude. This region has by now begun its poleward motion, now extending to ~74° magnetic latitude within the CUTLASS Finland radar f-o-v, several degrees north of the expected poleward boundary of the auroral oval. Beamswung velocity vectors indicate a slight decrease in the zonal flow within the auroral oval with typical west-east velocities not exceeding ~500 m s^{-1}. In the region of backscatter extending poleward from

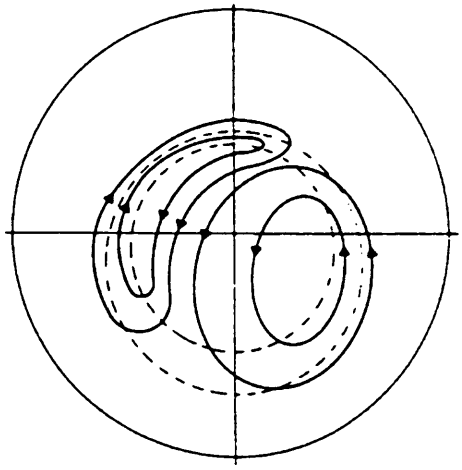

Figure 6.13. A schematic showing the form of the high latitude flows in the Northern hemisphere for IMF B_Y- B_Z- conditions. The figure presents flows as viewed from a position above the northern magnetic pole with the Sun located toward the top of the page. The predicted location of the auroral oval is indicated by *dashed lines* (from Cowley and Lockwood, 1992).

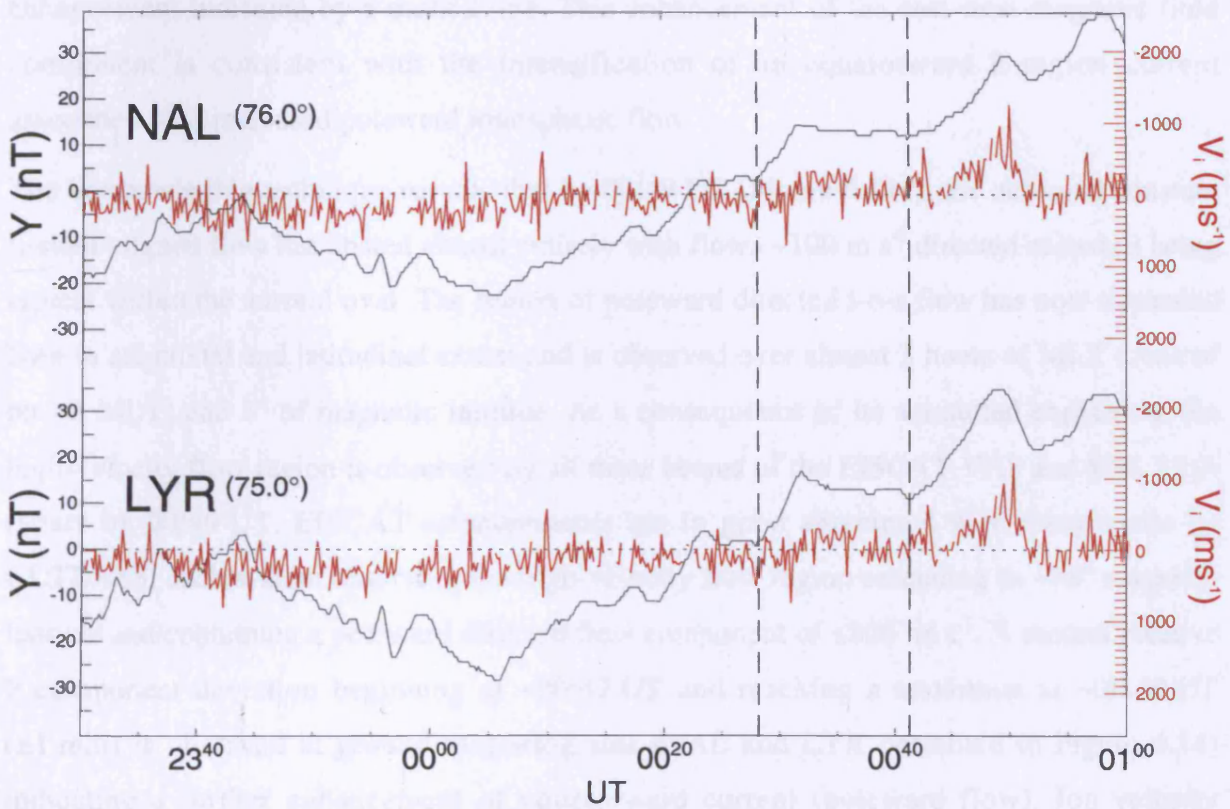

Figure 6.14. *Y* component magnetograms (*black traces*) from the IMAGE ground magnetometer stations NAL and LYR located at the magnetic latitudes indicated. Overlaid are measurements of ion velocity made by the 359.5° azimuth beam of the EISCAT VHF radar (*red traces*). Ion velocity measurements have been drawn from a range gate situated at 75.4° magnetic latitude. Velocity and magnetic field enhancements discussed in the text are indicated by *dashed lines*.

the auroral oval, beamswung vectors suggest that ionospheric flow is directed into the polar cap at ~45° to the local L-shell with flow velocity ~500 m s^{-1}. Whilst care must be taken not to ascribe total confidence in the derived beamswung vectors, it is clear that by 00:35 UT two distinct flow regimes have developed, one predominantly zonal in nature and another, located further dawnward and at higher latitudes, with a significant poleward component. This interpretation is supported by observations of near-simultaneous positive deviations (~20 nT) at ~00:28 UT in the *Y* component magnetograms from stations located poleward of the auroral oval. *Y* component magnetograms from NAL and LYR are presented in Figure 6.14 with the enhancement indicated by a dashed line. This enhancement of the east-west magnetic field component is consistent with the intensification of an equatorward E-region current associated with increased poleward ionospheric flow.

The beamswinging technique reveals that by 00:49 UT (Figure 6.11c), the assumed constant L-shell aligned flow has abated almost entirely with flows ~100 m s^{-1} directed eastward being typical within the auroral oval. The region of poleward directed l-o-s flow has now expanded both in azimuthal and latitudinal extent and is observed over almost 3 hours of MLT (centred on ~3 MLT) and 8° of magnetic latitude. As a consequence of its azimuthal expansion, the high-velocity flow region is observed by all three beams of the EISCAT VHF and ESR UHF radars by 00:49 UT. EISCAT measurements are in good agreement with those made by CUTLASS, each system observing the high-velocity flow region extending to ~78° magnetic latitude and containing a poleward directed flow component of ≤800 m s^{-1}. A second positive *Y* component deviation beginning at ~00:42 UT and reaching a maximum at ~00:49 UT (±1 min) is observed in ground magnetograms (NAL and LYR presented in Figure 6.14) indicating a further enhancement of equatorward current (poleward flow). Ion velocity measurements from the 359.5° azimuth beam of the EISCAT VHF radar are overlaid on Figure 6.14 in order to emphasise the good agreement between the magnetic field and ionospheric flow observations at 75° magnetic latitude (approximately midway between the two stations) during the 00:43 UT-00:49 UT magnetic field enhancement.

Over the following ~20 min, CUTLASS observations of the high-velocity flow region indicate a gradual decrease in poleward flow magnitude and spatial extent, with only a brief re-intensification of flow between 01:10 UT and 01:14 UT. By ~01:14 UT, the majority of ionospheric backscatter observed by the CUTLASS Finland radar is located with the statistical limits of the auroral oval.

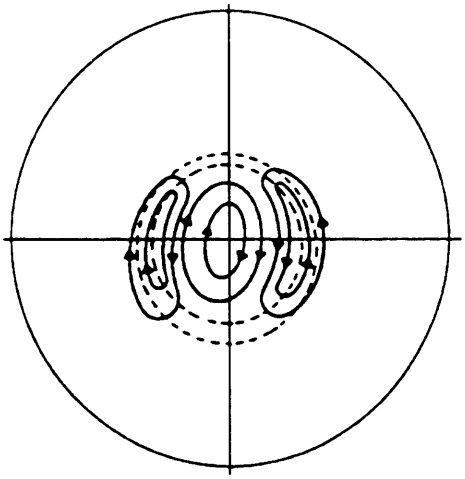

Figure 6.15. A schematic showing the form of the high latitude flows in the Northern hemisphere for IMF B_Y+ B_Z+ conditions. The figure presents flows as viewed from a position above the northern magnetic pole with the Sun located toward the top of the page. The predicted location of the auroral oval is indicated by *dashed lines* (from Cowley and Lockwood, 1992).

6.4 Discussion

Prior to 21:19 UT on 21st August 1998, the north/south component of the IMF had been oriented northward for approximately 20 hours. The reversal of the IMF B_Z component to negative values at 21:19 UT was accompanied by the near-simultaneous reversal of both the X and Y components to B_X- and B_Y- configuration indicated in Figure 6.5 (labelled ①). Growth phase characteristics are observed by the CUTLASS Finland radar at ~21:30 UT, presumably in response to the increased rate of reconnection at the dayside magnetopause. Onset of the subsequent expansion phase is observed at 22:50 UT by radars and ground magnetometers located in the Scandinavian sector. At 22:32 UT the B_X and B_Z components once again reverse (interval ②) for a period lasting ~22 min before returning to the previous IMF configuration at 23:54 UT (interval ③). The 22:32 UT realignment of the field is accompanied by a sharp reduction in the total magnetic field from ~6 nT to ~2 nT. During intervals ② and ③, the post-midnight ionospheric flow observed by the CUTLASS Finland radar is predominantly zonal and limited to the expected location of the auroral oval. In the final reconfiguration of this study, all three magnetic field components of the IMF undergo simultaneous reversal at 00:30 UT (interval ④). However, the observed development of a poleward-expanding region of poleward ionospheric flow is not consistent with the simple large-scale ionospheric flow pattern predicted by Cowley and Lockwood (1992) for positive B_Y and B_Z IMF components (Figure 6.15) suggesting that the observed flow region is due to some additional large-scale structure imposed upon the polar cap.

Whilst the previous section focussed on the development of the ionospheric flows observed by the CUTLASS and EISCAT radars, high-time resolution measurements of additional ionospheric parameters by the EISCAT radars yield further information regarding the nature of the structure under investigation. The 359.5° beam of the EISCAT VHF radar observed a strong (~300%) increase in ion temperature, co-located with the poleward propagating high-speed ion flow. This is indicative of ion frictional heating (e.g. Davies *et al.*, 1997; 1999), a consequence of the relative velocity between the ion and neutral populations in the F-region ionosphere. A similar enhancement of ion temperature was also observed by the EISCAT Svalbard UHF radar and the 345° beam of the mainland VHF radar even though these radars did not measure the highly enhanced velocity flow observed by the 359.5 beam of the VHF radar. Assuming that the F-region neutral particle population velocity remains approximately constant throughout the region of interest during the flow evolution described in the previous section, it is possible to interpret measurements of ion temperature as a proxy for ion flow speed. This suggests that all three radars beams observed the same high-speed ionospheric

flow region yet the viewing angle of each beam relative to the flow direction lead to quite different measurements of line-of-sight flow velocity.

The electron temperature enhancements (~50%) observed by the EISCAT VHF radar during the poleward motion of the high-speed flow region are comparable to those associated with the equatorward drifting arcs observed earlier in the interval (e.g. ~21:40 UT and ~22:10 UT in 359.5°beam). Elevated electron temperature is usually an indicator of energetic particle precipitation (section 1.3.3) suggesting that the poleward moving velocity feature observed during this interval may be associated with an auroral arc of some kind. It might naïvely be expected that an increase in electron precipitation would result in an enhancement of the electron concentration in the precipitation region, yet all three EISCAT beams observed a marked reduction in electron concentration during the poleward motion of the high-speed flow region. However, the elevation of ion temperature via the ion frictional heating effect discussed above results an increase in the recombination rate between ions and electrons leading to the observed reduction in the electron concentration (e.g. Lewis *et al.*, 1994).

These observations are consistent with the relative motion of an auroral arc into the beam of the EISCAT radar (Lewis *et al.*, 1994, Fox *et al.*, 2000). Observations of strong flows and reduced electron concentration are indicative of the strong electric fields often observed at the boundary of an auroral arc (Opgenoorth *et al.*, 1990) and these are associated with the observation of a region of enhanced electron temperature, suggesting increased electron precipitation within the arc.

Observations of arcs extending into the polar cap, have been reported previously during periods of IMF B_Z positive similar to those observed after 00:30 UT on 22nd August1998 (e.g. Gussenhoven, 1982; Carlson, 1994). Milan *et al.*, (1997) presented a study in which optical and coherent HF radar observations were compared in order to investigate the evolution of a post-midnight auroral structure that extended poleward from the auroral oval. Milan and co-authors suggested that the observed arc structure was similar to either *horse-collar* or *theta aurora*, both of which are common during B_Z positive conditions. As discussed in section 6.1, theta aurorae (Frank *et al.*, 1986) are a form of sun-aligned, transpolar arcs that extend continuously from the dayside to nightside sectors of the auroral oval. However the spatial extent of the observations presented here are insufficient to unambiguously identify the feature as a theta aurora. Observations of a polar arc extending from the dawn-sector auroral oval are also consistent with the development of the horse-collar auroral configuration discussed in section 6.1 (Figure 6.16a). This auroral form is most commonly observed in the

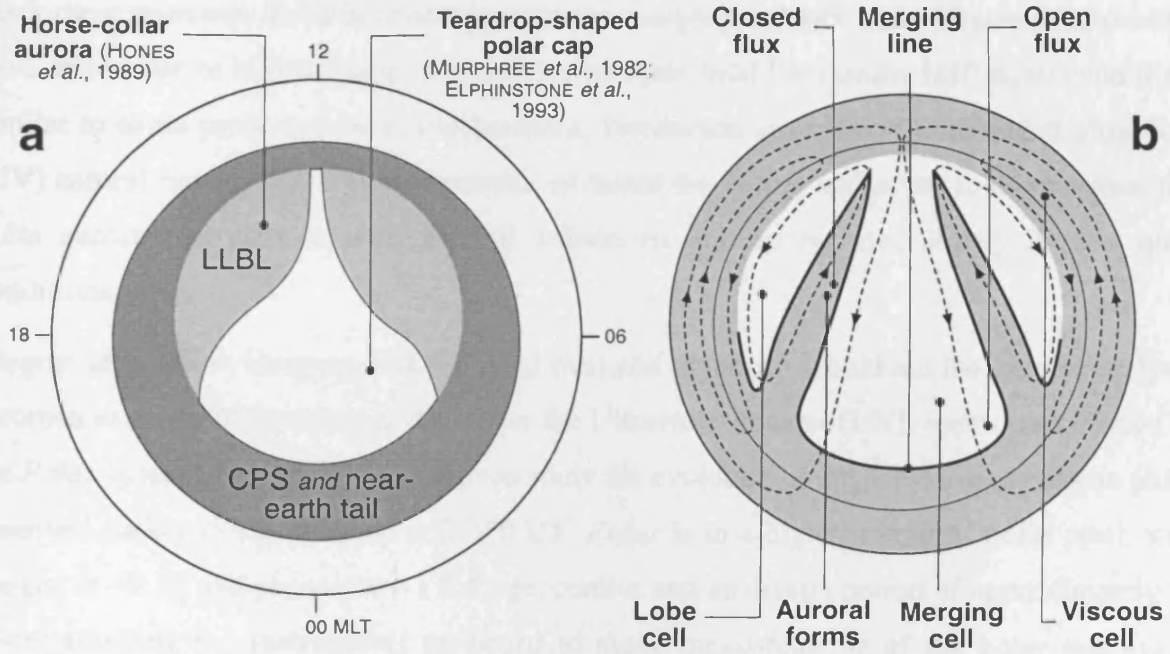

Figure 6.16. a The teardrop-shaped polar cap (Elphinstone *et al.,* 1993) and horse-collar auroral configuration (Hones *et al.,* 1989) proposed for northward IMF conditions; **b** The open and closed field regions (Henderson *et al.,* 1996) and the associated convection flow (Burch *et al.,* 1992) proposed for northward IMF conditions. Tongues of closed flux extending across the polar cap are associated with convection reversals and hence polar cap aurora (from Milan *et al.,* 1997).

northern hemisphere during intervals of $B_X > 0$ nT and B_Y, $B_Z \geq 0$ nT IMF conditions. Although, during the interval presented both B_Y and B_Z remain positive after the 00:30 UT IMF reorientation (Figure 6.5), B_X is small (~2 nT) and does not exceed 0 nT until 00:49 UT. The location of the dawn sector arc presented here is at odds with the expected location in the dusk sector for a single, transpolar arc during IMF $B_Y > 0$ conditions (Elphinstone *et al.*, 1990). However, the observation of an arc in the dawn sector is consistent with expected location of the dawn sector element of a horse-collar aurora.

Burch *et al.* (1992) and Henderson *et al.* (1996) have proposed that polar arcs and theta aurora mark the convection reversal boundary between merging and lobe cells (Figure 6.16b) which have arisen due to high-latitude reconnection of open field lines under IMF $B_Z > 0$ conditions, similar to those presented here. Furthermore, Henderson *et al.* (1996) employed ultraviolet (UV) auroral images taken by instruments on-board the *Viking* spacecraft to demonstrate that theta aurora can coexist with auroral substorms and so not necessarily require quiet conditions.

Clearly, large-scale imaging of the auroral oval and polar cap would aid the current analysis. Yeoman *et al.* (2000) employed data from the Ultraviolet Imager (UVI) instrument carried by the *Polar* spacecraft (Torr *et al.*, 1995) to study the evolution of the substorm expansion phase observed earlier in this interval at 22:50 UT. *Polar* is in a highly elliptical polar orbit, with apogee at ~9 R_E and perigee at ~1.8 R_E geocentric and an orbital period of approximately 18 hours allowing the instruments on-board to make measurements of the polar regions of geospace from both high- and low-altitude perspectives. However, by 00:30 UT on 22nd August the high-latitude region of interest in this study was no longer within the f-o-v of the UVI instrument. The Visible Imaging System (VIS) Earth camera (Frank *et al.*, 1995), also on-board the *Polar* spacecraft, records images of the UV aurora (wavelengths 124-149 nm) over a significantly larger field of view but at a reduced spatial resolution (~80x80 km at spacecraft apogee). Figure 6.17 presents such a VIS UV image acquired over a 12 second integration period beginning at 00:44:58 UT on 22nd August. This image is derived from preliminary data and has yet to be processed in order to remove any distortions caused by unintentional motion of the spacecraft over the integration period (i.e. spacecraft wobble). From this preliminary image, there is the suggestion of a region of enhanced UV emission poleward of the main auroral oval in the 03-06 MLT region. However, quantitative analysis of any structure within the UV emission is impossible until the requested validated data are made available.

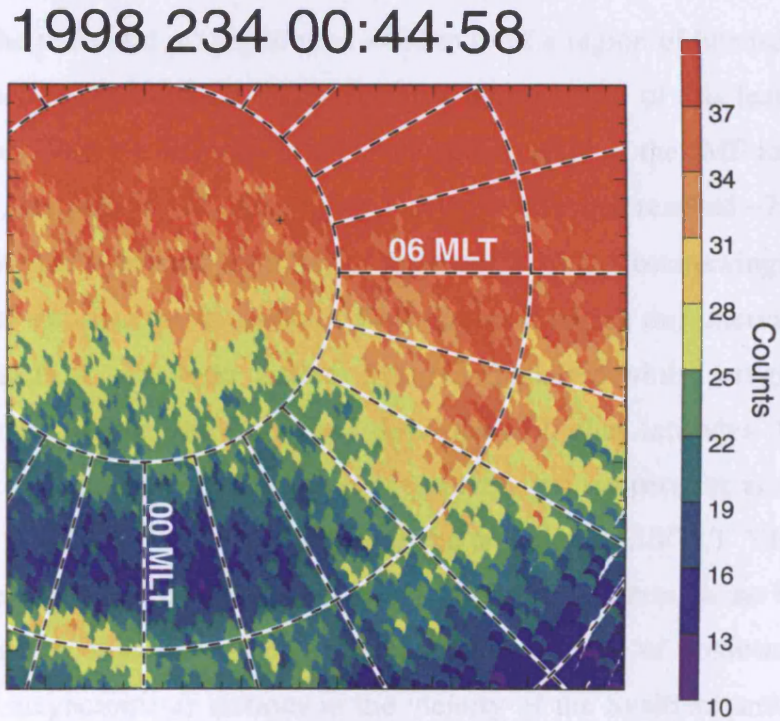

Figure 6.17. An image of the UV aurora taken by the VIS Earth Camera on board the *Polar* spacecraft from an altitude of ~3 R_E above the surface of the Earth at 00:44 58s on 22nd August 1998. The data are colour coded such that red indicated the areas of brightest UV emission and blue represents the faintest. Overlaid are lines of constant magnetic latitude at 10° intervals and magnetic local time meridians at 1 hour intervals. The nightside auroral oval is clearly visible in the lower left-hand corner of the image, extending in MLT toward the dawn terminator. Dayside solar illumination dominates at MLTs later than ~6 MLT. The feature of interest is centred on ~72° magnetic latitude and 04:30 MLT.

6.5 Summary

In this chapter, observations of high-latitude ionospheric flow during the recovery phase of an isolated magnetospheric substorm have been presented. This interval is of particular interest due to the favourable level of instrumental coverage, with observations being drawn from four radars and several ground magnetometers in the Scandinavian sector. Observations of mid-latitude Pi2 pulsations indicated expansion phase onset at ~22:50 UT with the associated magnetic disturbances reaching ~73° magnetic latitude by 23:18 UT. Beginning at ~00:30 UT, some 100 min after expansion phase onset, the CUTLASS Finland HF radar observed the poleward propagation at ~400 m s^{-1} of a region of intense (~800 m s^{-1}) poleward flow located at 03:30-04:00 MLT. The first observations of this feature occurred almost simultaneously with the reversal of all three components of the IMF to $B_X<0$, $B_Y>0$, and $B_Z>0$ conditions. By ~00:50 UT, this region of intense flow had reached ~78°, extending approximately 5° from the poleward boundary of the auroral oval. A beamswinging technique has been employed to estimate the ionospheric flow direction during this interval and reveals that the overall zonal flow within the auroral oval is suppressed whilst a region of strong (~500 m s^{-1}) flow directed into the polar cap develops at higher latitudes. Simultaneous observations of electron temperature, electron concentration, ion temperature and ion velocity made by the UHF EISCAT Svalbard radar and the mainland EISCAT VHF radar are consistent with those expected due to the passage of an auroral arc through the beam of each radar suggesting that the observations presented are of some type of poleward expanding auroral arc. Ground magnetometer stations in the vicinity of the Svalbard archipelago also observed indications of several intensifications of poleward directed ionospheric flow during the observed poleward motion. At its maximum extent, the poleward backscatter prominence extended to ~78° magnetic latitude and encompassed approximately 3 hours of magnetic local time.

These observations have been interpreted as consistent with the development of a polar arc, possibly either the horse-collar or theta aurora configuration during the recovery phase of the earlier substorm. These types of aurora are often observed during $B_Z>0$ conditions although there is debate over whether or not they are "quiet-time" features of the polar cap with some authors reporting their coexistence with classical auroral substorm phenomena. The confident identification of the feature observed during this interval as either of these auroral types would lend weight to the notion that polar arcs do not require quiet magnetic conditions in order to develop. Since the observations presented were made during the arctic summer, verification by ground-based optical observations will not be possible. However, large-scale

imaging of auroral UV emission may prove useful. Indeed, preliminary UV observations made by the VIS Earth Camera on-board the *Polar* spacecraft hint at some auroral structure extending poleward from the main auroral oval although conclusive identification of the observed structure will only be possible upon the delivery of verified data.

CHAPTER 7

Summary and suggestions for further work

7.1 Summary

Far from being an empty void, interplanetary space is filled with the remnants of the solar atmosphere, expelled from the Sun as a consequence of the colossal temperatures and magnetic fields within. As the solar wind flows out from the sun, carrying with it the interplanetary magnetic field, the Earth's magnetic field behaves as an obstacle around which the solar wind must flow. The Earth's magnetic field defines a cavity in the solar wind known as the magnetosphere and existing within this cavity is a complex system of plasma flows, currents and electric fields. Solar radiation falling upon the Earth leads to the partial ionisation of the atmosphere forming the ionosphere. The ionosphere is sufficiently conductive to support electrical current systems driven by the magnetosphere. Consequently, magnetosphere-ionosphere interactions result in both large- and small-scale phenomena in the Earth's ionosphere.

The mapping of magnetospheric structures to their footprints in the ionosphere presents us with the opportunity to derive information regarding magnetospheric processes from observations of ionospheric phenomena. Whilst spacecraft are able to provide excellent *in-situ* observations of the magnetosphere, they are widely dispersed and introduce many spatial/temporal ambiguities. By employing the wealth of ground-instruments currently available to study ionospheric features it is possible infer information regarding the structure and evolution of the magnetosphere on a routine basis. Each instrumental technique employed in this thesis has its own particular strengths and weaknesses. Whilst HF and VHF coherent-scatter radars such as CUTLASS and STARE provide routine measurements of the ionospheric drift velocity over a large area, they reveal no information regarding ionospheric composition. The EISCAT incoherent-scatter radars are able to characterise the ionosphere in much detail greater, each measuring many parameters, but the fields-of-view of such systems are significantly smaller than those of coherent-scatter radars. Chapters 4, 5, and 6 of this thesis present intervals during which simultaneous measurements drawn from ground magnetometers, instruments carried on spacecraft, coherent- and incoherent-scatter radars are synthesised to yield a comprehensive overview of the prevailing ionospheric conditions.

7.1.1 Azimuthally propagating vortical currents

High-time resolution CUTLASS observations and magnetic field measurements from ground-based magnetometers have been employed to study the occurrence of vortical flow structures propagating through the high latitude ionosphere during magnetospheric substorms. The fast-moving flow vortices (~800 m s^{-1}) have been interpreted as the signatures of vortical Hall currents flowing around upward directed field-aligned currents. The vortices are frequently observed propagating at high speed (~1 km s^{-1}) in an azimuthal direction, away from the region of the ionosphere associated with the location of the substorm expansion phase onset. Generally, flow vortices in the post-midnight (pre-midnight) sector usually propagate in an eastward (westward), although no relationship between propagation velocity and APVC separation from onset was apparent.

A statistical analysis drawn from over 1000 hours of high-time resolution nightside radar data has enabled the characterisation of the bulk properties of these vortical flow systems. Azimuthally Propagating Current Vortices (APVCs) generally propagate in the azimuthal direction at ~800 m s^{-1} at an average magnetic latitude ~65.5°. The vortices have scale sizes of ~300 km in the latitudinal direction, ~400 km in the longitudinal direction and typically contain ionospheric flows ~900 m s^{-1} although flows as high as 2000 m s^{-1} have been observed. APVCs are most commonly observed between 30-60 minutes after a substorm expansion phase onset/intensification, with only one instance of an APVC being observed in a quiet period preceding a substorm. The inferred occurrence rate of APVCs of ~1 per day is approximately one-quarter that of substorms (Borovsky *et al.*, 1993) although their rapid motion through the field-of-view of the CUTLASS radars implies that unless non-standard high-time resolution modes are implemented, the observation rate with these instruments will be significantly less.

7.1.2 Auroral omega bands

High-time resolution data from the CUTLASS Finland radar during the interval 01:30-03:30 UT on 11th May 1998 have been employed to characterise the ionospheric electric field due to a series of auroral omega bands extending ~5° in latitude at a resolution of 45 km in the meridional direction and ~50 km in the azimuthal direction. E-region observations from the STARE Norway VHF radar operating at a resolution of 15 km over a comparable region are also incorporated. These data have been combined with ground magnetometer observations from stations distributed over approximately 5 hours of magnetic

local time. This has enabled the investigation of the ionospheric equivalent current signatures and height integrated ionospheric conductances associated with omega bands as they passed through the fields-of-view of the CUTLASS and STARE radars. The omega bands observed during this interval have scale sizes ~500 km and an eastward propagation velocity ~0.75 km s^{-1} and are associated with characteristic Ps6 magnetic pulsations.

Omega bands are generally accepted to be a recovery phase phenomenon, usually observed in the morning sector at ~5 MLT and this is the case during the interval presented. However, the omega bands observed during this interval occur simultaneously with the onset/intensification of a substorm in the midnight sector. Pellinen *et al.* (1992) also discussed the possibility that auroral omega bands are not simply recovery phase structures, but the result of some process that requires an onset/intensification during recovery phase of an earlier substorm. The observations presented in Chapter 5 support this concept in that the omega bands are formed in the Scandinavian (morning) sector as a result of the new substorm onset in the midnight sector and have not been created in the midnight sector and subsequently drifted toward dawn.

The high-time resolution and multi-point nature of the observations has lead to an amendment of the previous models of omega band structure based upon the case study presented. It is also submitted that the observed structures are consistent with omega band formation due to a Kelvin-Helmholtz instability near or at the poleward boundary of the auroral oval and not the interchange instability as proposed by some authors (e.g. Yamamoto *et al.*, 1993; 1997).

7.1.3 High-latitude arc evolution

Multi-instrument observations of the evolution of a region high-latitude ionospheric flow during the recovery phase of an isolated magnetospheric substorm have been presented. Some 100 min after expansion phase onset, the CUTLASS Finland HF radar observed the poleward propagation at ~400 m s^{-1} of a region of intense (~800 m s^{-1}) poleward flow located at 03:30-04:00 MLT. The first observations of this feature occurred almost simultaneously with the reversal of all three components of the IMF to $B_X<0$, $B_Y>0$, and $B_Z>0$ conditions. Approximately 20 min later this region of intense flow had reached ~78°, extending approximately 5° from the poleward boundary of the auroral oval. By employing a beamswinging technique, the ionospheric flow direction during this interval has been estimated and reveals that the overall zonal flow within the auroral oval was suppressed whilst a region of strong (~500 m s^{-1}) flow directed into the polar cap developed at higher

latitudes. Simultaneous measurements of ionospheric parameters by the UHF EISCAT Svalbard radar and the mainland EISCAT VHF radar are consistent with those expected due to the passage of an auroral arc through the beams of each radar suggesting that the observations presented are of a poleward expanding auroral arc. Ground magnetometer stations in the vicinity of the Svalbard archipelago also observed indications of several intensifications of poleward directed ionospheric flow during the poleward motion of the arc which, at its maximum extent, extended to ~78° magnetic latitude and encompassed ~3 h of MLT. The observations presented have been interpreted as consistent with either the horse-collar or theta aurora configuration, superimposed upon the pre-existing auroral oval during the substorm recovery phase. These types of aurora are often observed during $B_Z>0$ conditions although it is not clear whether or not they are "quiet-time" features of the polar cap with some authors reporting their coexistence with classical auroral substorm phenomena (Henderson *et al.*, 1996).

7.2 Suggestions for future work

APVCs exhibit many characteristics similar to the ionospheric twin-vortex signature associated with flux transfer events at the dayside magnetopause (Lockwood *et al.*, 1990). This raises the possibility that nightside APVCs may be the ionospheric signatures of transient reconnection in the tail. Indeed, Yeoman *et al.* (1998) and Nakamura *et al.* (1999) have reported observations of deceleration and azimuthal diversion of bursty bulk flows (BBFs) in the tail, and in the case reported by Yeoman and co-authors, these observations occurred simultaneously with observations of APVCs in the nightside ionosphere. By studying *in-situ* measurements of flows in the magnetotail from spacecraft such as *Geotail* during intervals in which APVCs have been observed it should be possible to further examine the relationship between BBFs and the features observed by the CUTLASS radars. Special non-standard radar modes designed to run in conjunction with the recently launched *Cluster II* mission should allow much improved co-ordinated ionospheric/magnetospheric observations. *Cluster II*, which comprises four identical spacecraft orbiting in a tetrahedral configuration, is designed to make *in-situ* observations of the magnetosphere without the spatial/temporal ambiguities that are inherent in single-spacecraft observations. In addition, the routine operation of the CUTLASS radars (a fraction of which will be implementing high-time resolution modes) implies that the statistical dataset of APVC observations should, by now, have increased in size by approximately one-half. It is hoped that examination of CUTLASS data collected since August 1998 will allow the more accurate characterisation of APVCs and

their occurrence in relation to substorm phase. Of course, by including observations from the entire SuperDARN network, in both hemispheres, this dataset could be expanded even further. Lyons *et al.* (1999) have reported optical observations of intensifications at the poleward boundary of the aurora with similar occurrence rates in relation to substorms as APVCs and has also associated these features with bursty bulk flows. Therefore, co-ordinated high-time resolution HF radar and optical observations are desired so as to identify the auroral structure that the upward FACs associated with APVCs are expected to create and compare them with the features observed by Lyons and co-workers.

Having identified the signature of auroral omega bands in HF radar observations of l-o-s Doppler velocity it should now be possible to identify further examples the phenomenon in the 5 years of data collected since CUTLASS began routine operations. Having established a catalogue of examples it would then be possible to investigate the relationship between omega band occurrence and substorm phase. This would allow the proposed link between morning sector omega bands and the onset of a magnetospheric substorm during the recovery phase of a previous substorm, reported by Pellinen *et al.* (1992) and observed during the interval presented, to be examined. Also, *in-situ* observations of the magnetosphere by instruments carried on spacecraft should reveal much regarding the mechanism by which omega bands are generated.

The confident identification of the feature observed during the interval presented in Chapter 6 as either the horse-collar or theta type of aurora would support the argument that polar arcs do not require quiet magnetic conditions in order to fully develop. Optical observations are not available since the interval presented occurred during the arctic summer therefore optical verification of auroral distribution will not be possible. Alternatively, large-scale imaging of auroral UV emission from Earth orbit could prove invaluable, indeed the preliminary UV images from the VIS Earth Camera on-board the *Polar* spacecraft hint at some auroral structure extending poleward from the main auroral oval. It is hoped that conclusive identification of the observed structure will be possible upon the delivery of verified data. Such consistency between the observations of an auroral feature by 3 radar systems (comprising 19 beam directions) is unusual in itself and the radar data contain much valuable information regarding the structure and processes within the arc. By studying the width of the backscatter spectra measured by the CUTLASS radar and comparing this with incoherent-scatter observations of electron temperature it should be possible to further study precipitation feature within the observed arc structure in fashion similar to Milan *et al.* (1999). Further co-ordinated nighttime radar/optical observations would allow a more detailed

characterisation of the ionospheric flow within the region of auroral emission and also may reveal just how typical the example observed during the interval presented actually is.

APPENDIX A

Locations of SuperDARN radars

Name	Location	Geographic coordinates		Institution
		Lat (°N)	Lon (°E)	
Saskatoon	Canada	52.16	-106.53	Univ. of Saskatchewan (Can)
Kapuskasing	Canada	49.39	-82.32	JHU/APL (USA)
Goose Bay	Canada	53.32	-60.46	JHU/APL (USA)
Stokkseyri	Iceland	63.86	-22.02	CNRS/LPCE (France)
Þykkvibær*	Iceland	63.77	-20.54	Univ. of Leicester (UK)
Hankasalmi**	Finland	62.32	26.61	Univ. of Leicester (UK)
Prince George	Canada	53.98	-122.59	Univ. of Saskatchewan (Can)
Kodiak	Alaska	57.60	-152.20	Geophysical Institute, UAF (USA)
King Salmon	Alaska	57.0	-157.0	CRL (Japan)
Halley	Antarctica	-75.52	-26.63	BAS (UK)
SANAE	Antarctica	-71.68	-2.85	Univ. of Natal (S. Africa)
Syowa South	Antarctica	-69.00	39.58	NIPR (Japan)
Syowa East	Antarctica	-69.01	39.61	NIPR (Japan)
TIGER	Tasmania	-43.38	147.23	La Trobe Univ. (Aus)
Kerguelen	Kerguelen	-49.35	70.26	CNRS/LPCE (France)

**CUTLASS Iceland and ** CUTLASS Finland. Radars not yet in operation are indicated in pale type.*

APPENDIX B

Ground magnetometer locations

B.1 Greenland coastal magnetometers

Station Name	Station Code	Geographic		Geomagnetic	
		Lat. (°)	Lon. (°)	Lat. (°)	Lon. (°)
Nord	NRD	81.60	343.33	80.93	105.80
Danmarkshavn	DMH	76.77	341.37	77.24	87.10
Qaanaaq (Thule)	THL	77.47	290.77	85.39	33.51
Savissivik	SVS	76.02	294.90	83.64	35.91
Kullorsuaq	KUV	74.57	302.82	81.22	44.51
Daneborg	DNB	74.30	339.78	75.16	80.47
Upernavik	UPN	72.78	303.85	79.49	42.02
Uummannaq (Umanaq)	UMQ	70.68	307.87	76.90	43.93
Ittoqqortoormiit (Scoresbysund)	SCO	70.48	338.03	71.60	73.23
Qeqertarsuaq (Godhavn)	GDH	69.25	306.47	75.80	40.39
Attu	ATU	67.93	306.43	74.56	39.00
Kangerlussuaq (Sondre Stromfjord)	STF	67.02	309.28	73.16	41.74
Tasiilaq (Ammassalik)	AMK	65.60	322.37	69.29	54.63
Maniilsoq (Sukkertoppen)	SKT	65.42	307.10	71.99	37.97
Nuuk (Godthab)	GHB	64.17	308.27	70.56	38.53
Paamiut (Frederikshab)	FHB	62.00	310.32	68.01	39.65
Narsaruaq	NAQ	61.16	314.56	66.29	43.89

Names contained within brackets indicate alternative or former names. The geomagnetic station locations are presented here in Corrected Geomagnetic Co-ordinates (CGM) at the Earth's surface (altitude 0 km) and Epoch 1999.0. The Greenland magnetometer chain is deployed and operated by the Danish Meteorological Institute (DMI). The author thanks Dr. Jurgen Watermann for the Greenland magnetometer data included this thesis.

B.2 International Monitor for Auroral Geomagnetic Effects (IMAGE) magnetometers

Station Name	Station Code	Geographic		Geomagnetic	
		Lat. (°)	Lon. (°)	Lat. (°)	Lon. (°)
Ny Ålesund	NAL	78.92	11.95	76.07	112.25
Longyearbyen	LYR	78.20	15.82	75.12	113.00
Hornsund	HOR	77.00	15.60	74.02	110.48
Hopen Island	HOR	76.51	25.01	72.93	115.91
Bear Island	BJN	74.50	19.20	71.33	108.73
Sørøya	SOR	70.54	22.22	67.24	106.71
Alta	ALT	69.86	22.96	66.57	106.85
Kevo	KEV	69.76	27.01	66.21	109.73
Tromsø	TRO	69.66	18.94	66.54	103.44
Masi	MAS	69.46	23.70	66.07	106.92
Andenes	AND	69.30	16.03	66.36	100.92
Kilpisjärvi	KIL	69.02	20.79	65.78	104.31
Kautokeino	KAU	69.02	23.05	65.74	106.23
Abisko	ABK	68.35	18.82	65.21	102.27
Muonio	MUO	68.02	23.53	64.62	105.70
Lovozero	LOZ	67.97	35.08	64.10	114.89
Kiruna	KIR	67.84	20.42	64.60	103.14
Sodankylä	SOD	67.37	26.63	63.82	107.71
Pello	PEL	66.90	24.08	63.46	105.38
Rørvik	RVK	64.94	10.98	62.18	93.81
Lycksele	LYC	64.61	18.75	61.36	99.73
Oulujärvi	OUL	64.52	27.23	60.89	106.54
Hankasalmi	HAN	62.30	26.65	58.62	104.99
Nurmijärvi	NUR	60.50	24.65	56.81	102.54

Uppsala	UPS	59.90	17.35	56.45	96.22

The geomagnetic station locations are presented here in Corrected Geomagnetic Co-ordinates (CGM) at the Earth's surface (altitude 0 km) and Epoch 1998.0. The IMAGE magnetometer data are collected as a Finnish - German - Norwegian - Polish - Russian - Swedish project and distributed by the Finnish Meteorological Institute.

B.3 National Institute for Polar Research (NIPR) magnetometers

Station Name	Station Code	Geographic		Geomagnetic	
		Lat. (°)	Lon. (°)	Lat. (°)	Lon. (°)
Tjornes	TJO	66.20	342.88	66.69	73.12
Isafjördur	ISA	66.08	336.87	67.51	68.12
Husafell	HUS	64.67	338.97	65.69	68.74

The geomagnetic station locations are presented here in Corrected Geomagnetic Co-ordinates (CGM) at the Earth's surface (altitude 0 km) and Epoch 1998.0. The author thanks Akira Kadokura of the National Institute for Polar Research (NIPR) for Iceland magnetometer data included in this thesis.

B.4 UK Sub-Auroral Magnetometer Network (SAMNET) magnetometers

Station Name	Station Code	Geographic		Geomagnetic	
		Lat. (°)	Lon. (°)	Lat. (°)	Lon. (°)
Faroes	FAR	62.05	352.98	60.76	78.10
Nordli	NOR	64.37	13.36	61.43	95.49
Oulu	OUL	65.10	25.85	61.52	105.94
Hankasalmi	HAN	62.30	26.65	58.60	105.18
Glenmore	GML	57.16	356.32	54.91	78.22
Kvistaberg	KVI	59.50	17.63	56.00	96.45
Nurmijärvi	NUR	60.51	24.66	56.80	102.74
York	YOR	53.95	358.95	50.93	79.00
Hella	HLL	63.77	339.44	64.49	68.36
Kilpisjärvi	KIL	69.02	20.79	65.77	104.54

The geomagnetic station locations are presented here in Corrected Geomagnetic Co-ordinates (CGM) at the Earth's surface (altitude 120 km) and Epoch 1998.0. The author thanks Dr I.R. Mann and Dr D.K. Milling for

the SAMNET data. SAMNET is a PPARC National Facility deployed and operated by the University of York (UK).

B.5 Tromsø Auroral Observatory magnetometers

Station Name	Station Code	Geographic		Geomagnetic	
		Lat. (°)	Lon. (°)	Lat. (°)	Lon. (°)
Jan Mayen	JAN	70.09	351.30	69.59	83.42

Although the Tromsø Auroral Observatory operate many magnetometers in the Scandinavian sector, only data from the Jan Mayen station have been included in this thesis. The geomagnetic station location is presented here in Corrected Geomagnetic Co-ordinates (CGM) at the Earth's surface (altitude 0 km) and Epoch 1998.0. The author thanks Børre Holmeslet of the Tromsø Auroral Observatory for the Jan Mayen magnetometer data included in this thesis.

APPENDIX C

List of acronyms

AACGM	*Altitude-Adjusted Corrected Geomagnetic Co-ordinates*
ACF	*Auto-Correlation Function*
AMPTE	*Active Magnetospheric Particle Tracer Explorer (spacecraft)*
APL	*Applied Physics Laboratory*
APVC	*Azimuthally Propagating Vortical Current*
BAS	*British Antarctic Survey*
BBF	*Bursty Bulk Flow*
BLD	*Boundary Layer Dynamics (model)*
CCE	*Charge Composition Explorer (spacecraft)*
CGM	*Corrected Geomagnetic Co-ordinates*
CNRS	*Centre National de la Recherche Scientifique*
CP	*Common Program*
CUTLASS	*Co-operative UK Twin Located Auroral Sounding System*
DE	*Dynamics Explorer (spacecraft)*
DMSP	*Defense Meteorological Satellite Program*
EISCAT	*European Incoherent SCATter (radar)*
ESR	*EISCAT Svalbard Radar*
FAC	*Field-Aligned Current*
f-o-v	*Field-Of-View*
FMI	*Finnish Meteorological Institute*
GSE	*Geocentric Solar Ecliptic*
GSM	*Geocentric Solar Magnetospheric*
HF	*High Frequency*
IMAGE	*International Monitor for Auroral Geomagnetic Effects*
IMF	*Interplanetary Magnetic Field*
ISTP	*International Solar-Terrestrial Physics (program)*
JHU	*Johns Hopkins University*
LLBL	*Low Latitude Boundary Layer*
l-o-s	*Line-Of-Sight*

LPCE	*Laboratoire de Physique et Chimie de l'Environment*
MFI	*Magnetic Field Experiment*
MLT	*Magnetic Local Time*
MPAe	*Max-Planck-Institut für Aeronomie*
NASA	*National Aeronautic and Space Administration*
NENL	*Near-Earth Neutral Line*
NIPR	*National Institute for Polar Research*
OTH	*Over-The-Horizon*
PPARC	*Particle Physics and Astronomy Research Council*
RTV	*Range-Time-Velocity (plot)*
SAMNET	*Sub-Auroral Magnetometer NETwork*
SCW	*Substorm Current Wedge*
SP	*Special Program*
STARE	*Scandinavian Twin Auroral Radar Experiment*
SuperDARN	*Super Dual Auroral Radar Network*
SWE	*Solar Wind Experiment*
TCV	*Travelling Convection Vortex*
UAF	*University of Alaska, Fairbanks*
UT	*Universal Time*
UV	*Ultraviolet*
UVI	*Ultraviolet Imager*
UHF	*Ultra High Frequency*
VIS	*Visible Imaging System*
VHF	*Very High Frequency*

REFERENCES

Aikio, A. T., and K. U. Kaila, A substorm observed by EISCAT and other ground-based instruments – evidence for near Earth initiation, *J. Atmos. Terr. Phys.*, **58,** 5, 1996.

Akasofu, S. -I., The development of the auroral substorm, *Planet. Space. Sci.*, **12**, 273, 1964.

Akasofu, S. -I., *Polar and Magnetospheric substorms*, published by D. Reidel, Norwell, Mass., 1968.

Akasofu, S.-I., A study of auroral displays photographed from DMSP-2 satellite and from the Alaska meridian chain of stations, *Space Sci. Rev.,* **16,** 617, 1974.

Akasofu, S. -I., Interplanetary energy flux associated with magnetospheric substorms, *Planet. Space Sci.*, **27**, 425, 1979.

Akasofu, S. -I., The solar wind-magnetosphere energy coupling and magnetospheric disturbances, *Planet. Space Sci.*, **28**, 495, 1980.

Akasofu, S. -I.,Energy coupling between the solar wind and the magnetosphere, *Space Sci. Rev.*, **28**, 121, 1981.

Akasofu, S.-I., Auroral arcs and auroral potential structure, *in Physics of Auroral Arc formation, Geophys. Monogr. Ser.*, **25**, published by the American Geophysical Union, ed. S.-I. Akasofu and J. R. Kan, 1981.

Akasofu, S.-I., and D. S. Kimball, The dynamics of the aurora – I. Instabilities of the aurora, *J. Atmos. Terr. Phys.*, **26,** 205, 1964.

Akasofu, S. -I., and J. R. Kan, Auroral arc formation: Kinetic and MHD effects, *Space. Sci. Rev.,* **42**, 499, 1985.

Akasofu, S. –I., S. Chapman, and C. –I. Meng, The polar electrojet, *J. Atmos. Terr. Phys.,* **27**, 1275, 1965.

Angelopoulos, V., W. Baumjohann, C. F. Kennel, F. V. Coroniti, M. G. Kivelson, R. Pellat, R. J. Walker, H. Lühr, and G. Paschmann, Bursty bulk flows in the inner central plasma sheet, *J. Geophys. Res.*, **97**, 4027, 1992.

Angelopoulos, V., F. V. Coroniti, C. F. Kennel, M. G. Kivelson, R. J. Walker, C. T. Russell, R. L. McPherron, E. Sanchez, C. –I. Meng, W. Baumjohann, G. D. Reeves, R. D. Belian, N. Sato, E. Friis-Christensen, P. R. Sutcliffe, K. Yumoto, and T, Harris, Multipoint analysis of a bursty bulk flow event on April 11, 1985, *J. Geophys. Res.*, **101**, 4967, 1996.

Appleton, E. V., and M. A. F. Barnett, Local reflections of wireless waves from the upper atmosphere, *Nature*, **115**, 333, 1925a.

Appleton, E. V., and M. A. F. Barnett, On some evidence for downward atmospheric reflection of electric rays, *Proc. Roy. Soc (London).*, **A109**, 621, 1925b.

Aubry, M. P., C. T. Russell, and M. G. Kivelson, On inward motion of the magnetopause before a substorm, *Geophys. Res*, **75**, 7018, 1970.

Baker, D. N., and T. I. Pulkkinen, The Earthward edge of the plasma sheet in magnetospheric substorms, in *Magnetospheric Substorms, Geophys. Monogr. Ser.,* **64**, ed. J. R. Kan *et al.*, 147, 1991.

Baker, D. N., P. R. Higbie, E. W. Hones Jr., and R. D. Belian, High-resolution energetic particle measurements at 6.6 R_E, 3, Low-energy anisotropies and short-term substorm predictions, *J. Geophys. Res.*, **83**, 4863, 1978.

Baker, D. N., T. I. Pulkkinen, V. Angelopoulos, W. Baumjohann, and R. L. McPherron, Neutral line model of substorms: Past results and present view , *J. Geophys. Res.*, **101**, 12,975, 1996.

Baker, D. N., T. I. Pulkkinen, J. Büchner, and A. J. Klimas, Substorms: A global instability of the magnetosphere-ionosphere system, *J. Geophys. Res*, **104**, 14,601, 1999.

Baker, K. B., and S. Wing, A new magnetic coordinate system for conjugate studies at high latitudes, *J. Geophys. Res*, **94**, 9139, 1989

Bartels, J., The standardized index, K_S, and the planetary index, K_P, *Int. Union. Geod. Geophys. IATME Bull.*, **12b**, 97, 1949.

Bartels, J., and J. Veldkamp, Geomagnetic and solar data, *J. Geophys. Res*, **54**, 295, 1949.

Baumjohann, W., and R. A. Treumann, *Basic Space Plasma Physics*, published by Imperial College Press, 1997.

Baumjohann, W, R. J. Pellinen, H. J. Opgenoorth, and E. Nielsen, Joint two-dimensional observations of ground magnetic and ionospheric electric fields associated with auroral zone currents: current systems associated with local auroral break-ups, *Planet. Space. Sci.*, **29**, 431, 1981.

Baumjohann, W., G. Paschmann, and H. Lühr, Characteristics of high-speed ion flows in the plasma sheet, *J. Geophys. Res,* **95**, 3801, 1990.

Baumjohann, W., M. Hesse, S. Kokubun, T. Mukai, T. Nagai, and A. A. Petrukovich, Substorm dipolarization and recovery, *J. Geophys. Res*, **104**, 24,995, 1999.

Beaujardière, O. de La, R. Vondrak, and M. Baron, Radar observations of electric fields and currents associated with auroral arcs, *J. Geophys. Res*, **82**, 5051, 1977.

Birn, J., E. W. Hones, J. D. Craven, L. A. Frank, R. D. Elphinstone, and D. P. Stern, On open and closed field line regions in Tsyganenko's field model and their possible associations with horse collar auroras, *J. Geophys. Res*, **96**, 3811, 1991.

Borovsky, J. E., R. J. Nemzek, and R. D. Belian, The occurrence rate of magnetospheric-substorm onsets: random and periodic substorms, *J. Geophys. Res,* **98**, 3807, 1993.

Bowles, K. L., Observations of vertical incidence scatter from the ionosphere at 41Mc/sec., *Phys. Rev. Lett.*, **1**, 454, 1958.

Bowles, K. L., B. B. Balsey, and R. Cohen, Radio echoes from field aligned ionoization above the magnetic equator and their resemblance to auroral echoes, *J. Geophys. Res*, **65**, 1853, 1960.

Breit, G., and M. A. Tuve, A radio method of estimating the height of the conducting layer, *Nature*, **116**, 357, 1925.

Breit, G., and M. A. Tuve, A test of the existence of the conducting layer, *Phys. Rev.*, **28**, 554, 1926.

Buchert, S., W. Baumjohann, G. Haerendel, C. La Hoz, and H. Lühr, Magnetometer and incoherent scatter observations of an intense Ps 6 pulsation event, *J. Atmos. Terr. Phys.*, **50,** 357, 1988

Buneman, O., Excitation of field-aligned sound waves by electron streams, *Phys. Rev. Lett.*, **10**, 285,1963.

Burch, J. N., N. A. Saflekos, D. A. Gurnett, J. D. Craven, and L. A. Frank, The quiet time polar cap: DE 1 observations and conceptual model, *J. Geophys. Res*, **97**, 19,403, 1992.

Carlson, H. C., The dark polar ionosphere: progress and future challenges, *Radio Sci.*, **29**, 157, 1994.

Chapman, S., The absorption and dissociative or ionizing effect of monochromatic radiation in an atmosphere on a rotating Earth, *Proc, Phys. Soc. (London)*, **43**, 26, 1931a

Chapman, S., The absorption and dissociative or ionizing effect of monochromatic radiation in an atmosphere on a rotating Earth. II. Grazing incidence, *Proc, Phys. Soc. (London)*, **43**, 483, 1931b

Chapman, S., and V. C. A. Ferraro, A new theory of magnetic storms, *Nature*, **126**, 129, 1931.

Chapman, S., and V. C. A. Ferraro, A new theory of magnetic storms, *Terr. Magn. Atnosph. Elec.*, **36**, 171, 1932.

Clauer, C. R., and R. L. McPherron, Mapping the local time-universal time development of magnetospheric substorms using mid-latitude magnetic observations, *J. Geophys. Res*, **79**, 2811, 1974.

Cohen, R., and K. L. Bowles, The association of plane wave electron density irregularities with the equatorial electrojet, *J. Geophys. Res*, **68**, 2503, 1967.

Cowley, S. W. H., The magnetospheric and its interaction with the solar wind and with the ionosphere, *The behaviour of Systems in the Space Environment*, ed. R. N. DeWitt *et al.*, Kluwer Academic Publishers, 147, 1993.

Cowley, S. W. H., Magnetosphere-Ionosphere Interactions: A Tutorial Review, *Magnetospheric Current Systems, Geophys. Monogr. Ser.*, published by the American Geophysical Union, **118**, 91, 2000

Cowley, S. W. H., and M. Lockwood, Excitation and decay of solar wind-driven flows in the magnetosphere-ionosphere system, *Ann. Geophysicae*, **10**, 103, 1992.

Davies, J. A., M. Lester, and I. W. McCrea, A statistical study of ion frictional heating observed by EISCAT, *Ann. Geophysicae,* **15**, 1399, 1997.

Davies, J. A., M. Lester, and I. W. McCrea, Solar and seasonal dependence of ion frictional heating, *Ann. Geophysicae*, **17**, 682, 1999.

Davies, J. A., T. K. Yeoman, M. Lester, and S. E. Milan, A comparison of F-region ion velocity observations from the EISCAT Svalbard and VHF radars with irregularity drift velocity measurements from the CUTLASS Finland HF radar, *Ann. Geophysicae.* **18**, 589, 2000.

Dougherty, J. P., and D. T. Farley, A theory of incoherent scatter of radio waves by a plasma, *Proc. R. Soc.*, **A259**, 79, 1960.

Dungey, J. W., Interplanetary magnetic field and the auroral zones, *Phys. Rev. Lett.,* **6**, 47, 1961.

Eastman, T. E., L. A. Frank, and C. Y. Huang, The boundary layers as the primary transport regions of the earth's magnetotail, *J. Geophys. Res*, **90**, 9541, 1985.

Elphinstone, R. D., K. Jankowska, J. S. Murphree, and L. L. Cogger, The configuration of the auroral distribution for interplanetary magnetic field B_Z northward: 1. IMF B_X and B_Y dependencies as observed by the Viking satellite, *J. Geophys. Res*, **95**, 5791, 1990.

Elphinstone, R. D., J. S. Murphree, L. L. Cogger, D. J. Hearn, and M. G. Henderson, Observations of changes to the auroral distributions prior to substorm onset, in *Magnetospheric Substorms, Geophys. Monogr. Ser.,* **64**, ed. J. R. Kan *et al.*, 257, 1991.

Elphinstone, R. D., J. S. Murphree, D. J. Hearn, W. Heikkila, M. G. Henderson, L. L. Cogger, and I. Sandahl,The auroral distribution and its mapping according to substorm phase, *J. Atmos. Terr. Phys.*, **55**, 1741, 1993.

Elphinstone, R. D., J. S. Murphree, and L. L. Cogger, What is a global auroral substorm?, *Rev. Geophys.*, **34**, 169, 1996.

Fairfeild, D. H., and G. D. Mead, Magnetospheric mapping with a quantitative geomagnetic field model, *J. Geophys. Res*, **80**, 535, 1975.

Farley, D. T., A plasma instability resulting in field-aligned irregularities in the ionosphere, *J. Geophys. Res*, **63**, 6083, 1963.

Fejer, J., Scattering of radio waves by an ionised gas in thermal equilibium, *J. Geophys. Res*, **65**, 2635, 1960

Feldstein, Y. I., and G. V. Starkov, Dynamics of auroral belt and polar geomagnetic disturbances, *Planet. Space. Sci.*, **15**, 209, 1967.

Fox, N. J., S. W. H. Cowley, J. A. Davies, R. A. Greenwald, M. Lester, M. Lockwood, and H Lühr, Ionospheric ion and electron heating at the poleward boundary of a poleward-expanding substorm-disturbed region, *J. Geophys. Res.*, in press, 2000

Frank, L. A., J. D. Craven, D. A. Gurnett, S. D. Shawhan, D. R. Weimer, J. L. Burch, J. D. Winningham, C. R. Chappell, J. H. Waite, R. A. Heelis, N. C. Maynard, M. Sugiura, W. K. Peterson, and E. G. Shelley, The theta aurora, *J. Geophys. Res*, **91**, 3177, 1986.

Frank, L. A., J. B. Sigwarth, J. D. Craven, J. P. Cravens, J. S. Dolan, M. R. Dvorsky, P. K. Hardebeck, J. D. Harvey, and D. W. Muller, The Visible Imaging System (VIS) for the Polar spacecraft, *Space Sci. Rev.*, **71**, 297, 1995.

Freeman, M. P., and C. J. Farrugia, A statistical study of the possible effects of solar wind variability on the recurrence rate of substorms, *J. Geophys. Res*, **100**, 23,607, 1995.

Freeman, M. P., J. M. Ruohoniemi, and R. A. Greenwald, The determination of time-stationary two-dimensional convection patterns with single-station radars, *J. Geophys. Res*, **96**, 15,735 1991.

Fujii, R., R. A. Hoffman, P. C. Anderson, J. D. Craven, M. Sugiura, L. A. Frank, and N. C. Maynard, Electrodynamic parameters in the nighttime sector during auroral substorms, *J. Geophys. Res.*,**99**, 6093, 1994.

Glassmeier, K.-H., Travelling magnetospheric convection twin-vortices: observations and theory, *Ann. Geophysicae*, **10**, 547, 1992.

Goertz, R. A., Physics of auroral arc formation, in *The Chapman conference on 'The formation of auroral arcs'*, published by the American Geophysical Union, 1981.

Goertz, R. A., and R. A. Smith, Thermal catastrophe model of substorms, *J. Geophys. Res*, **94**, 6581, 1989.

Gordon, W. E., Incoherent scatter of radio waves by free electrons with applications to space exploration by radar, *Proc. IRE,* **46**, 1824, 1958.

Greenwald, R. A., W. Weiss, and E. Nielsen, STARE: A new radar auroral backscatter experiment in northern Scandinavia, *Radio Sci.,* **13**, 1021, 1978.

Greenwald, R. A., K. B. Baker, R. A. Hutchins, and C. Hanuise, An HF radar phase-array for studying small-scale structure in the high-latitude ionosphere, *Radio. Sci.,* **20**, 63, 1985.

Greenwald, R. A., K. B. Baker, J. R. Dudeney, M. Pinnock, T. B. Jones, E. C. Thomas, J.-P. Villain, J. –C. Cerisier, C. Senior, C. Hanuise, R. D. Hunsucker, G. Sofko, J. Koehler, E. Nielsen, R. Pellinen, A. D. M. Walker, N. Sato, and H. Yamagishi, Darn/SuperDARN: a global view of the dynamics of high-latitude convection, *Space Sci. Rev,* **71,** 761, 1995.

Gussenhoven, M. S., Extremely high latitude auroras, *J. Geophys. Res*, **87**, 2401, 1982.

Haerendel, G., Disruption, ballooning, or auroral avalanche: On the cause of substorms, *Proc. ICS-1,* **ESA SP-335**, 417, 1992.

Hagfors, T., Density fluctuations in a plasma in a magnetic field with applications to the ionosphere, *J. Geophys. Res*, **66**, 1699, 1961.

Haldoupis, C., A review on radio studies of auroral E-region ionospheric irregularities, *Ann. Geophysicae*, **7**, 239, 1988.

Hallinan, T. J., Auroral spirals: 2. Theory, *J. Geophys. Res.*, **81,** 3959, 1976.

Hargreaves, J. K., *The upper atmosphere and solar-terrestrial relations*, published by the Van Nostrand Reinhold Company, 1979.

Henderson, M. G., and J. S. Murphree, Comparison of Viking onset locations with the predictions of the thermal catastrophe model, *J. Geophys. Res*, **100**, 21,857, 1995.

Henderson, M. G., J. S. Murphree, and J. M. Weygand, Observations of auroral substorms occurring together with preexisting "quiet time" auroral pattern, *J. Geophys. Res*, **101**, 24,621, 1996

Henderson, M. G., G. D. Reeves, and J. S. Murphree, Are north-south aligned auroral structures an ionospheric manifestation of bursty bulk flows?, *Geophys. Res. Lett.,* **25**, 3737, 1998.

Heppner, J. P., and N. C. Maynard, Empirical high latitude electric field models, *J. Geophys. Res*, **92**, 4467, 1987.

Holzworth, R. H., and C. –I. Meng, Mathematical representation of the auroral oval, *Geophys. Res. Lett.*, **2**, 377, 1975.

Hones, E. W., Plasma sheet behaviour during subtorms, in *Magnetic reconnection in space and laboratory plasmas, Geophys. Monogr. Ser.*, **30**, 178, published by the American Geophysical Union, edited by E. W. Hones, 1984

Hones, E. W., J. D. Craven, L. A. Frank, D. S. Evans, and P. T. Newell, The horse-collar aurora – a frequent pattern of the aurora in quiet times, *Geophys. Res. Lett.*, **16**, 37, 1989.

Hughes, W. J., The Magnetopause, Magnetotail, and Magnetic Reconnection, in *Introduction to Space Plasma Physics*, ed. M. G. Kivelson and C. T. Russell, published by Cambridge University Press, 227, 1995.

Iijima, T., and T. A. Potemra, Large-scale characteristics of filed-aligned currents associated with substorms, *J. Geophys. Res*, **83**, 599, 1978.

Ismail, S., and C. –I. Meng, A classification of polar cap auroral arcs, *Planet. Space. Sci.*, **30**, 319, 1982.

Jacquey, C., J. A. Sauvard, and J. Dandouras, Location and propagation of the magnetotail current disruption during substorm expansion: analysis and simulation of an ISEE multi-onset event, *Geophys. Res. Lett.*, **18**, 389, 1991.

Kawasaki, K., and G. Rostoker, Perturbation magnetic fields and current systems associated with eastward drifting auroral structures, *J. Geophys. Res.*, **84,** 1464, 1979.

Kelley, M. C., *The earth's Ionosphere: Plasma Physics and Electrodynamics*, published by Academic Press Inc, 1989.

Khan, H., and S. W. H. Cowley, Observations of the response time of high-latitude ionospheric convection to variations in the interplanetary magnetic field using EISCAT and IMP-8 data, *Ann. Geophysicae.,* **17**, 1306, 1999.

Kivelson, M. G., and C. T. Russell, *Introduction to Space Physics*, published by Cambridge University Press, 1995.

Kokubun, S., and R. L. McPherron, Substorm signatures at synchronous altitudes, *J. Geophys. Res*, **86**, 11,265, 1981.

Koskinen, H. E. J., R. E. Lopez, R. J. Pellinen, T. I. Pulkkinen, D. N. Baker, and T. Bösinger, Pseudobreakup and substorm growth phase in the ionosphere and magnetosphere, *J. Geophys. Res*, **98**, 5801, 1993.

Lepping, R. P., M. H. Acuna, L. F. Burlaga, W. M. Farrell, J. A. Slavin, K. H. Schatten, F. Mariani, N. F. Ness, F. M. Neubaur, Y. C. Whang, J. Byrnes, R. S. Kennon, P. V. Panetta, J. Scheifele, and E. M. Worley, The Wind magnetic field investigation, *Space. Sci. Rev.*, **71**, 207, 1995.

Lester, M., W. J. Hughes, and H. J. Singer, Longitudinal structure in Pi 2 pulsations and the substorm current wedge, *J. Geophys. Res.*, **89**, 5489, 1984.

Lewis, R. V., P. J. S. Williams, G. O. L. Jones, H. J. Opgenoorth, and M. A. L. Persson, The elctrodynamics of a drifting auroral arc, *Ann. Geophysicae*, **12**, 478, 1994.

Lewis, R. V., M. P. Freeman, A. S. Rodger, G. D. Reeves, and D. K. Milling, The electric field response to the growth phase and expansion phase onset of a small substorm, *Ann. Geophysicae*, **15**, 289, 1997.

Lockwood, M, and S. W. H. Cowley, Ionospheric convection and the substorm cycle, *Proc. Inst. Conf. On Substorms,* ESA SP-335, **99**, 1992.

Lockwood, M., S. W. H. Cowley, P. E. Sandholt, and R. P. Lepping, The ionospheric signatures of flux transfer events and solar wind dynamic pressure changes, *J. Geophys. Res,* **95**, 17,113, 1990.

Lopez, R. E., and A. T. Y. Lui, A multi-satellite case study of the expansion of a substorm current wedge in the near-earth magnetotail, *J. Geophys. Res*, **95**, 1990.

Lühr, H., The IMAGE magnetometer network, *STEP International Newsletter*, **4**, (10), 4, 1994.

Lühr, H., and K. Schlegel, Combined measurements of EISCAT and the EISCAT magnetometer cross to study Ω bands, *J. Geophys. Res.*, **99**, 8951, 1994.

Lühr, H., W. Blawert, and H. Todd, Ionospheric plasma and current patterns of travelling convection vortices: a case study, *J. Atmos. Terr. Phys.,* **55**, 1717, 1993.

Lühr, H., M. Lockwood, P. E. Sandholt, T. L. Hansen, and T. Moretto, Multi-instrument ground based observations of a travelling convection vortices event, *Ann. Geophysicae,* **14**, 162, 1996.

Lui, A. T. Y., A synthesis of Magnetospheric Substorm Models, *J. Geophys. Res*, **96**, 1849, 1991.

Lui, A.T. Y., R. E. Lopez, S. M. Krimigis, R. W. McEntire, L. J. Zanetti, and T. A. Potemra, A case study of magnetotail current sheet disruption and diversion, *Geophys. Res. Lett.*, **15**, 721, 1988.

Lui, A. T. Y., A. Mankofsky, C. –L. Chang, K. Papadopolous, and C. S. Wu, A current disruption mechanism in the neutral sheet: a possible trigger for substorm expansion, *Geophys. Res. Lett.*, **17**, 745, 1990.

Lui, A.T. Y., W. Baumjohann, and G. Rostoker, Substorm expansion onset mechanism debated, *EOS (Transactions of the American Geophysical Union)*, **81(7)**, 70, 2000.

Lyons, L. R., and R. L. Walterscheid, Generation of aurora omega bands by shear instability in the neutral wind, *J. Geophys. Res*, **90**, 12,321, 1985.

Lyons, L. R., T. Nagai, G. T. Blanchard, J. C. Samson, T. Yamamoto, T. Mukai, A. Nishida, and S. Kokubun, Association between Geotail plasma flows and auroral poleward boundary intensifications observed by CANOPUS photometers, *J. Geophys. Res,* **104**, 4485, 1999.

Marklund, G., Auroral arc classification scheme based on the observed arc-associated electric field pattern, *Planet. Space Sci.*, **32**, 193, 1984.

McPherron, R. L, Growth phase of magnetospheric substorms, *J. Geophys. Res*, **75**, 5592, 1970.

McPherron, R. L., C. T. Russell, and M. Aubry, Satellite studies of magnetospheric substorms on August 15, 1978, Phenomenological model for substorms, *J. Geophys. Res*, **78**, 3131, 1973.

Milan, S. E., T. B. Jones, M. Lester, E. M. Warrington, and G. D. Reeves, Substorm correlated absorption on a 3200 km trans-auroral HF propagation path, *Ann. Geophysicae,* **14**, 182, 1996.

Milan, S. E., M. Lester, and J. Moen, A comparison of optical and coherent HF radar backscatter observations of a post-midnight aurora, *Ann. Geophysicae.*, **15** 1388, 1997.

Milan, S. E., J. A. Davies, and M. Lester, Coherent HF radar backscatter characateristics associated with auroral forms identified by incoherent techniques: a comparison of CUTLASS and EISCAT observations, *J. Geophys. Res*, **104**, 22,591, 1999.

Morelli, J. P., R. J. Bunting, S. W. H. Cowley, C. J. Farrugia, M. P. Freeman, E. Friis-Christensen, G. O. L. Jones, M. Lester, R. V. Lewis, H. Lühr. D. Orr, M. Pinnock, G. D. Reeves, P. J. S. Willliams, and T. K. Yeoman, Radar observations of auroral zone flows during a multiple onset substorm, *Ann. Geophysicae*, **13**, 1144, 1995.

Mravlag, E, M. W. J. Scourfield, A. D. M. Walker, P. R. Sutcliffe, and E. Nielsen, Simultaneous observations of omega band related phenomena in both hemispheres, *J. Atmos. Terr. Phys.*, **53,** 309, 1991.

Murphree. J. S., R. D. Elphinstone, L. L. Cogger, and D. Hearn, *Viking* optical substorm signatures, in *Magnetospheric Substorms, Geophys. Monogr. Ser.,* **64**, published by the American Geophysical Union, ed. J. R. Kan *et al.*, 241, 1991.

Nakamura, R., G. Haerendel, W. Baumjohann, A. Vaivads, H. Kucharek, B. Klecker, E. Georgescu, J. Birn, L. M. Kistler, T. Mukai, S. Kokubun, P. Eglitis, L. A. Frank, and J. B. Sigwarth, Substorm observations in the early morning sector with Equator-S and Geotail, **17**, 1602, 1999.

Nielsen, E., Coherent radar techniques, *WITS Handbook*, Chapter 11, SCOSTEP, 1989.

Ogilvie, K. W., D. J. Chornay, R. J. Fritzenreiter, F. Hunaker, J. Keller, J. Lobell, G. Miller, J. D. Scudder, E. C. Sittler Jr., R. B. Torbert, D. Bodet, G. Needell, A. J. Lazarus, J. T. Steinberg, J. H. Tappen, A. Mavretic, and E. Gergin, SWE, a comprehensive plasma instrument for the Wind spacecraft, *Space Sci. Rev.*, **71**, 55, 1995.

Opgenoorth, H. J., and R. J. Pellinen, The reaction of the global convection electrojets to the onset and expansion of the substorm current wedge, *Proceedings of ICS-4,* edited by S. Kokubun and Y. Kamide, Kluwer Academic Publishers, 1998.

Opgenoorth, H. J., J. Oksman, K. U. Kaila, E. Nielsen, and W. Baumjohann, Characteristics of eastward drifting omega bands in the morning sector of the auroral oval, *J. Geophys. Res.*, **88,** 9171,1983.

Opgenoorth, H. J., I. Häggström, P. J. S. Williams, and G. O. L. Jones, Regions of strongly enhanced perpendicular electric fields adjacent to auroral arcs, *J. Atmos. Terr. Phys.*, **52**, 449, 1990.

Opgenoorth, H. J., M. A. L. Persson, T. I. Pulkkinen, and R. J. Pellinen, Recovery phase of magnetospheric substorms and its association with morning sector aurora, *J. Geophys. Res.*, **99,** 4115, 1994.

Ossakow, S. L., and P. K. Chaturverdi, Current convection instability in the diffuse aurora, *Geophys. Res. Lett.*, **6**, 332, 1979.

Parker, E. N., *Interplanetary Dynamical Processes,* published by Wiley-Inter-Science, New York, 1963.

Parks, G. K., M. McCarthy, R. J. Fitzenreiter, J. Etcheto, K. A. Anderson, R. R. Anderson, T. E. Eastman, L. A. Frank, D. A. Gurnett, C. Huang, R. P. Lin, A. T. Y. Lui, K. W. Ogilvie, A. Pedersen, H. Reme, and D. J. Williams, Particle and field characteristics of the high-latitude boundary layer, *J. Geophys. Res*, **89**, 8885, 1984.

Pellinen, R. J., H. J. Opgenoorth, and T. I. Pulkkinen, Substorm recovery phase: relationship to next activation, *Proceedings of ICS -1,* **ESA SP-335,** 469-475, 1992.

Perreault, P., and S. –I. Akasofu, A study of geomagnetic storms, *Geophys. J. R. Astr. Soc.*, 54, 547, 1978.

Pinnock, M., A. S. Rodger, J. R. Dudeney, F. Rich, and K. B. Baker, High spatial and temporal resolution observations of the ionospheric cusp, *Ann. Geophysicae*, **13**, 919, 1995.

Priest, E. R., The Sun and its magnetohydrodynamics, in *Introduction to Space Plasma Physics*, ed. M. G. Kivelson and C. T. Russell, published by Cambridge University Press, 58, 1995.

Prikryl, P., and L. L. Cogger, Statistical analysis of the spatial relationship between the radio and optical aurora: Further evidence for refraction, *Rad. Sci.*, **27**, 469, 1992.

Provan, G., Coherent scatter radar observations of field line resonances and flux transfer events, PhD. Thesis, University of Leicester, 1998.

Risheth, H., and O. K. Garriott, *Introduction to Ionospheric Physics*, published by Academic Press, 1969.

Rishbeth, H., and P. J. S. Williams, The EISCAT Ionospheric radar: the system and its early results, *Q. Jl. R. astr. Soc*, **26**, 478, 1985.

Robinson, T. R., Towards a self-consistent non-linear theory of radar auroral backscatter, *J. Atmos. Terr. Phys.*, **48**, 417, 1986.

Rodger, A. S., Recent scientific advances in geospace research using coherent- and incoherent-scatter radars, in *Review of Radio Science*, ed. W. Ross Stone, published by Oxford University Press, 1999.

Roelof, E. C., and D. G. Sibeck, Magnetopause shape as a bivariate function of interplanetary magnetic field BZ and solar wind dynamic pressure, *J. Geophys. Res*, **98**, 21,421, 1993.

Rostoker, G., Geomagnetic indices, *Rev. Geophys. Space Phys.*, **10**, 935, 1972.

Rostoker, G., Phenomenology and physics of magnetospheric substorms, *J. Geophys. Res.*, **101**, 12,955, 1996.

Rostoker, G., and J. C. Barichello, Seasonal and diurnal variation of Ps 6 magnetic disturbances, *J. Geophys. Res.*, **85,** 161, 1980.

Rostoker, G., and T. E. Eastman, A boundary layer model for magnetospheric substorms, *J. Geophys. Res*, **92**, 12,187, 1987.

Rostoker, G., S. –I. Akasofu, J. Foster, R. A. Greenwald, Y. Kamide, K. Kawasaki, A. T. Y. Lui, R. L. McPherron, and C. T. Russell, Magnetospheric substorms – definitions and signatures, *J. Geophys. Res*, **85**, 1663, 1980.

Rostoker, G., S, –I. Akasofu, W. Baumjohann, Y. Kamide, and R. L. McPherron, The roles of direct input of energy from the solar wind and unloading of stored magnetotail energy in driving magnetospheric substorms, *Space Sci. Rev.*, **46**, 93, 1987.

Ruohoniemi, J. M., R. A. Greenwald, K. B. Baker, J. –P. Villain, C. Hanuise, and J. Kelly, Mapping High-Latitude Plasma Convection with Coherent HF radars, *J. Geophys. Res.*, **94**, 13,463, 1989.

Russell, C. T., A brief history of solar-terrestrial physics, in *Introduction to Space Plasma Physics*, ed. M. G. Kivelson and C. T. Russell, published by Cambridge University Press, 1, 1995.

Russell, C. T., and R. L. McPherron, The magnetotail and substorms, *Space Sci. Rev.*,**11**, 111, 1973.

Saito, T., Long-period irregular magnetic pulsations, Pi3, *Space Sci. Rev,* **21,** 427, 1978.

Sato, N., H, Fukunishi, and Th. Saemundsson, Operation plan for the Iceland-Syowa conjugate campaign in 1983-1985, *Mem. Natl. Inst. Polar Res.*, **31**, 169, 1984.

Shiokawa, K., W. Baumjohann, G. Haerendel, G. Paschmann, J. F. Fennell, , E. Friis-Christensen, H. Lühr, G. D. Reeves, C. T. Russell, P. R. Sutcliffe, K. Takahashi, High-speed ion flow, substorm current wedge, and multiple Pi 2 pulsations, *J. Geophys. Res*, **103**, 4491, 1998.

Smith, R. A., C. K. Goertz, and W. Grossmann, Thermal catastrophe in the plasma sheet boundary layer, *Geophys. Res. Lett.*, **13**, 1380, 1986.

Snyder, A. L., Jr., and S. I. Akasofu, Major auroral substorm features in the dark sector observed by a USAF DMSP satellite, *Planet. Space Sci.*, **22,** 1511, 1974.

Sudan, R. N., J. Akinrimisi, and D. T. Farley, Generation of small-scale irregularirues in the equatorial electrojet, *J. Geophys. Res*, **78**, 240, 1973.

Takahasi, K., L. J. Zanetti, R. E. Lopez, R. W. McEntire, T. A. Potemra, and K. Yumoto, Disruption of the magnetotail current sheet observed by AMPTE/CCE, *Geophys. Res. Lett.*, **14,** 1019, 1987.

Thomson, J. J., *Conduction of electricity through gases*, published by Cambridge University Press, 1906.

Torr, M. R., D. G. Torr, M. Zukic, R. B. Johnson, J. Ajello, P. Banks, K. Clark, K. Cole, C. Keffer, G. Parks, B. Tsurutani, and J. Spann, A far ultraviolet imager for the international solar-terrestrial physics mission, *Space Sci. Rev*, **71,** 329, 1995.

Untiedt, J., and W. Baumjohann, Studies of current systems using the IMS Scandinavian magnetometer array, *Space Sci. Rev.*, **63**, 245, 1993.

Villain, J. P., R. A. Greenwald, K. B. Baker, and J. M. Ruohoniemi, HF radar observations of E region plasma irregularities produced by oblique electron streaming, *J. Geophys. Res*, **92**, 12,327, 1987

Walker, R. J., K. N. Erikson, R. L. Swanson, and J. R. Winckler, Substorm-associated particle boundary motion at synchronous orbit, *J. Geophys. Res.*, **81**, 5541, 1976.

Wannberg, G., I. Wolf, L. –G. Vanhainen, K. Koskenniemi, J. Röttger, M. Postila, J. Markkanen, R. Jacobsen, A. Stenberg, R. Larsen, S. Eliassen, S. Heck, and A. Huuskonen, The EISCAT Svalbard Radar: A case study in modern incoherent scatter radar system design, *Radio Sci.* **32**, 2283, 1997.

Wild, J. A., and T. K. Yeoman, CUTLASS HF radar observations of high latitude azimuthally propagating vortical currents in the nightside ionosphere during magnetospheric substorms, *Ann. Geophysicae*, **18**, 640, 2000.

Wild, J. A., T. K. Yeoman, P. Eglitis, and H. J. Opgenoorth, Multi-instrument observations of the electric and magnetic field structure of omega bands, *Ann. Geophysicae*, **18**, 99, 2000.

Wilhjelm, J., and E. Friis-Christensen, Electric fields and high latitude zonal currents induced by merging of field lines, *Geophys. Pap R-31*, Dan. Meteorol. Inst., Charlottenlund, Denmark, 1976.

Yamamoto, T., K. Makita, M. Ozaki, and C.-I. Meng, A particle simulation of auroral bands and torch-like structures, *J. Geomag. Geoelectr.*, **45**, 619, 1993.

Yamamoto, T., S. Inoue, and C.-I. Meng, Formation of auroral omega bands in the paired region 1 and region 2 field-aligned current system, *J. Geophys. Res.*, **102,** 2531, 1997.

Yeoman, T. K., and M. Pinnock, The high-latitude convection response to an interval of substorm activity, *Ann. Geophysicae,* **14**, 518, 1996.

Yeoman, T. K., and H. Lühr, CUTLASS/IMAGE observations of high-latitude convection features during substorms, *Ann. Geophysicae,* **15**, 692, 1997.

Yeoman, T. K., and J. A. Wild, HF radar observations of azimuthally propagating transient convection features in the substorm electrojets, *Proceedings of ICS-4*, edited by S. Kokubun and Y. Kamide, Kluwer Academic Publishers, 1998.

Yeoman, T. K., and J. A. Wild, Transient ionospheric convection features associated with substorms and BBFs, *Proceedings of ICS-5*, in press, 2000.

Yeoman, T. K., M. D. Burrage, M. Lester, T. R. Robinson, and T. B. Jones, Long–Term variation of Radar-Auroral Backscatter and the Interplanetary Sector Structure, *J. Geophys. Res.*, **95**, 21,123, 1990a.

Yeoman, T. K., D. K. Milling, and D. Orr, Pi2 pulsation polarisation patterns on the U.K. Sub-auroral Magnetometer Network (SAMNET), *Planet. Space Sci.*, **38**, 589-602, 1990b.

Yeoman, T. K., N. Mattin, J. M. Ruohoniemi, M. Lester, and M. Pinnock, An assessment of the *L* shell fitting beam-swinging technique for measuring ionospheric *E* region irregularity drift patterns, *J. Geophys. Res*, **97**, 14,885, 1992.

Yeoman, T. K., T. Mukai, and T. Yamamoto, Simultaneous ionospheric and magnetospheric observations of azimuthally propagating transient features during substorms, *Ann. Geophysicae,* **16**, 754, 1998.

Yeoman, T. K., J. A. Davies, N. M. Wade, G. Provan, and S. E. Milan, Combined CUTLASS, EISCAT, and ESR observations of an isolated substorm, *Ann. Geophysicae,* in press 2000.